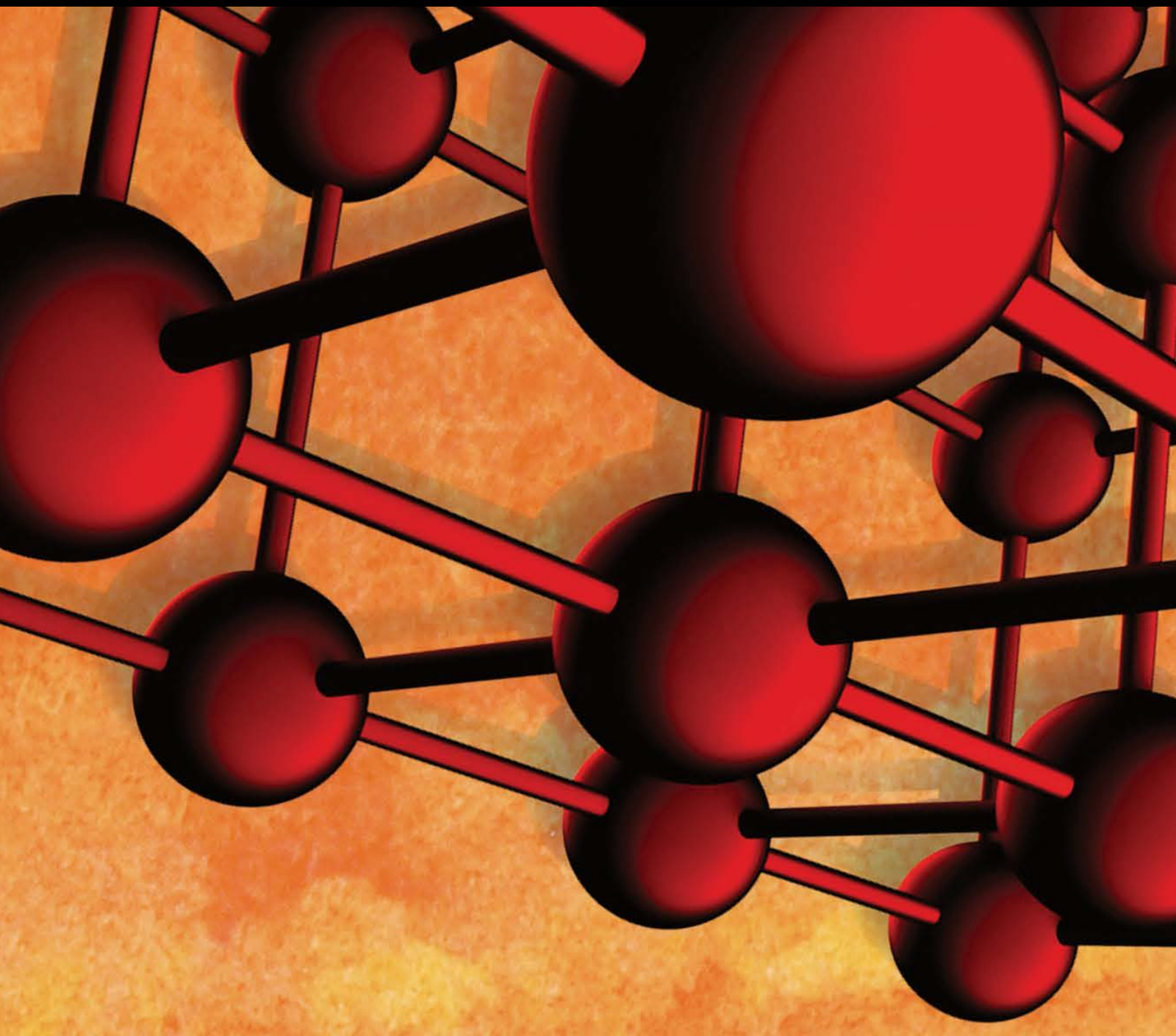


Advances in Materials Science and Engineering

# Metamaterials and Smart Structures in a Big Data Era

Guest Editors: Ying Wang, Francesco dell'Isola, Tiejun Liu, and Chunhui Yang





---

# **Metamaterials and Smart Structures in a Big Data Era**

Advances in Materials Science and Engineering

---

## **Metamaterials and Smart Structures in a Big Data Era**

Guest Editors: Ying Wang, Francesco dell'Isola,  
Tiejun Liu, and Chunhui Yang



---

Copyright © 2017 Hindawi Publishing Corporation. All rights reserved.

This is a special issue published in “Advances in Materials Science and Engineering.” All articles are open access articles distributed under the Creative Commons Attribution License, which permits unrestricted use, distribution, and reproduction in any medium, provided the original work is properly cited.

## Editorial Board

- M. S.A. Abdel-Mottaleb, Egypt  
Michael Aizenshtein, Israel  
Jarir Aktaa, Germany  
K. G. Anthymidis, Greece  
Amit Bandyopadhyay, USA  
Arun Bansil, USA  
Massimiliano Barletta, Italy  
Mikhael Bechelany, France  
Jozef Bednarcik, Germany  
Avi Bendavid, Australia  
Jamal Berakdar, Germany  
Giovanni Berselli, Italy  
Patrice Berthod, France  
Susmita Bose, USA  
H.-G. Brokmeier, Germany  
Steve Bull, UK  
Peter Chang, Canada  
Daolun Chen, Canada  
Gianluca Cicala, Italy  
Gabriel Cuello, France  
Narendra B. Dahotre, USA  
João P. Davim, Portugal  
Angela De Bonis, Italy  
Francesco Delogu, Italy  
Seshu B. Desu, USA  
Guru P. Dinda, USA  
Yong Ding, USA  
N. Tzankova Dintcheva, Italy  
Kaveh Edalati, Japan  
Philip Eisenlohr, USA  
Paolo Ferro, Italy  
Massimo Fresta, Italy  
Eric Freysz, France  
Sergi Gallego, Spain  
Santiago Garcia-Granda, Spain  
Filippo Giannazzo, Italy  
Daniel Guay, Canada
- Hiroki Habazaki, Japan  
Joke Hadermann, Belgium  
Satoshi Horikoshi, Japan  
David Houivet, France  
Rui Huang, USA  
Michele Iafisco, Italy  
Katsuyuki Kida, Japan  
Jae-Ho Kim, Republic of Korea  
Akihiko Kimura, Japan  
Takayuki Kitamura, Japan  
Hongchao Kou, China  
Prashant Kumta, USA  
Luciano Lamberti, Italy  
Heinrich Lang, Germany  
Pavel Lejcek, Czech Republic  
Cristina Leonelli, Italy  
Ying Li, USA  
Jun Liu, China  
Meilin Liu, Georgia  
Wei Liu, France  
Yunqi Liu, China  
F. Lusquiños, Spain  
Peter Majewski, Australia  
Philippe Miele, France  
Hossein Moayedi, Iran  
Paul Munroe, Australia  
Rufino M. Navarro, Spain  
Luigi Nicolais, Italy  
Hirosi Noguchi, Japan  
Chérif Nouar, France  
José L. Ocaña, Spain  
Tsutomu Ohzuku, Japan  
Olanrewaju Ojo, Canada  
Gianfranco Palumbo, Italy  
A. M. Paradowska, Australia  
Matthew Peel, UK  
Gianluca Percoco, Italy
- Giorgio Pia, Italy  
J.-F. Pierson, France  
Simon C. Potter, Canada  
Manijeh Razeghi, USA  
Yuri Ribakov, Israel  
Anna Richelli, Italy  
Antonio Riveiro, Spain  
Pascal Roussel, France  
Timo Sajavaara, Finland  
Antti Salminen, Finland  
F.H. Samuel, Canada  
Carlo Santulli, Italy  
F.-J. Schmitt, Germany  
Fridon Shubitidze, USA  
Maria A. Signore, Italy  
Donato Sorgente, Italy  
C. C. Sorrell, Australia  
Costas M. Soukoulis, USA  
Sam-Shajing Sun, USA  
Kohji Tashiro, Japan  
Achim Trampert, Germany  
Filip Tuomisto, Finland  
Qiang Wang, China  
Rong Wang, USA  
Rui Wang, China  
Lu Wei, China  
Jörg M. K. Wieszorek, USA  
Wei Wu, USA  
Hemmige S. Yathirajan, India  
Wenbin Yi, China  
Belal F. Yousif, Australia  
Jinghuai Zhang, China  
Li Zhang, China  
Ming-Xing Zhang, Australia  
Wei Zhou, China

# Contents

---

## **Metamaterials and Smart Structures in a Big Data Era**

Ying Wang, Francesco Dell'Isola, Tiejun Liu, and Chunhui Yang  
Volume 2017, Article ID 6358497, 1 page

## **Musical Tone Law Method for the Structural Damage Detection**

Weisong Yang, Weixiao Xu, Xun Guo, and Liguang Yang  
Volume 2017, Article ID 8560596, 10 pages

## **Seismic Performance and Ice-Induced Vibration Control of Offshore Platform Structures Based on the ISO-PFD-SMA Brace System**

Jigang Zhang, Zhehao Ma, Feifei Liu, Chunwei Zhang, Pezhman Sharafi, and Maria Rashidi  
Volume 2017, Article ID 3596094, 15 pages

## **On Finite Element Computations of Contact Problems in Micropolar Elasticity**

Victor A. Eremeyev, Andrzej Skrzat, and Feliks Stachowicz  
Volume 2016, Article ID 9675604, 9 pages

## **Plane Wave-Perturbative Method for Evaluating the Effective Speed of Sound in 1D Phononic Crystals**

J. Flores Méndez, M. Salazar Villanueva, R. C. Ambrosio Lázaro, B. Calixto Sirene, M. L. Mota González, and F. Candia García  
Volume 2016, Article ID 3017835, 9 pages

## **Experimental Research on 2 : 1 Parametric Vibration of Stay Cable Model under Support Excitation**

Li-Na Zhang, Feng-Chen Li, Xiang Yu, Peng-Fei Cui, and Xiao-Yong Wang  
Volume 2016, Article ID 9804159, 9 pages

## **Impact-Induced Delamination Detection of Composites Based on Laser Ultrasonic Zero-Lag Cross-Correlation Imaging**

Yun-Kyu An  
Volume 2016, Article ID 6474852, 8 pages

## **A Bridge Deflection Monitoring System Based on CCD**

Baohua Shan, Lei Wang, Xiaoyang Huo, Wenting Yuan, and Zhilin Xue  
Volume 2016, Article ID 4857373, 11 pages

## **Experimental Research on Quick Structural Health Monitoring Technique for Bridges Using Smartphone**

Xuefeng Zhao, Kwang Ri, Ruicong Han, Yan Yu, Mingchu Li, and Jinping Ou  
Volume 2016, Article ID 1871230, 14 pages

## **Effect of Nanosilica on the Fresh Properties of Cement-Based Grouting Material in the Portland-Sulphoaluminate Composite System**

Shengli Li and Tingting Xu  
Volume 2016, Article ID 2707465, 10 pages

## **Study on Acoustic Emission Characteristics of a Semirigid Base of Dense Skeleton Type during Complete Uniaxial Compression Tests**

Shengli Li, Guangming Wu, and Hao Wu  
Volume 2016, Article ID 9238698, 8 pages

**Emergency Communication and Quick Seismic Damage Investigation Based on Smartphone**

Ruicong Han, Xuefeng Zhao, Yan Yu, Quanhua Guan, Deli Peng, Mingchu Li, and Jinping Ou

Volume 2016, Article ID 7456182, 15 pages

**Magnetodielectric and Metalomagnetic 1D Photonic Crystals Homogenization:  $\epsilon$ - $\mu$  Local Behavior**

J. I. Rodríguez Mora, J. Flores Méndez, B. Zenteno Mateo, F. Severiano Carrillo, and R. C. Ambrosio Lázaro

Volume 2016, Article ID 7451941, 5 pages

## Editorial

# Metamaterials and Smart Structures in a Big Data Era

**Ying Wang,<sup>1</sup> Francesco Dell'Isola,<sup>2</sup> Tiejun Liu,<sup>3</sup> and Chunhui Yang<sup>4</sup>**

<sup>1</sup>*Department of Civil and Environmental Engineering, University of Surrey, Guildford, Surrey, UK*

<sup>2</sup>*Faculty of Engineering, University of Rome "La Sapienza", Rome, Italy*

<sup>3</sup>*School of Civil and Environment Engineering, Urban & Civil Engineering Disaster Prevention & Reduction Research Center, Shenzhen Graduate School of Harbin Institute of Technology, Shenzhen, Guangdong, China*

<sup>4</sup>*School of Computing, Engineering and Mathematics, Western Sydney University, Sydney, NSW, Australia*

Correspondence should be addressed to Ying Wang; [ying.wang@surrey.ac.uk](mailto:ying.wang@surrey.ac.uk)

Received 18 December 2016; Accepted 19 December 2016; Published 8 February 2017

Copyright © 2017 Ying Wang et al. This is an open access article distributed under the Creative Commons Attribution License, which permits unrestricted use, distribution, and reproduction in any medium, provided the original work is properly cited.

Nowadays, there is no doubt that we have been into the big data era. Under such a circumstance, developing future smart materials and structural systems is largely dependent on big data analysis. This offers not only opportunities to help engineers improve the safety and maintainability of critical structures but also new challenges which required further advances in fundamental research and applied technologies. On the other hand, wide technical possibilities are opened by the design of new metamaterials in sound and vibration control, biomechanics, nanotechnology, and extreme mechanics.

Based on the above considerations, we gathered together in 2016 and proposed this special issue which is aimed at serving a research milestone that summarizes the most recent progress in the field of metamaterials and smart structures.

To ensure the paper quality, rigorous reviews have been performed, and the final acceptance rate is around 40%. The 12 papers appearing in this special issue address a wealth of topics relevant to the proposed topics. This special issue discusses various materials including different characteristics and performances of 1D photonic crystals and the effect of nanosilica on the fresh properties of cement-based grouting material. It also discusses different structural damage detection methods, including musical tone law method by using vibration data, delamination detection based on laser ultrasonic imaging, bridge deflection monitoring using CCD cameras, and quick structural monitoring and damage assessment technique using smartphone. Further, it addresses the

finite element computations of contact problems in micropolar elasticity, as well as vibration and acoustic emission tests on scaled structural models.

## Acknowledgments

As the guest editors of this special issue, we would like to thank the authors who willingly submitted their works of high quality to bring about this special issue. Likewise, the great help of the reviewers is also appreciated, and their careful observations, valuable comments, and suggestions contributed significantly to improve the content of this special issue. Finally, we would like to express our sincere gratitude to the editors of this journal, for encouraging and agreeing to this special issue, which was indispensable in putting together this special issue.

*Ying Wang  
Francesco Dell'Isola  
Tiejun Liu  
Chunhui Yang*

## Research Article

# Musical Tone Law Method for the Structural Damage Detection

Weisong Yang,<sup>1</sup> Weixiao Xu,<sup>1</sup> Xun Guo,<sup>2</sup> and Liguang Yang<sup>2</sup>

<sup>1</sup>School of Civil Engineering, Qingdao University of Technology, Qingdao 266033, China

<sup>2</sup>Institute of Disaster Prevention, Sanhe 065200, China

Correspondence should be addressed to Weixiao Xu; wxgodspeed@163.com

Received 20 July 2016; Revised 26 October 2016; Accepted 23 November 2016; Published 31 January 2017

Academic Editor: Tiejun Liu

Copyright © 2017 Weisong Yang et al. This is an open access article distributed under the Creative Commons Attribution License, which permits unrestricted use, distribution, and reproduction in any medium, provided the original work is properly cited.

Damage detection tests of inclined cables, steel pipes, spherical shells, and an actual cable-stayed bridge were conducted based on the proposed musical tone law method. The results show that the musical tone law method could be used in the damage detection of isotropic material structures with simple shape, like cables, pipes, plates, and shells. Having distinct spectral lines like a comb with a certain interval distribution rule is the main characteristic of the music tone law. Damage detection baseline could be established by quantizing the fitting relationship between modal orders and the corresponding frequency values. The main advantage of this method is that it could be used in the structural damage detection without vibration information of an intact structure as a reference.

## 1. Introduction

Structural damage detection is an ancient but novel technology. In the past, visual inspections were used to detect the structural damage by trained engineers. However, this traditional method may be costly or inefficient [1]. Since Vandiver [2] studied the failure of a steel lighthouse by the change of structural dynamic frequency in 1975, damage detection methods using modal properties such as natural frequencies and modal shapes, which can be obtained from sensors placed on the structure, have been widely discussed in order to assess structural integrity.

Various studies have since then been proposed to promote the development of this field. In general, the past studies have three main characteristics. First, algorithm about the signal processing was mainly studied, such as neural network algorithm, genetic algorithm, Hilbert-Huang algorithm, and EMA method [3–6]. Second, device for the damage detection was developed, such as fiber optic sensors and wireless sensors [7, 8]. In addition, the application in major engineering was also conducted in recent years [9, 10].

There is no doubt that the structure is damaged when structural stiffness decreased obviously. However, the square of frequency is in proportional to stiffness, so when the structure was damaged with attenuation of stiffness, the variation of frequency is not obvious, which has been proved

by many research works [11–15]. And a baseline is also needed to judge whether the frequency decreased or not. Then, FEA model or test result of intact structures was usually used as the healthy benchmark. For the reason of reliability and measuring accuracy, many difficulties were faced in the actual application. Finding an effective way to detect structural damage by further analysis of frequency information would have a meaningful theoretical and applicable value.

Based on the musical tone law method, three typical structures, including inclined cables with transverse vibration, steel pipes with longitudinal vibration, and spherical shells with out-of-plane vibration, were conducted for the vibration test and damage detection in this paper. The frequencies distributions of intact structures and structures with different damaged levels were collected and analyzed. And a convenient and effective criterion for damage detection is established. Furthermore, the application of this method was tested in an actual cable-stayed bridge. Before going into detail regarding the application project, some basic considerations about the musical tone law method are introduced below.

## 2. Musical Tone Law Method

Sound wave is the transmission of vibration in the air. Music tone is the combination of fundamental wave and harmonic

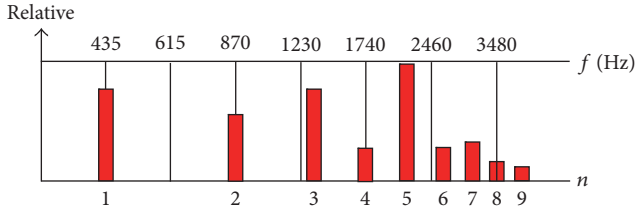


FIGURE 1: Fourier spectrum of a violin string sound.

wave, and the ratio between frequency of harmonic wave and that of the fundamental wave is a group of regular constants. The Fourier spectrum of a violin string sound is shown in Figure 1. Note that frequencies of the 1st, 2nd, 4th, and 8th order appear as multiplication distribution, and it is in accord with the music tone law. In auditory sense, the sound meeting the above law is melodious; otherwise, it is always harsh. Having distinct spectral lines like a comb with a certain interval distribution rule is the main characteristic of the music tone law.

In the past, the quality test of ceramic plates was essentially using the music tone law. Knock test of intact and damaged ceramic plate was also conducted. Three ceramic plates with the same batch were chosen as the test specimens. Specimen 1 and specimen 2 were intact; specimen 3 has a slight crack in the radial direction, as shown in Figure 2. The time history and Fourier spectrum of the knock vibration of specimens 1, 2, and 3 were shown in Figure 3. There is a large difference between the sound signals of the intact and damaged plates. The duration of the intact plate sound is about 0.6 s, while that of the damaged one is only about 0.1 s. The frequency spectrum of intact plate tap is similar to that of musical tone with distinct and regular spectral lines, while the damaged plate tap has indistinct spectral lines. Besides, for the intact plates, the relationship between the spectral lines order and the frequency value remained unchanged to the tap location. For the damaged plate, the relationship changed with different tap locations, but the main feature remained unchanged.

It may propose a new method to explore the change of structural frequency after damage. The intact structural distribution of frequency could serve as a benchmark for damage detection. In the mechanical principle, ceramic plate is similar to a shell structure and both of them follow a similar vibration criterion. The study also found that the frequency lines of one- and two-dimensional elastic structures with regular shape are clear and sharp and have a certain interval distribution. And this phenomenon, named the musical tone law method, could be used in the structural damage detection. Based on this cognition, three types of model structures and an actual engineering were tested in this paper, and the baseline and application range were studied.

### 3. Damage Detection Tests of Inclined Cables

Cable-stayed and suspension bridges are two important structural systems of bridges, where the steel cable is one of

the most important bearing members. If corrosion or abrasion occurs in the cables, the safety of the whole bridge would be threatened. The following test would study the application of the musical tone law method in the cables. LC0405T piezoelectric accelerometers, NEXUS2692-OS4 charge amplifier, and SigLab20-42 data acquisition instrument were used in all the vibration tests of this paper. And the resolution was set as 0.0625 Hz.

Inclined cables were tightened in the lab to simulate the actual force status, and two test cases, that is, intact and damaged cables, were tested. The cables were formed by one core fiber and 6 cover wires with total length of 28 m, diameter of 10 mm, and unit mass of 0.385 kg/m. The damaged cable was set by cutting 3 cover wires in the midspan with cut length of 2.8 m, as shown in Figure 4. The ends of the cable were fixed, respectively, in the top of the reaction wall and floor, as shown in Figure 5. Tandem tension spring was used to monitor the tension force of the cable, as shown in Figure 6. Overview of the test model is shown in Figure 7. The equivalent sectional area of the damaged cable is 95% of the intact one. As the tension force of the intact cable is 4.5 kN, the tension force of the damaged one was set as 4.25 kN.

Pulse excitation was conducted by knocking the cable by exciting hammer. The accelerometer was also installed in the 1/3 part away from the root of the cable to monitor the transverse vibration, as shown in Figure 8. The stiffness of the tandem tension spring was standardized before the test. Five times of the vibration signals with duration of 40 s were collected, and the transformed autopower spectrum was analyzed.

The theoretical solution of cable frequency is a problem of nonlinear vibration; many methods were studied to solve this problem [16–19], such as fitting method and finite difference method. Ran and Li [20] used the singular perturbation method to solve the nonlinear dynamic equation and verified this method by tests and numerical simulation. The suggested analytical expression of inclined cable fixed at both ends was developed as

$$f_n^2 = \frac{n^2 T}{4mL^2} + \Delta\lambda(n, \xi) \frac{T}{4\pi^2 mL^2} + \frac{n^2}{mL^3} \sqrt{EIT} + \frac{n^4 \pi^2 EI}{4mL^4} + \frac{3n^2 EI}{mL^4} \quad (1)$$

in which  $n$  denotes the modal orders,  $T$  is the average of cable force,  $m$  is mass per unit length of the cable,  $EI$  is the flexural stiffness of the cable,  $L$  is cable length,  $\Delta\lambda$  is the correction term, and  $\xi$  is cable sag. And the 3rd and 5th terms in (1) are corrections of boundary conditions. The expression of inclined cable hinged at both ends could be developed as

$$f_n^2 = \frac{n^2 T}{4mL^2} + \Delta\lambda(n, \xi) \frac{T}{4\pi^2 mL^2} + \frac{n^4 \pi^2 EI}{4mL^4} \quad (2)$$

For flexible cables with short length, the last two terms in (2) could be ignored as an approximate method. Then, the frequency could be solved by (3) [21], where  $T$  is the cable force,  $L$  is the length of cable, and  $m$  is mass per unit length of the cable. However, as the sag effect is significant for the

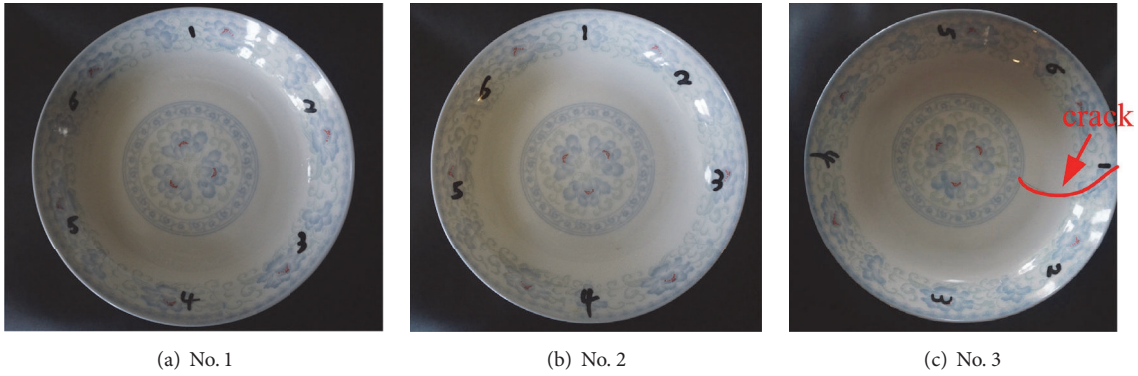


FIGURE 2: Three ceramic plates for the test.

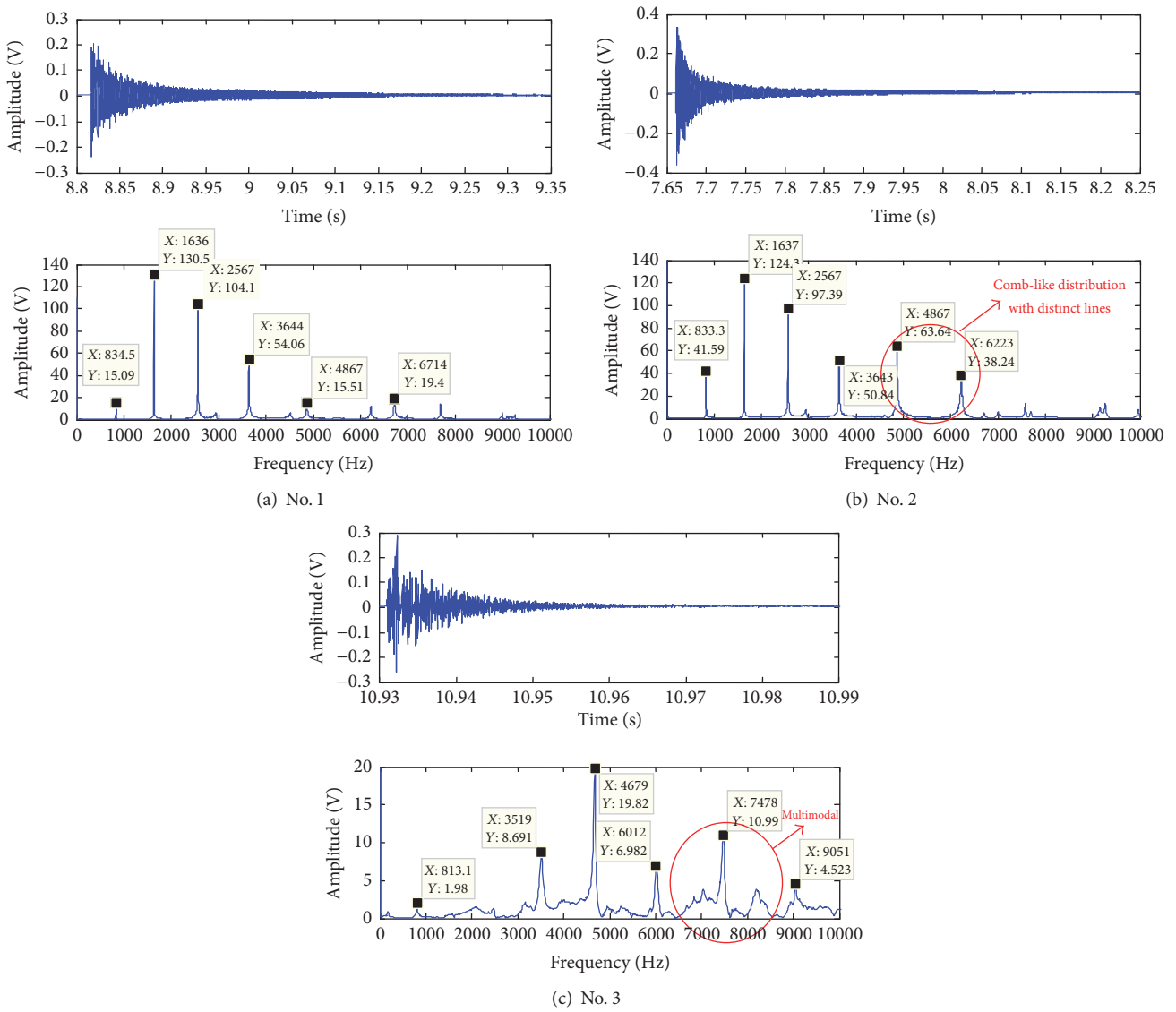


FIGURE 3: Time history and FFT of the plates tap.



FIGURE 4: Damaged part of the cable.

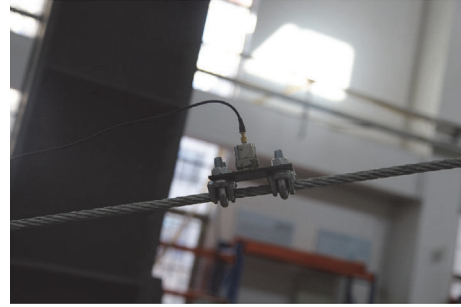


FIGURE 8: Installation of the accelerometer.



FIGURE 5: Fixed device.



FIGURE 6: Tension spring.

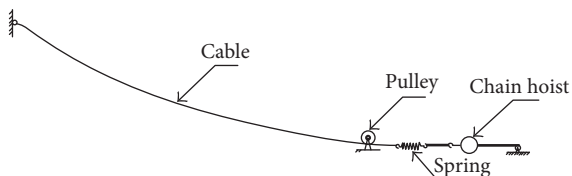


FIGURE 7: Overview of the test model.

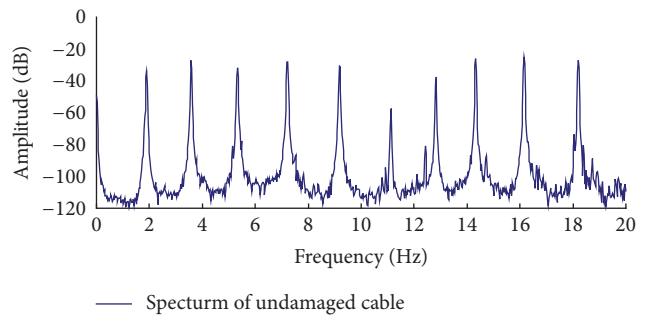


FIGURE 9: Spectral lines of the intact cable.

long cable, the 2nd term in (2) could not be ignored when used for long cables.

$$f_n = \frac{\omega}{2\pi} = \frac{n}{2L} \sqrt{\frac{T}{m}} \tag{3}$$

The test result is shown in Table 1. The frequencies of the inclined cable vibration mainly appear as multiplication distribution, which suggests that the reliability of (3) based on approximate method is basically satisfactory. For vibration tests of actual long inclined cables, the frequencies could not be fitted as multiplication distribution, and the study in Section 6 shows that the frequencies could be approximately regarded as in exponential distribution. Autopower spectrums of the cable vibration are shown as in Figures 9 and 10. The results show that the intact cable has distinct and regular spectral lines. While the spectral lines interval of the damaged cable changed, the coupling energy around the predominant frequency increased. Figure 11 shows the relationship between the neighbouring frequency interval and the modal orders. For the damaged cable, the neighbouring frequency intervals are rather changeable and no longer equal. Note that the frequencies of the damaged cable are larger than those of the intact one, which do not agree with traditional cases, in which the damaged structure has a lower stiffness. This phenomenon could be explained by (3). As the damaged cable was set by cutting 3 cover wire ropes in the midspan with cut length of 2.8 m, the mass per unite length is lighter than that of the intact one. Thus, the damaged cable has a larger frequency. And the same situation would be met in the next section, that is, tests of steel pipes.

TABLE 1: Frequencies of the inclined cables.

Test cases	1st order	2nd order	3rd order	4th order	5th order	6th order	7th order	8th order	9th order	10th order
Frequency of the intact cable/Hz	1.90	3.63	5.32	7.25	9.25	11.13	12.94	14.50	16.31	18.20
Neighbouring frequency interval of the intact cable/Hz	—	1.73	1.69	1.93	2.00	1.88	1.82	1.56	1.81	1.89
Frequency of the damaged cable/Hz	1.95	3.55	5.50	7.15	9.51	11.11	13.26	14.51	16.51	18.35
Neighbouring frequency interval of the damaged cable/Hz	—	1.6	1.95	1.65	2.36	1.6	2.15	1.25	2.00	1.84

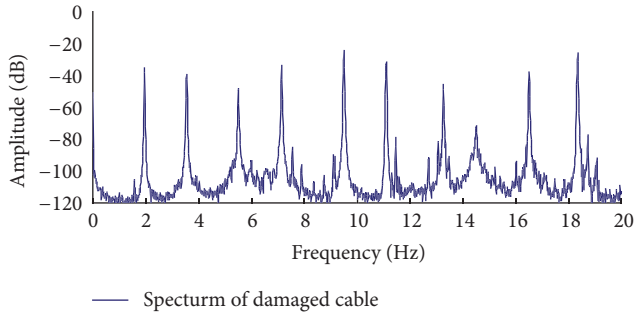


FIGURE 10: Spectral lines of the damaged cable.

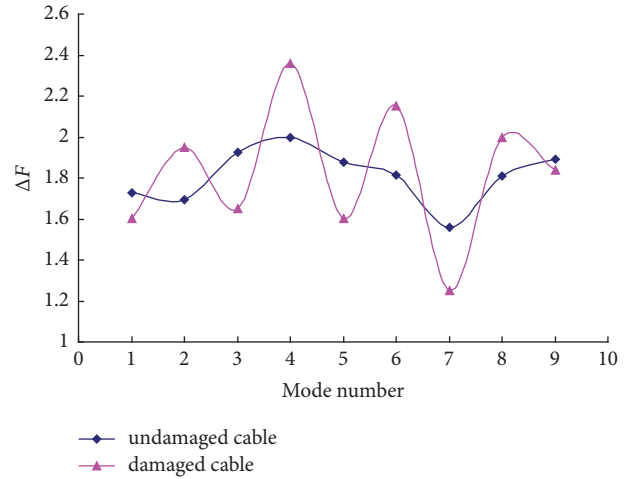


FIGURE 11: Neighbouring frequency interval of both models.

#### 4. Damage Detection Tests of Steel Pipes

Damage detection tests of one-dimensional steel pipes were conducted, and the longitudinal vibration excited by knock at the pipe end was collected. The test models were hollow straight pipes with length of 9500 mm, external diameter of 61.2 mm, and inner diameter of 51.2 mm, as shown in Figure 12(a). Specimen A was intact, while in the damaged model, specimen B was set by cutting part of the intact pipe in the midspan with cut length of 100 mm and depth of 30 mm, as shown in Figure 12(b). Knock excitation at the pipe end was conducted by exciting hammer, and a piezoelectric accelerometer was installed on the surface of the pipe to monitor the longitudinal vibration, as shown in Figure 12(c). Frequency domain within 2 kHz was analyzed.

The longitudinal vibration frequencies of steel pipes could be solved by (4), and the transverse vibration frequency could be solved by (5) based on classical mechanics [22, 23].

$$f_n = \frac{nc}{2L}, \quad (4)$$

$$f_n = \frac{n^2\pi}{2L^2} \sqrt{\frac{EI}{\rho A}}, \quad (5)$$

where  $n$  is the order of mode,  $EI$  is the flexural stiffness,  $c$  is the wave velocity, and  $A$  is the sectional area, and this could be solved as  $c = \sqrt{E/\rho}$ , where  $E$  is the elastic modulus of steel ( $2.1 \times 10^5$  N/mm<sup>2</sup>) and  $\rho$  is the steel density (7850 kg/m<sup>3</sup>). Note that (5) could be derived by (2) if the 3rd term in (2) is kept. It is because the axial force  $T$  is zero, and the sag effect

could be ignored, while the bending stiffness influences are significant for transverse vibration of pipes. In this section, the longitudinal vibration test was performed. Then, the theoretical fundamental frequency of the intact steel pipe could be solved as 272 Hz. The inherent frequencies appear as multiplication distribution.

Autopower spectrums of the pipe vibration are shown as in Figures 13 and 14. Spectral lines of the intact steel pipe (Figure 13) are distinct and the intervals are regular, following the musical tone law. While the spectral lines of the damaged pipe become irregular, some frequencies are even hard to be identified. In this paper, as an intact pipe could be used as a reference, we select the frequency peak of the damaged pipe around the frequency peak of the intact pipe. Besides, the amplitude decreased exponentially compared with the intact pipes.

The above test results show that the musical tone law method could detect the structural damage effectively. The top seven-order frequencies are shown in Table 2. Figure 15 shows the relationship between the neighbouring frequency intervals and the modal order. Spectral lines of the intact pipe followed the theoretical equal-interval distribution, while those of the damaged pipe are rather changeable. So, the structural damage could be detected by quantifying the



FIGURE 12: Test models.

TABLE 2: Natural frequencies of steel pipes under various damage cases.

Test cases	1st order	2nd order	3rd order	4th order	5th order	6th order	7th order
Frequency of the intact pipe/Hz	275	541	819	1085	1362	1631	1903
Neighbouring frequency interval of the intact pipe/Hz	—	266	278	266	277	269	272
Frequency of the damaged pipe/Hz	288	538	859	1050	1350	1625	1906
Neighbouring frequency interval of the damaged pipe/Hz	—	250	321	191	300	275	281

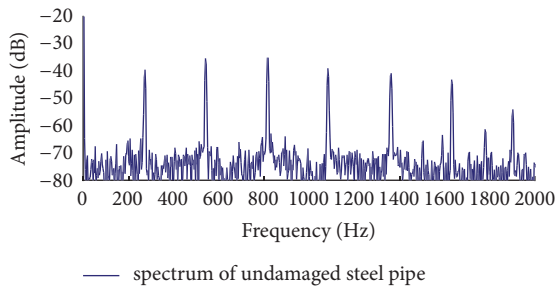


FIGURE 13: Spectral lines of the intact pipe.

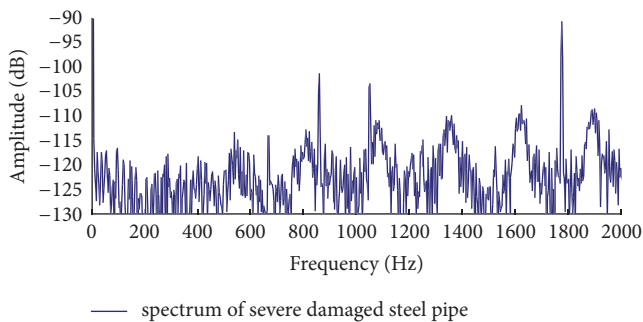


FIGURE 14: Spectral lines of the damaged pipe.

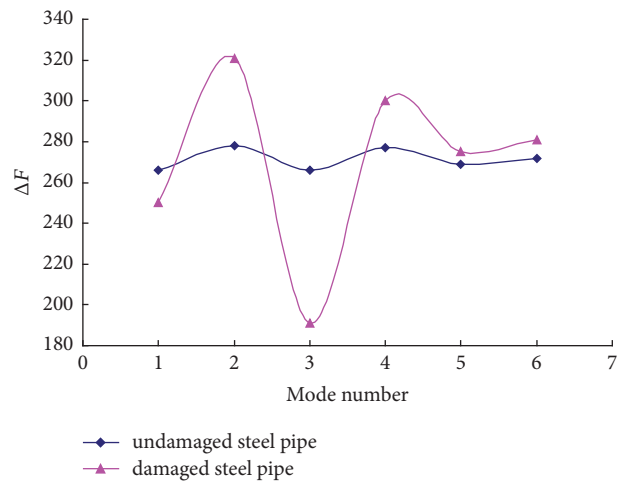


FIGURE 15: Neighbouring frequency interval of both models.

### 5. Damage Detection Tests of Steel Shells

The application of shell structures increases in recent years, and continuous elastic shell is always adopted in the dynamic analysis, and rigid joint, small deformation, and elastic assumption are also accepted [24]. So, the musical tone law method may be used in the damage detection of large-scale shell structures. And small-scale shell model was tested in this section.

Test models are two spherical steel shells with radius of 1000 mm, thickness of 4 mm, and rise of 250 mm. Four accelerometers were installed symmetrically on the edge of the shell, as shown in Figure 16(a). Figure 16(b) shows the test

distribution of frequencies based on the musical tone law method.

TABLE 3: Natural frequencies of both shells.

Test cases	1st order	2nd order	3rd order	4th order	5th order	6th order	7th order	8th order	9th order	10th order
Intact shell	5.25	14.00	26.00	40.75	57.50	77.63	97.75	120.88	145.00	171.75
Damaged shell	4.75	11.38	24.00	35.88	58.88	75.25	94.75	117.63	141.75	160.75

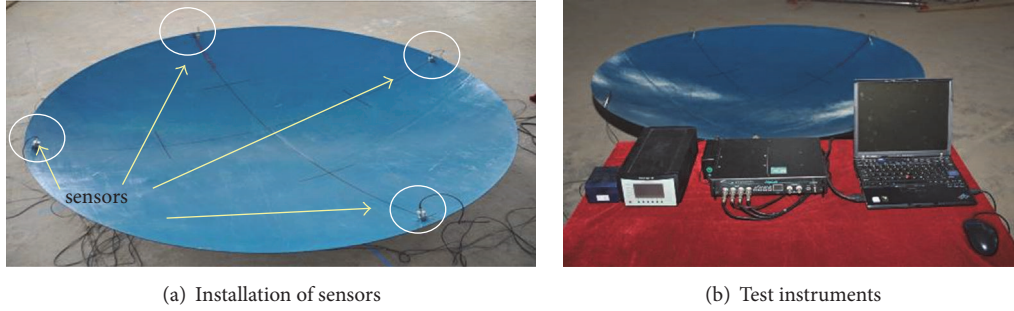


FIGURE 16: Specimen and test setup for damage detection of steel shells.

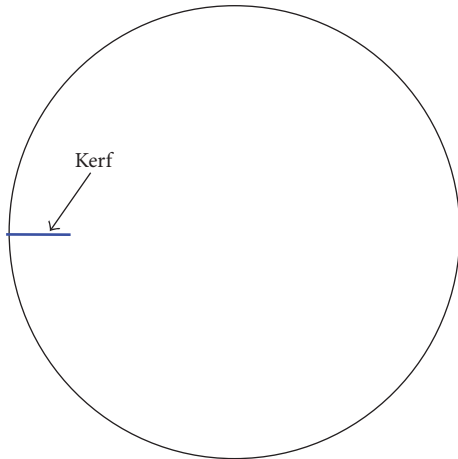


FIGURE 17: Description of damage on the shell.

instruments, which were the same as the above tests. Radial kerf was set artificially in one shell to simulate the damage case, as shown in Figure 17, and the size of the kerf is 1 mm × 40 mm.

Two weights of 5 kg were tied on both ends of the shell along the diameter by strings, which aimed to set an initial deformation. Then, free vibration was excited by burning out the strings suddenly. Figure 18 shows the spectral lines of both shells. The measured frequencies are shown in Table 3. Note that frequencies of the intact shell no longer follow the equal-interval distribution. Exponential fitting of the measured frequencies was conducted; the result is shown in Figure 19. Goodness of fit index  $R^2$  was used to evaluate the fitting and it is calculated as (6). The value is between 0 and 1. As the value of  $R^2$  is closer to 1, the fitting goodness is more satisfactory. In (6),  $Y_i$  is the actual value;  $\bar{Y}_i$  is the value in the fitting curve. Equations (7) and (8) are the fitting function of the intact and

damaged shells, in which  $x$  denotes the modal order and  $y$  denotes the frequency value.

$$R^2 = 1 - \frac{\sum_i (\bar{Y}_i - Y_i)^2}{(\sum_i Y_i^2) - (1/n) (\sum_i Y_i)^2}, \quad (6)$$

$$y = 89.8e^{0.11x} - 97.3; \quad (R^2 = 99.93\%), \quad (7)$$

$$y = 117.1e^{0.09x} - 127.8; \quad (R^2 = 99.62\%). \quad (8)$$

The results show that the special lines of the intact shell are distinct, while multimodal phenomenon around the predominant frequency is quite obvious in the damaged shell. Actually, the frequency peak of the damaged shell is hard to be selected. In this paper, as an intact shell could be used as a reference, we select the frequency peak of the damaged shell around the frequency peak of the intact shell. Although the fitted  $R^2$  of intact and damaged shells are closer as 99.93% and 99.62%, the spectral lines of the damaged one are multimodal, not in accord with the comb-like distribution, which is similar to the ceramic plate test in Figure 3. So, the radial damage could be detected based on the musical tone law method. And during the test, the hammering sound of the intact shell was clangorous and perpetual, while that of the damaged shell was depressing and rushing. This phenomenon agreed with the knock test of ceramic plates, in which the musical tone law method was proposed.

## 6. Baseline of the Musical Tone Law Method and Engineering Application

In the above tests, vibration of small-scale inclined cable and steel pipe is one-dimensional and that of steel shell is two-dimensional. The results show that frequencies of small-scale inclined cable and steel pipes appear as multiplication distribution, and the interval between neighbouring

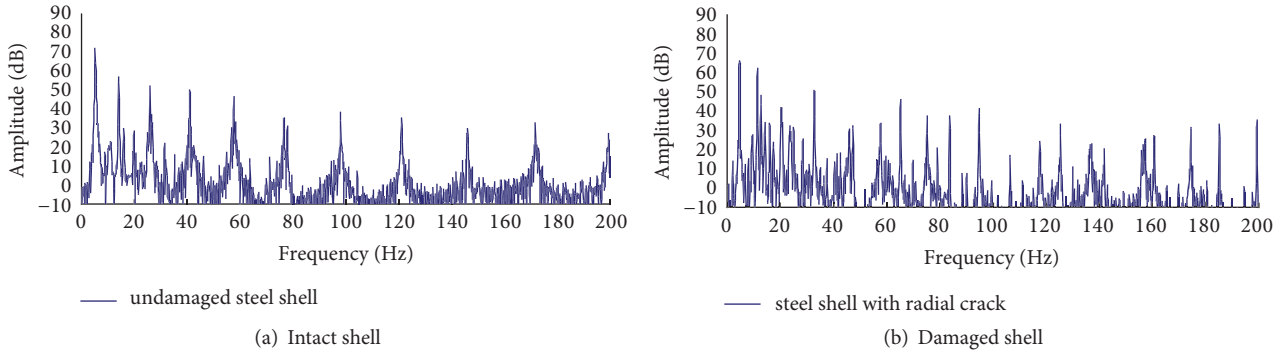


FIGURE 18: Spectral lines of the intact and damaged shells.

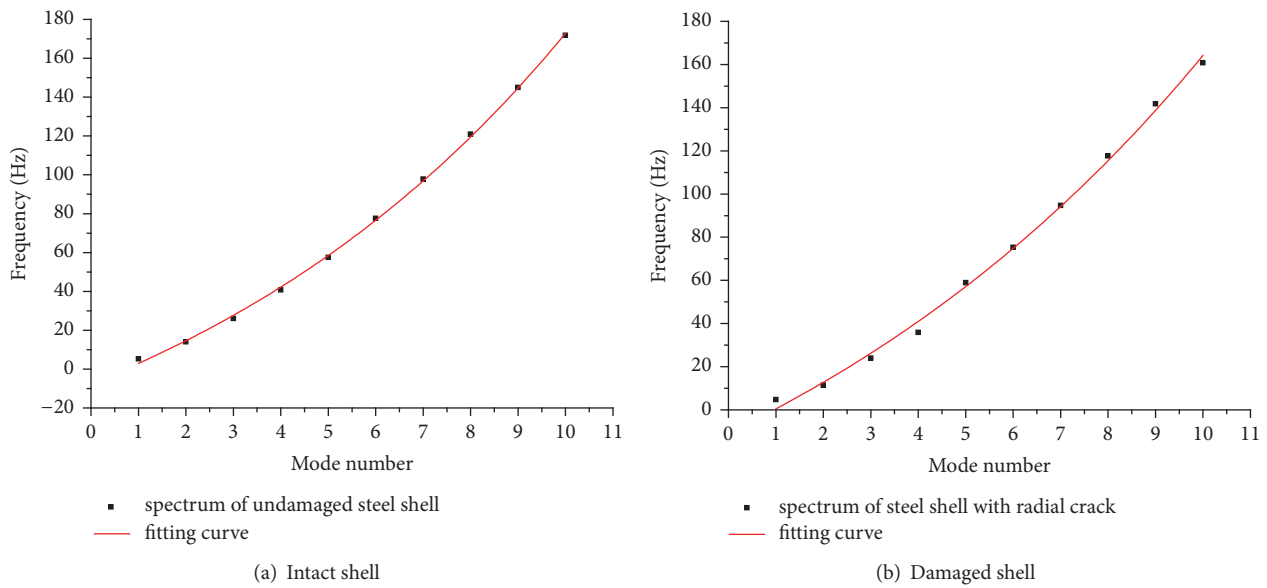


FIGURE 19: Comparison of spectrum fitting of intact and damaged shells.

frequencies is equal. Frequencies of two-dimensional shells appear as exponential distribution. In the elastic mechanics, theoretical frequencies of cantilever also present as equal-interval distribution. In conclusion, the musical tone law method could be used in the damage detection of isotropic material structures with simple shape, like cables, pipes, plates, and shells. In general, frequencies of one-dimensional vibration structures present as multiplication distribution, while those of two-dimensional vibration structures present as exponential or logarithm distribution. So, the goodness of fit could be used as a baseline in the damage detection.

The application of the above method was examined in an actual cable-stayed bridge. Theoretical solution of long cable frequencies shows that the relationship between the modal order and the frequency value is exponential distribution. The tested Songyuan bridge is a cable-stayed bridge with total length of 2546.5 m. Two symmetrical bridge towers were built in the midspan. The overview of the bridge is shown in Figure 20. Vibration tests of two symmetrical cables at either side of the tower were conducted, and test results of



FIGURE 20: Overview of the Songyuan bridge.

the two cables are almost the same. The test instruments including data acquisition, charge amplifier, and piezoelectric accelerometer are all same as the above model test (Figure 21). The sampling bandwidth was set as 200 Hz, the resolution was set as 0.0156 Hz, and the sampling duration was set as 200 s. Fourier spectrum of time history signal is shown in Figure 22. Table 4 shows the top ten frequencies of the cable. Fitting curve of the relationship between the modal order and the

TABLE 4: Tested frequencies of the cable.

Order	1st order	2nd order	3rd order	4th order	5th order	6th order	7th order	8th order	9th order	10th order
Frequency/Hz	4.641	9.343	14.125	19.09	24.266	29.687	35.23	41.467	47.734	54.483

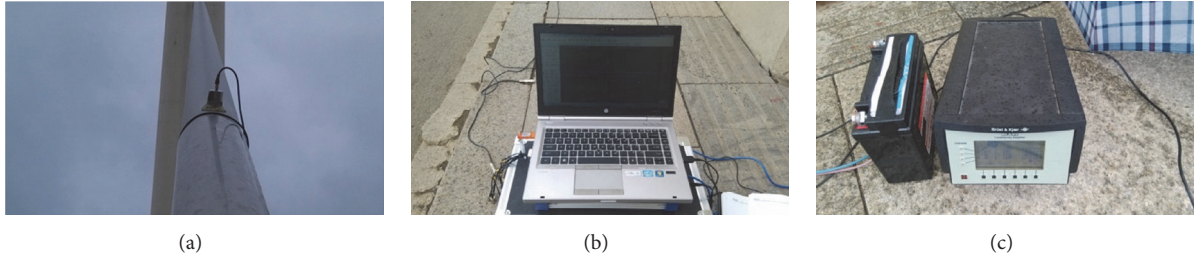


FIGURE 21: Test instruments.

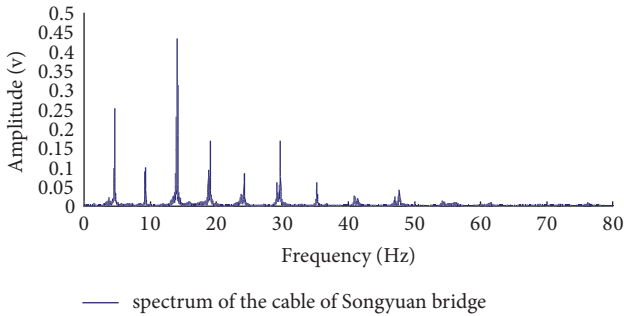


FIGURE 22: Frequency spectrum of the transverse vibration of the cable.

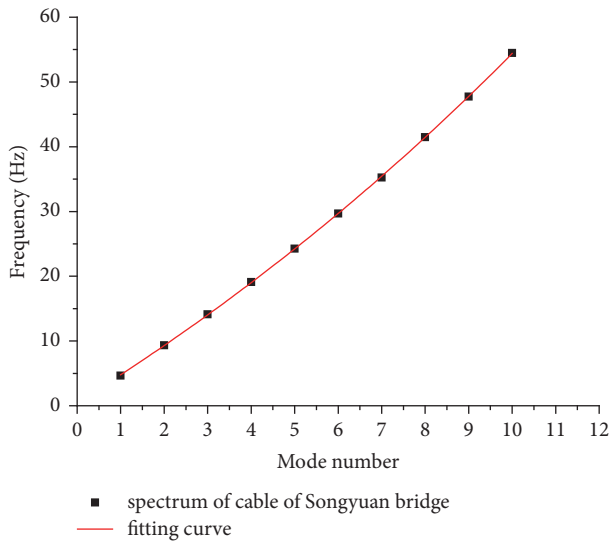


FIGURE 23: Spectrum fitting of cables in the Songyuan Bridge.

frequency value is shown in Figure 23. The fitting function and goodness is shown in

$$y = 87.71e^{0.048x} - 87.24; \quad (R^2 = 99.995\%). \quad (9)$$

The test and fitting results show that the spectral lines are distinct and like a comb, frequency presented as exponential distribution, and the goodness of fit is more than 99.9%. The example shows that the baseline of the musical tone law method could be used in the damage detection of actual engineering.

### 7. Conclusions

Based on the phenomenon of musical tone law, damage detection tests of three simple models and an actual cable-stayed bridge were conducted. The following conclusions were obtained by the test results and further analysis.

- (1) The musical tone law method could be used in the damage detection of isotropic material structures with simple shape, like cables, pipes, plates, and shells. The frequency lines of the above intact structures are distinct and like a comb. And the multimodal phenomenon around the predominant frequency is quite obvious in the damaged structures.
- (2) In general, frequencies of one-dimensional vibration structures, like pipes, present as multiplication distribution, while those of two-dimensional vibration structures, like shells and long cables, present as exponential or logarithm distribution. So, the distribution characteristic of structural frequencies and the fitting goodness could be used as a baseline in the damage detection. And the damage level could be quantized by the value of fitting goodness in the congeneric structures.
- (3) The main advantage of this method is that it could be used in the structural damage detection without vibration information of an intact structure as a reference. And the application of the above method was examined in an actual cable-stayed bridge.

### Competing Interests

The authors declare that they have no competing interests.

## Acknowledgments

Financial support for this study has been provided by National Natural Science Foundation of China (Grants nos. 51608287, 51378271, and 51508295), the Natural Science Foundation of Shan Dong Province (Grant no. ZR2016EEP17), and Taishan Scholar Priority Discipline Talent Group Program funded by the Shan Dong Province. Special thanks are due to the programs for providing the financial support to complete this project.

## References

- [1] M. Moore, B. Phares, B. Graybeal, D. Rolander, and G. Washer, "Reliability of visual inspection for highway bridges," Tech. Rep. #FHWA-RD-01-020, Federal Highway Administration, Washington, DC, USA, 2001.
- [2] J. K. Vandiver, "Detection of structural failure on fixed platforms by measurement of dynamic response," in *Proceedings of the 7th Annual Offshore Technology Conference (OTC '75)*, pp. 243–252, Houston, Tex, USA, 1975.
- [3] H. Adeli and N.-T. Cheng, "Integrated genetic algorithm for optimization of space structures," *Journal of Aerospace Engineering*, vol. 6, no. 4, pp. 315–328, 1993.
- [4] L. Qiao, A. Esmaily, and H. G. Melhem, "Signal pattern recognition for damage diagnosis in structures," *Computer-Aided Civil and Infrastructure Engineering*, vol. 27, no. 9, pp. 699–710, 2012.
- [5] H. Sarparast, M. R. Ashory, M. Hajiazizi, M. Afzali, and M. M. Khatibi, "Estimation of modal parameters for structurally damped systems using wavelet transform," *European Journal of Mechanics—A/Solids*, vol. 47, pp. 82–91, 2014.
- [6] H. Wang, A.-Q. Li, and J. Li, "Progressive finite element model calibration of a long-span suspension bridge based on ambient vibration and static measurements," *Engineering Structures*, vol. 32, no. 9, pp. 2546–2556, 2010.
- [7] B. F. Spencer Jr., "Opportunities and challenges for smart sensing technology," in *Proceedings of the 1st International Conference on Structural Health Monitoring and Intelligent Infrastructure (SHMII-1 '03)*, pp. 65–71, Tokyo, Japan, November 2003.
- [8] H. Li, J. P. Ou, and Z. Zhou, "Applications of optical fibre Bragg gratings sensing technology-based smart stay cables," *Optics and Lasers in Engineering*, vol. 47, no. 10, pp. 1077–1084, 2009.
- [9] H. Wang, J. X. Mao, J. H. Huang, and A. Q. Li, "Modal Identification of Sutong Cable-Stayed Bridge during Typhoon Haikui Using Wavelet Transform Method," *Journal of Performance of Constructed Facilities*, vol. 30, no. 5, 2016.
- [10] H. Li, J. Ou, X. Zhao et al., "Structural health monitoring system for the Shandong Binzhou Yellow River Highway Bridge," *Computer-Aided Civil and Infrastructure Engineering*, vol. 21, no. 4, pp. 306–317, 2006.
- [11] G. Yan, Z. Duan, and J. Ou, "Review on structural damage detection based on vibration data," *Journal of Earthquake Engineering and Engineering Vibration*, vol. 27, no. 3, pp. 95–103, 2007.
- [12] X. Guo, B. F. Spencer, and S. Lu, "Application of clan member signal method in structural damage detection," *Earthquake Engineering and Engineering Vibration*, vol. 6, no. 1, pp. 29–34, 2007.
- [13] P. Cawley and P. D. Adams, "The location of defects in structures from measurements of natural frequencies," *Journal of Strain Analysis*, vol. 14, no. 2, pp. 49–57, 1979.
- [14] S. Hassiotis and G. D. Jeong, "Assessment of structural damage from natural frequency measurements," *Computers & Structures*, vol. 49, no. 4, pp. 679–691, 1993.
- [15] P.-L. Liu, "Identification and damage detection of trusses using modal data," *Journal of Structural Engineering*, vol. 121, no. 4, pp. 599–608, 1995.
- [16] H. Zui, T. Shinke, and Y. Namita, "Practical formulas for estimation of cable tension by vibration method," *Journal of Structural Engineering*, vol. 122, no. 6, pp. 651–656, 1996.
- [17] W. X. Ren and G. Chen, "Practical formulas to determine cable tension by using cable fundamental frequency," *China Civil Engineering Journal*, vol. 38, no. 11, pp. 26–31, 2005.
- [18] A. B. Mehrabi and H. Tabatabai, "Unified finite difference formulation for free vibration of cables," *Journal of Structural Engineering*, vol. 124, no. 11, pp. 1313–1322, 1998.
- [19] Q. Zhang, Z. Ran, Y. Bu, and Q. Li, "Theory and parameter estimation for nonlinear vibration of cables," *China Civil Engineering Journal*, vol. 42, no. 6, pp. 86–92, 2009.
- [20] Z. Ran and Q. Li, "Singular perturbation method for solving non-linear vibration of inclined cables," *Journal of Southwest Jiaotong University*, vol. 41, no. 3, pp. 355–359, 2006.
- [21] W. D. Pilkey, *Mechanics of Solids*, Quantum Publishers, New York, NY, USA, 1974.
- [22] Z. P. Liao, *Introduction to Wave Motion Theories in Engineering*, Science Press, Beijing, China, 2002.
- [23] L. L. Wang, *Foundation of Stress Wave*, National Defence of Industry Press, Beijing, China, 2005.
- [24] S. Z. Shen, "Development of long-span structures—a review and prospect," *China Civil Engineering Journal*, vol. 31, no. 3, pp. 5–15, 1998.

## Research Article

# Seismic Performance and Ice-Induced Vibration Control of Offshore Platform Structures Based on the ISO-PFD-SMA Brace System

Jigang Zhang,<sup>1</sup> Zhehao Ma,<sup>1</sup> Feifei Liu,<sup>1</sup> Chunwei Zhang,<sup>1</sup> Pezhman Sharafi,<sup>2</sup> and Maria Rashidi<sup>2</sup>

<sup>1</sup>School of Civil Engineering, Qingdao University of Technology, Qingdao 266033, China

<sup>2</sup>Center for Infrastructure Engineering, Western Sydney University, Locked Bag 1797, Penrith South DC, NSW 2751, Australia

Correspondence should be addressed to Jigang Zhang; [jigangzhang@126.com](mailto:jigangzhang@126.com)

Received 14 July 2016; Revised 31 October 2016; Accepted 29 November 2016; Published 15 January 2017

Academic Editor: Ying Wang

Copyright © 2017 Jigang Zhang et al. This is an open access article distributed under the Creative Commons Attribution License, which permits unrestricted use, distribution, and reproduction in any medium, provided the original work is properly cited.

Pall-typed frictional damper (PFD) has higher capacity of energy dissipation, whereas shape memory alloy (SMA) has excellent superelastic performance. Therefore, combining PFD and SMA together as a brace system has a great prospect in vibration control of structures. This paper investigates the performance of offshore platform with three structural configurations including the SMA brace system, the ISO-SMA (where ISO stands for isolation) brace system, and the ISO-PFD-SMA brace system, which are subjected to seismic and ice-induced excitations. In this study, PFD-SMA brace system is installed on the isolation layer of jacket platform, which is under earthquake excitations and ice loading. Then, the reduction of vibration is evaluated by using ANSYS program. The results show that the PFD-SMA brace system is useful in reducing the seismic response and ice-induced response of offshore platform structures; meanwhile, it also demonstrates excellent energy dissipation and hysteretic behavior.

## 1. Introduction

In 1947, the world's first self-contained steel jacket offshore platform was built in the gulf of Mexico. It reached in a new era of exploitation of ocean. Following the rapid development of offshore petroleum industry, nearly 10000 offshore platforms are widely used in many fields at present, mainly in petroleum engineering. For the sake of better adaptation to the social and economic development and ensuring the supply of energy, many offshore platforms are built. Because of severe working environment and complicated load condition, its security and stability must be concerned.

Offshore platforms are subjected to different environmental loads during their life time, such as earthquake, wave, wind, and ice. Particularly, seismic load should be taken into account comprehensively due to its unpredictability and randomness. Therefore, it is necessary to ensure the platform does not fall in the earthquake and decrease the loss of disaster to a minimum. JZ20-2MUQ offshore platform was built in the Bohai gulf, which is in earthquake zone.

In the higher latitudes, ice load is taken as design control load based on estimation. Intensive vibration induced by continuous crushing of ice will influence security and comfort of workers. At the same time, the degradation of resistance induced by the excessive and large amplitude vibration may lead to the fatal results. In 1964, two platforms that were completed in 1962-1963 collapsed, due to sea ice in Cook Inlet in Alaska; in 1969, a new offshore platform collapsed under the repeated hit of large ice loads (average ice thickness of flat ice was about 60 cm; the biggest thickness was above 1 m) [1].

Liaodong Bay is one of the important producing oil regions in the Bohai oilfield which is located at the unique sea ice covered waters in our country. At the same time, Liaodong Bay is the worst ice blockages along the Bohai Sea. Bohai Oilfield Services limited company preformed the observation of sea ice; the maximum acceleration of deck on JZ20-2MUQ platform hits a peak of 3-4 m/s<sup>2</sup> (300-400 gal).

Shape memory alloys (SMA) are metallic alloys that can withstand great strains, while recovering their initial state after unloading or by heating, without permanently

deformation due to their excellent superelastic performance. Research efforts have been made to use SMA based materials or devices for reducing earthquake damage of civil structures [2–8]: base isolation systems [2, 3], dampers [4], bracing systems for structure [5, 6], application in bridge [7], and beam-column connections [8]. These studies demonstrated the feasibility and effectiveness of SMA as a structural self-centering and damping component. Since Pall-typed frictional damper (PFD) has higher capacity of energy dissipation [9], shape memory alloy (SMA) has excellent superelastic performance [10]. In this work, a finite element model of JZ20-2MUQ platform with PFD-SMA brace system is built, and time history response of the model impacted by Tianjin, El Centro, and Taft seismic wave is analyzed. Simultaneously, ice-induced vibration control is also conducted. In order to have a comparative study more comprehensively, based on the results of simulation, seismic behavior on JZ20-2MUQ offshore platform with and without PFD-SMA brace system is contrasted through the finite element analysis software ANSYS. The results show that PFD-SMA brace system has good energy dissipation and good self-centering performance.

## 2. Structure Parameters and FEM Model of JZ20-2MUQ Platform

*2.1. Structure Parameters of JZ20-2MUQ Platform.* JZ20-2MUQ offshore platform is located in the shallow waters in Bohai bay. The design depth is 15 m. JZ20-2MUQ platform consists of jacket, jacket cap, pillar, deck (including two device layers), and living quarters [12]. Its foundation is composed of four jacket pipes and driven into the seabed through the piles. The photo of JZ20-2MUQ is shown in Figure 1.

The main parameters of JZ20-2MUQ are shown as follows. This platform is mainly made of steel with density of  $7.85 \text{ kg/m}^3$ , Young's modulus of  $2.10 \times 10^5 \text{ Mpa}$ , and Poisson ratio of 0.3; the length of pipe below the mud line is equivalent to 6.4 times the diameter of pipe ( $L = 6.4; D = 8.8 \text{ m}$ ), so the overall height is about 64 meters; The total mass of structure is around 2000 tons, and the size of guide pipes is  $\phi 59.5 \times 1.25 \text{ (in)}$ . The elevation view of JZ20-2MUQ is shown in Figure 2.

*2.2. FEM Model of JZ20-2MUQ and Arrangement of PFD-SMA Bracing System.* A 3D frame model of original platform is created by finite element analysis software ANSYS as shown in Figure 4; the steel beams are modeled with ANSYS BEAM188. The mass is including deck and other masses which is used by ANSYS MASS21 [13]. Based on code for seismic design of buildings (GB50011-2001) in China, the gravity load value is determined by the combinational coefficient, and all masses are concentrated on the joints of member bars.

PFD-SMA brace system consists of SMA supports and Pall-typed friction damper; the connection of SMA brace and PFD ordinary steel plate is bolted joint. Figure 3 shows the PFD-SMA brace system. In order to improve antivibration character of the platform structure, we set two SMA braces

TABLE 1: Measured frequencies and damping ratio of JZ20-2MUQ platform structure.

Mode number	1	2	3
Frequency (Hz)			
Measured 1 [11]	0.90	1.05	1.15
Measured 2 [11]	0.85	1.12	
Damping ration [11] (%)		4.0~5.5	

TABLE 2: Calculated natural frequencies of JZ20-2MUQ platform structure.

Mode number	Frequency (Hz)
1	0.742
2	0.787
3	0.792
4	1.481
5	1.604
6	2.247
7	2.657
8	2.861
9	3.008
10	3.091

between living deck and jacket cap on the model, as shown in Figure 5. The SMA bracing is modeled with ANSYS SOLID185, and the Pall friction damper is modeled with the combination of ANSYS COMBIN40, BEAM4, and LINK8.

*2.3. Dynamic Characteristic of JZ20-2MUQ.* Based on the measurement in the field, the first three frequencies and damping ratio of JZ20-2MUQ platform have been acquired (summarized in Table 1).

Structural modal identification based on environmental excitation is available, using measured data to obtain the modal parameters. Accordingly, though the modal analysis, the dynamic characteristics of JZ20-2MUQ platform are analyzed; the first ten nature frequencies of model are gained and listed in Table 2. It could be found that the first three frequencies and damping ratio measured in the field are larger than those calculated, compared with the results in Table 1. The differences between the two could be attributed to several reasons, mainly caused by the effective mass values of the structure which are higher than simulated model due to the contribution of nonstructural components.

## 3. Seismic and Ice-Induced Vibration Analysis of JZ20-2MUQ with PFD-SMA Bracing System

*3.1. Seismic Analysis.* By using ANSYS program, the dynamic finite element analytic model of the JZ20-2MUQ platform with SMA bracing is established. The numerical simulations are executed. Seismic input is modeled by using three different earthquake excitations including Tianjin (1976, EW),



FIGURE 1: Photo of JZ20-2MUQ.

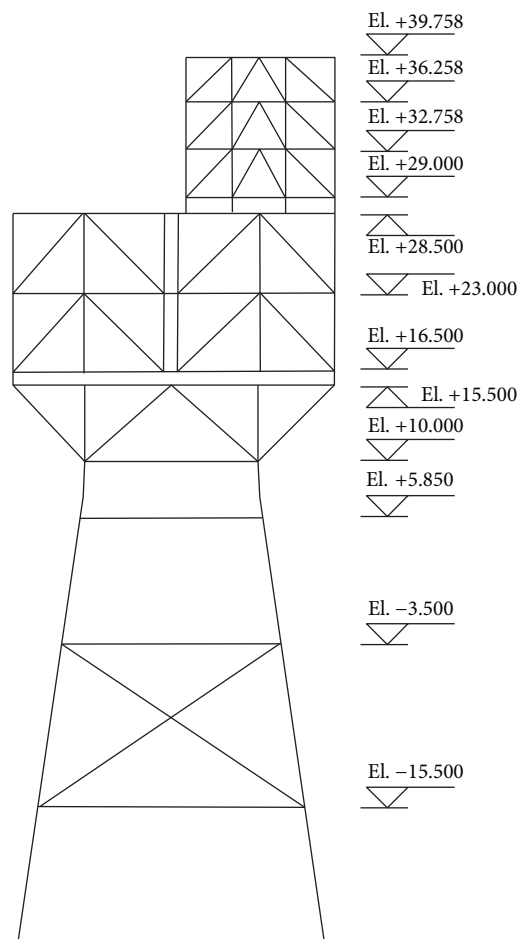


FIGURE 2: Elevation view of JZ20-2MUQ.

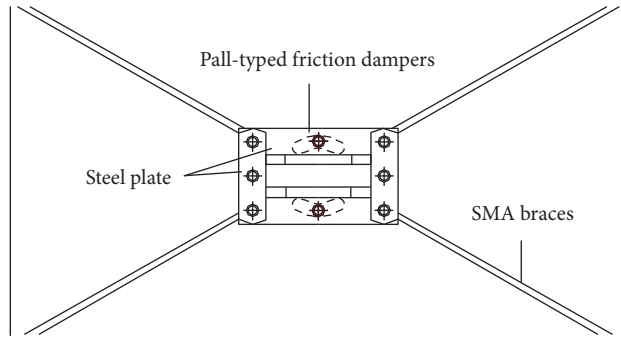


FIGURE 3: PFD-SMA brace system.

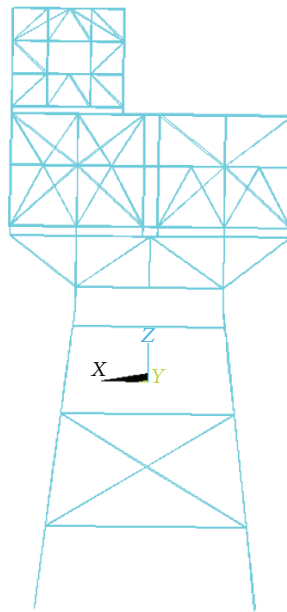


FIGURE 4: FEM of original structure.

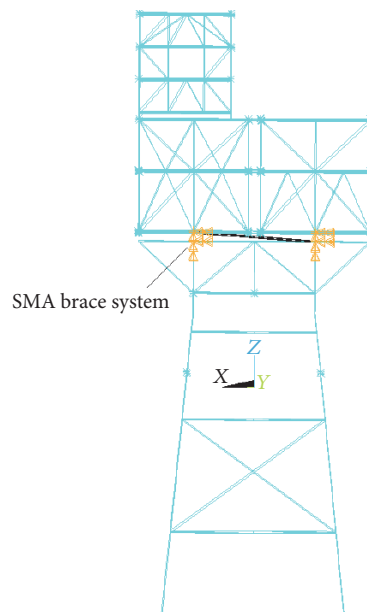


FIGURE 5: FEM of structure with SMA brace system.

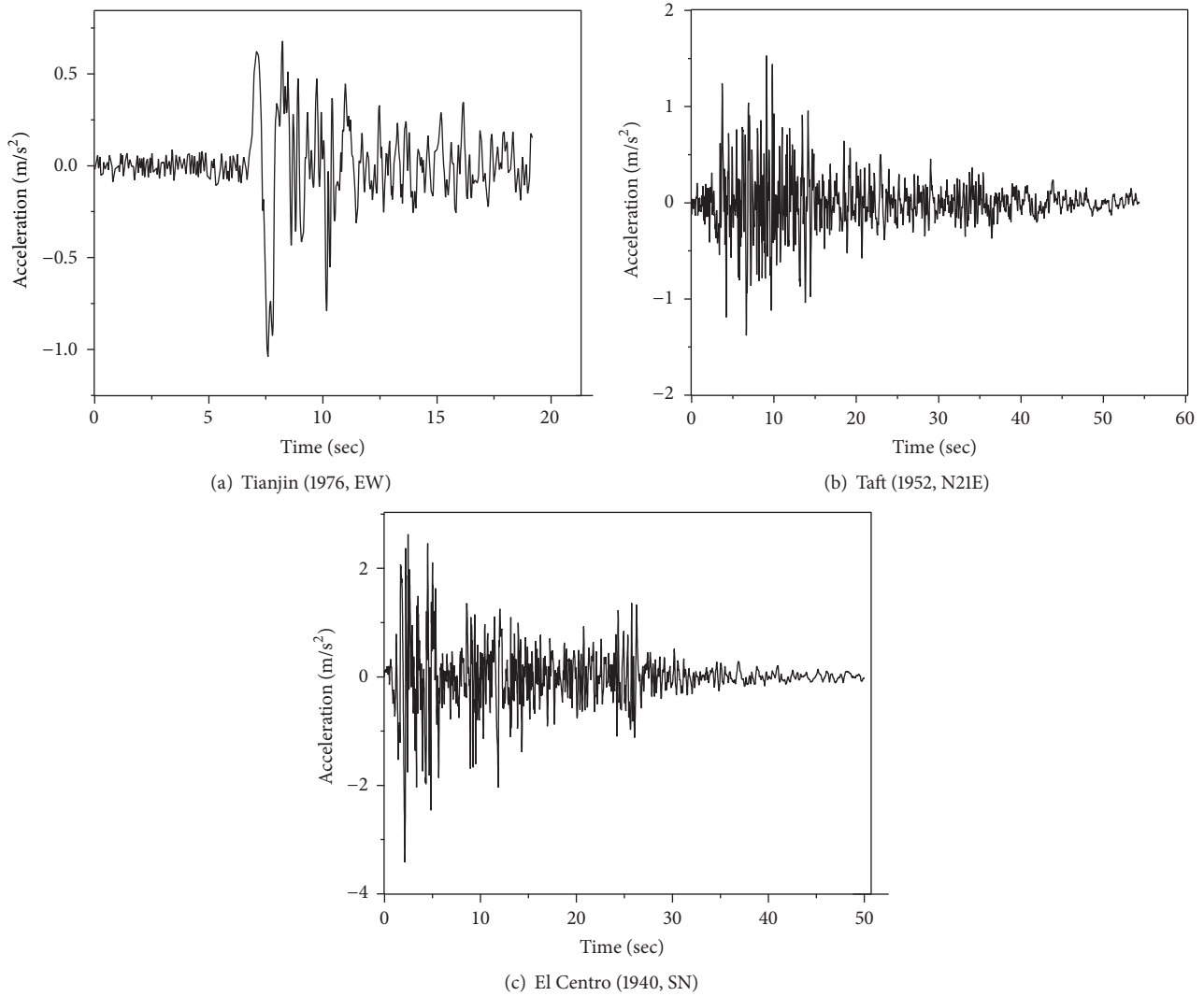


FIGURE 6: Acceleration time history curves of three earthquake excitations.

Taft (1952, N21E), and El Centro (1940, SN); their acceleration time history curves are shown in Figure 6.

The dynamical characteristics contrastive analysis of platform with and without SMA bracing system is analyzed, and seismic response contrastive analysis is calculated by the method of elastic time history response of systems [14]. The response of the structure to ground motion under three earthquake excitations was carried out, which is shown in Table 3. The ground acceleration is applied in  $X$ -direction modes. From Table 3, it can be found that the reduction of vibration under three earthquake excitations is not obvious; the maximum deformation of jacket cap reduces by only 4.3%, even though it reduces by 1% or almost zero percent under the Tianjin waves. Besides, the maximum acceleration of top deck and lower deck decreases slightly, and the percentage of reduction is 10.7% and 30.8%, respectively. Particularly, jacket plays a crucial role in maintaining stability and security of the entire platform. Once jacket oversized displacement leads to the collapses of platform, the

subsequent consequence is unbearable. Furthermore, the top deck is living quarters, and there is no doubt that large acceleration will affect the level of comfort of the workers on platform. Thus, such a small effect of mitigating vibration will not be able to meet the requirements obviously. Figure 7 shows the time history curves of the maximum displacement on jacket cap. Figures 8 and 9 show the time history curves of maximum acceleration on the top deck and the lower deck, respectively.

Considering the above numerical analysis, it is found that SMA bracing system is not efficient in reducing the response of vibration under earthquake excitation, compared with uncontrolled structure. The reason why SMA bracing could not give full play to their potential is that the overall stiffness of the platform structure is too large, and the deformation is too small. Thus, increasing the deformation of SMA and its capacity of energy dissipation to achieve the desired effect is considered. In order to enhance the energy consumption, the damping isolation system is placed between the bottom of

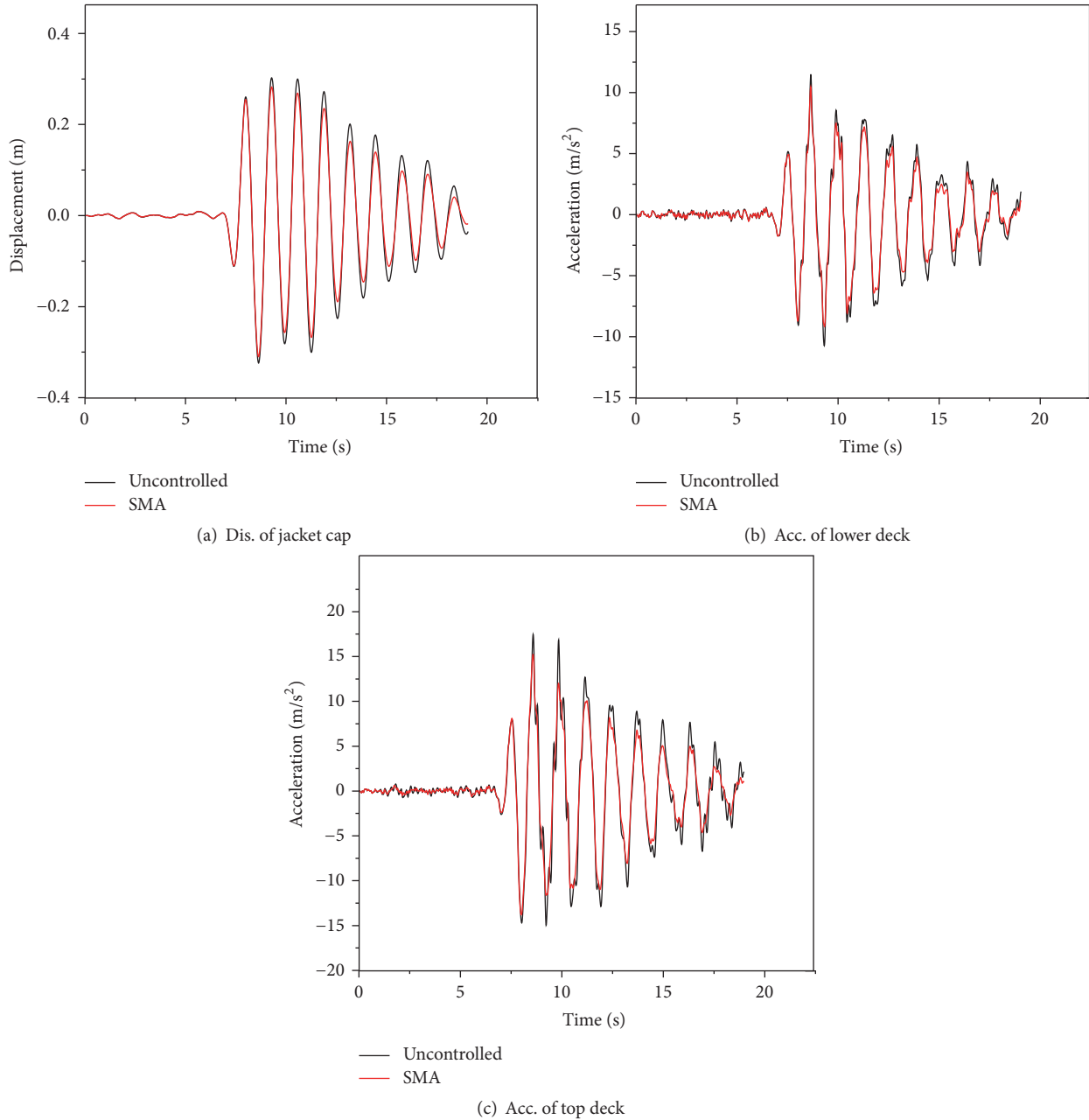


FIGURE 7: Computational response of JZ20-2MQU model under Tianjin earthquake excitation.

TABLE 3: Maximum test results of earthquake excitation of the platform with SMA brace.

Earthquake	Structural type	Displacement of jacket (cm)	Acceleration of lower deck (cm/s <sup>2</sup> )	Acceleration of top deck (cm/s <sup>2</sup> )
Tianjin	Original	30.3	1150	1750
	SMA	30.3 (0.043)	1050 (0.087)	1520 (0.131)
TAFT	Original	10.2	747	914
	SMA	9.76 (0.043)	667 (0.107)	829 (0.093)
El Centro	Uncontrolled	9.52	589	1066
	SMA	9.29 (0.024)	576 (0.022)	738 (0.308)

Note: the figure in brackets is the percentage of effectiveness of mitigating vibration which is equal to (uncontrolled structure – control structure)/uncontrolled structure).

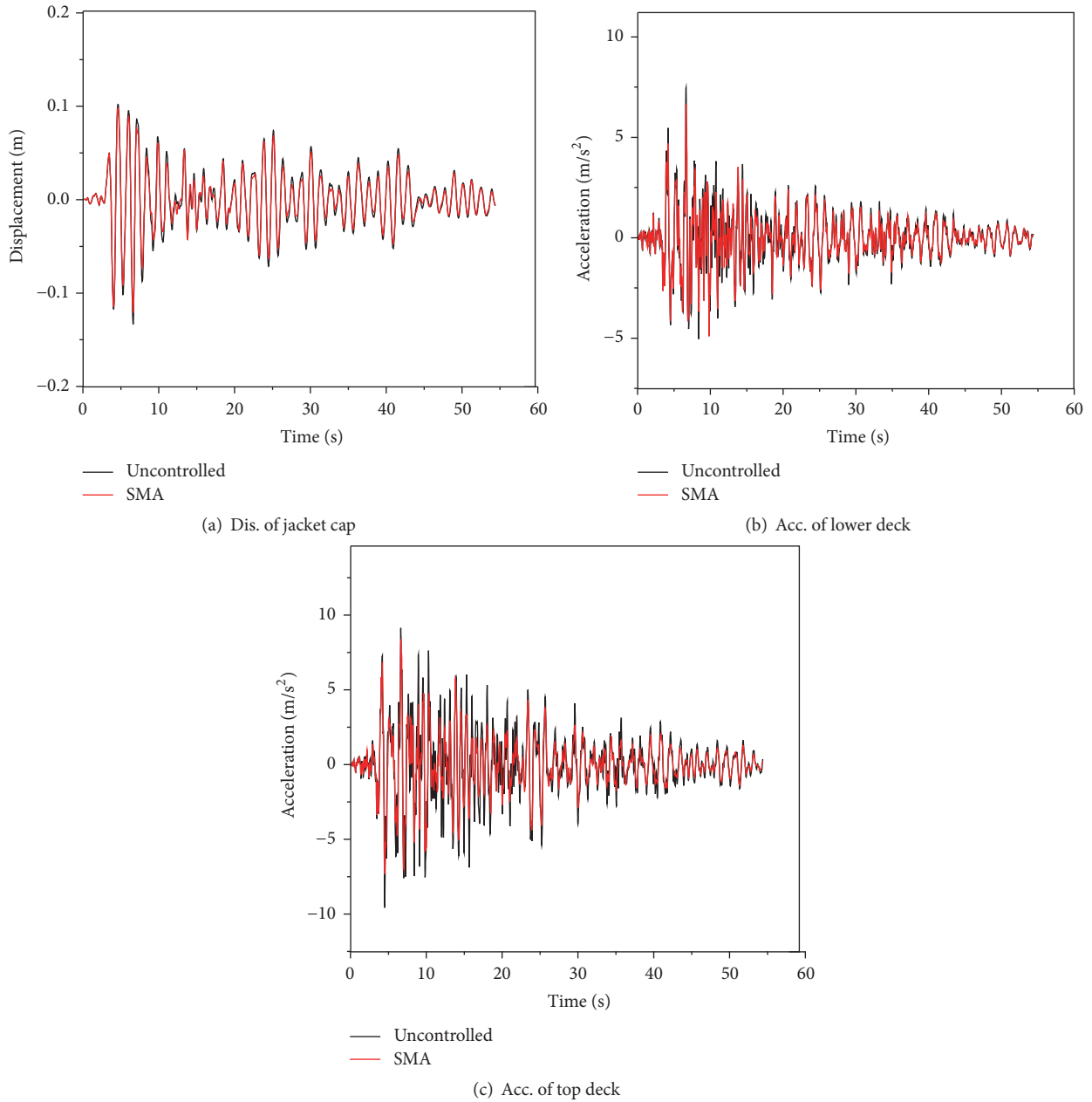


FIGURE 8: Computational response of JZ20-2MQU model under Taft earthquake excitation.

the deck and the top of the jacket structure [15]. The rubber layer is modeled by ANSYS COMBIN14 and CONBIN40. The horizontal forces are analyzed mostly by the former, and the latter undertakes vertical forces mainly. COMBIN14 has longitudinal or torsional capability in one-, two-, or three-dimensional application; COMBIN40 is a combination of a spring-slider and damper in parallel, coupled to a gap in series. In the meantime, two SMA supports and two PFD-SMA supports are set in isolation layer between living deck and jacket cap on the model, respectively, as shown in Figures 10 and 11.

The numerical simulations are conducted for platform model including three structure styles: the uncontrolled

structure, the structure with isolation layer and SMA bracing system (called ISO-SMA structure), and the structure with isolation layer and PFD-SMA bracing system (called ISO-PFD-SMA structure).

The response of the ISO-SMA structure under three earthquake excitations is carried out and summarized in Table 4. Figure 12 shows the time history curves of the maximum displacement on jacket cap. Figures 13 and 14 show the time history curves of maximum acceleration on the top deck and the lower deck, respectively.

According to Table 4, the results of simulated calculation indicate that each different kind of control scheme could reduce the response of earthquake excitation. The ISO-SMA

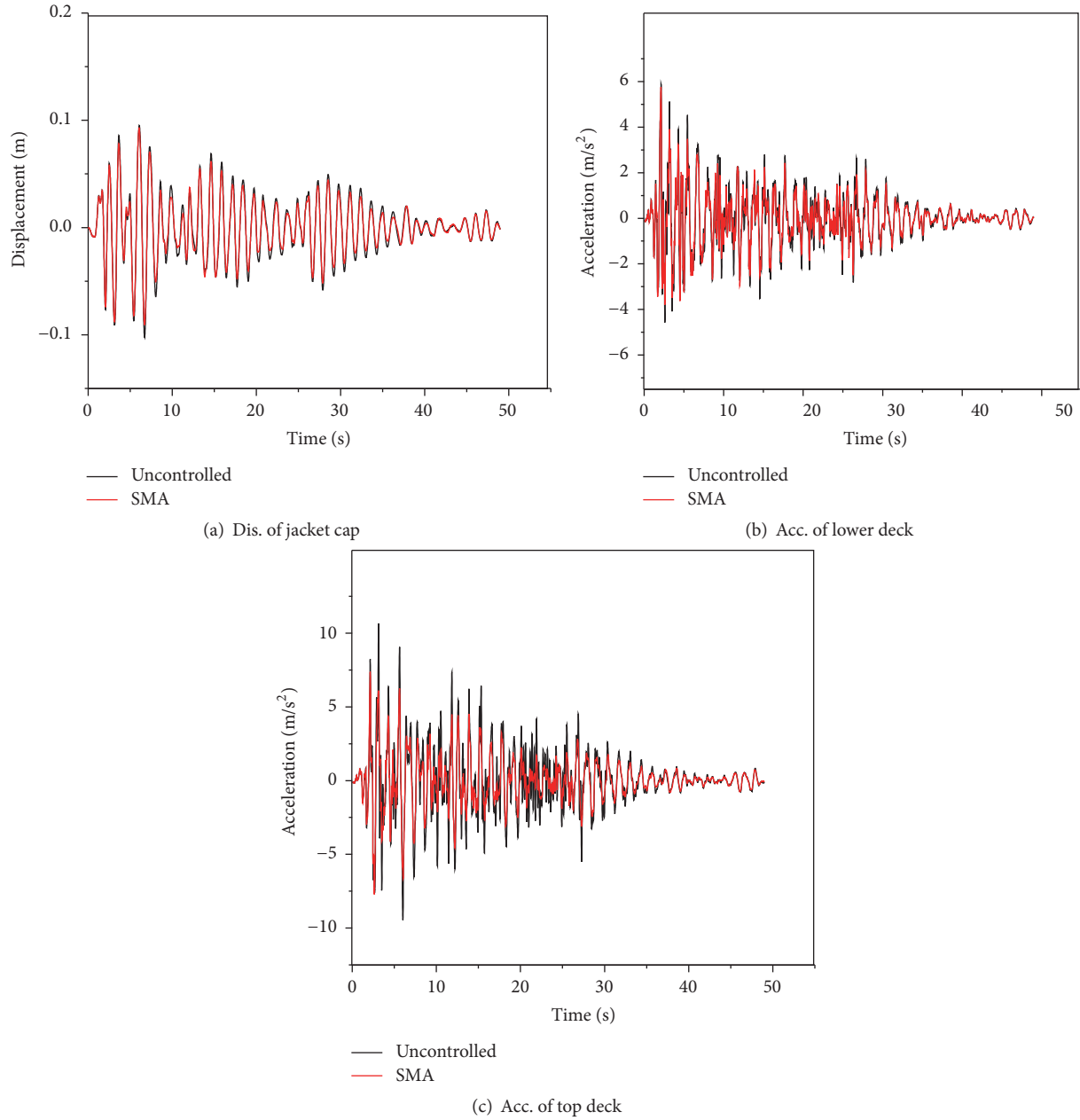


FIGURE 9: Computational response of JZ20-2MQU model under El Centro earthquake excitation.

TABLE 4: Maximum test results of earthquake excitation of the platform.

Earthquake	Structural type	Displacement of jacket (cm)	Acceleration of lower deck (cm/s <sup>2</sup> )	Acceleration of top deck (cm/s <sup>2</sup> )
Tianjin	Uncontrolled	30.3	1150	1750
	ISO-SMA	7.84 (0.741)	558 (0.515)	638 (0.635)
	ISO-PFD-SMA	2.26 (0.925)	444 (0.614)	467.9 (0.733)
TAFT	Uncontrolled	10.2	747	914
	ISO-SMA	4.6 (0.549)	377 (0.495)	411 (0.550)
	ISO-PFD-SMA	2.0 (0.804)	504.2 (0.325)	516.6 (0.436)
El Centro	Uncontrolled	9.52	589	1066
	ISO-SMA	5.68 (0.403)	392 (0.334)	468 (0.561)
	ISO-PFD-SMA	4.67 (0.509)	398 (0.324)	470 (0.559)

Note: the figure in brackets is the percentage of effectiveness of mitigating vibration which is equal to (uncontrolled structure – control structure)/uncontrolled structure).

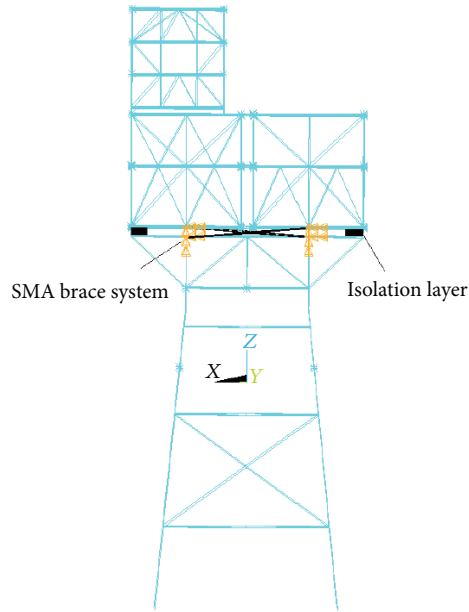


FIGURE 10: FEM of structure with ISO-SMA.

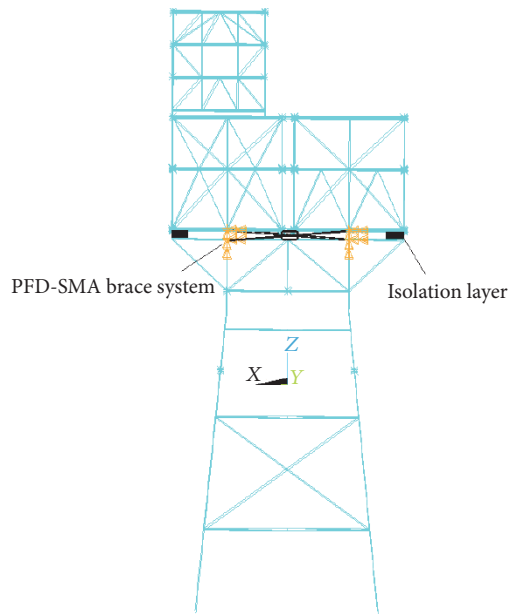


FIGURE 11: FEM of structure with ISO-PFD-SMA.

system is an effective way to reduce the seismic responses of platform structure under the earthquake motion input. The proportional reduction of maximum relative displacement of jacket cap is all over 40.3% in three circumstances. And the percentage of reduction is up to 74.1% under Tianjin seismic excitation. Both the maximum accelerations of top deck and lower deck are reduced by at least 33.4% in the same excitations.

However, it is noticed that ISO-PFD-SMA system is superior to the ISO-SMA system from Table 4. It even

achieves a 92.5% reduction on the maximum displacement of jacket under Tianjin seismic excitation, 18.4% higher than ISO-SMA. Under Taft, ISO-PFD-SMA system also has a better control effect on the maximum displacement of jacket; the percentage of reduction is up to 80.4%, 25% higher than ISO-SMA. From these results, ISO-PFD-SMA system possesses obvious effects on displacement suppression. Although ISO-PFD-SMA system is slightly lower on the acceleration control, compared to ISO-SMA, it matches security and comfort requirements indeed. Moreover, it could be found

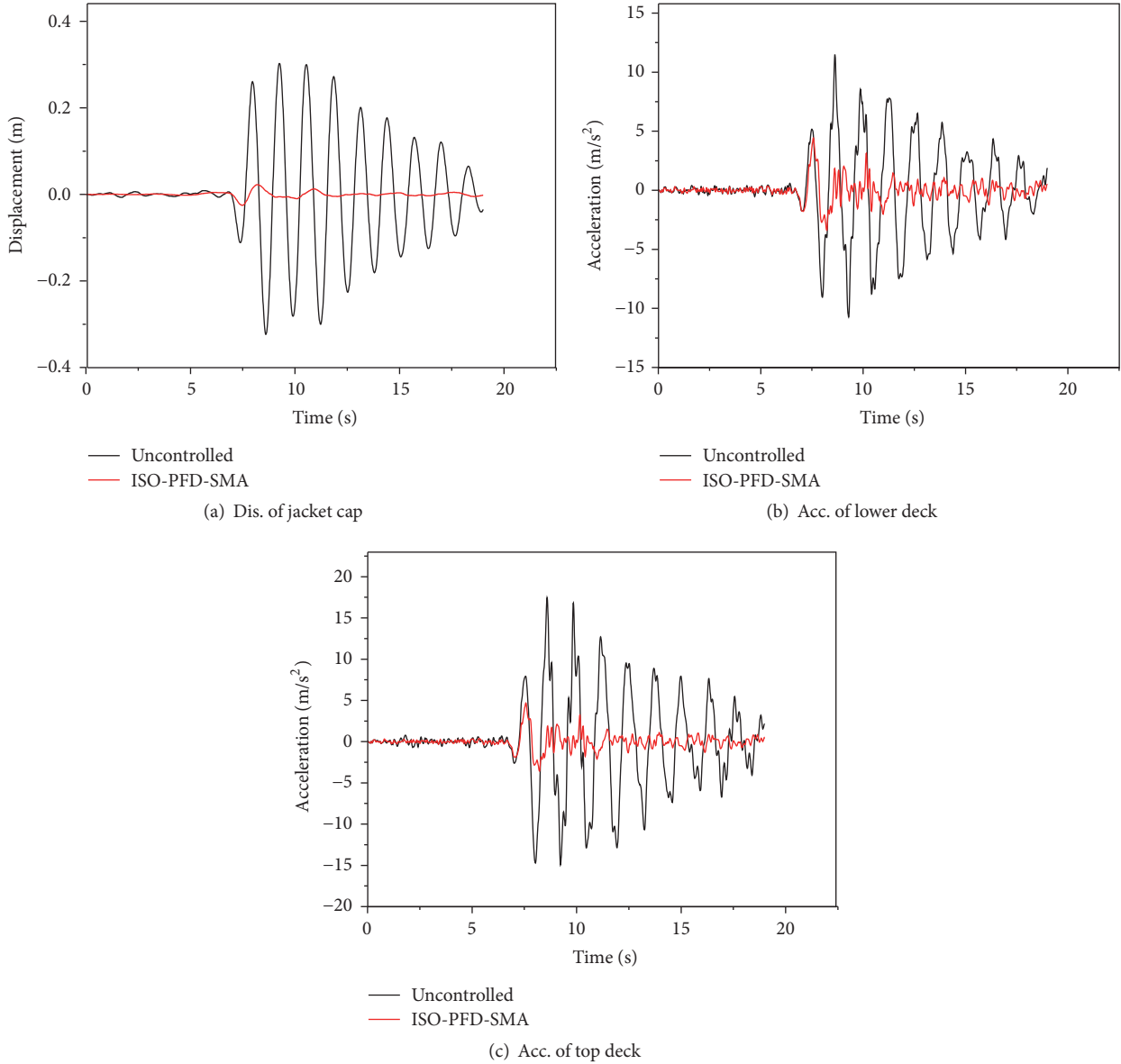


FIGURE 12: Computational response of JZ20-2MQU model under Tianjin earthquake excitation.

that the structure with ISO-PFD-SMA brace system nearly returns to the initial position after the seismic excitation, which confirms that this system has a good self-centering capability.

**3.2. Ice-Induced Vibration Analysis.** With the land on three sides, Bohai gulf is located on the east coast of mid-latitude and mainly influenced by monsoon circulation. Since it is isolated, less heat is exchanged with seas off the semiclosed bays. In winter, Bohai gulf will be affected by strong Mongolia cold high pressure. Additionally, the water of the Bohai is not very salty, because many fresh rivers flow into it. Thus, it freezes more easily. Considering the above, Bohai bay is one of the sea areas with serious ice condition in China [16]. Since last century, ice condition on a large scale has happened seven

TABLE 5: The basic data of ice condition in the Bohai bay.

Period	Fast ice		Sea ice		
	Coverage (km)	Thickness (cm)	Coverage (km)	Thickness (cm)	Speed (m/s)
Nov. to Mar.	5–10	30–40	110–130	20–30	0.4–0.8

times in this area. In the winter of 1968, one platform on Bohai gulf collapsed, because of the worst ice blockages along Bohai Sea. Table 5 shows the basic data of ice condition in the Bohai bay. The model simulation uses the actual three bending ices and three pushing ices. To save space, one bending ice and one pushing ice time history curves are shown in Figure 15.

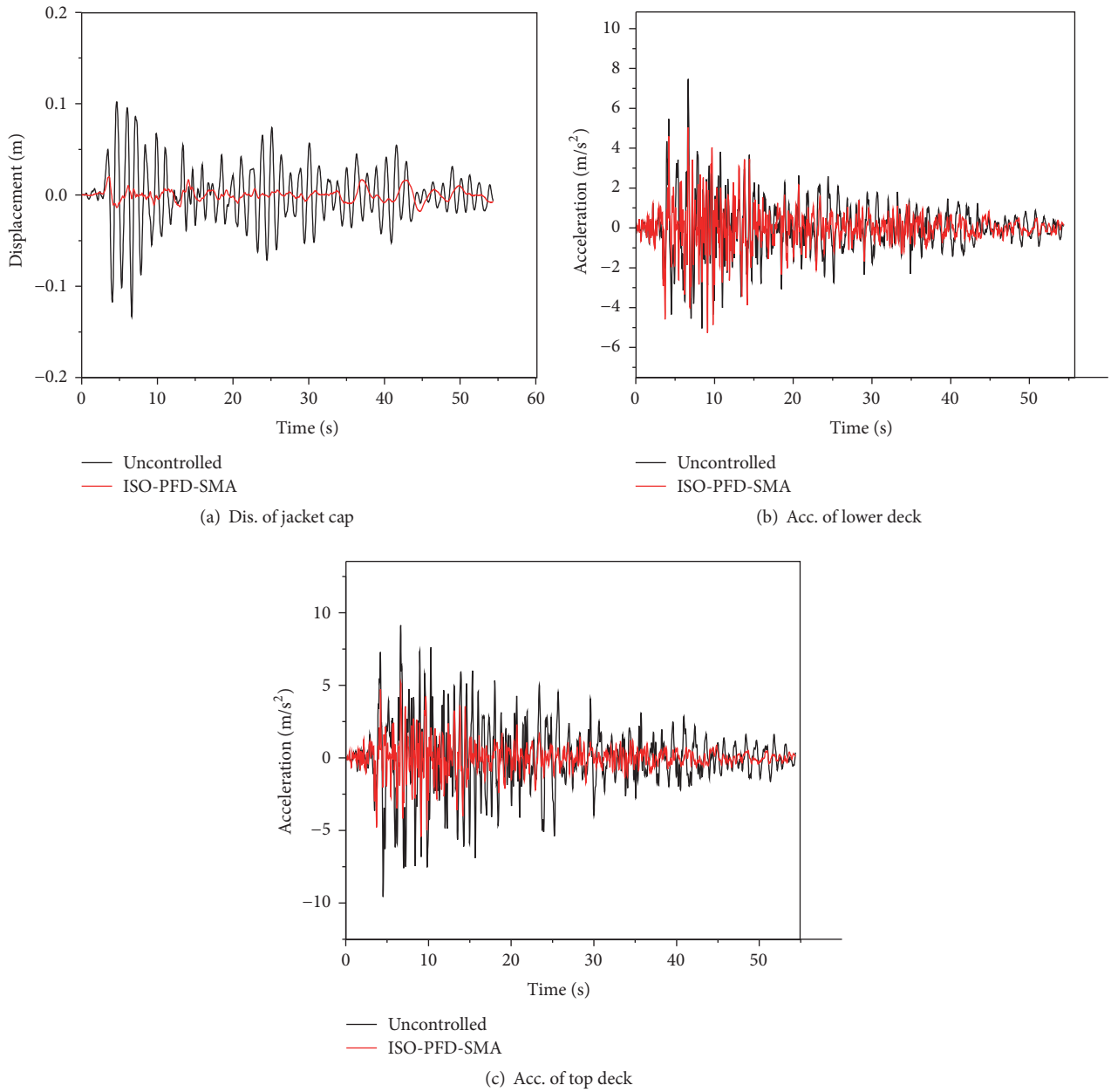


FIGURE 13: Computational response of JZ20-2MQU model under Taft earthquake excitation.

To validate the effectiveness of PFD-SMA bracing system in vibration control under the ice loads, numerical analysis has been conducted by ANSYS software. The ice-induced vibration simulation uses three platform structure styles including the uncontrolled structure, the structure with ISO-SMA bracing system, and the structure with ISO-PFD-SMA bracing system.

The responses are shown in Table 6. According to the results, the peak response of the structure with ISO-PFD-SMA is significantly reduced. From Table 6, the maximum control effect of acceleration of deck could achieve 81% under the pushing ice. But the maximum displacement of deck decreases not obviously. Compared with the acceleration,

the percentage of reduction is 29.8%. Regarding bending ice, the vibration control effect is also very evident. It could achieve a 78% reduction in acceleration of deck; however, the maximum displacement of deck only reduces by 11%. In addition, it could be found that the structure with ISO-PFD-SMA brace system nearly returns to the initial position after the ice-induced excitation.

Based on Table 6, the analysis results show that ISO-PFD-SMA system contributes to greater assurance of comfort of offshore platform structure, compared with ISO-SMA. Meanwhile, it plays a very important role in maintaining the stability of the whole structure and also has a good self-centering capability. Figures 16 and 17 show the time

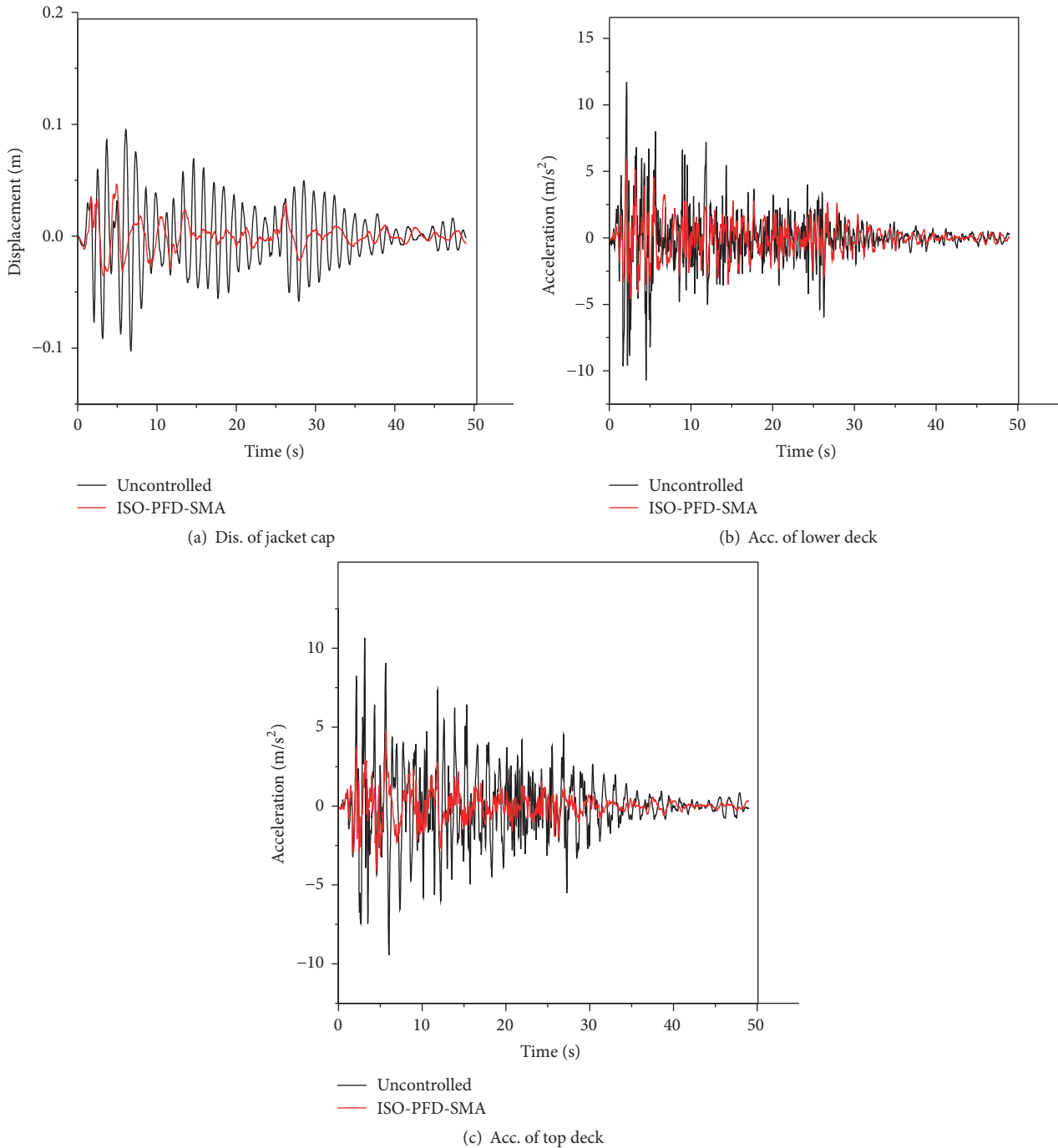


FIGURE 14: Computational response of JZ20-2MQU model under El Centro earthquake excitation.

history curves of platform structure under two ice loads, respectively.

**4. Conclusion**

This paper introduces the PFD-SMA bracing system applied in the vibration control of JZ20-2MUQ offshore platform in Bohai bay, which is subjected to action of ice and seismic

excitation by numerical method. The major conclusions of this study are summarized below:

- (1) ISO-PFD-SMA bracing system set between the deck and jacket cap has a better effect on mitigating vibration, compared with uncontrolled structure and even ISO-SMA bracing system, especially in the control of maximum acceleration of top and lower deck. Both the Pall friction damping and the SMA

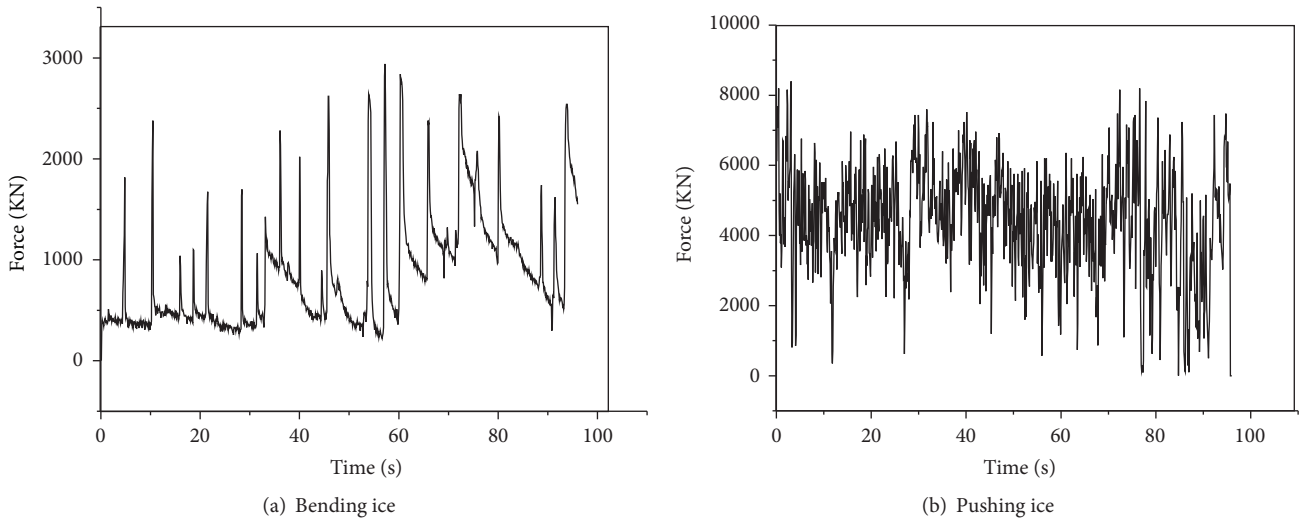


FIGURE 15: Time history of ice forces.

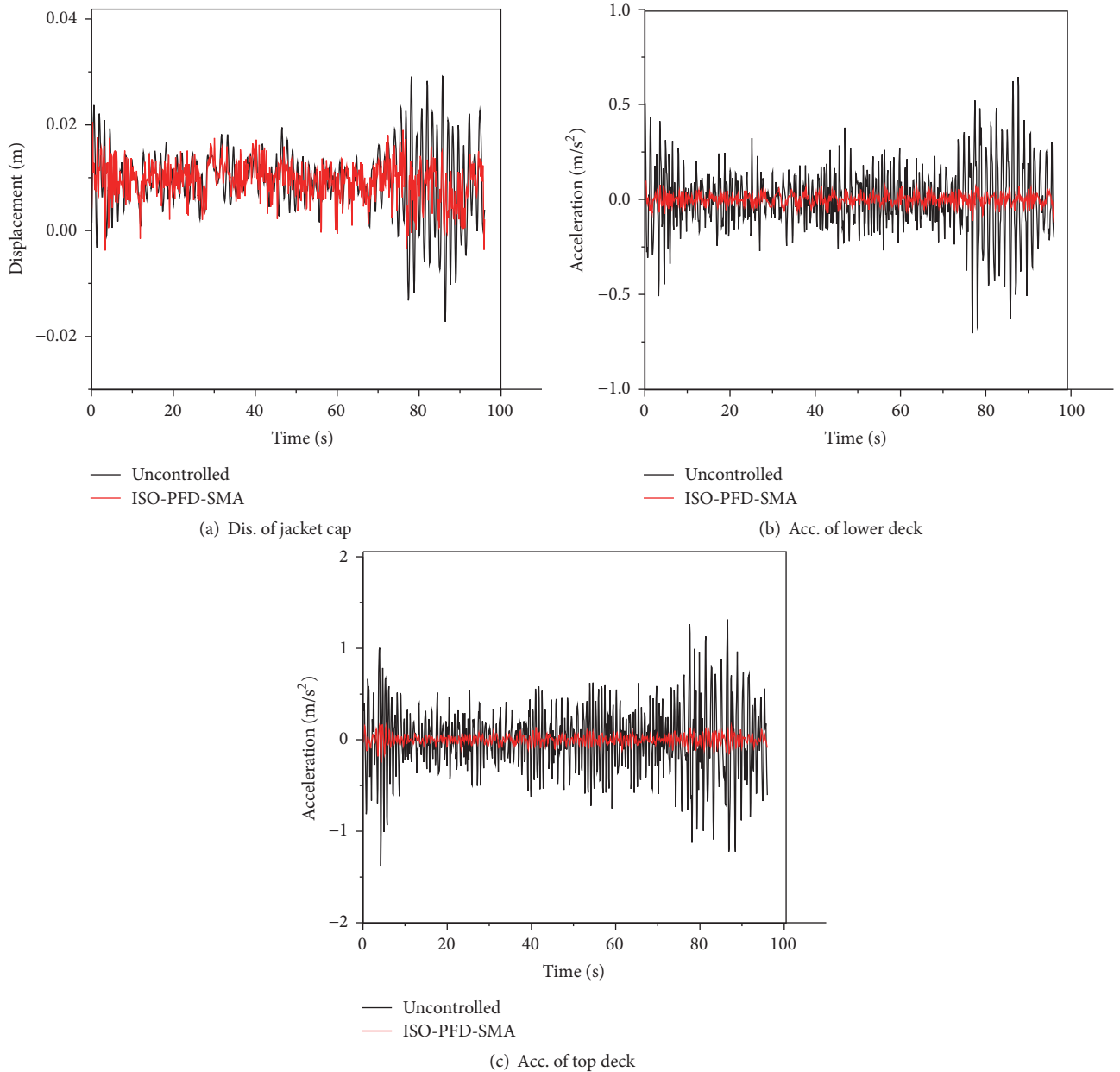


FIGURE 16: Time history curves of platform structure under pushing ice.

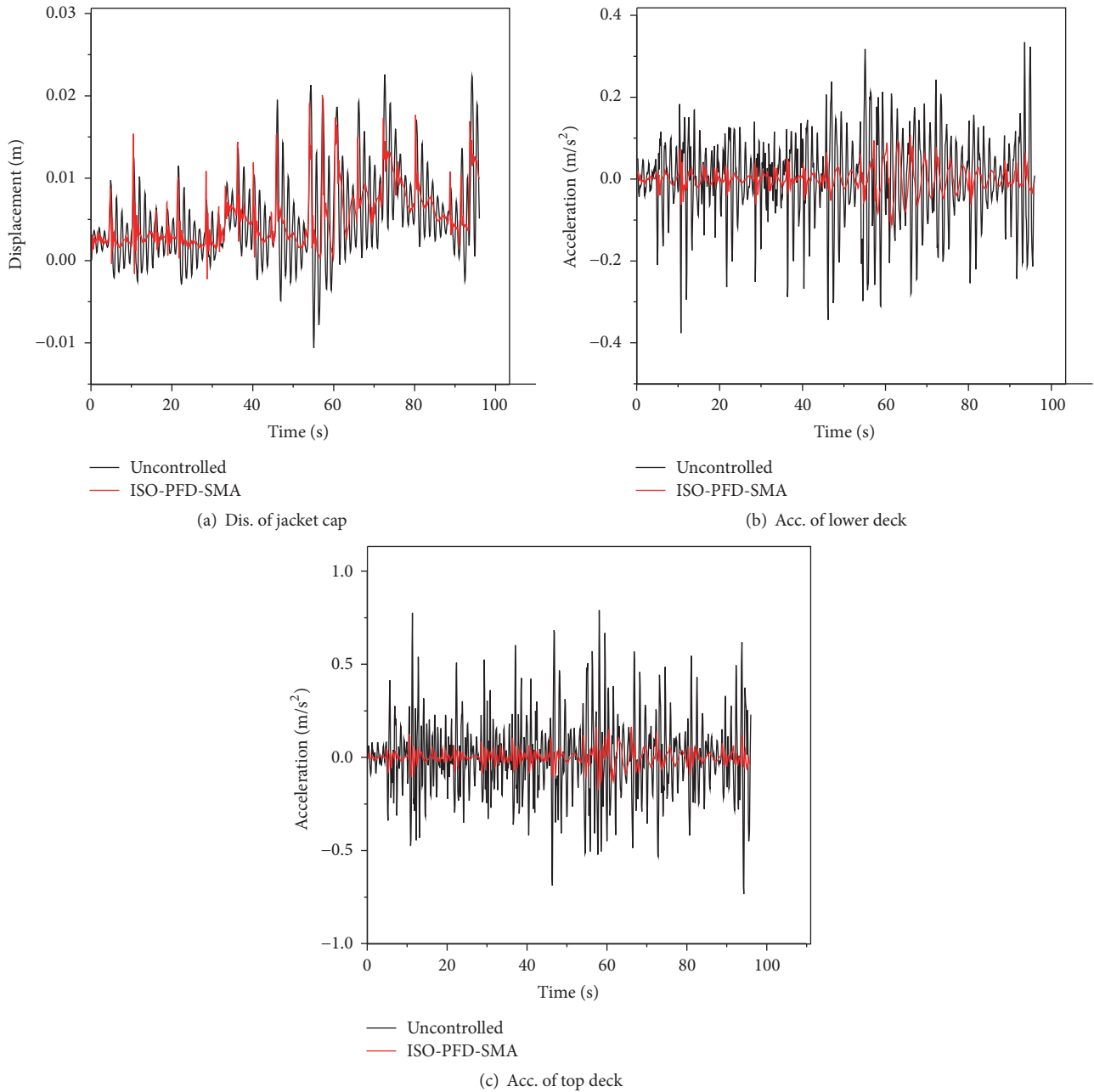


FIGURE 17: Time history curves of platform structure under bending ice.

TABLE 6: Maximum test results of ice excitation of the platform.

Ice load	Structural type	Displacement of jacket (cm)	Acceleration of lower deck (cm/s <sup>2</sup> )	Acceleration of top deck (cm/s <sup>2</sup> )
Pushing	Uncontrolled	2.92	64.52	131.41
	ISO-SMA	1.89 (0.353)	13.70 (0.788)	26.20 (0.800)
	ISO-PFD-SMA	2.05 (0.298)	12.26 (0.810)	25.0 (0.810)
Bending	Uncontrolled	2.26	33.4	79.0
	ISO-SMA	2.18 (0.298)	10.9 (0.674)	18.9 (0.761)
	ISO-PFD-SMA	2.01 (0.11)	11.12 (0.667)	16.8 (0.787)

Note: the figure in brackets is the percentage of effectiveness of mitigating vibration which is equal to (uncontrolled structure – control structure)/uncontrolled structure).

bracing consume a portion of energy, respectively. So, combining the two parts, the desired effect in vibration control will be achieved.

- (2) Only setting SMA bracing system may not lead to ideal results since its bracing could not give full play to their potential, because the overall stiffness of the structure is too large, and the deformation is too small. According to the results, the damping isolation system (ISO) is placed between the bottom of the deck and the top of the jacket structure, which could enhance the energy consumption and make the SMA bracing system become fully effective.

## Competing Interests

The authors declare that there is no conflict of interests regarding the publication of this paper.

## Acknowledgments

The authors acknowledge the financial support by the National Natural Science Foundation of China (51378271), Taishan Scholar Priority Discipline Talent Group program funded by the Shandong Province, and Qingdao Construction Commission funds for development (JK2015-13).

## References

- [1] W. Wei, *Research on seismic Damage States of Jacket Offshore Platform Structures*, Ocean University of China, 2004 (Chinese).
- [2] M. Dolce, D. Cardone, and R. Marnetto, "SMA Re-centering devices for seismic isolation of civil structures," in *SPIE Proceedings of the Smart Systems for Bridges, Structures, and Highways-Smart Structures and Materials*, vol. 4330, pp. 238–249, SPIE, Newport Beach, Calif, USA, March 2001.
- [3] M. Dolce, D. Cardone, and F. C. Ponzio, "Shaking-table tests on reinforced concrete frames with different isolation systems," *Earthquake Engineering and Structural Dynamics*, vol. 36, no. 5, pp. 573–596, 2007.
- [4] S. A. Motahari, M. Ghassemieh, and S. A. Abolmaali, "Implementation of shape memory alloy dampers for passive control of structures subjected to seismic excitations," *Journal of Constructional Steel Research*, vol. 63, no. 12, pp. 1570–1579, 2007.
- [5] M. Speicher, D. E. Hodgson, R. Desroches, and R. T. Leon, "Shape memory alloy tension/compression device for seismic retrofit of buildings," *Journal of Materials Engineering and Performance*, vol. 18, no. 5-6, pp. 746–753, 2009.
- [6] O. E. Ozbulut, P. N. Roschke, P. Y. Lin, and C. H. Loh, "GA-based optimum design of a shape memory alloy device for seismic response mitigation," *Smart Materials and Structures*, vol. 19, no. 6, 2010.
- [7] A. M. Sharabash and B. O. Andrawes, "Application of shape memory alloy dampers in the seismic control of cable-stayed bridges," *Engineering Structures*, vol. 31, no. 2, pp. 607–616, 2009.
- [8] S. Moradi and M. S. Alam, "Feasibility study of utilizing superelastic shape memory alloy plates in steel beam-column connections for improved seismic performance," *Journal of Intelligent Material Systems and Structures*, vol. 26, no. 4, pp. 463–475, 2015.
- [9] B. Wu, J. Zhang, and J. Ou, "Experimental research and numerical analysis of Pall-typed frictional dampers," *Journal of Building Structures*, vol. 24, no. 2, pp. 7–13, 2003 (Chinese).
- [10] J. Zhang, Y. Liu, Y. Gao, and J. Han, "Experimental research of PFD-SMA support system," *Applied Mechanics and Materials*, vol. 71–78, pp. 4521–4524, 2011.
- [11] Annual report of ice forces measurement on JZ20-2MUQ jacket platform, Bohai Inspection Company for Offshore Structure, Institute of Engineering Mechanics, China Seismological Bureau, 1995 (Chinese).
- [12] JZ20-2MUQ platform structure design report, China Offshore Oil Engineering Co., Ltd, 1990.
- [13] K. Bargi, S. R. Hosseini, M. H. Tadayon, and H. Sharifian, "Seismic response of atypical fixed jacket-type offshore platform (SPD1) under sea waves," *Open Journal of Marine Science*, no. 1, pp. 36–42, 2011.
- [14] J.-G. Zhang and A.-Z. Lu, "Hysteretic behavior of advanced PFD-SMA frictional damping brace system," *Journal of Central South University (Science and Technology)*, vol. 42, no. 10, pp. 3157–3163, 2011 (Chinese).
- [15] Q. Yue and X. Bi, "Ice-induced jacket structure vibrations in Bohai Sea," *Journal of Cold Regions Engineering*, vol. 14, no. 2, pp. 81–92, 2000.
- [16] J. Ou, X. Long, Q. S. Li, and Y. Q. Xiao, "Vibration control of steel jacket offshore platform structures with damping isolation systems," *Engineering Structures*, vol. 29, no. 7, pp. 1525–1538, 2007.

## Research Article

# On Finite Element Computations of Contact Problems in Micropolar Elasticity

**Victor A. Eremeyev, Andrzej Skrzat, and Feliks Stachowicz**

*Rzeszów University of Technology, Al. Powstańców Warszawy 8, 35959 Rzeszów, Poland*

Correspondence should be addressed to Victor A. Eremeyev; [eremeyev.victor@gmail.com](mailto:eremeyev.victor@gmail.com)

Received 22 July 2016; Accepted 27 November 2016

Academic Editor: Ying Wang

Copyright © 2016 Victor A. Eremeyev et al. This is an open access article distributed under the Creative Commons Attribution License, which permits unrestricted use, distribution, and reproduction in any medium, provided the original work is properly cited.

Within the linear micropolar elasticity we discuss the development of new finite element and its implementation in commercial software. Here we implement the developed 8-node hybrid isoparametric element into ABAQUS and perform solutions of contact problems. We consider the contact of polymeric stamp modelled within the micropolar elasticity with an elastic substrate. The peculiarities of modelling of contact problems with a user defined finite element in ABAQUS are discussed. The provided comparison of solutions obtained within the micropolar and classical elasticity shows the influence of micropolar properties on stress concentration in the vicinity of contact area.

## 1. Introduction

Nowadays the interest grows to further development and application extended models of continuum mechanics in order to model micro- and nanostructured materials with complex inner structure. The basic idea of enhancement of classic Cauchy continuum model is to add additional fields describing additional degrees of freedom into constitutive equations or/and consider higher-order gradients of deformations. Among these generalized models there are the surface elasticity, micropolar or Cosserat continua, microstretched and micromorphic media, media with internal variables, gradient elasticity, and so forth. In particular, the micropolar model [1–3] proposed by Cosserat brothers more than hundred years ago found applications for modelling such materials as porous solids [4, 5], bones [6–8], masonries [9, 10], beam lattices [11], and other composite materials; see [1, 12–15] and reference therein. The micropolar elasticity possesses the description of size-effects and may be useful for description of the microstructured solids such as foam, bones, powders, and soils. In particular, the influence of micropolar properties may be important for the analysis of the stress concentration near holes and

notches or in the vicinity of contact area. Within the Cosserat continuum model the translations and rotations determine the kinematics of the medium and the stress and couple stress tensors are introduced. The micropolar properties of material may be important near singularities or to describe observed experimentally size-effect [16–19]. Let us also note that for such complex media even more general models of continuum mechanics such as gradient elasticity may be useful; see, for example, [20–24]. Application of extended models of continuum for modelling of such structures as open-cell foams, beam lattices, and pantographic systems is motivated by their complex inner structure. For example, in the classic beam theory moments play an important role and their influence is inherited by the homogenized models. Let us also note that for structured and nonhomogeneous beams used as structural elements for foam or lattice description some extended models were proposed in [25–31]. For rods and beams there are some phenomena as warping of cross-section, instabilities, and sensibility to imperfections are also important; see, for example, [32–41]. Considering all of these phenomena may lead to rather complex models of homogenized media. From this point of view the micropolar elasticity may be treated as first step towards modelling of

microstructured materials and their contact. Further extensions of the indentation problems can be performed based on the other enriched models of continuum; see, for example, strain gradients models [42, 43].

Let us note that the effective solution of boundary value problems of micropolar elasticity as well as of other enhanced models requires advanced numerical code such as the finite element method. The generalized models of continua require usually more computational efforts than the classical elasticity since there exist more degrees of freedom. For the micropolar continuum we use an isogeometric analysis [44, 45] as efficient FEM strategy which together with a hybrid mixed formulation was applied for generalized continua and structures; see, for example, [46–50]. For the moment commercial FEM software gives one the possibility to use user defined elements and user defined procedure for implementation of nonstandard material models. Here we developed new finite element and implement it in ABAQUS.

The paper is organized as follows. In Section 2 we present the basic equations of the linear micropolar elasticity. The equilibrium equations, static and kinematic boundary conditions, and constitutive equations are given. Here we are restricted by isotropic case using the Voigt notation. In Section 3 we discuss the finite element modelling for the micropolar solids. Finally, in Section 4 we present the solution of contact problem for micropolar parabolic stamp and an elastic thick plate.

## 2. Basic Equations of the Micropolar Elasticity

Following [1–3] we recall here the basic equations of the linear micropolar elasticity of isotropic solids. The kinematic of a micropolar solid is described by two fields, that is, the field of translations  $u_i$  and the field of rotations  $\theta_i$ . The latter is responsible for the description of moment interactions of the material particles. Hereinafter the Latin indices take on value 1, 2, or 3 and we use the Einstein summation rule over repeating indices. The equilibrium equations take the form

$$\begin{aligned} t_{ij,i} + f_j &= 0, \\ m_{ij,i} + e_{jmn}t_{mn} + c_j &= 0, \end{aligned} \quad (1)$$

where  $t_{ij}$  and  $m_{ij}$  are the stress and couple stress tensors, respectively,  $e_{ijk}$  is the Levi-Civita third-order tensor, and  $f_j$  and  $c_j$  are external forces and couples. Unlike in classical (Cauchy-type) continua, the tensors  $t_{ij}$  and  $m_{ij}$  are not symmetric. Equations (1) constitute the local balance of momentum and moment of momentum, respectively.

The static and kinematic boundary conditions have the following form:

$$\begin{aligned} n_i t_{ij} \Big|_{A_t} &= \varphi_j, \\ n_i m_{ij} \Big|_{A_t} &= \eta_j, \\ u_i \Big|_{A_u} &= u_i^0, \\ \theta_i \Big|_{A_u} &= \theta_i^0, \end{aligned} \quad (2)$$

where  $n_i$  is the unit vector of external normal to the boundary  $A = A_t \cup A_u$ ,  $\varphi_j$  and  $\eta_j$  are external forces and couples, and  $u_i^0$  and  $\theta_i^0$  are given on  $A_u$  surface fields of translations and rotations, respectively. Obviously, other mixed boundary conditions can be introduced.

In what follows we are restricting ourselves by isotropic case. For a linear isotropic micropolar solid the constitutive equations are

$$\begin{aligned} t_{ij} &= \lambda \varepsilon_{kk} \delta_{ij} + (\mu + \kappa) \varepsilon_{ij} + \mu \varepsilon_{ji}, \\ m_{ij} &= \alpha \kappa_{kk} \delta_{ij} + \beta \kappa_{ji} + \gamma \kappa_{ij}, \end{aligned} \quad (3)$$

where  $\delta_{ij}$  is the Kronecker symbol, and  $\lambda$ ,  $\mu$ ,  $\kappa$ ,  $\alpha$ ,  $\beta$ , and  $\gamma$  are the elastic moduli. In (3) we also introduced the stretch tensor  $\varepsilon_{ij}$  and the wryness tensor  $\kappa_{ij}$  given by formulas

$$\begin{aligned} \varepsilon_{ij} &= u_{j,i} - e_{ijn} \theta_n, \\ \kappa_{ij} &= \theta_{j,i}. \end{aligned} \quad (4)$$

Using the Voigt notation modified for the micropolar elasticity and introducing the stress and moment stress vectors with stretch and wryness vectors by the formulas

$$\begin{aligned} \{\mathbb{T}\} &= \{t_{11}, t_{22}, t_{33}, t_{12}, t_{21}, t_{23}, t_{32}, t_{13}, t_{31}\}^T, \\ \{\mathbb{M}\} &= \{m_{11}, m_{22}, m_{33}, m_{12}, m_{21}, m_{23}, m_{32}, m_{13}, m_{31}\}^T, \\ \{\mathbb{E}\} &= \{\varepsilon_{11}, \varepsilon_{22}, \varepsilon_{33}, \varepsilon_{12}, \varepsilon_{21}, \varepsilon_{23}, \varepsilon_{32}, \varepsilon_{13}, \varepsilon_{31}\}^T, \\ \{\mathbb{K}\} &= \{\kappa_{11}, \kappa_{22}, \kappa_{33}, \kappa_{12}, \kappa_{21}, \kappa_{23}, \kappa_{32}, \kappa_{13}, \kappa_{31}\}^T, \end{aligned} \quad (5)$$

we represent the constitutive equations in the following unified form:

$$\begin{aligned} \{\sigma_M\} &= [\mathbb{C}] \{\varepsilon_M\}, \\ [\mathbb{C}] &= \begin{pmatrix} \mathbb{A} & 0 \\ 0 & \mathbb{B} \end{pmatrix}, \\ \{\sigma_M\} &= \begin{Bmatrix} \mathbb{T} \\ \mathbb{M} \end{Bmatrix}, \\ \{\varepsilon_M\} &= \begin{Bmatrix} \mathbb{E} \\ \mathbb{K} \end{Bmatrix} \end{aligned} \quad (6)$$

with  $18 \times 18$  symmetric stiffness matrix  $[\mathbb{C}]$ , where  $\mathbb{A}$  and  $\mathbb{B}$  are three-diagonal symmetric  $9 \times 9$  matrices given by

$$\begin{aligned}
[\mathbb{A}] &= \begin{pmatrix} \lambda + 2\mu + \kappa & \lambda & \lambda & 0 & 0 & 0 & 0 & 0 & 0 & 0 \\ \lambda & \lambda + 2\mu + \kappa & \lambda & 0 & 0 & 0 & 0 & 0 & 0 & 0 \\ \lambda & \lambda & \lambda + 2\mu + \kappa & 0 & 0 & 0 & 0 & 0 & 0 & 0 \\ 0 & 0 & 0 & \mu + \kappa & \mu & 0 & 0 & 0 & 0 & 0 \\ 0 & 0 & 0 & \mu & \mu + \kappa & 0 & 0 & 0 & 0 & 0 \\ 0 & 0 & 0 & 0 & 0 & \mu + \kappa & \mu & 0 & 0 & 0 \\ 0 & 0 & 0 & 0 & 0 & \mu & \mu + \kappa & 0 & 0 & 0 \\ 0 & 0 & 0 & 0 & 0 & 0 & 0 & \mu + \kappa & \mu & 0 \\ 0 & 0 & 0 & 0 & 0 & 0 & 0 & 0 & \mu & \mu + \kappa \end{pmatrix}, \\
[\mathbb{B}] &= \begin{pmatrix} \alpha + \beta + \gamma & \alpha & \alpha & 0 & 0 & 0 & 0 & 0 & 0 & 0 \\ \alpha & \alpha + \beta + \gamma & \alpha & 0 & 0 & 0 & 0 & 0 & 0 & 0 \\ \alpha & \alpha & \alpha + \beta + \gamma & 0 & 0 & 0 & 0 & 0 & 0 & 0 \\ 0 & 0 & 0 & \gamma & \beta & 0 & 0 & 0 & 0 & 0 \\ 0 & 0 & 0 & \beta & \gamma & 0 & 0 & 0 & 0 & 0 \\ 0 & 0 & 0 & 0 & 0 & \gamma & \beta & 0 & 0 & 0 \\ 0 & 0 & 0 & 0 & 0 & \beta & \gamma & 0 & 0 & 0 \\ 0 & 0 & 0 & 0 & 0 & 0 & 0 & \gamma & \beta & 0 \\ 0 & 0 & 0 & 0 & 0 & 0 & 0 & \beta & \gamma & 0 \end{pmatrix}.
\end{aligned} \tag{7}$$

Unlike classical elasticity where the stiffness matrix in the Voigt notations is a symmetric  $6 \times 6$  matrix here we have larger matrices. The values of used micropolar elastic moduli can be found from direct experiments provided in [4, 5, 8, 14] or using homogenization technique [6, 7, 9–11, 51]. Let us note that the homogeneous micropolar model can be derived on the base of the passage from heterogeneous classical (Cauchy) continuum and on using passage from inhomogeneous micropolar (Cosserat) material; see [52–55]. Analysis of general constitutive equations of anisotropic micropolar solids on the base of the material symmetry groups is performed in [2, 56, 57].

From the experimental point of view it is better to use another set of material parameters [4, 5, 8, 14] listed in Table 1.

The boundary value problems of the micropolar isotropic elasticity contain also the boundary value problems of classical elasticity as a special case. This coincidence may be used for verification of the developed code. The first way to reduce the problem is to assume  $\kappa = 0$  or  $N = 0$ . Indeed, if the coupling modulus  $\kappa = 0$  the stress tensor becomes symmetric and takes the form

$$t_{ij} = \lambda u_{k,k} \delta_{ij} + \mu (u_{i,j} + u_{j,i}). \tag{8}$$

Thus,  $(1)_1$  transforms to the classic equilibrium equation of the linear elasticity which is independent of rotations whereas  $(1)_2$  includes only rotations. Let us also note that  $(1)_2$  has similar form to  $(1)_1$  but with different elastic moduli. So in this case the problem is decoupled and translations can be determined independently of microrotations.

The second reduction is possible if one assumes the microrotations to be fixed,  $\theta_j = 0$ . In this case  $(1)_1$  again coincides with classic equilibrium equation with Lamé's moduli  $\lambda$  and  $\mu$ . In what follows we use both methods for verification and validation of the developed code.

### 3. Implementation of Micropolar Elasticity into FEM Software

Efficient solution of large boundary value problems requires application of an advanced software. In this research ABAQUS commercial program has been extended by the implementation of the user element (UEL) to solve the micropolar elasticity problems. Special code written in Fortran is linked with ABAQUS software allowing the user to practice all the ABAQUS features without paying an attention to their numerical implementation. From the practical point of view the most important features are creation of sophisticated geometry, application of loads and boundary conditions, applications of constraints and contact conditions, generation of 3D meshes, using the material library, and, the most important feature, being very effective solver.

During the solver execution UEL procedure is called twice for each Gaussian point in every element. In the first call the element stiffness should be provided by UEL procedure. Very often user element procedure requires calling UELMAT code (user material procedure) necessary to obtain the relation between stress and strain increments. Another call

of UEL procedure is necessary to compute residual forces, element nodal forces resulting from element stresses, which is essential in the convergence monitoring during solving nonlinear problems. Designing of own finite elements is an ambiguous task recommended to advanced users only. It should be mentioned that UEL procedures should be very carefully tested and validated. There are some important disadvantages of using user elements in ABAQUS program. First of all, ABAQUS does not recognize the shape of the element; the element is represented by the set of nodes only. For example, 2D four nodes' element can be defined as a truss structure, as a frame made up of beams, or as a quadrilateral flat element. In each of the mentioned cases different type of loads can be applied; for example, the pressure can be applied to quadrilateral element only, the bending moment can be applied to beam, and so forth. The visualization of obtained results is another matter. The visualization is not possible without detailed description of an element topology; the set of nodes does not provide this information. That is why only nodal displacements of the user elements can be displayed in ABAQUS postprocessor. Displaying strains and stresses requires developing own graphical programs or using uncomfortable techniques with "ghost" meshes made of ordinary ABAQUS elements constrained to meshes consisting of user elements.

The typical call of UEL procedure is presented below:

```
subroutine uelmat (rhs, amatrix, svars, energy,
ndofel, nrhs, nsvars,
1 props, nprops, coords, mcrd, nnode, u, du, v,
a, jtype, time,
```

- 2 dtime, kstep, kinc, jelem, params, ndload, jldtyp, admag,
- 3 predef, npredef, lflags, mlvarx, ddlmag, mdload, pnnewdt,
- 4 jprops, njpro, period, materiallib)

The most important parameters are *amatrix* (element stiffness matrix) and *rhs* (right-hand side vector of residuals necessary to check the convergence of computation). In the most simple case of static linear analysis the *rhs* parameter can be omitted because the convergence (equilibrium equations at nodes) is achieved in the first iteration. The meaning of other parameters is described in ABAQUS documentation. UEL procedure can be slightly simplified if it contains constitutive properties; the call of UELMAT procedure is not necessary, therefore.

The whole procedure is typical for the isoparametric finite element formulation in 3D problems with the exception of considered degrees of freedom (in micropolar elasticity there are three displacement components and additionally three microrotations) and strain and stress measures (strain and stress tensors contain more components and are not symmetric). In UEL implementation of micropolar elasticity the same shape functions are used for displacement and microrotations

$$N_i(\xi, \eta, \zeta) = \frac{1}{8} (1 + \xi \xi_i) (1 + \eta \eta_i) (1 + \zeta \zeta_i), \quad (9)$$

where  $\xi_i$ ,  $\eta_i$ , and  $\zeta_i$  are the nodal coordinates in the local coordinate system. For the Eringen strain measure the matrix of the shape functions derivatives is

$$\begin{Bmatrix} \varepsilon_{11} \\ \varepsilon_{22} \\ \varepsilon_{33} \\ \varepsilon_{12} \\ \varepsilon_{21} \\ \varepsilon_{23} \\ \varepsilon_{32} \\ \varepsilon_{13} \\ \varepsilon_{31} \\ \kappa_{11} \\ \kappa_{22} \\ \kappa_{33} \\ \kappa_{12} \\ \kappa_{21} \\ \kappa_{23} \\ \kappa_{32} \\ \kappa_{13} \\ \kappa_{31} \end{Bmatrix} = \begin{pmatrix} f_{1,1} & 0 & 0 & 0 & 0 & 0 & \cdots & f_{8,1} & 0 & 0 & 0 & 0 & 0 \\ 0 & f_{1,2} & 0 & 0 & 0 & 0 & \cdots & 0 & f_{8,2} & 0 & 0 & 0 & 0 \\ 0 & 0 & f_{1,3} & 0 & 0 & 0 & \cdots & 0 & 0 & f_{8,3} & 0 & 0 & 0 \\ 0 & f_{1,1} & 0 & 0 & 0 & f_1 & \cdots & 0 & f_{8,1} & 0 & 0 & 0 & f_8 \\ f_{1,2} & 0 & 0 & 0 & 0 & -f_1 & \cdots & f_{8,2} & 0 & 0 & 0 & 0 & -f_8 \\ 0 & 0 & f_{1,2} & f_1 & 0 & 0 & \cdots & 0 & 0 & f_{8,2} & f_8 & 0 & 0 \\ 0 & f_{1,3} & 0 & -f_1 & 0 & 0 & \cdots & 0 & f_{8,3} & 0 & -f_8 & 0 & 0 \\ 0 & 0 & f_{1,1} & 0 & -f_1 & 0 & \cdots & 0 & 0 & f_{8,1} & 0 & -f_8 & 0 \\ f_{1,3} & 0 & 0 & 0 & f_1 & 0 & \cdots & f_{8,3} & 0 & 0 & 0 & f_8 & 0 \\ 0 & 0 & 0 & f_{1,1} & 0 & 0 & \cdots & 0 & 0 & 0 & f_{8,1} & 0 & 0 \\ 0 & 0 & 0 & 0 & f_{1,2} & 0 & \cdots & 0 & 0 & 0 & 0 & f_{8,2} & 0 \\ 0 & 0 & 0 & 0 & 0 & f_{1,3} & \cdots & 0 & 0 & 0 & 0 & 0 & f_{8,3} \\ 0 & 0 & 0 & f_{1,2} & 0 & 0 & \cdots & 0 & 0 & 0 & f_{8,2} & 0 & 0 \\ 0 & 0 & 0 & 0 & f_{1,1} & 0 & \cdots & 0 & 0 & 0 & 0 & f_{8,1} & 0 \\ 0 & 0 & 0 & 0 & f_{1,3} & 0 & \cdots & 0 & 0 & 0 & 0 & f_{8,3} & 0 \\ 0 & 0 & 0 & 0 & 0 & f_{1,2} & \cdots & 0 & 0 & 0 & 0 & 0 & f_{8,2} \\ 0 & 0 & 0 & f_{1,3} & 0 & 0 & \cdots & 0 & 0 & 0 & f_{8,3} & 0 & 0 \\ 0 & 0 & 0 & 0 & 0 & f_{1,1} & \cdots & 0 & 0 & 0 & 0 & 0 & f_{8,1} \end{pmatrix} \begin{Bmatrix} u_1^1 \\ u_2^1 \\ u_3^1 \\ \theta_1^1 \\ \theta_2^1 \\ \theta_3^1 \\ \vdots \\ u_1^8 \\ u_2^8 \\ u_3^8 \\ \theta_1^8 \\ \theta_2^8 \\ \theta_3^8 \end{Bmatrix}, \quad (10)$$

TABLE 1: Micropolar material parameters.

Description	Symbol	Formula
Shear modulus [MPa]	$G$	$G = \frac{2\mu + \kappa}{2}$
Poisson's ratio [—]	$\nu$	$\nu = \frac{\lambda}{2\lambda + 2\mu + \kappa}$
Coupling number [—]	$N$	$N^2 = \frac{\kappa}{2(\mu + \kappa)}$
Characteristic length (torsion) [m]	$l_t$	$l_t = \frac{\beta + \gamma}{2\mu + \kappa}$
Characteristic length (bending) [m]	$l_b$	$l_b = \frac{\gamma}{2\mu + \kappa}$
Polar ratio [—]	$\Psi$	$\Psi = \frac{\beta + \gamma}{\alpha + \beta + \gamma}$

where  $u_i^j$  and  $\theta_i^j$  are the  $i$ th displacement or microrotation components in the  $j$ th node, respectively.

In the isoparametric element the shape functions (9) are applied for the mapping of local coordinates  $\xi, \eta, \zeta$  to the coordinates  $x, y, z$  of the global Cartesian coordinate system

$$\begin{aligned} x &= \sum N_i(\xi, \eta, \zeta) x_i; \\ y &= \sum N_i(\xi, \eta, \zeta) y_i; \\ z &= \sum N_i(\xi, \eta, \zeta) z_i. \end{aligned} \quad (11)$$

Calculation of derivatives  $f_{i,j}$  requires application of chain rule; that is,

$$\begin{Bmatrix} N_{i,x} \\ N_{i,y} \\ N_{i,z} \end{Bmatrix} = \begin{pmatrix} \xi_{,x} & \eta_{,x} & \zeta_{,x} \\ \xi_{,y} & \eta_{,y} & \zeta_{,y} \\ \xi_{,z} & \eta_{,z} & \zeta_{,z} \end{pmatrix} \begin{Bmatrix} N_{i,\xi} \\ N_{i,\eta} \\ N_{i,\zeta} \end{Bmatrix} \quad (12)$$

or

$$\begin{Bmatrix} N_{i,x} \\ N_{i,y} \\ N_{i,z} \end{Bmatrix} = \mathbb{J}^{-1} \begin{Bmatrix} N_{i,\xi} \\ N_{i,\eta} \\ N_{i,\zeta} \end{Bmatrix}, \quad (13)$$

where  $\mathbb{J}$  is the Jacobian matrix

$$\mathbb{J} = \begin{pmatrix} x_{,\xi} & y_{,\xi} & z_{,\xi} \\ x_{,\eta} & y_{,\eta} & z_{,\eta} \\ x_{,\zeta} & y_{,\zeta} & z_{,\zeta} \end{pmatrix}, \quad (14)$$

which can be found from (9) and (11).

The stiffness matrix of developed element is

$$\mathbb{K} = \int_V \mathbb{D}^T \mathbb{C} \mathbb{D} dV, \quad (15)$$

where the constitutive stiffness matrix  $\mathbb{C}$  is presented in the previous section. The integration in (15) is performed as the loop over the Gaussian points. The  $2 \times 2 \times 2$  Gaussian quadrature is used.

Short description of micropolar elasticity 8-node isoparametric element implementation consists of several steps. The user element procedure based on (9) and (11)–(15) is shortly summarized below.

(i) Calculation of stiffness matrix of 8-node isoparametric element for micropolar elasticity. In the loop over the Gaussian points (there are 8 Gaussian points)

- (1) Find the shape functions at each Gaussian point and their derivatives with respect to natural coordinates
- (2) Find the Jacobian matrix (14); numerically compute its inverse and determinant
- (3) Find the shape functions derivatives (13) with respect to Cartesian coordinates  $x, y, z$
- (4) Find the matrix of shape functions derivatives  $\mathbb{D}$  (the relation between strain components and nodal displacements and microrotations)
- (5) Find the constitutive matrix  $\mathbb{C}$  (the relation between stress and strain tensors)
- (6) Compute  $\mathbb{D}^T \mathbb{C} \mathbb{D}$  (for the 2-point Gaussian quadrature all weights are equal to ones) and add it as the contribution to the stiffness matrix which uses the determinant of Jacobian matrix as the multiplier

(ii) Additional computations

- (1) Find the element nodal forces resulting from element stresses and subtract them from the external nodal forces in order to compute residuals (necessary to check the rate of the solution convergence)
- (2) Make other computations; for example, update the strain energy

#### 4. Parabolic Stamp Indentation

Using the presented above finite element we analyzed few 3D static problems for solids with certain singularities such as notch, hole, or small contact area for the contact problem of two solids [17]. For comparison of solutions with the linear elasticity we used the fact that the micropolar elasticity provides the same solutions as classic elasticity if we assume specific form of microrotations ( $\theta_i = 0$ ) or for specific set of elastic moduli that is without coupling ( $\kappa = 0$ ).

Similar results obtained by the commercial software using the classical theory of elasticity and the results acquired by use of user element while reduced number of material data is used prove that the solution obtained by the UEL procedure is reliable. In this research the Hertzian contact between a parabolic stamp and a half space is considered. For classical Hertz theory of an elastic contact we refer, for example, to [58, pp. 102–14], where formulas for stress distribution are also given. By parabolic stamp we mean a solid with surface in the form of an elliptic paraboloid that is a surface given by equation  $p^2 y = x^2 + z^2$ , where  $p$  is a parameter, and  $x, y$ , and

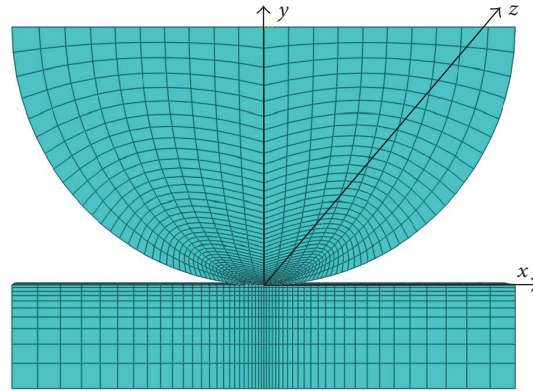


FIGURE 1: Fine element mesh in the contact problem.

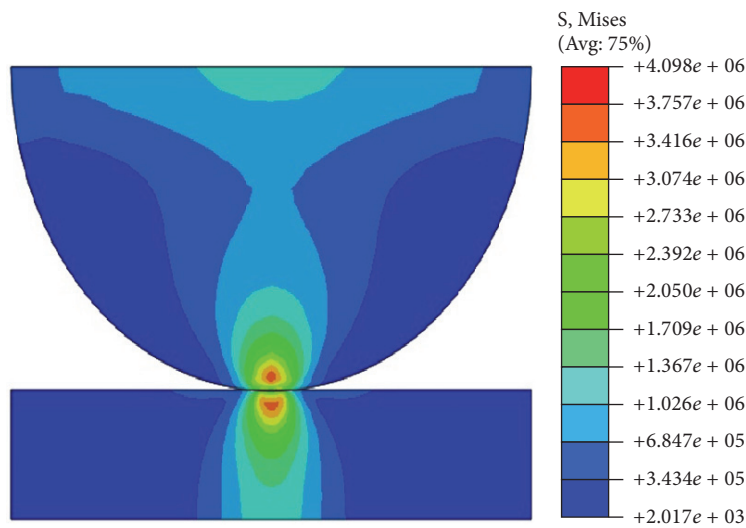


FIGURE 2: Von Mises stress [Pa]: commercial software, classical theory of elasticity.

$z$  are the Cartesian coordinates, respectively; see Figure 1. The main problem arising in this type of analysis is that ABAQUS program does not recognize the volumes and faces of user elements (user element is represented by a set of nodes). The only possible contact formulation is the contact between the surface (ordinary finite elements implemented in ABAQUS) and the set of nodes (UEL elements), therefore. The solution is less precise than the solution of the same problem considering the contact of two surfaces although reasonable results can be achieved for sufficiently dense meshes.

The contact of a parabolic stamp made of polystyrene foam with the flat elastic plate is considered. The foam is modelled as a micropolar material. For the foam we use following material data [5]: shear modulus  $G = 104$  MPa, Poisson's ratio  $\nu = 0.4$ , characteristic length for torsion  $l_t = 0.62$  mm, characteristic length for bending  $l_b = 0.33$  mm, coupling number  $N = 0.04$ , and polar ratio  $\Psi = 1.5$ . The average cell size of the foam is about 1 mm; it correlates with characteristic lengths. As in the case of homogenization of regular lattice structures [11], the foam cell size plays a role of a characteristic length parameter, and  $l_b$  and  $l_t$  depend on

it. For the plate we consider the classic elastic material with the same shear modulus and Poisson's ratio as for foam.

In Figure 1 the finite element mesh is presented which is dense enough in the contact zone in order to obtain the results confirming Hertz's formulas. The distribution of von Mises stress obtained by ABAQUS within classical linear theory of elasticity is shown in Figure 2. Very similar results (distribution and magnitude) are obtained using developed micropolar user elements when microrotations are fixed. This demonstrates excellent convergence of the distribution of stress and stress magnitudes using the developed element to the classical solutions. So the developed UEL procedure is reliable.

In Figure 3 the distribution of couple stress  $m_{yy}$  in the vicinity of the contact zone is shown; here  $y$  is the vertical axis. Couple stress appears only in the stamp (modelled as the micropolar medium) near the contact zone. As expected the distribution of  $m_{yy}$  is antisymmetric. The magnitude of couple stress (all components) is several orders smaller than the magnitude of Cauchy stresses. Thus, the influence of the micropolar properties is restricted only to zones

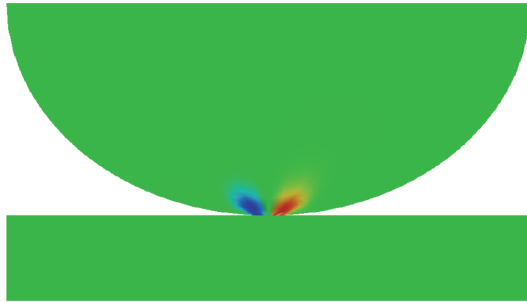


FIGURE 3: The distribution of couple stress  $m_{yy}$ .

with singularities such as sudden change in normal stresses in contact area and free surface. On the other hand, the micropolar elasticity gives the possibility to capture size-effect, observed for microstructured solids such as foams as well as in the case of nanoindentation. All solved benchmark tests for  $\kappa \neq 0$  considered here have shown that the difference between classical elasticity and micropolar one is essential in an area of size of the characteristic length. In such areas the stresses are not symmetric and there is a redistribution of the deformation energy among translational and rotational degrees of freedom; one can expect rotations of microstructural elements such as foam struts in foams or grains in granular media. So for local behavior such as in the case of contact problem with small area and deformations near other types of stress concentrators and at the micro- and nanoscales the influence of micropolar properties can be important.

## 5. Conclusions

We discussed finite element approach adopted to the linear micropolar elasticity in order to model microstructured solids such as porous materials and beam lattices. The new 8-node hybrid micropolar isoparametric element and its implementation in ABAQUS are presented. Here we analyzed the contact problem between two elastic solids. Comparison of solutions based on classical and micropolar elasticity is carefully discussed. Numerical tests have shown that couple stress appears almost in the vicinity of contact zone.

## Competing Interests

The publication of the paper does not lead to any conflict of interests.

## Acknowledgments

Authors acknowledge the support by the People Program (Marie Curie ITN transfer) of the European Union's Seventh Framework Programme for research, technological development, and demonstration under Grant Agreement no. PITN-GA-2013-606878.

## References

- [1] V. A. Eremeyev, L. P. Lebedev, and H. Altenbach, *Foundations of Micropolar Mechanics*, Springer Briefs in Applied Sciences and Technology, Springer, Heidelberg, Germany, 2013.
- [2] A. C. Eringen, *Microcontinuum field theories. I. Foundations and solids*, Springer, New York, USA, 1999.
- [3] W. Nowacki, *Theory of Asymmetric Elasticity*, Pergamon, Oxford, UK, 1986.
- [4] R. S. Lakes, "Experimental micro mechanics methods for conventional and negative Poisson's ratio cellular solids as Cosserat continua," *Journal of Engineering Materials and Technology*, vol. 113, no. 1, pp. 148–155, 1991.
- [5] R. S. Lakes, "Experimental microelasticity of two porous solids," *International Journal of Solids and Structures*, vol. 22, no. 1, pp. 55–63, 1986.
- [6] I. Goda, M. Assidi, S. Belouettar, and J. F. Ganghoffer, "A micropolar anisotropic constitutive model of cancellous bone from discrete homogenization," *Journal of the Mechanical Behavior of Biomedical Materials*, vol. 16, no. 1, pp. 87–108, 2012.
- [7] I. Goda and J.-F. Ganghoffer, "Identification of couple-stress moduli of vertebral trabecular bone based on the 3D internal architectures," *Journal of the Mechanical Behavior of Biomedical Materials*, vol. 51, pp. 99–118, 2015.
- [8] J. F. C. Yang and R. S. Lakes, "Experimental study of micropolar and couple stress elasticity in compact bone in bending," *Journal of Biomechanics*, vol. 15, no. 2, pp. 91–98, 1982.
- [9] D. Besdo, "Towards a Cosserat-theory describing motion of an originally rectangular structure of blocks," *Archive of Applied Mechanics*, vol. 80, no. 1, pp. 25–45, 2010.
- [10] P. Trovalusci, M. Ostoja-Starzewski, M. L. De Bellis, and A. Murralli, "Scale-dependent homogenization of random composites as micropolar continua," *European Journal of Mechanics—A/Solids*, vol. 49, pp. 396–407, 2015.
- [11] F. Dos Reis and J. F. Ganghoffer, "Construction of micropolar continua from the asymptotic homogenization of beam lattices," *Computers & Structures*, vol. 112–113, pp. 354–363, 2012.
- [12] H. Altenbach and V. A. Eremeyev, "Strain rate tensors and constitutive equations of inelastic micropolar materials," *International Journal of Plasticity*, vol. 63, pp. 3–17, 2014.
- [13] V. A. Eremeyev, "On effective properties of materials at the nano- and microscales considering surface effects," *Acta Mechanica*, vol. 227, no. 1, pp. 29–42, 2016.
- [14] R. S. Lakes, "Experimental methods for study of Cosserat elastic solids and other generalized continua," in *Continuum Models for Materials with Micro-Structure*, H. Mühlhaus, Ed., pp. 1–22, John Wiley & Sons, New York, NY, USA, 1995.
- [15] H. Reda, Y. Rahali, J. F. Ganghoffer, and H. Lakiss, "Wave propagation in 3D viscoelastic auxetic and textile materials by homogenized continuum micropolar models," *Composite Structures*, vol. 141, pp. 328–345, 2016.
- [16] T. Ariman, "On the stresses around a circular hole in micropolar elasticity," *Acta Mechanica*, vol. 4, no. 3, pp. 216–229, 1967.
- [17] V. A. Eremeyev, A. Skrzat, and A. Vinakurava, "Application of the micropolar theory to the strength analysis of bioceramic materials for bone reconstruction," *Strength of Materials*, vol. 48, no. 4, pp. 573–582, 2016.
- [18] P. N. Kaloni and T. Ariman, "Stress concentration effects in micropolar elasticity," *Zeitschrift für angewandte Mathematik und Physik ZAMP*, vol. 18, no. 1, pp. 136–141, 1967.

- [19] S. H. Salehi and M. Salehi, "Numerical investigation of nanoin-dentation size effect using micropolar theory," *Acta Mechanica*, vol. 225, no. 12, pp. 3365–3376, 2014.
- [20] F. dell'Isola and D. Steigmann, "A two-dimensional gradient-elasticity theory for woven fabrics," *Journal of Elasticity. The Physical and Mathematical Science of Solids*, vol. 118, no. 1, pp. 113–125, 2015.
- [21] F. dell'Isola, I. Giorgio, M. Pawlikowski, and N. L. Rizzi, "Large deformations of planar extensible beams and pantographic lattices: heuristic homogenization, experimental and numerical examples of equilibrium," *Proceedings of the Royal Society of London A: Mathematical, Physical and Engineering Sciences*, vol. 472, no. 2185, Article ID 20150790, 2016.
- [22] F. Dell'Isola, D. Steigmann, and A. Della Corte, "Synthesis of fibrous complex structures: designing microstructure to deliver targeted macroscale response," *Applied Mechanics Reviews*, vol. 67, no. 6, Article ID 060804, 21 pages, 2015.
- [23] D. Scerrato, I. Giorgio, and N. L. Rizzi, "Three-dimensional instabilities of pantographic sheets with parabolic lattices: numerical investigations," *Zeitschrift für Angewandte Mathematik und Physik*, vol. 67, no. 3, article 53, pp. 1–19, 2016.
- [24] D. Scerrato, I. A. Zhurba Eremeeva, T. Lekszycki, and N. L. Rizzi, "On the effect of shear stiffness on the plane deformation of linear second gradient pantographic sheets," *Zeitschrift für Angewandte Mathematik und Mechanik*, vol. 96, no. 11, pp. 1268–1279, 2016.
- [25] H. Altenbach, M. Birsan, and V. A. Eremeyev, "Cosserat-type rods," in *Generalized Continua from the Theory to Engineering Applications*, vol. 541 of *CISM International Centre for Mechanical Sciences*, pp. 179–248, Springer, Vienna, Austria, 2013.
- [26] H. Aminpour and N. Rizzi, *On the Continuum Modelling of Carbon Nano Tubes*, vol. 108 of *Civil-Comp Proceedings*, 2015.
- [27] H. Aminpour and N. Rizzi, "On the modelling of carbon nano tubes as generalized continua," in *Generalized Continua as Models for Classical and Advanced Materials. Advanced Structured Materials*, H. Altenbach and S. Forest, Eds., vol. 42 of *Advanced Structured Materials*, pp. 15–35, Springer International, Cham, Switzerland, 2016.
- [28] J. L. Ericksen and C. Truesdell, "Exact theory of stress and strain in rods and shells," *Archive for Rational Mechanics and Analysis*, vol. 1, no. 1, pp. 295–323, 1958.
- [29] A. E. Green and P. M. Naghdi, "Non-isothermal theory of rods, plates and shells," *International Journal of Solids and Structures*, vol. 6, no. 2, pp. 209–244, 1970.
- [30] A. E. Green, P. M. Naghdi, and M. L. Wenner, "On the theory of rods. II. Developments by direct approach," *International Journal of Solids and Structures*, vol. 337, no. 1611, pp. 485–507, 1974.
- [31] M. B. Rubin, *Cosserat Theories: Shells, Rods and Points*, Kluwer, Dordrecht, The Netherlands, 2000.
- [32] H. Aminpour and N. Rizzi, "A one-dimensional continuum with microstructure for single-wall carbon nanotubes bifurcation analysis," *Mathematics and Mechanics of Solids*, vol. 21, no. 2, pp. 168–181, 2016.
- [33] H. Aminpour, N. Rizzi, and G. Salerno, "A one-dimensional beam model for single-wall carbon nano tube column buckling," in *Proceedings of the 12th International Conference on Computational Structures Technology*, Stirlingshire, UK, September 2014.
- [34] M. Birsan, H. Altenbach, T. Sadowski, V. A. Eremeyev, and D. Pietras, "Deformation analysis of functionally graded beams by the direct approach," *Composites Part B: Engineering*, vol. 43, no. 3, pp. 1315–1328, 2012.
- [35] S. Gabriele, N. Rizzi, and V. Varano, "On the imperfection sensitivity of thin-walled frames," in *Proceedings of the 11th International Conference on Computational Structures Technology*, B. H. V. Topping, Ed., vol. 99, Civil-Comp Press, 2012.
- [36] S. Gabriele, N. Rizzi, and V. Varano, "A 1D nonlinear TWB model accounting for in plane cross-section deformation," *International Journal of Solids and Structures*, vol. 94–95, pp. 170–178, 2016.
- [37] S. Gabriele, N. L. Rizzi, and V. Varano, "A one-dimensional nonlinear thin walled beam model derived from koiter shell theory," in *Civil-Comp Proceedings*, vol. 106, 2014.
- [38] D. H. Hodges, *Nonlinear Composite Beam Theory*, vol. 213 of *Progress in Astronautics and Aeronautics*, American Institute of Aeronautics and Astronautics, Reston, Va, USA, 2006.
- [39] D. Iesan, *Classical and Generalized Models of Elastic Rods*, CRC Press, Boca Raton, Fla, USA, 2009.
- [40] M. Pignataro, G. Ruta, N. Rizzi, and V. Varano, "Effects of warping constraints and lateral restraint on the buckling of thin-walled frames," in *Proceedings of the ASME International Mechanical Engineering Congress and Exposition (IMECE '09)*, pp. 803–810, Lake Buena Vista, Fla, USA, November 2009.
- [41] N. L. Rizzi and V. Varano, "On the post buckling analysis of thin-walled frames," in *Proceedings of the 13th International Conference on Civil, Structural and Environmental Engineering Computing, CC 2011*, Lecture Notes in Computer Science, p. 14, Springer, Chania, Greece, 2011.
- [42] E. C. Aifantis, "Update on a class of gradient theories," *Mechanics of Materials*, vol. 35, no. 3–6, pp. 259–280, 2003.
- [43] D. C. C. Lam, F. Yang, A. C. M. Chong, J. Wang, and P. Tong, "Experiments and theory in strain gradient elasticity," *Journal of the Mechanics and Physics of Solids*, vol. 51, no. 8, pp. 1477–1508, 2003.
- [44] J. A. Cottrell, T. J. R. Hughes, and Y. Bazilevs, *Isogeometric Analysis: Toward Integration of CAD and FEA*, John Wiley & Sons, Chichester, UK, 2009.
- [45] T. J. Hughes, J. A. Cottrell, and Y. Bazilevs, "Isogeometric analysis: CAD, finite elements, NURBS, exact geometry and mesh refinement," *Computer Methods in Applied Mechanics and Engineering*, vol. 194, no. 39–41, pp. 4135–4195, 2005.
- [46] R. De Borst, L. J. Sluys, H.-B. Mühlhaus, and J. Pamin, "Fundamental issues in finite element analyses of localization of deformation," *Engineering Computations*, vol. 10, no. 2, pp. 99–121, 1993.
- [47] P. Fischer, M. Klassen, J. Mergheim, P. Steinmann, and R. Müller, "Isogeometric analysis of 2D gradient elasticity," *Computational Mechanics*, vol. 47, no. 3, pp. 325–334, 2011.
- [48] H. Gómez, V. M. Calo, Y. Bazilevs, and T. J. Hughes, "Isogeometric analysis of the Cahn-Hilliard phase-field model," *Computer Methods in Applied Mechanics and Engineering*, vol. 197, no. 49–50, pp. 4333–4352, 2008.
- [49] L. Greco and M. Cuomo, "An isogeometric implicit  $G^1$  mixed finite element for Kirchhoff space rods," *Computer Methods in Applied Mechanics and Engineering*, vol. 298, pp. 325–349, 2016.
- [50] L. Placidi, "A variational approach for a nonlinear 1-dimensional second gradient continuum damage model," *Continuum Mechanics and Thermodynamics*, vol. 27, no. 4–5, pp. 623–638, 2015.
- [51] D. Bigoni and W. J. Drugan, "Analytical derivation of Cosserat moduli via homogenization of heterogeneous elastic materials,"

- American Society of Mechanical Engineers. Transactions of the ASME. Journal of Applied Mechanics*, vol. 74, no. 4, pp. 741–753, 2007.
- [52] G. Hu, X. Liu, and T. J. Lu, “A variational method for non-linear micropolar composites,” *Mechanics of Materials*, vol. 37, no. 4, pp. 407–425, 2005.
- [53] R. Larsson and S. Diebels, “A second-order homogenization procedure for multi-scale analysis based on micropolar kinematics,” *International Journal for Numerical Methods in Engineering*, vol. 69, no. 12, pp. 2485–2512, 2007.
- [54] Q. Liu, “A new version of Hill’s lemma for Cosserat continuum,” *Archive of Applied Mechanics*, vol. 85, no. 6, pp. 761–773, 2015.
- [55] P. Sharma and A. Dasgupta, “Average elastic fields and scale-dependent overall properties of heterogeneous micropolar materials containing spherical and cylindrical inhomogeneities,” *Physical Review B*, vol. 66, no. 22, Article ID 224110, 2002.
- [56] V. A. Eremeyev and W. Pietraszkiewicz, “Material symmetry group of the non-linear polar-elastic continuum,” *International Journal of Solids and Structures*, vol. 49, no. 14, pp. 1993–2005, 2012.
- [57] V. A. Eremeyev and W. Pietraszkiewicz, “Material symmetry group and constitutive equations of micropolar anisotropic elastic solids,” *Mathematics and Mechanics of Solids*, vol. 21, no. 2, pp. 210–221, 2016.
- [58] K. L. Johnson, *Contact Mechanics*, Cambridge University Press, Cambridge, UK, 1985.

## Research Article

# Plane Wave-Perturbative Method for Evaluating the Effective Speed of Sound in 1D Phononic Crystals

J. Flores Méndez,<sup>1,2</sup> M. Salazar Villanueva,<sup>1</sup> R. C. Ambrosio Lázaro,<sup>1</sup> B. Calixto Sirene,<sup>1</sup> M. L. Mota González,<sup>3</sup> and F. Candia García<sup>1</sup>

<sup>1</sup>Benemérita Universidad Autónoma de Puebla, Ciudad Universitaria, Blvd. Valsequillo y Esquina, Av. San Claudio s/n, Col. San Manuel, 72570 Puebla, PUE, Mexico

<sup>2</sup>Instituto Tecnológico de Puebla, División de Estudios de Posgrado e Investigación, Av. Tecnológico No. 420, Maravillas, 72220 Puebla, PUE, Mexico

<sup>3</sup>CONACYT, Dirección Adjunta al Desarrollo Científico, Dirección de Cátedras, Insurgentes Sur 1582, Crédito Constructor, Benito Juárez, 03940 Ciudad de México, Mexico

Correspondence should be addressed to J. Flores Méndez; [xavier\\_snk@hotmail.com](mailto:xavier_snk@hotmail.com)

Received 6 July 2016; Revised 1 October 2016; Accepted 3 November 2016

Academic Editor: Tiejun Liu

Copyright © 2016 J. Flores Méndez et al. This is an open access article distributed under the Creative Commons Attribution License, which permits unrestricted use, distribution, and reproduction in any medium, provided the original work is properly cited.

A method for calculating the effective sound velocities for a 1D phononic crystal is presented; it is valid when the lattice constant is much smaller than the acoustic wave length; therefore, the periodic medium could be regarded as a homogeneous one. The method is based on the expansion of the displacements field into plane waves, satisfying the Bloch theorem. The expansion allows us to obtain a wave equation for the amplitude of the macroscopic displacements field. From the form of this equation we identify the effective parameters, namely, the effective sound velocities for the transverse and longitudinal macroscopic displacements in the homogenized 1D phononic crystal. As a result, the explicit expressions for the effective sound velocities in terms of the parameters of isotropic inclusions in the unit cell are obtained: mass density and elastic moduli. These expressions are used for studying the dependence of the effective, transverse and longitudinal, sound velocities for a binary 1D phononic crystal upon the inclusion filling fraction. A particular case is presented for 1D phononic crystals composed of W-Al and Polyethylene-Si, extending for a case solid-fluid.

## 1. Introduction

At present there is a great interest in fabricating artificial materials, having extraordinary properties, which considerably extend those of natural materials. Such a new class of materials is known as metamaterials. From the beginning, the photonic metamaterials, possessing negative index of refraction, have intensively been investigated. It was established that such an unusual optical property is found in periodic structures (photonic crystals) whose dielectric function is spatially modulated. A peculiarity of the photonic metamaterials is the high dielectric contrast between the components. The negative refraction has been observed in double negative metamaterials with simultaneously negative effective permittivity and permeability [1–6]. However, this

phenomenon is also manifested in anisotropic materials, as simple as a one-dimensional (1D) photonic crystal or superlattice, having elements in the effective permittivity tensor of different sign [7–10]. Analogously, metamaterials with uncommon acoustic properties have also searched among phononic crystals (PCs), that is, materials with periodic modulation of their elastic properties. As in the photonic case, the calculation of the effective parameters of a phononic crystal is an important task, for designing of resonant elastic metamaterials and acoustic lenses; there is a great interest in investigating the effective mass density and compliance tensors, as well as the effective sound velocity.

Several homogenization theories, which are valid when the acoustic wavelength is much longer than the lattice constant of the phononic crystal, have been proposed

[11–15]. Among homogenization theories, we can identify two commonly used approaches. One of them provides effective acoustic parameters within the framework of multiple scattering [11–13] in which the effective parameters are not obtained according to the direction of propagation; for example, for a sonic crystal the solid material is simply considered rigid; the study is done on the propagation of sound in the air of the structure's matrix, neglecting the modes that can propagate in the solid. The second, which is based on the Fourier formalism, makes use of the expansion of the microscopic acoustic field into plane waves and allows calculating the effective parameters as a function of the direction of propagation [14, 15]. The latter approach is of particular interest because it can be applied to different geometries of the inclusions inside the unit cell. Here, we will precisely use the Fourier formalism to calculate the effective velocities of elastic wave propagation in 1D solid-solid and fluid-solid phononic crystals. The very first known experimental observation of 1D phononic crystals was when Narayanamurti et al. investigated the propagation of high-frequency phonons through a GaAs/AlGaAs superlattice; other domains in which 1D phononic crystals have potential applications are crystal sensors, waveguide, and resonant transmission [16–19]. As in the case of 1D photonic crystals, such an inherently anisotropic elastic system is a potential metamaterial. However, the main goal of the present work is to establish the basis for the development of a general homogenization theory of (1D, 2D, or 3D) elastic phononic crystals based on the plane wave expansion.

The work is divided as follows: in Section 2, the Fourier formalism applied to a binary elastic superlattice is presented. The proposed method for calculating the effective acoustic parameters for a phononic superlattice, which is based upon the derivation of the wave equation for the macroscopic displacements field, is described in Section 3. Finally, we shall apply the derived explicit formulas for the effective sound velocities to binary superlattices composed of W-Al and Polyethylene-Si and thus study the behavior of this parameter effective in crystals with high and low contrast between the mechanical properties of its components; also a case solid-fluid is presented.

## 2. One-Dimensional Phononic Crystals

Let us consider a one-dimensional phononic crystal (or elastic superlattice) composed of alternating layers of isotropic elastic materials, A and B (Figure 1). Their thicknesses are, respectively,  $d$  and  $a - d$ , where  $a$  is the lattice constant. Assuming that the  $z$ -axis is parallel to the superlattice growth direction, the mass density  $\rho$ , as well as the longitudinal and transverse sound velocities,  $C_l$  and  $C_t$ , turn out to be functions of the  $z$ -coordinate only.

In this case, the second Newton's law for the displacement vector  $\vec{u}(z, t)$ , in the absence of external forces, acquires the form [20, 21]:

$$\frac{\partial \sigma_{ik}}{\partial x_k} = \rho(z) \frac{\partial^2 u_i}{\partial t^2}. \quad (1)$$

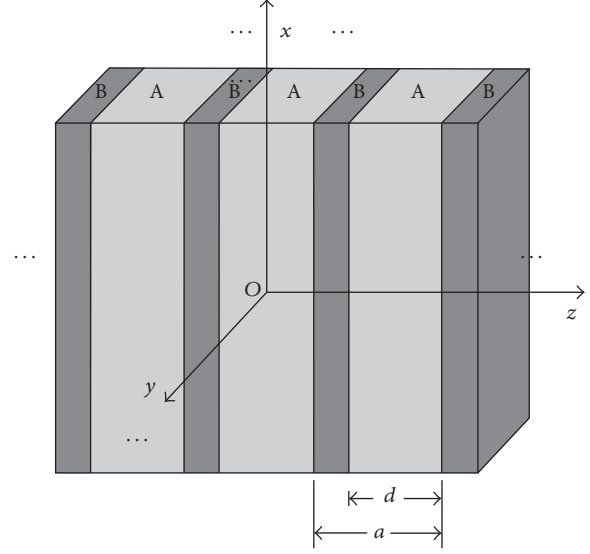


FIGURE 1: Scheme of the binary superlattice.

Here, the Cauchy stress tensor  $\sigma_{ij}$  is expressed in terms of the strain tensor

$$u_{ik} = \frac{1}{2} \left( \frac{\partial u_i}{\partial x_k} + \frac{\partial u_k}{\partial x_i} \right), \quad (2)$$

according to the relation

$$\sigma_{ik} = 2\rho(z) C_t^2(z) u_{ik} + \rho(z) (C_l^2(z) - 2C_t^2(z)) u_{ll} \delta_{ik}, \quad (3)$$

where  $\delta_{ik}$  is Kronecker's delta. Substituting (2) and (3) into (1), the wave equation for an elastic inhomogeneous medium is obtained [22, 23]:

$$\begin{aligned} \rho \frac{\partial^2 u_i}{\partial t^2} = & \nabla \cdot (\rho C_t^2 \nabla u_i) + \nabla \cdot \left( \rho C_t^2 \frac{\partial \vec{u}}{\partial x_i} \right) \\ & + \frac{\partial}{\partial x_i} [(\rho C_l^2 - 2\rho C_t^2) \nabla \cdot \vec{u}]. \end{aligned} \quad (4)$$

Due to the periodicity of the functions  $\rho(z)$ ,  $C_l(z)$ , and  $C_t(z)$ , we can expand them into Fourier series as

$$\rho(z) = \sum_{G_z} \rho(G_z) e^{iG_z z}, \quad (5)$$

$$C_{11}(z) = \rho(z) C_l^2(z) = \sum_{G_z} \Lambda(G_z) e^{iG_z z}, \quad (6)$$

$$C_{44}(z) = \rho(z) C_t^2(z) = \sum_{G_z} \tau(G_z) e^{iG_z z}, \quad (7)$$

where  $C_{11}$  and  $C_{44}$  are the longitudinal and transversal elastic constants for an isotropic elastic medium, and the components for the vectors of the reciprocal lattice are expressed as

$$G_z = \frac{2\pi}{a} n, \quad n = 0, \pm 1, \pm 2, \pm 3, \dots \quad (8)$$

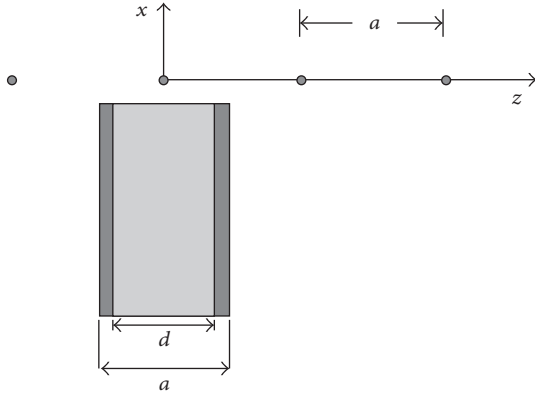


FIGURE 2: Unit cell of the binary superlattice.

The component  $C_{12}$  for an isotropic medium is given by the relation:

$$C_{12}(z) = C_{11}(z) - 2C_{44}(z). \quad (9)$$

According to our geometry (see Figures 1 and 2), the Fourier coefficients  $\rho(G_z)$ , appearing in (5), can be calculated with the formula

$$\begin{aligned} \rho(G_z) &= \frac{1}{a} \int_{-a/2}^{a/2} \rho(z) e^{-iG_z z} dz \\ &= \rho_B \delta_{0G_z} + (\rho_A - \rho_B) F(G_z), \end{aligned} \quad (10)$$

where  $F(G_z)$  is the form factor of the inclusion A,

$$F(G_z) = f \frac{\sin(G_z d/2)}{G_z d/2}, \quad (11)$$

and the ratio  $f = d/a$  is its filling fraction. Similarly, the Fourier coefficients  $\Lambda(G_z)$  and  $\tau(G_z)$  of the expansions (6) and (7) can, respectively, be written as

$$\begin{aligned} \Lambda(G_z) &= \Lambda_B \delta_{0G_z} + (\Lambda_A - \Lambda_B) F(G_z), \\ \tau(G_z) &= \tau_B \delta_{0G_z} + (\tau_A - \tau_B) F(G_z). \end{aligned} \quad (12)$$

For a periodic system, the solution of (4) should satisfy the Bloch theorem [24]. Therefore, we can write the displacement vector in the form

$$\vec{u}(\vec{r}, t) = e^{-i\omega t} e^{i\vec{K}\cdot\vec{r}} \vec{u}_{\vec{K}}(z), \quad (13)$$

where  $\vec{u}_{\vec{K}}(z)$  is a periodic function with the same period as for the superlattice and  $\omega$  is the frequency. We should note that the component  $K_z$  is here the Bloch wave number and  $\vec{K}_{||}$  is an independent vector parallel to the  $x$ - $y$  plane. After expanding the function  $\vec{u}_{\vec{K}}(z)$  into Fourier series, an expression can be obtained

$$\vec{u}(\vec{r}, t) = e^{-i\omega t} e^{i\vec{K}\cdot\vec{r}} \sum_{G_z} \vec{u}_{\vec{K}}(G_z) e^{iG_z z}. \quad (14)$$

It is worth emphasizing that the Fourier formalism for solving the wave equation (4) allows us to avoid the application

of boundary conditions for the displacement vector  $\vec{u}(\vec{r})$ , since the structural information of the system is explicitly contained in the Fourier coefficients  $\vec{u}_{\vec{K}}(G_z)$ . This is owing to the fact that the boundary conditions for  $\vec{u}(\vec{r})$  are consistent with the wave equation (4).

Substituting (5)–(7) and (14) into (4), we obtain

$$\begin{aligned} \sum_{G'_z} \{ &\tau(G_z - G'_z) \vec{u}(G'_z) (\vec{K}_{||} + (K_z + G'_z) \hat{z}) \\ &\cdot (\vec{K}_{||} + (K_z + G_z) \hat{z}) + \tau(G_z - G'_z) \vec{u}(G'_z) \\ &\cdot (\vec{K}_{||} + (K_z + G_z) \hat{z}) (\vec{K}_{||} + (K_z + G'_z) \hat{z}) \\ &+ \Lambda(G_z - G'_z) \vec{u}(G'_z) \\ &\cdot (\vec{K}_{||} + (K_z + G_z) \hat{z}) (\vec{K}_{||} + (K_z + G_z) \hat{z}) \\ &- 2\tau(G_z - G'_z) \vec{u}(G'_z) \\ &\cdot (\vec{K}_{||} + (K_z + G'_z) \hat{z}) (\vec{K}_{||} + (K_z + G_z) \hat{z}) \\ &- \omega^2 \rho(G_z - G'_z) \vec{u}(G'_z) \} = 0. \end{aligned} \quad (15)$$

We can rewrite (15) in dyadic form as

$$\sum_{G'_z} \left[ \overleftrightarrow{B}(G_z, G'_z) - \omega^2 \rho(G_z - G'_z) \overleftrightarrow{I} \right] \cdot \vec{u}(G'_z) = 0, \quad (16)$$

where

$$\begin{aligned} \overleftrightarrow{B}(G_z, G'_z) &= \tau(G_z - G'_z) (\vec{K}_{||} + (K_z + G'_z) \hat{z}) \\ &\cdot (\vec{K}_{||} + (K_z + G_z) \hat{z}) \overleftrightarrow{I} \\ &+ \tau(G_z - G'_z) (\vec{K}_{||} + (K_z + G'_z) \hat{z}) \\ &\cdot (\vec{K}_{||} + (K_z + G_z) \hat{z}) + \Lambda(G_z - G'_z) \\ &\cdot (\vec{K}_{||} + (K_z + G_z) \hat{z}) \\ &\cdot (\vec{K}_{||} + (K_z + G_z) \hat{z}) - 2\tau(G_z - G'_z) \\ &\cdot (\vec{K}_{||} + (K_z + G'_z) \hat{z}) \\ &\cdot (\vec{K}_{||} + (K_z + G_z) \hat{z}), \end{aligned} \quad (17)$$

and  $\overleftrightarrow{I}$  is the unit dyadic [ $(\overleftrightarrow{I})_{ij} = \delta_{ij}$ ].

The inverse  $v(G_z, G'_z)$  of matrix  $\rho(G_z, G'_z) \equiv \rho(G_z - G'_z)$  in Eq. (17) satisfies the relation

$$\sum_{G''_z} v(G_z, G'_z) \rho(G'_z, G''_z) = \delta_{G_z, G''_z}, \quad (18)$$

and its elements are directly calculated by using the expression

$$\begin{aligned} v(G_z, G'_z) &= v(G_z - G'_z) \\ &= \frac{1}{a} \int_{-a/2}^{a/2} \frac{1}{\rho(z)} e^{-i(G_z - G'_z)z} dz \\ &= \frac{1}{\rho_B} \delta_{G_z, G'_z} + \left( \frac{1}{\rho_A} - \frac{1}{\rho_B} \right) F(G_z - G'_z). \end{aligned} \quad (19)$$

Multiplying (17) by  $v(G_z, G'_z)$  (19), we get

$$\sum_{G'_z} \left[ \overleftrightarrow{M}(G_z, G'_z) - \omega^2 \delta_{G_z, G'_z} \overleftrightarrow{T} \right] \cdot \vec{u}(G'_z) = 0, \quad (20)$$

where we have introduced the dyadic  $\overleftrightarrow{M}(G_z, G'_z)$ :

$$\overleftrightarrow{M}(G_z, G'_z) = \sum_{G''_z} v(G_z, G''_z) \overleftrightarrow{B}(G''_z, G'_z). \quad (21)$$

The system (20) represents a homogeneous system of algebraic equations, which has a nontrivial solution if the determinant of the associated matrix is identical to zero; that is,

$$\det \left\{ \overleftrightarrow{M}(G_z, G'_z) - \omega^2 \delta_{G_z, G'_z} \overleftrightarrow{T} \right\} = 0. \quad (22)$$

The condition (22) provides the dispersion relation  $\omega(K_z)$  for vibrational eigenmodes in the PC. It should be noted that such a phononic dispersion parametrically depends upon the wave vector component  $\vec{K}_{||}$ . Thus, the phononic dispersion can be straightforwardly calculated by numerically diagonalizing the matrix  $\overleftrightarrow{M}(G_z, G'_z)$ . In doing that, we should use a finite matrix of sufficiently large size to guarantee accurate results.

### 3. Effective Sound Velocity

In the case when the wave length of sound is much larger than the lattice constant of the phononic crystal, this artificial periodic heterostructure can be modeled as a homogeneous medium with effective acoustic parameters. In this section, we shall calculate the effective sound velocities for both transverse and longitudinal vibrational modes, propagating along the growth direction of a superlattice like that considered in the previous sections.

From the Bloch theorem, given by (14), we can write the displacements field as

$$\begin{aligned} \vec{u}(\vec{r}, t) &= e^{-i\omega t} \left\{ e^{i\vec{K}\cdot\vec{r}} \vec{u}_{\vec{K}}(0) + e^{i\vec{K}\cdot\vec{r}} \sum_{G_z \neq 0} \vec{u}_{\vec{K}}(G_z) e^{iG_z z} \right\}. \end{aligned} \quad (23)$$

Assuming  $|K_z a| \ll 1$  and  $\vec{K}_{||} = 0$ , the first term on the right-hand side of (23) describes the smooth variations of the displacement vector  $\vec{u}(\vec{r}, t)$  as a function of the coordinates, whereas the second term therein is associated with the rapid

oscillations (fluctuations) over the unit cell. So, we can define the average (macroscopic) displacements field as

$$\vec{U}(\vec{r}, t) \equiv e^{-i\omega t} e^{i\vec{K}\cdot\vec{r}} \vec{u}_{\vec{K}}(0) = e^{-i\omega t} e^{i\vec{K}\cdot\vec{r}} \vec{U}_0. \quad (24)$$

According to (20), the Fourier coefficients  $\vec{u}(G_z)$  satisfy the system of equations

$$\sum_{G'_z} \overleftrightarrow{D}(G_z, G'_z) \cdot \vec{u}(G'_z) = 0, \quad (25)$$

where we have introduced the dyadic

$$\overleftrightarrow{D}(G_z, G'_z) = \overleftrightarrow{M}(G_z, G'_z) - \omega^2 \delta_{G_z, G'_z} \overleftrightarrow{T}. \quad (26)$$

One can express the coefficients  $\vec{u}(G_z \neq 0)$  in terms of  $\vec{U}_0$  by using (25) for  $G_z \neq 0$ . Thus,

$$\vec{u}(G_z) = - \sum_{G'_z \neq 0} \overleftrightarrow{D}_S^{-1}(G_z, G'_z) \overleftrightarrow{D}(G'_z, 0) \cdot \vec{U}_0. \quad (27)$$

Here,  $\overleftrightarrow{D}_S(G_z, G'_z)$  is a submatrix, obtained from  $\overleftrightarrow{D}(G_z, G'_z)$  (26) after eliminating its block rows (columns) with  $G_z = 0$  ( $G'_z \neq 0$ ). As it was demonstrated in [25], the inverse of the submatrix  $\overleftrightarrow{D}_S(G_z, G'_z)$  is related with the inverse of the matrix  $\overleftrightarrow{D}(G_z, G'_z)$  according to the formula:

$$\begin{aligned} \overleftrightarrow{D}_S^{-1}(G_z, G'_z) &= \overleftrightarrow{D}^{-1}(G_z, G'_z) \\ &\quad - \overleftrightarrow{D}^{-1}(G_z, 0) \left\{ \overleftrightarrow{D}^{-1}(0, 0) \right\}^{-1} \overleftrightarrow{D}^{-1}(0, G'_z), \end{aligned} \quad (28)$$

where  $\overleftrightarrow{D}^{-1}(0, 0)$  is a  $3 \times 3$  block, which is obtained from the original matrix  $\overleftrightarrow{D}^{-1}(G_z, G'_z)$  (26) of infinite size, and  $\{\dots\}^{-1}$  symbolizes the inverse of the  $3 \times 3$  matrix block.

Let us rewrite (25) for  $G_z = 0$  as

$$\omega^2 \vec{U}_0 = \overleftrightarrow{M}(0, 0) \cdot \vec{U}_0 + \sum_{G'_z \neq 0} \overleftrightarrow{D}(0, G'_z) \cdot \vec{u}(G'_z). \quad (29)$$

Substituting (27) and (28) into (29), we obtain the macroscopic wave equation:

$$\omega^2 \vec{U}_0 = \overleftrightarrow{M}_{\text{eff}}(K_z) \cdot \vec{U}_0, \quad (30)$$

where the effective matrix  $\overleftrightarrow{M}_{\text{eff}}$  is given by

$$\overleftrightarrow{M}_{\text{eff}}(K_z) = \left\{ \overleftrightarrow{D}^{-1}(K_z; 0, 0) \right\}^{-1} + \omega^2 \overleftrightarrow{T}. \quad (31)$$

From the macroscopic wave equation (30), we can define an effective dyadic representing the Christoffel tensor, divided by the mass density, as

$$\left( \frac{\overleftrightarrow{T}}{\rho} \right)_{\text{eff}} = \frac{\overleftrightarrow{M}_{\text{eff}}(K_z)}{K_z^2}. \quad (32)$$

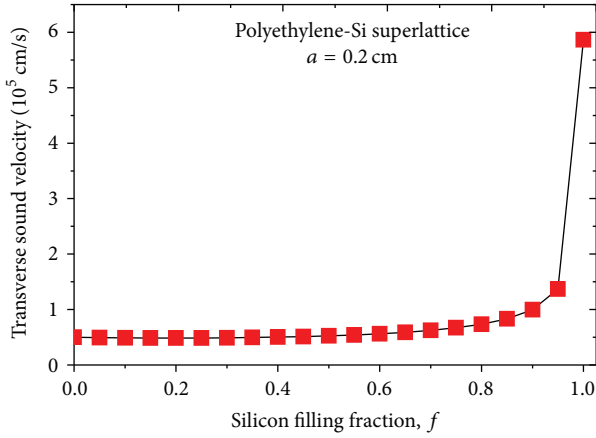


FIGURE 3: Effective sound velocity for transverse vibrational modes propagating along the growth direction of a Polyethylene-Si superlattice. Here, solid line was obtained by using formula (33) and squares were obtained by using formula (35).

Thus,

$$\left(\frac{\overleftrightarrow{\Gamma}}{\rho}\right)_{\text{eff}} = \frac{1}{K_z^2} \left\{ \overleftrightarrow{D}^{-1}(K_z; 0, 0) \right\}^{-1} + \left(\frac{\omega}{K_z}\right)^2 \overleftrightarrow{\Gamma}. \quad (33)$$

In the situation, considered here, of acoustic waves propagating along the growth direction, the effective tensor (33) turns out to be diagonal; that is,  $(\overleftrightarrow{\Gamma}/\rho)_{\text{eff},ij} = C_{\text{eff},i}\delta_{ij}$  with  $C_{\text{eff},x} = C_{\text{eff},y}$ . The principal values  $C_{\text{eff},x}$  ( $= C_{\text{eff},y}$ ) and  $C_{\text{eff},z}$  are, in fact, the effective sound velocities for transverse and longitudinal modes, respectively. It should be emphasized that formula (33) is valid in the long-wavelength limit, that is, when both  $K_z \rightarrow 0$  and  $\omega \rightarrow 0$ .

#### 4. Numerical Results and Validation

Let us apply the derived formula (33) for calculating the effective sound velocities of modes propagating along the growth direction of specific binary 1D phononic crystals. First, we shall consider a Polyethylene-silicon superlattice having a period  $a = 0.2$  cm. The parameters used in the calculations are mass densities  $\rho_A = 2.32$  gr/cm<sup>3</sup> and  $\rho_B = 0.89$  gr/cm<sup>3</sup>, transverse sound velocities  $C_{t,A} = 5.86 \times 10^5$  cm/s and  $C_{t,B} = 0.5 \times 10^5$  cm/s, and longitudinal sound velocities  $C_{l,A} = 8.45 \times 10^5$  cm/s and  $C_{l,B} = 1.9 \times 10^5$  cm/s for silicon and Polyethylene, respectively (the material parameters were taken from [24]). In the numerical calculations, 300 plane waves were needed to achieve good convergence of the results.

Figures 3 and 4 (continuous line) show the dependencies of the transverse ( $C_{\text{eff},t}$ ) and longitudinal ( $C_{\text{eff},l}$ ) effective sound velocities upon the silicon filling fraction  $f$  ( $f = d/a$ ). As it is seen, both transverse and longitudinal effective sound velocities slowly vary with increasing the silicon filling fraction  $f$  up to  $f \approx 0.9$ . In contrast, at  $f > 0.9$ , the slopes of the curves  $C_{\text{eff},t}(f)$  and  $C_{\text{eff},l}(f)$  are relatively large, because

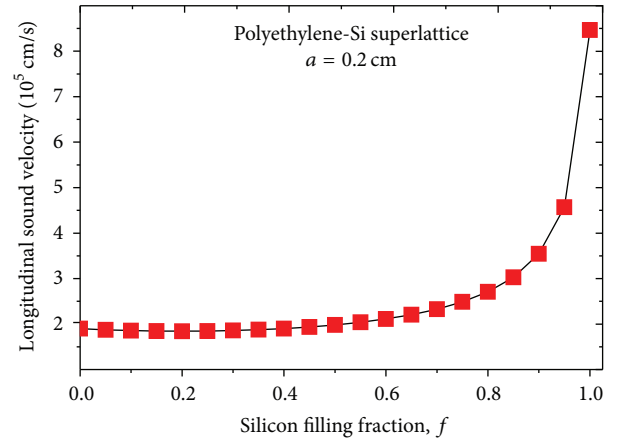


FIGURE 4: Effective sound velocity for longitudinal vibrational modes propagating along the growth direction of a Polyethylene-Si superlattice. Here, solid line was obtained by using formula (33) and squares were obtained by using formula (36).

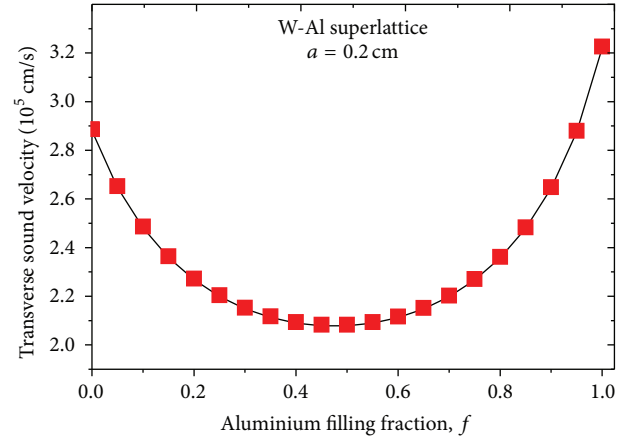


FIGURE 5: Effective sound velocity for transverse vibrational modes propagating along the growth direction of a W-Al superlattice. Here, solid line was obtained by using formula (33) and squares were obtained by using formula (35).

of the large contrast between the acoustic impedance  $\rho_A C_{i,A}$  and  $\rho_B C_{i,B}$  ( $i = t, l$ ) of the system.

Figures 5 and 6 (continuous line) exhibit numerically calculated effective parameters,  $C_{\text{eff},t}$  and  $C_{\text{eff},l}$ , for a W-Al 1D phononic crystal. The parameters used here are [24]  $\rho_A = 2.69$  gr/cm<sup>3</sup> and  $\rho_B = 19.3$  gr/cm<sup>3</sup>, transverse sound velocities  $C_{t,A} = 3.22 \times 10^5$  cm/s and  $C_{t,B} = 2.88 \times 10^5$  cm/s, and longitudinal sound velocities  $C_{l,A} = 6.45 \times 10^5$  cm/s and  $C_{l,B} = 5.21 \times 10^5$  cm/s for aluminium and tungsten, respectively. In this case, the effective sound velocity for transverse [longitudinal] modes decreases with the Al filling fraction  $f$  up to its minimum value at  $f \approx 0.45$ . For larger values of  $f$  (i.e., in the interval  $0.5 < f < 1$ ) the effective parameter  $C_{\text{eff},t}$  [ $C_{\text{eff},l}$ ] increases with  $f$ .

In order to verify our numerical results in Figures 3–6 (continuous line), we use the effective nonlocal-response

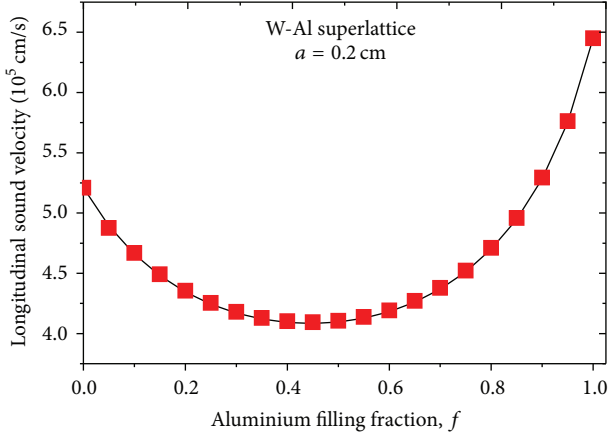


FIGURE 6: Effective sound velocity for longitudinal vibrational modes propagating along the growth direction of a W-Al superlattice. Here, solid line was obtained by using formula (33) and squares were obtained by using formula (36).

matrix  $\overline{\overline{A}}_{\text{eff}}(\vec{K})$  in the quasistatic limit ( $\omega \rightarrow 0, \vec{K} \rightarrow 0$ ). The block structure of the matrix  $\overline{\overline{A}}_{\text{eff}}(\vec{K})$  for such systems has the form [26]

$$\begin{aligned} \overline{\overline{A}}_{\text{eff}}(\vec{K} \rightarrow 0) &= \begin{pmatrix} \overline{\rho}_{\text{eff}}(\vec{K} \rightarrow 0) & 0_{3 \times 6}(\vec{K} \rightarrow 0) \\ 0_{6 \times 3}(\vec{K} \rightarrow 0) & \overline{\overline{S}}_{\text{eff}}(\vec{K} \rightarrow 0) \end{pmatrix}, \end{aligned} \quad (34)$$

where  $\overline{\rho}_{\text{eff}}(\vec{K} \rightarrow 0)$  and  $\overline{\overline{S}}_{\text{eff}}(\vec{K} \rightarrow 0)$  are the effective mass density and compliance tensors within the long-wavelength limit.

Figure 7 exhibits graphs of the nonzero elements in the matrices  $\overline{\rho}_{\text{eff}}$  (only principal value  $\overline{\rho}_{\text{eff},zz}$ ) and  $\overline{\overline{C}}_{\text{eff}} = \overline{\overline{S}}_{\text{eff}}^{-1}$  (only the effective stiffness constants  $\overline{\overline{C}}_{\text{eff},44}$  and  $\overline{\overline{C}}_{\text{eff},33}$ ) in (34) for a W/Al and Polyethylene/Si 1D phononic crystals versus the inclusion filling fraction  $f$ . The principal  $z$ -axis of the 1D phononic crystal has been oriented parallel to periodicity direction. Hence, the homogenized phononic crystal acquires tetragonal symmetry in the interval  $0 < f < 1$ , for which the effective sound velocity for transverse and longitudinal vibrational modes in the low frequency limit propagating along the growth direction is given according to the formulas (see [27], where Christoffel's equation for the tetragonal system can be factored to obtain the solutions for the transverse and longitudinal acoustic velocity):

$$C_{\text{eff},t} = \sqrt{\frac{C_{44,\text{eff}}}{\rho_{\text{eff},zz}}}, \quad (35)$$

$$C_{\text{eff},l} = \sqrt{\frac{C_{33,\text{eff}}}{\rho_{\text{eff},zz}}}. \quad (36)$$

Applying formulas (35) and (36), the effective sound velocity for transverse and longitudinal vibrational modes is shown in Figures 3–6 (squares). We have found that our numerical

results given by formula (33) coincide with those predicted by equations (35) and (36). The effective nonlocal-response matrix method is based on matrix inversion of  $n \times n$  size ( $n$ : number of plane waves); the number of plane waves increases as the contrast between the mechanical properties of the components of phononic crystal is large and this represents a great disadvantage for the numerical convergence of the method. Formula (33) shows that the sums over  $\vec{G}$  and  $\vec{G}'$  converge more rapidly than the matrix inversion with finite number of plane waves; therefore numerical calculation of the sum is not a time consuming procedure at all.

Otherwise, formula (33) can be applied for determining the effective sound velocity of 1D-phononic crystals with a type fluid component, which has zero shear modulus; this is possible by using a very small value of  $C_{44}$  ( $C_{44} \rightarrow 0$ ) in order to avoid numerical errors. With this mathematical artifice, we have calculated the effective sound velocity for the longitudinal vibrational mode for a water-aluminium superlattice having a period  $a = 1$  cm (see Figure 8). The parameters used for water are  $\rho = 1$  gr/cm<sup>3</sup> and longitudinal sound velocity  $C_l = 6.45 \times 10^5$  cm/s. The graph shows the dependence of the effective longitudinal sound velocity upon the aluminium filling fraction  $f$ ; note that until filling fractions near 0.8 the values of the effective velocity remain close to the water, for later ascending quickly until reaching the values of the solid, thanks to the large mismatches at the interfaces of the water-aluminium building-block (due to high contrast of the acoustic impedance of the materials in the unit cell).

## 5. Discussion

In the developed method in this work, the homogenization is achieved in the limit  $\omega, \vec{K} \rightarrow 0$  and the effective Christoffel tensor  $(\Gamma_{ij})_{\text{eff}}$  is calculated from the wave equation for an unidimensional elastic inhomogeneous medium; this tensor relates the elastic constants with the propagation velocities of the elastic waves according to different directions of the principal axes that are entirely dependent on the normal wave  $\vec{n} = (n_i)$  on the direction of  $\vec{K}$  but not its magnitude, so that the phase velocity is defined by the square roots of the eigenvalues of the effective matrix  $(\overline{\overline{\Gamma}}/\rho)_{\text{eff}}$ . We solve the determinant of the effective matrix taking into account the solution method proposed by [27]. It should be noted that [27] does not present a methodology of homogenization for different layers of materials but only develops the general theory of wave propagation. In this way, we obtain the relationship between the propagation velocity in the direction  $\vec{n}$  and the elastic and mechanical homogenized properties of the PC. Therefore, our formula simultaneously calculates the effective velocities to which the transverse and longitudinal elastic waves propagate in the PC. On the other hand, when the 1D-PC has fluid type components, close to zero values are ingressed for  $C_{44}$  (transversal elastic constant) to calculate the effective sound velocity for the longitudinal vibrational mode. This allows establishing a more general homogenization methodology for calculating the effective

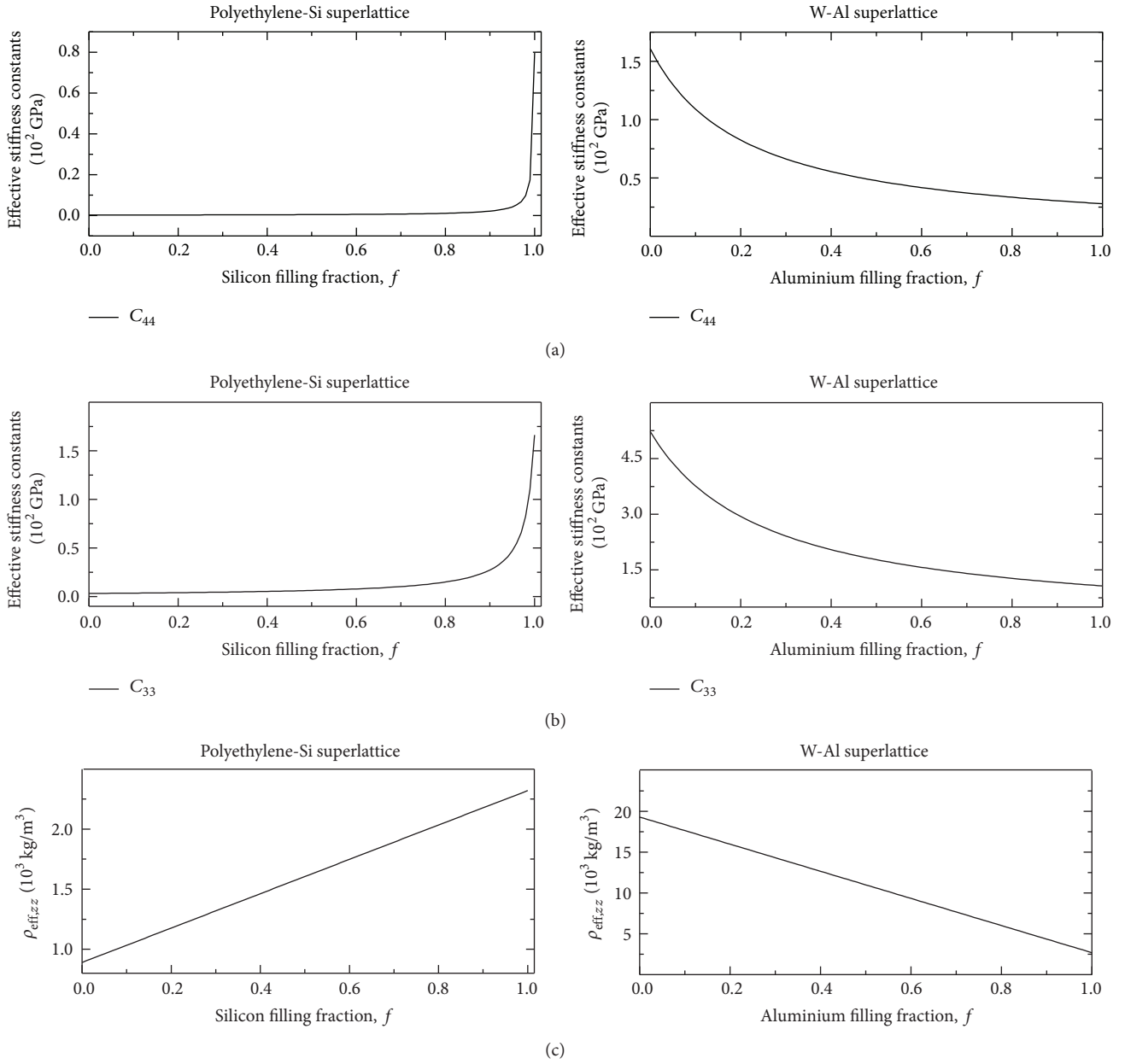


FIGURE 7: Graphs of the effective mass density  $\bar{\rho}_{\text{eff},zz}$  (c) and the effective stiffness constants  $\bar{C}_{\text{eff},44}$  (a) and  $\bar{C}_{\text{eff},33}$  (b) of Polyethylene-Si and W-Al superlattices.

velocity of propagation of sound waves in phononic crystals with elastic constituents of solid and fluid type, which is useful to define a methodology towards the development of a theory for two- and three-dimensional systems. In contrast to the methodology presented in [14, 15] which presents a separate analysis to study the propagation of acoustic waves in fluid-fluid and solid-solid phononic crystals, in such studies, the first case is based on solving the equation sound wave propagating in a gas for the longitudinal modes; in the second case the equation of motion for an elastic medium is solved considering only transverse modes. The effective sound velocity in the homogenized system is obtained by

taking the limit  $\omega, \vec{K} \rightarrow 0$ ; in this limit the group velocity is equal to the phase velocity, which is calculated as  $c_{\text{eff}} = \omega/K$ . With the above considerations, the authors obtain for each case the formula for the effective sound velocity; also they do not show results for a solid-liquid PC.

## 6. Conclusions

We have derived explicit formulas for the calculation of the effective sound velocities in a 1D phononic crystal in the long-wavelength limit. The formulas were applied for analyzing

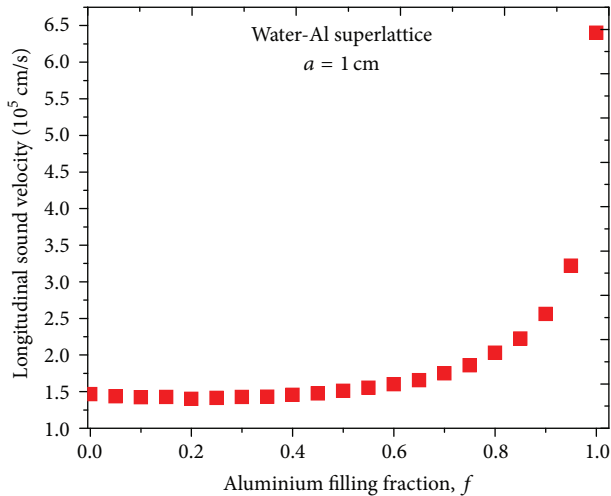


FIGURE 8: Dependence of the effective longitudinal sound velocity for a homogenized 1D phononic crystal of aluminium embedded in water upon the aluminium filling fraction  $f$ .

the dependence of the effective, transverse and longitudinal, sound velocities upon the inclusion filling fraction for binary superlattices composed of Polyethylene-Si and W-Al. In the latter case, the contrast of material parameters is relatively larger and, as a result, at Al filling fractions  $f \approx 0.45$ , the effective sound velocity for both transverse ( $C_{\text{eff},t}$ ) and longitudinal ( $C_{\text{eff},l}$ ) modes, propagating along the superlattice growth direction, takes values smaller than the sound velocity for each component (W or Al). For this reason, we can say that the homogenized 1D W-Al phononic crystal behaves as a metamaterial. We have verified that our results in the quasistatic limit for Polyethylene-Si and W-Al 1D phononic crystals coincide with the results predicted by the effective mass density and compliance tensors method. Finally, formula (33) can also be applied for determining the effective sound velocity of 1D-phononic crystals with a type fluid component having zero shear modulus.

Although the homogenization theory developed here is valid only for phononic crystals with one-dimensional periodicity and isotropic inclusions, it shows the usefulness of the plane wave expansion method to obtain explicit expressions for theoretical results of the effective sound velocity. The generalization of this approach to 2D and 3D periodic elastic structures with anisotropic inclusions and arbitrary contrast of the materials parameters will be presented elsewhere.

## Competing Interests

The authors declare that they have no competing interests.

## Acknowledgments

This work was partially supported by VIEP-BUAP (Grant FOMJ-ING16-I). The authors also thank the support of PRODEP program (Grant BUAP-PTC-384, Agreement no. DSA/103.5/15/7449).

## References

- [1] J. B. Pendry, A. J. Holden, D. J. Robbins, and W. J. Stewart, "Magnetism from conductors and enhanced nonlinear phenomena," *IEEE Transactions on Microwave Theory and Techniques*, vol. 47, no. 11, pp. 2075–2084, 1999.
- [2] D. R. Smith, W. J. Padilla, D. C. Vier, S. C. Nemat-Nasser, and S. Schultz, "Composite medium with simultaneously negative permeability and permittivity," *Physical Review Letters*, vol. 84, no. 18, pp. 4184–4187, 2000.
- [3] L. Zhang, G. Tuttle, and C. M. Soukoulis, "GHz magnetic response of split ring resonators," *Photonics and Nanostructures—Fundamentals and Applications*, vol. 2, no. 2, pp. 155–159, 2004.
- [4] C. Enkrich, M. Wegener, S. Linden et al., "Magnetic metamaterials at telecommunication and visible frequencies," *Physical Review Letters*, vol. 95, no. 20, Article ID 203901, 2005.
- [5] S. Zhang, W. Fan, N. C. Panoiu, K. J. Malloy, R. M. Osgood, and S. R. J. Brueck, "Experimental demonstration of near-infrared negative-index metamaterials," *Physical Review Letters*, vol. 95, no. 13, Article ID 137404, pp. 1–4, 2005.
- [6] J. A. Reyes-Avedaño, U. Algreto-Badillo, P. Halevi, and F. Pérez-Rodríguez, "From photonic crystals to metamaterials: the bianisotropic response," *New Journal of Physics*, vol. 13, Article ID 073041, pp. 1–33, 2011.
- [7] V. A. Podolskiy and E. E. Narimanov, "Strongly anisotropic waveguide as a nonmagnetic left-handed system," *Physical Review B—Condensed Matter and Materials Physics*, vol. 71, no. 20, Article ID 201101, 2005.
- [8] B. Wood, J. B. Pendry, and D. P. Tsai, "Directed subwavelength imaging using a layered metal-dielectric system," *Physical Review B*, vol. 74, no. 11, Article ID 115116, pp. 1–8, 2006.
- [9] A. L. Rakhmanov, V. A. Yampol'Skii, J. A. Fan, F. Capasso, and F. Nori, "Layered superconductors as negative-refractive-index metamaterials," *Physical Review B*, vol. 81, no. 7, Article ID 075101, 2010.
- [10] B. Zenteno-Mateo, V. Cerdáan-Ramírez, B. Flores-Desirena, M. P. Sampedro, E. Juárez-Ruiz, and F. Pérez-Rodríguez, "Effective permittivity tensor for a metal-dielectric superlattice," *Progress in Electromagnetics Research Letters*, vol. 22, pp. 165–174, 2011.
- [11] J. Mei, Zh. Liu, W. Wen, and P. Sheng, "Effective mass density of fluid-solid composites," *Physical Review Letters*, vol. 96, no. 2, Article ID 024301, pp. 1–4, 2006.
- [12] D. Torrent, A. Håkansson, F. Cervera, and J. Sánchez-Dehesa, "Homogenization of two-dimensional clusters of rigid rods in air," *Physical Review Letters*, vol. 96, no. 20, Article ID 204302, 2006.
- [13] D. Torrent and J. Sánchez-Dehesa, "Effective parameters of clusters of cylinders embedded in a nonviscous fluid or gas," *Physical Review B—Condensed Matter and Materials Physics*, vol. 74, no. 22, Article ID 224305, 2006.
- [14] A. A. Krokhin, J. Arriaga, and L. N. Gumen, "Speed of sound in periodic elastic composites," *Physical Review Letters*, vol. 91, no. 26, Article ID 264302, pp. 1–4, 2003.
- [15] L. N. Gumen, J. Arriaga, and A. A. Krokhin, "Metafluid with anisotropic dynamic mass," *Low Temperature Physics*, vol. 37, no. 11, pp. 1221–1224, 2011.
- [16] V. Narayanamurti, H. L. Störmer, M. A. Chin, A. C. Gossard, and W. Wiegmann, "Selective transmission of high-frequency phonons by a superlattice: the "dielectric" phonon filter," *Physical Review Letters*, vol. 43, no. 27, pp. 2012–2016, 1979.

- [17] R. Lucklum, J. Li, and M. Zubtsov, "1D and 2D phononic crystals sensors," *Procedia Engineering*, no. 5, pp. 436–439, 2010.
- [18] M. Xiao, G. Ma, Z. Yang, P. Sheng, Z. Q. Zhang, and C. T. Chan, "Geometric phase and band inversion in periodic acoustic systems," *Nature Physics*, vol. 11, no. 3, pp. 240–244, 2015.
- [19] H. Sanchis-Alepuz, Y. A. Kosevich, and J. Sánchez-Dehesa, "Acoustic analogue of electronic bloch oscillations and resonant zener tunneling in ultrasonic superlattices," *Physical Review Letters*, vol. 98, no. 13, Article ID 134301, 2007.
- [20] L. D. Landau and E. M. Lifshitz, *Theory of Elasticity*, Butterworth Heinemann, New York, NY, USA, 1995.
- [21] L. M. Brekhovskikh and O. A. Godin, *Acoustics of Layered Media I: Plane and Quasi-plane Waves*, Springer, Berlin, Germany, 1998.
- [22] M. S. Kushwaha, P. Halevi, G. Martínez, L. Dobrzynski, and B. Djafari-Rouhani, "Theory of acoustic band structure of periodic elastic composites," *Physical Review B*, vol. 49, no. 4, pp. 2313–2322, 1994.
- [23] M. S. Kushwaha, "Classical band structure of periodic elastic composites," *International Journal of Modern Physics B*, vol. 10, no. 9, pp. 977–1094, 1996.
- [24] Ch. Kittel, *Introduction to Solid State Physics*, John Wiley & Sons, New York, NY, USA, 1995.
- [25] V. Cerdán-Ramírez, B. Zenteno-Mateo, M. P. Sampedro, M. A. Palomino-Ovando, B. Flores-Desirena, and F. Pérez-Rodríguez, "Anisotropy effects in homogenized magnetodielectric photonic crystals," *Journal of Applied Physics*, vol. 106, no. 10, Article ID 103520, 2009.
- [26] J. Flores-Méndez and F. Pérez-Rodríguez, "Metasolid with anisotropic mass density," *Europhysics Letters*, vol. 103, no. 5, Article ID 54001, 2013.
- [27] B. M. Lempriere, *Ultrasound and Elastic Waves*, Academic Press, New York, NY, USA, 2002.

## Research Article

# Experimental Research on 2 : 1 Parametric Vibration of Stay Cable Model under Support Excitation

Li-Na Zhang,<sup>1</sup> Feng-Chen Li,<sup>2</sup> Xiang Yu,<sup>2</sup> Peng-Fei Cui,<sup>3</sup> and Xiao-Yong Wang<sup>1</sup>

<sup>1</sup>College of Engineering, Department of Architectural Engineering, Kangwon National University, Chuncheon 200-701, Republic of Korea

<sup>2</sup>Faculty of Civil and Architectural Engineering, East China University of Technology, Nanchang, Jiangxi 330013, China

<sup>3</sup>College of Civil Engineering, Hunan University, Changsha, Hunan 410082, China

Correspondence should be addressed to Feng-Chen Li; [fcli\\_1980@163.com](mailto:fcli_1980@163.com)

Received 21 August 2016; Accepted 10 October 2016

Academic Editor: Ying Wang

Copyright © 2016 Li-Na Zhang et al. This is an open access article distributed under the Creative Commons Attribution License, which permits unrestricted use, distribution, and reproduction in any medium, provided the original work is properly cited.

For 2 : 1 parametric vibration problem of stay cable under support excitation, a sliding support only in the vertical moving is designed to simulate the bridge stay cable's vibration test model. Meanwhile, using numerical simulation of cable free vibration and dynamic characteristic test analysis, the experimental research under various conditions is implemented in the actual cable-stayed bridge as the research object, which is compared with the corresponding numerical simulation results. According to the analysis results, it shows that as the vibration test model has 2 : 1 parametric vibration under the support excitation the results of maximum cable displacement from experimental analysis and numerical simulation are basically consistent which revealed that the parametric vibration of stay cable exists and is easy to occur. Additionally, when the bridge bearing excitation frequency is similar to the 2 : 1 frequency ratio, small excitation can indeed lead to the sharp "beat" vibration of cable; therefore it is very necessary to limit the amplitude of support excitation to prevent the occurrence of a large main parametric resonance.

## 1. Introduction

Parametric vibration system means the excitation depends on time and is used as a parameter in the governing equation; one of the characteristics of the vibration system is that the parameters of the system are changed with time. Different from the external incentive system, in the parametric excitation system, when the frequency of the excitation is equal to multiple system natural frequency of a certain order, small incentives can also stimulate a large system response [1–3].

During the research on the parametric vibration of stay cable, domestic and overseas scholars carried out some experimental research work related to the parametric vibration according to different theoretical models and research purposes. Abdel-Ghaffar and Khalifa [4] studied parametric vibration of cable-beam composite structure, of which test model is a single cable with single beam, and applied harmonic excitation to the horizontal and vertical direction of the beam to explore the dynamic response characteristics when parametric vibration of the cable and beam occurs,

in order to further study the nonlinear vibration of cable-beam composite structure, Gattulli et al. [5, 6] obtained the internal resonance response of cable-beam composite structure by numerical simulation analysis, at the same time, the finite element model is established to carry out comparative analysis, and the analysis results are verified by model test. Through experiments Zhou [7] studied the nonlinear dynamic characteristics of cable-beam composite structure and verified the nonlinear phenomena such as jumps, which shows that there is a strong coupling effect between the cable and the beam.

In this paper, the stay cable model is based on theory and numerical simulation of 2 : 1 parametric vibration under the support excitation; the test model is studied experimentally under different support excitation amplitudes and frequencies. The cable vibration test model is designed by itself, dynamic characteristics of test model are obtained using numerical simulation and dynamic characteristic test analysis of the free vibration of stayed cable to carry out the discussion on 2 : 1 parametric excitation resonance test, and

TABLE 1: Material properties and geometric parametric vibration of the stayed cable model.

$L$ (m)	$D$ (mm)	$m$ (kg/m)	$E_{eq}$ ( $10^{11}$ N/m <sup>2</sup> )	$\theta$ (°)
14.00	8.00	0.33	1.999	31.6

the conclusion which is valuable for engineering application can be obtained.

## 2. Test Scheme Design of Parametric Vibration of Stay Cable under Support Excitation

*2.1. Overview of Stay Cable Model.* In order to better understand the parametric vibration of the stay cable under the support excitation, in this paper, based on the theory and numerical simulation of the parametric vibration of the stay cable under the support excitation, experimental study on parameter vibration of stay cable under support excitation was carried out. The paper's author designed sliding bearing which can only move vertically to simulate the effect of the bridge deck, one end of the cable is hinged with this bearing, the other end is connected with the antiforce frame which has a large rigidity, the upper part of the frame is free, and the bottom is connected with ground via anchor bolt, the connection of the cable and the antiforce frame is through the guide angle device, to simulate the tower frame by using of antiforce frame, and the actuator is connected with the cover plate over the sliding bearing. By controlling the travel and frequency of the actuator, the vertical excitation effect of the bridge is simulated. At this time, the test model of the stay cable is changed into the parameter vibration model of the vertical excitation at the end of the deck. The overall arrangement of the test model is shown in Figure 1; photos of the tower support and deck connection are shown in Figures 2 and 3, respectively.

*2.2. Test Principle and Site Layout.* The test cable model is a scaled model of Shandong Binzhou Yellow River highway bridge with a length of 220 meters and N26 cable [8], the model satisfies the geometric similarity ratio 1:16, and the experiment was carried out in the lab of structure and earthquake resistance protection of the Civil Engineering Institute of Harbin Institute of Technology. Cable length of stay cable model is 14 m, in order to reach the similar quality, a total of 100 lumped mass blocks are fixed on the stay cable with 140 mm equal spacing, the quality of each lumped mass is 0.14 kg, and the material properties and geometrical parameters of the stay cable model are shown in Table 1.

The basic principle of this experiment is as follows. First, after opening the MTS control system, the bridge support can be reached to the center position of the stroke by adjusting the vertical displacement of the actuator. At this point, keep the actuator from moving and continue to oil, which is equivalent to the static state of the bridge deck. Then using the cable force adjusting device at the support end, to change fundamental frequency through adjusting the cable force, value of the cable force at this time can be measured

by the end of the force sensor. Then adopting the release method, the fundamental frequency of stay cable is obtained by spectral analysis of the test system, which serves as a basis for the parametric vibration analysis of the actuator excitation frequency. Finally, start the actuator, by adjusting the excitation amplitude and excitation frequency of actuating device, to simulate parametric vibration problem of cable under the excitation of bridge bearings; site layout photos of cable parametric vibration test under bearing excitation are shown in Figure 4. Several questions to be noted here are as follows. First, need to fix the ball hinges well at the end of actuator, making sure it moves vertically only and without rotation; second, after the test of a fixed amplitude excitation, it is necessary to return the displacement of the actuator to the initial equilibrium position; at the same time, to verify whether the cable force of the cable is consistent with the initial setting tension values by observing the voltage value of the force sensor, only in this way we can guarantee cable frequency invariant in the next excitation amplitude; then it is better to carry out the experimental research of next work condition.

*2.3. Test System.* The test system is composed of four parts, the test specimens, the excitation system, the testing system, and the analysis system. The test pieces consist of the cable model, bridge bearing device, and tower counter force frame; incentive system is realized by vertical excitation on bridge deck bearing from actuator which is controlled by MTS electrohydraulic servo testing system; the test system is composed of a force sensor, acceleration sensor, and corresponding acquisition instrument; and analysis system is composed of Beijing spectrum dynamic strain data collection instrument and laptop. The arrangement of the test system is shown in Figure 5.

*2.4. Testing Instruments and Equipment.* The test data acquisition instrument is WS3811 16 channel digital strain instrument which produced by Pope Beijing Century Technology Development Co., Ltd. The instrument has characteristics of small volume, the high integration, strain amplification, and filtering full automation, which could be dynamic strain measurement in laboratory and field test, as shown in Figure 6, and power amplifier is shown in Figure 7, pressure sensor is shown in Figure 8, and acceleration sensor is shown in Figure 9.

## 3. Experimental Studies on 2:1 Parameter Vibration of Stay Cable under Support Period Excitation

*3.1. Analysis on Free Vibration Test of Stay Cable.* Before the parametric vibration test of the cable is carried out, dynamic characteristics analysis of the test model cable is needed to accurately determine the first-order natural frequency, which can be used as the effective basis for the excitation frequency of the end support in the process of cable parameters test. In order to satisfy the requirement of test, the connection way of model test cable in the end supports is complicated, including cable force adjusting device, force sensor, and the

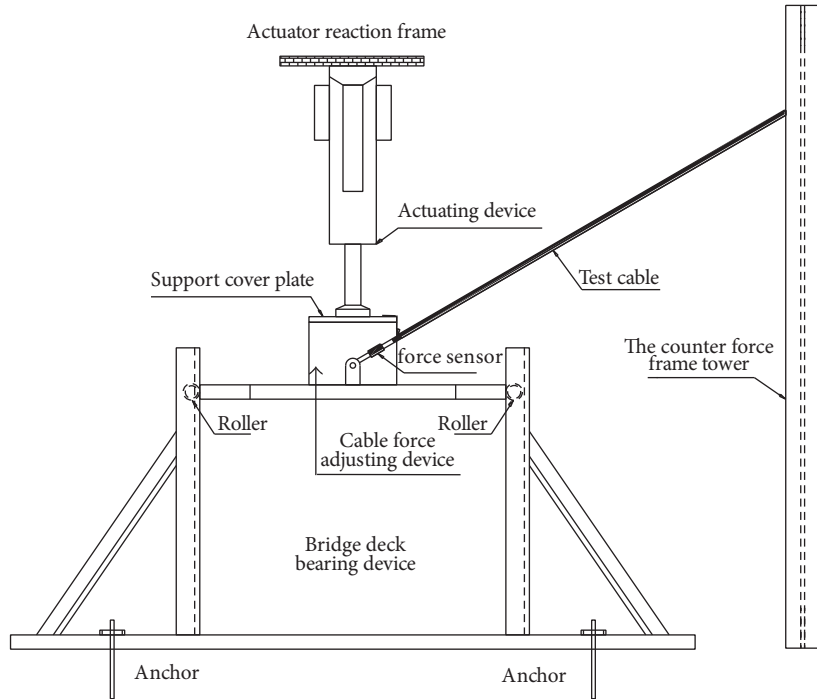


FIGURE 1: The overall layout of the test model.

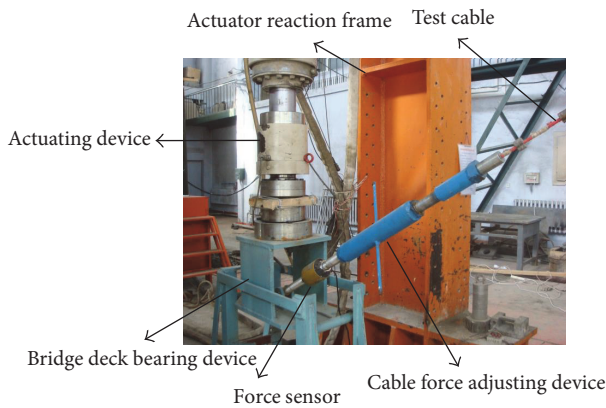


FIGURE 2: The photo of the joints between bridge and support.

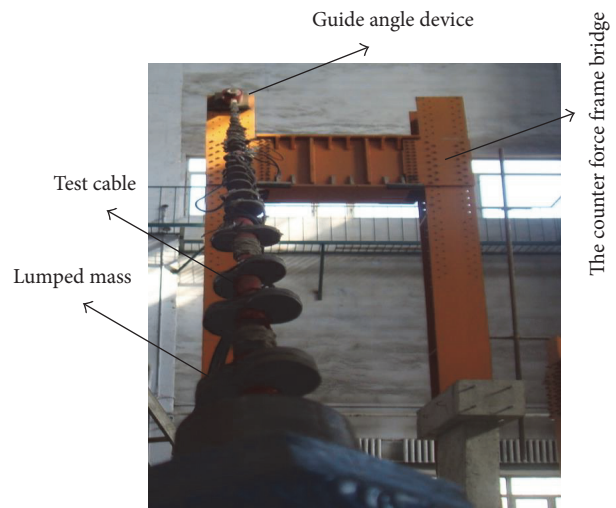


FIGURE 3: The photo of the joints between bridge and tower.

corresponding connecting pieces between components. So in this paper, two ways, the finite element modeling and laboratory site test, are used for verification and comparison analysis, to make sure a more accurate cable first-order natural frequency is determined.

*3.1.1. Finite Element Modeling Analysis of Dynamic Characteristics of Model Cable.* Firstly, arranged lumped mass blocks and complex end connections to model cable using the ANSYS finite element modeling and basic parameters in the process of modeling are cable and end connecting pieces with a total length of 15.82 m, cable line density 0.33 kg/m, and concentrated quality block with equal spacing arrangement 0.14 m, its quality is 0.14 kg, and bearing's connecting piece is

equivalent to solid round steel with diameter 0.036 m. At this time, the cable force sensor reads 0.27 V, and the calibration curve of sensor's voltage and pull is shown in Figure 10.

From the calibration results of Figure 10, we can see that the calibration results of the tension sensor are consistent with the rated design value, that is, 10 t-3 V; at this time the cable force value is 9 kN.

The finite element model of the cable is shown in Figure 11, and its dynamic characteristics analysis results are shown in Table 2.



FIGURE 4: The photo of the field layout of cable parametric vibration test.

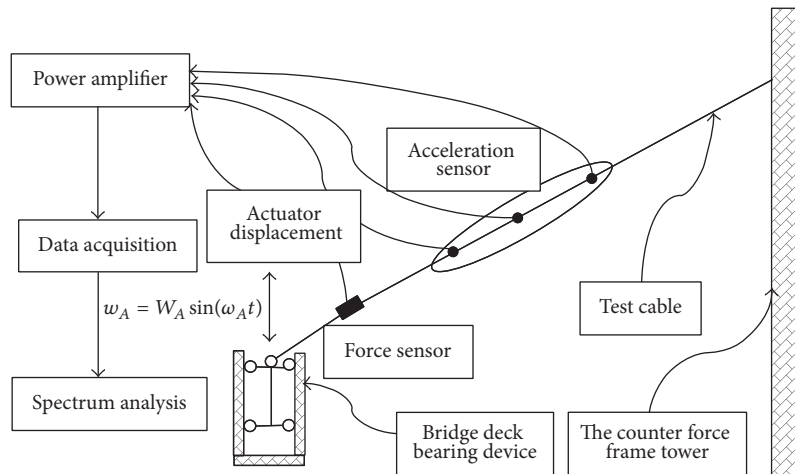


FIGURE 5: The schematic diagram of the test system of cable parametric vibration.

From Table 2 we can see that model cable vibration mode is including in-plane vibration and out-plane vibration, due to the influence of end connections, modal frequency of each order is not equally spaced arrangement within the model plane, and the first natural frequency value of cable was obtained as 2.5914 Hz.

**3.1.2. Indoor Experimental Analysis on Dynamic Characteristics of Model Cable.** Using released method to carry out free vibration test on indoor test model cable, the acceleration signal got by acceleration sensor of cable span is shown in Figure 12, cable displacement signal obtained by the frequency domain integral method is shown in Figure 13, and the spectrum curve got after FFT on model cable free vibration displacement time history is shown in Figure 14.

From Figure 14 we found that first-order natural frequency of cable is 2.45 Hz from model cable indoor free

vibration test, which is very similar to ANSYS finite element simulation results 2.5914 Hz. Therefore, the first-order modal frequency value of the cable is set to 2.45 Hz in the subsequent parameter vibration test of model cable, which is considered as the setting reference of parameter vibration test.

**3.2. Analysis on 2:1 Parameter Vibration Test of Stay Cable under Support Period Excitation.** Based on the indoor free vibration test of the model cable in the previous section, make sure that the first-order natural frequency value is 2.45 Hz under the condition of voltage value of the end sensor which is 0.27 V. Therefore, the excitation frequency of the actuator is 4.90 Hz, when the 2:1 parameter vibration test of cable was carried out under support excitation. Two kinds of working conditions, the end support's displacement excitation amplitudes  $W_B = 3$  mm and  $W_B = 5$  mm, are analyzed, respectively, in this paper. Under the conditions



FIGURE 6: The dynamic strain sensor WS3811 developed by the Beijing Wavespectrum.



FIGURE 8: Pressure sensor.



FIGURE 7: Power amplifier.



FIGURE 9: Acceleration sensor.

of the given support displacement excitation amplitude and excitation frequency and displacement time history of which actual effect on cable end is feedback from displacement sensor at the tip of the actuator to MTS controller and is recorded, the true displacement time history signal and corresponding amplitude-frequency characteristic curve under the two working conditions are shown in Figures 15 and 17, respectively. Due to the fact that acceleration records are voltage signal, change voltage signal into the actual acceleration signal by calibration relationship in this paper, and using frequency domain integral method, finally get the displacement response signal under the condition of cable 2:1 parameter vibration; at the same time, with review of [9], it is known that the study of parametric vibration problem of cable at one end bearing excitation is a special case in [9]: bridge bearing  $A$  terminal's displacement  $W_A = 0$ , only bridge bearing  $B$  terminal has vibration, the numerical simulation analysis is similar to [9], and the comparison analysis results of model cable's experimental analysis and numerical simulation under two kinds of working conditions are shown in Figures 16 and 18.

From actuator displacement time history in Figures 6 and 17 we can see that although displacement excitation amplitude instruction sending to the actuator is  $W_B = 3$  mm and  $W_B = 5$  mm, the actual displacement excitation amplitude which interacts on bridge support did not be

reached, which is lower than the given value, and they are  $W_B = 2.5$  mm and  $W_B = 4$  mm, respectively; the excitation frequency can be obtained from the spectrum curve,  $\omega_B = 4.763$  Hz and  $\omega_B = 4.766$  Hz, respectively, which are also not the given value 4.90 Hz, so in the process of numerical simulation, the excitation amplitude and frequency of bridge bearing should be analyzed by adopting the real value of the actuator, which is reliable and effective.

As for the working condition of  $W_B = 3$  mm and  $\omega_B = 4.90$  Hz, the actual bearing excitation amplitude is  $W_B = 2.5$  mm, excitation frequency is  $\omega_B = 4.763$  Hz, and at this time the comparison results of model cable test analysis and numerical simulation are shown in Figure 16. From Figure 16 we can see that the time when model cable reaches the first "beat" is different from the result of numerical simulation, but the magnitude of the peak is basically the same, test cable's "beat" amplitude value decreases over time, the time interval of "beat" vibration peak is longer than the simulation results, and the comparison results of test and numerical simulation further demonstrate the existence of parametric vibration.

As for the working condition of  $W_B = 5$  mm and  $\omega_B = 4.90$  Hz, the actual bearing excitation amplitude is  $W_B = 4$  mm, excitation frequency is  $\omega_B = 4.766$  Hz, and at this time the comparison results of model cable test analysis and numerical simulation are shown in Figure 18. From Figure 16 we can see that, with deck support excitation amplitude

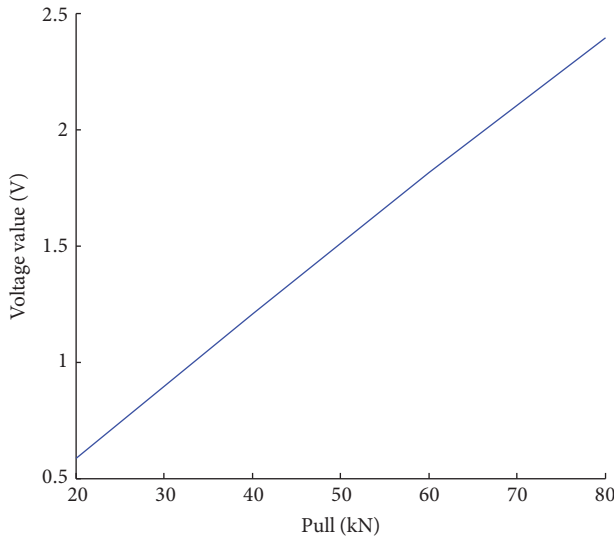


FIGURE 10: Calibration curve of the force sensor.

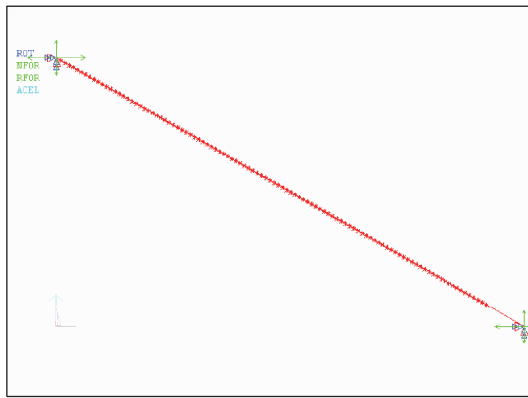


FIGURE 11: ANSYS finite element model of stayed cable.

increases, model cable's "beat" amplitude increases, and the time interval of "beat" is longer; namely, the "beat" appears to reduce the frequency, but both displacement amplitudes in the first "beat" are basically the same. It is further explained that cable presents large amplitude vibration when parametric vibration happens, which is an important characteristic.

From the analysis results of above two kinds of working conditions, cable displacement maximum amplitude results from experimental analysis and numerical simulation are basically the same, the main difference is the test results attenuation faster, and time interval between "beat" and "beat" is larger. Experimental analysis and numerical simulation results have some differences, the main reasons are as follows: on the one hand model cables in the numerical simulation are seen as the whole ideal homogeneous cable, without considering the influence of cable lumped mass block and deck support end's complex connection in actual model cable, meanwhile, because of the complexity of the test cable connection, the damping at the end connection

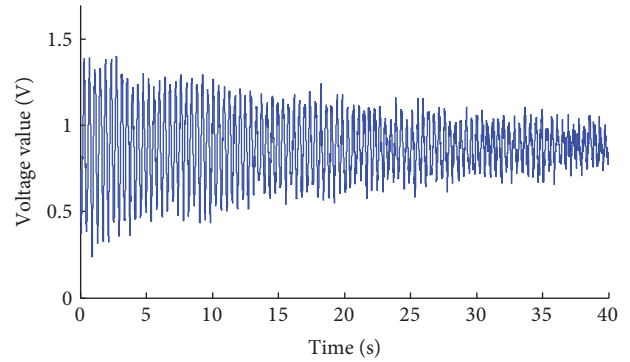


FIGURE 12: Piezoelectric time history of cable model free vibration.

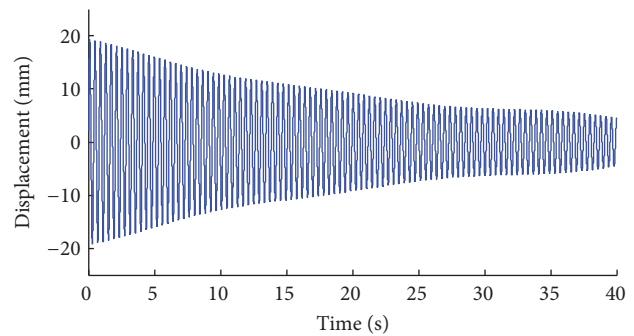


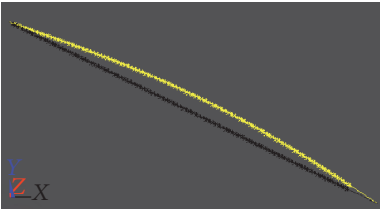
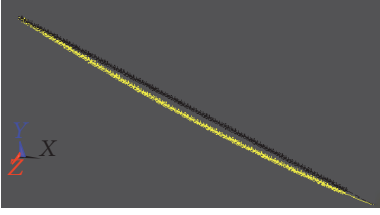
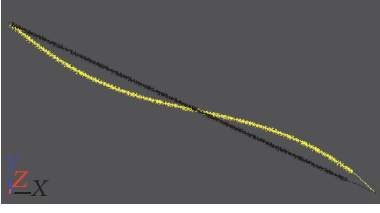
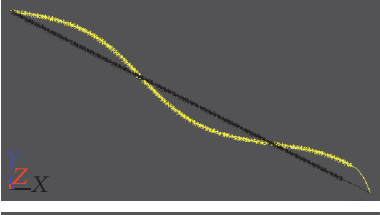
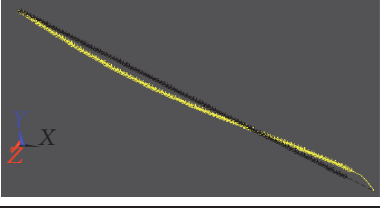
FIGURE 13: Displacement time history of cable model free vibration.

is also larger in the process of model cable vibration, and connecting piece is rigid elements and not flexible cable, in the process of test which also greatly limits the rapid vibration of cables; on the other hand, when the bridge excitation amplitude is large, the cable does not only do single in-plane vibration, which is also accompanied by out-plane vibration; while the numerical simulation model only considers in-plane vibration, about the out-plane vibration problem in the process of stay cable vibration, it could be obviously observed during the experiment, which also makes these two have certain difference. Based on the above two aspects, although there is certain difference between experimental analysis and numerical simulation results, but the parametric vibration test of the model cable reveals two important points: firstly, the parameter vibration of stay cable is easy to occur; secondly, small excitation can indeed lead to the sharp "beat" vibration of cable when excitation frequency of bridge bearing approximately satisfies the frequency ratio of 2 : 1.

#### 4. Conclusion

In view of theory and numerical simulation analysis results in [9], the test scheme of stay cable parametric resonance under bearing excitation was self-designed indoors for better understanding the problem essence of parametric vibration in this paper. According to the comparative analysis on the

TABLE 2: Vibration mode and frequency of the cable model analyzed by the software ANSYS.

Modal order	Mode shape	Modal frequency/Hz
In-plane first order		2.5914
Out-of-plane first order		5.0011
In-plane second order		5.0530
In-plane third order		7.1689
Out-of-plane second order		7.7940

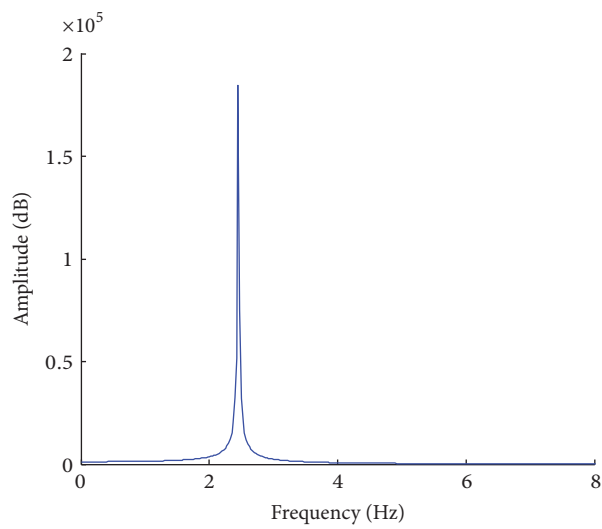


FIGURE 14: Spectral curve of cable model free vibration.

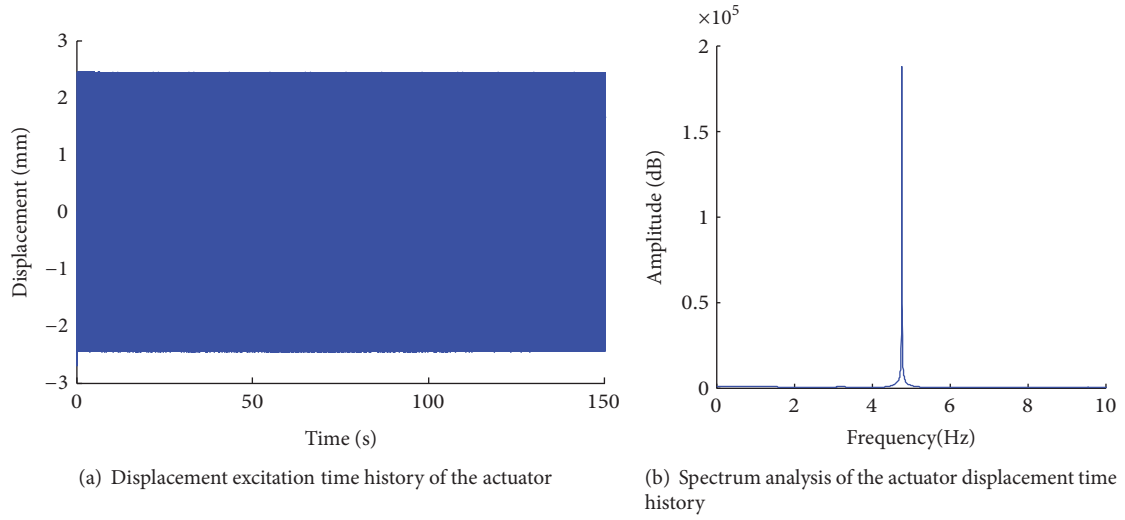


FIGURE 15: Displacement time history and its amplitude-frequency curve of the actuator.

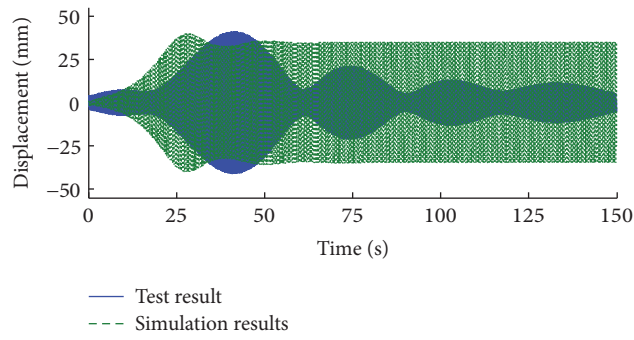


FIGURE 16: Contrast of the experiment and numerical stimulation of cable displacement while  $W_B$  equals 3 mm.

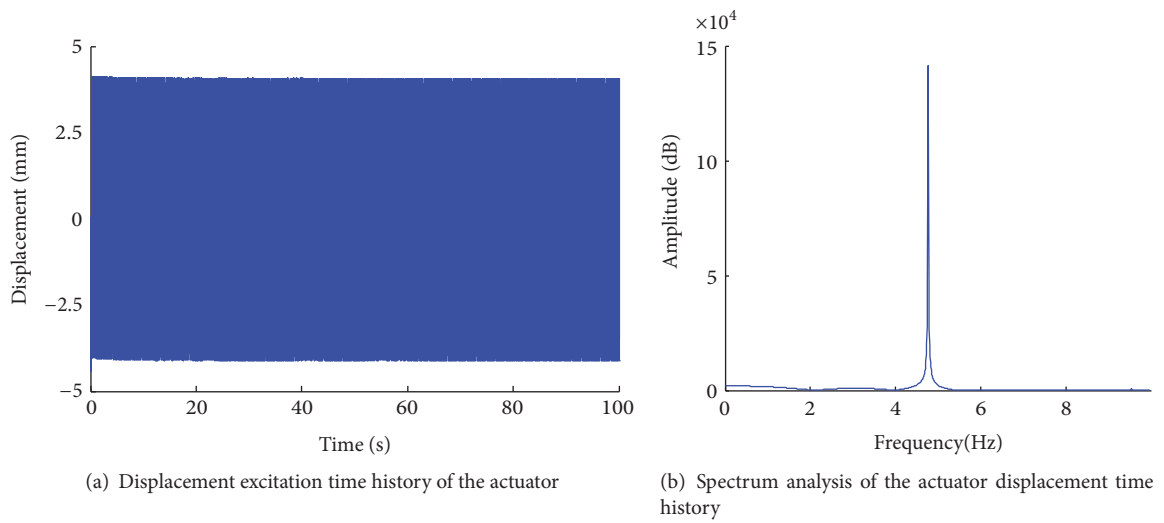


FIGURE 17: Displacement time history and its amplitude-frequency curve of the actuator.

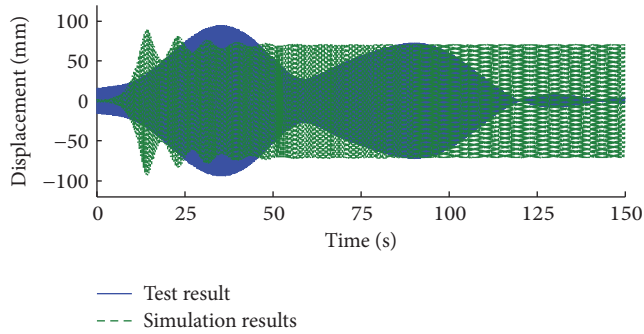


FIGURE 18: Contrast of the experiment and numerical stimulation of cable displacement while  $W_B$  equals 5 mm.

results of test and numerical simulation, some conclusions are as follows:

- (1) In order to obtain the support excitation frequency's accurate value in the parametric vibration, before the parametric vibration test, the first-order natural frequency of the cable is determined by free vibration test, due to the complicated connection modes of the test model cable in the end supports. Meanwhile, the dynamic characteristics analysis on model cable is carried out by using of the finite element modeling. According to the contrasting and confirming of two methods' solving results, it showed that the first-order natural frequency obtained by free release method could be used as an effective basis of supports excitation frequency during parametric vibration test.
- (2) Model cable's 2:1 parametric vibration problem is studied by selecting the support excitation amplitude of two kinds of working conditions:  $W_B = 3$  mm and  $W_B = 5$  mm, which is compared with the numerical simulation results. Analysis results show that the results, stay cable's displacement amplitude from test analysis and numerical simulation, are basically the same. However, the test results attenuated faster, and the time interval between "beat" and "beat" is longer, which is because when large amplitude vibration of stay cable happens, in addition to the in-plane vibration, there is still significant out-plane vibration. Meanwhile, because the excitation frequency of bearings is larger and the model cable end is rigidly connected components, rigid connection element motion is uncoordinated with vibration of cables when the actuator excited the bearings, which limits the cable vibration.

## Competing Interests

The authors declare that they have no competing interests.

## Acknowledgments

This research was financed by National Natural Science Foundation of China (51208088 and 51468001), the Science

and Technology Support Program of Jiangxi Province (20133BBE50032), and Young Scientists (Jing Gang star) Training Object Program of Jiangxi Province (20133BCB23021).

## References

- [1] A. H. Nayfeh and D. T. Mook, *Nonlinear Vibrations*, Higher Education Press, 1990.
- [2] A. Y. Kovrega and E. P. Kubyshkin, "Features of the behavior of solutions to a nonlinear dynamical system in the case of two-frequency parametric resonance," *Journal of Vibration and Control*, vol. 53, no. 5, pp. 573–579, 2013.
- [3] I. G. Raftoyiannis, "Parametric resonance of steel bridges pylons due to periodic traffic loads," *Archive of Applied Mechanics*, vol. 82, no. 10-11, pp. 1601–1611, 2012.
- [4] A. M. Abdel-Ghaffar and M. A. Khalifa, "Importance of cable vibration in dynamics of cable-stayed bridges," *ASCE Journal of Engineering Mechanics*, vol. 117, no. 11, pp. 2571–2589, 1991.
- [5] R.-F. Fung, L.-Y. Lu, and S.-C. Huang, "Dynamic modelling and vibration analysis of a flexible cable-stayed beam structure," *Journal of Sound and Vibration*, vol. 254, no. 4, pp. 717–726, 2002.
- [6] V. Gattulli, M. Morandini, and A. Paolone, "A parametric analytical model for non-linear dynamics in cable-stayed beam," *Earthquake Engineering and Structural Dynamics*, vol. 31, no. 6, pp. 1281–1300, 2002.
- [7] H. Zhou, *Experimental Study on Nonlinear Dynamics of Cable-Beam Composite Structure*, Hunan University, Changsha, China, 2007.
- [8] M. Liu, *Magneto Rheological Fluid Damper Control System and Energy Dissipation System of Shape Memory Alloy*, Harbin Institute of Technology Doctoral Dissertation, Harbin, China, 2007.
- [9] F. Li, *Parametric vibration and cable force identification of staying cable of large-span bridges [Ph.D. dissertation]*, Harbin Institute of Technology, Harbin, China, 2010.

## Research Article

# Impact-Induced Delamination Detection of Composites Based on Laser Ultrasonic Zero-Lag Cross-Correlation Imaging

**Yun-Kyu An**

*Department of Architectural Engineering, Sejong University, Seoul 05006, Republic of Korea*

Correspondence should be addressed to Yun-Kyu An; [yunkyu@sejong.ac.kr](mailto:yunkyu@sejong.ac.kr)

Received 17 July 2016; Revised 19 September 2016; Accepted 28 September 2016

Academic Editor: Ying Wang

Copyright © 2016 Yun-Kyu An. This is an open access article distributed under the Creative Commons Attribution License, which permits unrestricted use, distribution, and reproduction in any medium, provided the original work is properly cited.

This paper presents impact-induced delamination visualization by zero-lag cross-correlation (ZLCC) imaging computed using fully noncontact laser scanned ultrasonic wavefields. The proposed technique enables instantaneous visualizing of invisible delamination of composite materials without any sensor installation. Moreover, it provides robust damage diagnosis without comparing with baseline data obtained from the undamaged condition of a target structure, making it possible to minimize false alarms. First, the existence of internal delamination-induced standing waves is proven by employing a finite element analysis. Then, how ZLCC can physically isolate and visualize only the standing wave feature from the measured ultrasonic wavefields is shown. To experimentally validate the proposed technique, a fully noncontact laser ultrasonic imaging system is introduced, and the internal delamination is visualized by laser scanning in a graphite fiber composite plate. The experimental results reveal that hidden delamination is successfully and automatically visualized and quantified without any users' intervention.

## 1. Introduction

Composite materials have gained popularity for various structures of aerospace and civil and mechanical fields, because they have many advantages such as lightweight and higher strength over other existing materials. For example, composite materials corresponding to more than 20% of total weight are used for Air Bus 380 and more than 40% are used for Boeing 787. However, these composite materials typically have higher brittleness than metals and are intrinsically susceptible to external bending and shear forces between laminated layers. Aircraft structures are often subjected to these external forces such as a bird strike, cyclic loading under in-service conditions, and other abrupt impact loads, resulting in delamination between internal layers. The most challenging issue for delamination detection is that typical delamination cannot be observed by naked eyes on the structure surface even though it seriously deteriorates the strength of composite structures. Thus, a number of nondestructive testing (NDT) techniques have been adopted to tackle the issue. One of the widely accepted NDT techniques is an ultrasonic NDT technique. Zhao et al. conducted experiments on

a full-scale aircraft composite wing for damage identification and localization using a lead zirconate titanate (PZT) sensor array [1]. Di Scalea et al. studied the monitoring of the composite wing skin-to-spar joint in an unmanned aerial vehicle using guided waves obtained from a pair of macro-fiber composites [2]. More recently, An et al. investigated the feasibility of the integrated impedance and guided wave technique for monitoring of a full-scale aircraft wing structure under temperature and external loading variations [3].

However, these conventional approaches often suffer technical challenges from the use of contact-type transducers. First, spatially limited ultrasonic responses obtained from sensors installed at several discrete points may not achieve spatial resolution high enough to detect small incipient damage. Second, damage localization may not be accomplished using spatially limited sensors. Third, installed transducers, electric wires, and the associated onboard data acquisition devices not only augment the weight of a target structure but also increase the system complexity. Furthermore, the repair or replacement with respect to malfunctioned transducers permanently installed on a target structure is a challenging task.

To overcome these technical limitations, noncontact NDT techniques are strongly desired to be adopted. In particular, fully noncontact laser ultrasonic imaging (LUI) techniques have been extensively studied as emerging damage detection techniques with the remarkable development of laser technology and the corresponding measurement devices. The advantages of the LUI technique are that (1) ultrasonic wavefield images with high spatial and temporal resolutions are constructed without any sensor installation, providing intuitive damage diagnosis; (2) damage diagnosis can be performed without relying on baseline data obtained from the pristine condition of a target structure, enabling it to be less vulnerable to false alarms due to environmental and operational variations; and (3) it is nonintrusive, cost-effective, rapidly deployable, and applicable to harsh environments such as high temperature and radioactive conditions.

With these advantages, a number of fully noncontact LUI techniques have been recently developed. Dhital and Lee developed a fully noncontact LUI technique using a Q-switched pulsed laser for ultrasonic generation and an air coupled transducer (ACT) for ultrasonic measurement [4]. An et al. proposed a complete noncontact LUI technique by combining a Q-switched pulsed laser for ultrasonic generation and a laser Doppler vibrometer (LDV) for ultrasonic measurement and demonstrated hidden crack visualization on an aluminum plate [5]. Such complete noncontact LUI system has been also used for internal damage detection in composite structures. Chia et al. proposed an adjacent wave subtraction method for internal defect detection in a composite wing structure [6], and Park et al. visualized internal delamination in composite structures [7]. Then, Harb and Yuan also developed a fully noncontact system by integrating ACT for ultrasonic generation with LDV for Lamb wave characterization [8]. However, the development of rapid and computational cost-effective imaging techniques is still necessary.

To come up with the demand, the zero-lag cross-correlation (ZLCC) imaging technique using fully noncontact LUI technique is proposed for internal delamination visualization in a composite plate in this study. To achieve it, the ultrasonic wave interactions with an internal delamination are thoroughly investigated by employing a finite element (FE) method. Based on delamination-induced standing waves identified as a unique feature representing the delamination existence and location, a ZLCC imaging technique is theoretically developed to isolate and visualize only the standing wave components from the measured ultrasonic wavefields. Finally, the proposed technique is experimentally validated by visualizing hidden delamination of a composite plate using the LUI system.

This paper is organized as follows. First, the existence of standing waves generated by an internal delamination is investigated through the FE analysis in Section 2. Then, the ZLCC imaging technique is theoretically developed in Section 3. In Section 4, a target composite specimen with an internal delamination and the LUI system are described for the experimental validation. The corresponding experimental results are shown in Section 5. Finally, this paper concludes with brief discussions in Section 6.

TABLE I: Material properties of a composite plate: mass density ( $\rho$ ), Young's modulus ( $E$ ), shear modulus ( $G$ ), Poisson coefficient ( $\nu$ ), and thickness ( $t$ ).

$\rho$ (kg/m <sup>3</sup> )	$E_x$ (GPa)	$E_y$ (GPa)	$\nu$	$G_{xy}$ (GPa)	$t$ (mm)
1700	131	8.2	0.281	4.5	3

## 2. Delamination-Induced Standing Waves

First, the existence of standing waves induced by an internal delamination in a composite structure is investigated through FE simulation. To simplify and clarify the problem, Lamb wave propagation along a composite plate is assumed in the simulation. Note that laser-generated ultrasonic waves propagating along a thin plate-like structure eventually make Lamb waves in the far-field from the excitation laser source [9]. A 2D composite plate model with an internal delamination is shown in Figure 1. The 2D plane strain model with four-node bilinear quadrilateral (CPS4R) elements is made by using ABAQUS/Standard 6.11 [10]. The 2D composite plate model has a dimension of  $210 \times 3$  mm<sup>2</sup>, and the dimension of an APC 850 type PZT [11] is  $10 \times 0.508$  mm<sup>2</sup> as shown in Figure 1. Here, PZT is used for Lamb wave generation, and the corresponding responses are measured at all nodes across delamination in the time domain for visualizing the wave interactions with the delamination. The material properties of the composite plate are summarized in Table 1. Since 2D plane strain model is used in this simulation, four parameters are only considered due to the symmetricity.

To precisely investigate the Lamb wave interactions with the entrance and exit of delamination, the internal delamination is modeled under varying its width as shown in Figure 1. The width varying delamination is modeled using a double-node [10], and the constraint conditions of the double-node between two delamination interfaces are defined as follows. For normal behavior, the delamination surfaces transmit contact stresses only when they are in contact, but no penetration is allowed at each constraint location. For tangential behavior, the relative sliding motion between the two surfaces is prevented as long as the corresponding normal contact constraints are active. The delamination widths are varied from 0 to 20  $\mu$ m as shown in Figure 1. The PZT attached on the top surface is used to generate Lamb waves by applying the input waveform of 7-cycle toneburst signals with a driving frequency of 100 kHz. To guarantee proper simulation results, the spatial and time resolution should be well designed. The mesh size of  $0.5 \times 0.5$  mm<sup>2</sup> and the sampling rate of 20 MHz are determined by the following spatial discretization rule [12]:

$$\begin{aligned} \max(\Delta x, \Delta y) &< \frac{\delta_{\min}}{10} \\ \Delta t &< \frac{0.7 \min(\Delta x, \Delta y)}{C_L}, \end{aligned} \quad (1)$$

where  $\Delta x$ ,  $\Delta y$ , and  $\delta_{\min}$  represent  $x$  and  $y$  directional element dimensions and the shortest wavelength at a given frequency, respectively.  $\Delta t$  denotes time interval.

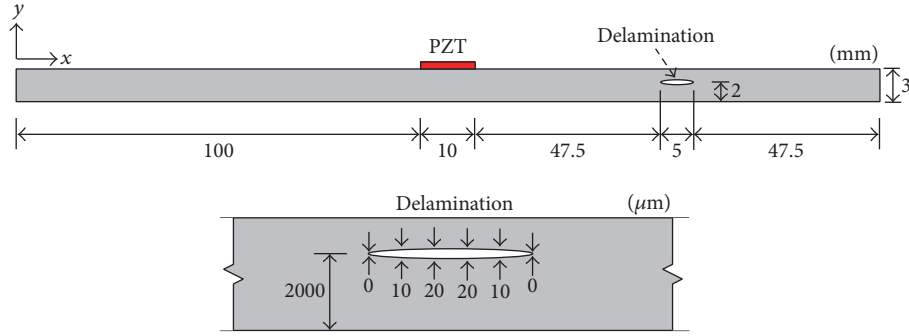
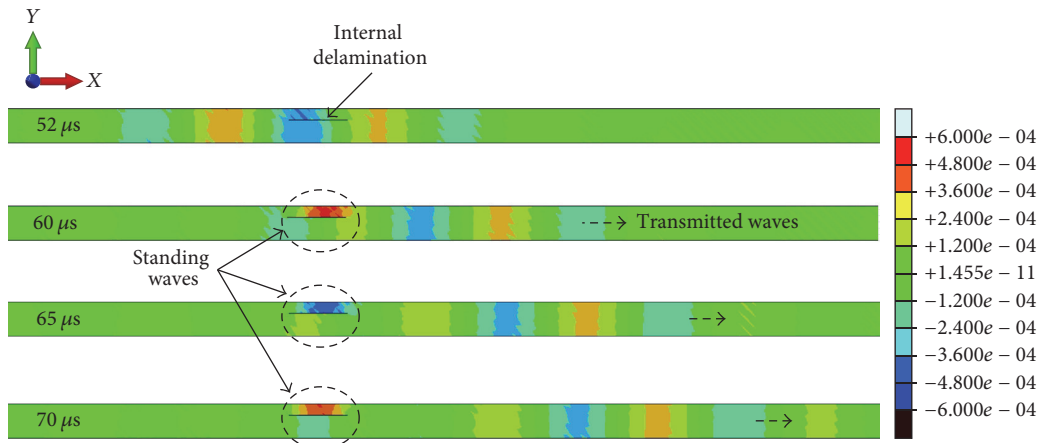


FIGURE 1: Description of 2D plane strain FE model.

FIGURE 2: Representative out-of-plane velocities of Lamb wave propagation at 52  $\mu$ s, 60  $\mu$ s, 65  $\mu$ s, and 70  $\mu$ s.

The representative out-of-plane velocities of Lamb wave propagation at 52  $\mu$ s, 60  $\mu$ s, 65  $\mu$ s, and 70  $\mu$ s are shown in Figure 2. Since the magnitude of fundamental antisymmetric ( $A_0$ ) modes is dominant rather than fundamental symmetric ( $S_0$ ) modes in this frequency range, the responses of Figure 2 mainly show  $A_0$  Lamb wave modes. When  $A_0$  modes propagating along the composite plate encounter the internal delamination, a portion of them is trapped within the delamination, and others are transmitted through the delamination. It is interesting to see here that the waves reflected from the delamination entrance are hardly observed. On the other hand, the delamination exits act as dominant reflectors once the waves go into the delamination boundary. Therefore, the trapped waves undergo multiple reflections from the delamination boundary, generating standing waves within the delamination. These standing waves can be effectively used as the strong evidence of the delamination existence.

### 3. Zero-Lag Cross-Correlation (ZLCC) Imaging

The ZLCC concept was firstly proposed by Zhu et al. for fast damage imaging based on the time reversal principle [13]. As the follow-up studies, the ZLCC concept has been applied to damage detection in composite [14] and metallic [15] structures. This section explains how ZLCC is calculated from the measured wavefield. In particular, the relationship

between ZLCC and the standing waves caused by impact-induced delamination is thoroughly investigated. As the first step, total ultrasonic wavefield ( $W_T$ ) is measured in the time-space ( $t$ - $s$ ) domain on the target area of interest. Here,  $W_T$  typically includes wave propagation, wave interactions with delamination, and measurement noises. Once  $W_T$  is obtained at all spatial points of interest, it can be decomposed into forward ( $W_F$ ) and backward ( $W_B$ ) propagating waves using the frequency-wavenumber ( $f$ - $k$ ) domain analysis [5, 7, 16, 17].  $W_T$  in the  $t$ - $s$  domain is transformed into the  $f$ - $k$  domain using a 3D Fourier transform

$$U_T(k_x, k_y, \omega) = \iiint_{-\infty}^{\infty} W_T(x, y, t) e^{-i(k_x x + k_y y + \omega t)} dx dy dt, \quad (2)$$

where  $U_T$  is the ultrasonic wavefield in the  $f$ - $k$  domain.  $k$  and  $\omega$  are the wavenumber and angular frequency, respectively.  $x$  and  $y$  denote spatial coordinates.

Now, window functions,  $\Phi_F$  and  $\Phi_B$ , are introduced so that forward ( $U_F$ ) and backward ( $U_B$ ) propagating waves are decomposed from  $U_T$  in the  $f$ - $k$  domain

$$U_{F(B)}(k_x, k_y, \omega) = U_T(k_x, k_y, \omega) \cdot \Phi_{F(B)} \quad \forall \omega, \quad (3)$$

where

$$\Phi_F = \begin{cases} 0 & k_x, k_y \leq 0 \\ 1 & k_x, k_y > 0 \end{cases} \quad (4)$$

$$\Phi_B = \begin{cases} 1 & k_x, k_y < 0 \\ 0 & k_x, k_y \geq 0. \end{cases}$$

Next, the resultant waves in the frequency-space ( $f$ - $s$ ) domain are obtained using the following inverse 2D Fourier transform:

$$V_{F(B)}(x, y, \omega) = \frac{1}{2\pi} \iint_{-\infty}^{\infty} U_{F(B)}(k_x, k_y, \omega) e^{i(k_x x + k_y y + \omega t)} dk_x dk_y, \quad (5)$$

where  $V_F$  and  $V_B$  are the forward and backward wavefields in the  $f$ - $s$  domain.

Then, the ZLCC values at each spatial point are obtained using

$$Z(x, y) = \int V_F(x, y, \omega) V_B^*(x, y, \omega) d\omega, \quad (6)$$

where the superscript  $*$  denotes the complex conjugate. Note that the ZLCC computation in the  $f$ - $s$  domain is more effective than the  $t$ - $s$  domain computation in terms of reducing the computational costs. The relationship between standing wave generation mechanism and the internal delamination is described in Section 2. Multiple reflections within the delamination boundary momentarily make standing waves, meaning that the two different directional waves have the same wavelength and frequency conditions inside the delamination boundary. Such conditions well satisfy the ZLCC condition which physically means that the similarity indicator of two waves is zero-delayed or in-phase [15]. Therefore, the ZLCC values will abruptly increase within the delamination boundary compared to the intact region.

Next, an additional denoising process is necessary to remove the undesired measurement noises which can cause false alarms. The essence of the denoising process is that a threshold value (TR) computed by extreme value statistics [18] is employed with respect to the values of ZLCC. The probability density function of the ZLCC values is estimated by fitting a Weibull distribution to the ZLCC populations, and TR corresponding to a one-sided 95% confidence interval is established. Finally, the values of ZLCC exceeding TR highlight impact-induced delamination without noise components. This denoising process physically means that delamination should be automatically visualized and emphasized in the final ZLCC image if the delamination is large enough to create standing waves beyond the measurement noise level.

#### 4. Experimental Description

To experimentally validate the proposed technique for delamination visualization, a complete noncontact LUI system [7] is introduced first. Because the LUI system can generate

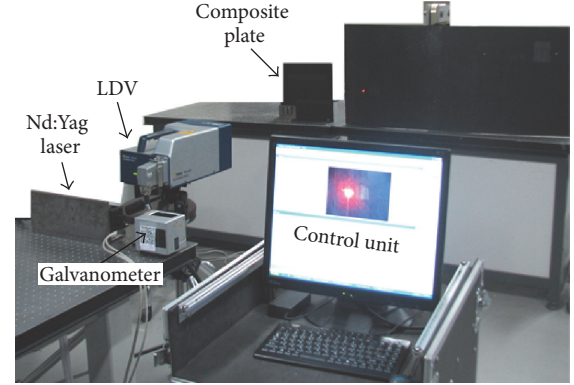


FIGURE 3: Experimental setup for delamination visualization in a composite plate.

and measure  $W_T$  by scanning fully noncontact laser beams onto the target surface, no ultrasonic transducer installation is required.

Figure 3 shows the LUI system composed of a Q-switched Nd:Yag pulse laser for ultrasonic generation, LDV for ultrasonic measurement, a galvanometer for laser scanning, and a control unit. The overall working principle is as follows. First, virtual grid points on the target surface are created using a built-in digital camera, and the sequences of excitation and sensing scanning points are predetermined. Then, the controller in the control unit sends out a trigger signal to the Nd:Yag pulse laser to fire the excitation laser beam to the first prescribed excitation point through the galvanometer with a focal lens. The same trigger signal is simultaneously transmitted to LDV to activate data acquisition. Then, the response signal is measured at a specified measurement point, transmitted to, and stored in the control unit. Next, the control unit moves the excitation or sensing laser beam automatically to the next scanning point by sending control signals to the relevant galvanometer. By repeating the ultrasonic excitation and sensing over the prescribed grid points,  $W_T$  can be constructed over the target surface.

The Q-switched Nd:Yag pulse laser employed in this system has 532 nm wavelength and 3.7 MW peak power and generates a pulse input with 8 ns pulse duration at a repetition rate of 20 Hz. The galvanometer has a maximum rotating speed of 5730°/s, angular resolution of  $6.6 \times 10^{-4}^\circ$ , and an allowable scanning angle of  $\pm 21.8^\circ$ . The initial laser beam diameter emitted from the galvanometer is about 4 mm. Because this beam size is relatively large to achieve high spatial resolution, the focal lens installed in front side of the galvanometer adjusts the beam size to 0.5 mm at the optical focal length of 2 m. Ultrasonic waves are created through the thermal expansion of an infinitesimal area heated by the high-power laser. The power level, laser pulse duration, and laser beam size need to be carefully tailored because high-power density of the laser beam above a certain threshold will cause ablation phenomena [19].

For ultrasonic response measurement, a commercial scanning LDV (Polytec PSV-400-M4) with a built-in galvanometer and an autofocal lens is used in this system [20].

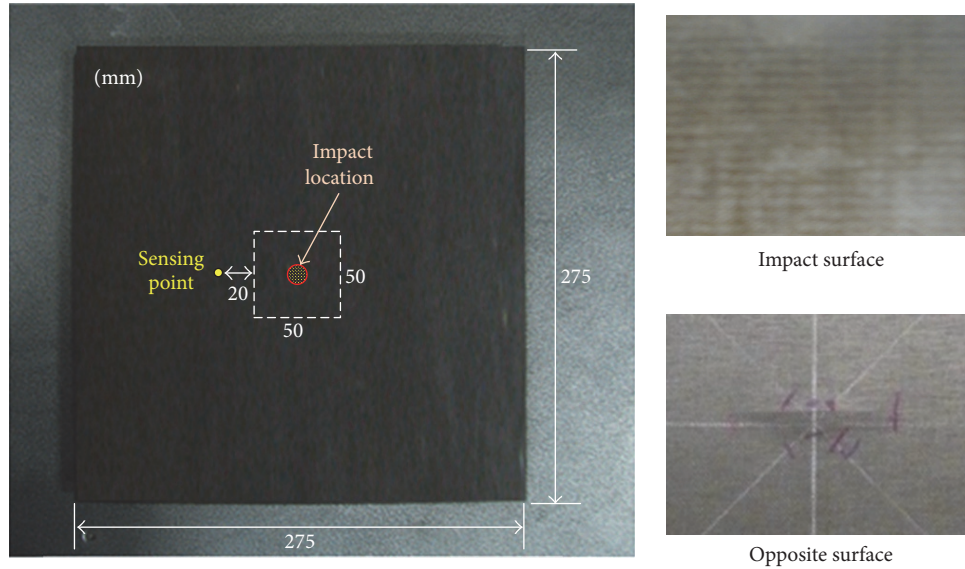


FIGURE 4: Target composite plate with the impact-induced delamination and the laser scanning scheme.

The laser source used for LDV is the He-Ne laser with a wavelength of 633 nm, and the optimal measurement distance is repeated itself at  $99+204n$  (mm), where  $n$  denotes an integer number. Then, the minimum focal length of the autofocal lens is 0.35 mm, and the allowable scanning angle range and scanning speed are  $\pm 20^\circ$  and  $2000^\circ/\text{s}$ , respectively. This 1D LDV measures the out-of-plane velocity in the range of  $0.01 \mu\text{m/s}$  to  $10 \text{ m/s}$  over a target surface based on the Doppler frequency-shift effect of light. Since the intensity of the signal laser beam reflected from the target surface highly depends on the surface condition, a special surface treatment is often necessary to improve the reflectivity of the returned laser beam.

The control unit consists of a personal computer (PC), controller, velocity decoder with the maximum velocity sensitivity of  $1 \text{ mm/s/V}$ , and a 14-bit digitizer with a maximum sampling frequency of 350 kHz. The controller sends out trigger signals to launch the excitation laser beam and to simultaneously start the data collection. In addition, the controller generates control signals to aim the excitation and sensing laser beams at desired target positions. The velocity decoder records the out-of-plane velocity by computing the frequency shifts between the laser beam reflected from the target surface and the reference laser beam. Then, the measured signals are processed on PC.

Figure 4 shows the target composite plate with a dimension of  $275 \times 275 \times 1.8 \text{ mm}^3$ . The composite plate is composed of IM7 graphite fibers with 977-3 resin material and consists of 12 plies with a layup of  $[0/\pm 45/0/\pm 45]_s$ . Then, the composite plate is subjected to impact, causing an internal delamination. The created delamination is invisible on the impact surface, but partially broken fibers can be observed on the opposite surface to the impact surface as shown in Figure 4. The laser scanning is performed on the impact surface, and an area of  $50 \times 50 \text{ mm}^2$  is scanned by the excitation laser beam with spatial resolution of 2 mm. Then, the corresponding

ultrasonic waves are measured by LDV at 20 mm apart from the left edge of the scanning area as shown in Figure 4. The distances from the Nd:Yag laser for scanning ultrasonic generation and LDV for ultrasonic measurement to the target specimen are 2 m and 1.6 m, respectively. For the Nd:Yag laser, the repetition rate, peak power, and laser beam size are set to 20 Hz, 1 MW, and 4 mm, respectively. Then, the sampling rate of LDV is 5.12 MHz, and the sensitivity of the velocity measurement is set to  $10 \text{ mm/s/V}$ . A retroreflective tape is placed at the sensing point of the target specimen to improve reflectivity of the sensing laser beam. The response signals are measured 50 times for each excitation point, averaged in the time domain, and bandpass-filtered with 10 kHz and 300 kHz cutoff frequencies to improve signal-to-noise ratio.

## 5. Experimental Results

Once  $W_T$  is collected from all scanning points of the composite plate using the LUI system, the  $W_T$  image is obtained by assembling all  $W_T$  data within the scanning area. Figure 5 shows the representative snapshots of  $W_T$  obtained from the composite plate with delamination at  $26.60 \mu\text{s}$ ,  $34.80 \mu\text{s}$ , and  $43.01 \mu\text{s}$ . Here, the amplitude of each snapshot is normalized with respect to its maximum value. It is clearly observed that incident waves propagating from left to right are trapped by interacting with the internal delamination, and others are mainly transmitted through the delamination rather than reflected from the delamination. The experimental observation is well matched with the numerical expectation described in Section 2.

Subsequently,  $W_T$  is transformed to  $U_T$  using the 3D Fourier transform in (2) and  $U_F$  and  $U_B$  are obtained using (3). The corresponding wavenumber plots are displayed in Figure 6. It can be easily observed that  $U_T$  is successfully decomposed into  $U_F$  and  $U_B$ . Note that the waves mainly

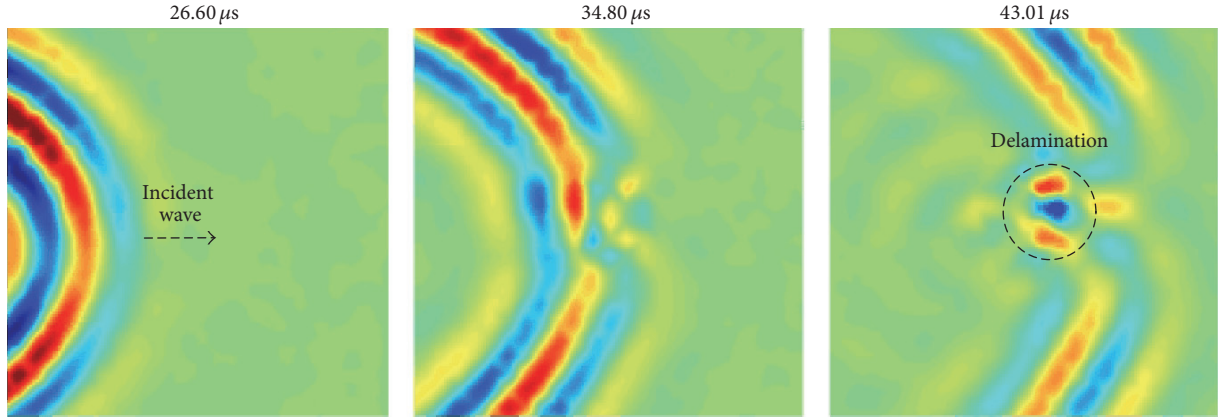


FIGURE 5: Representative  $W_T$  images at 26.60  $\mu\text{s}$ , 34.80  $\mu\text{s}$ , and 43.01  $\mu\text{s}$ .

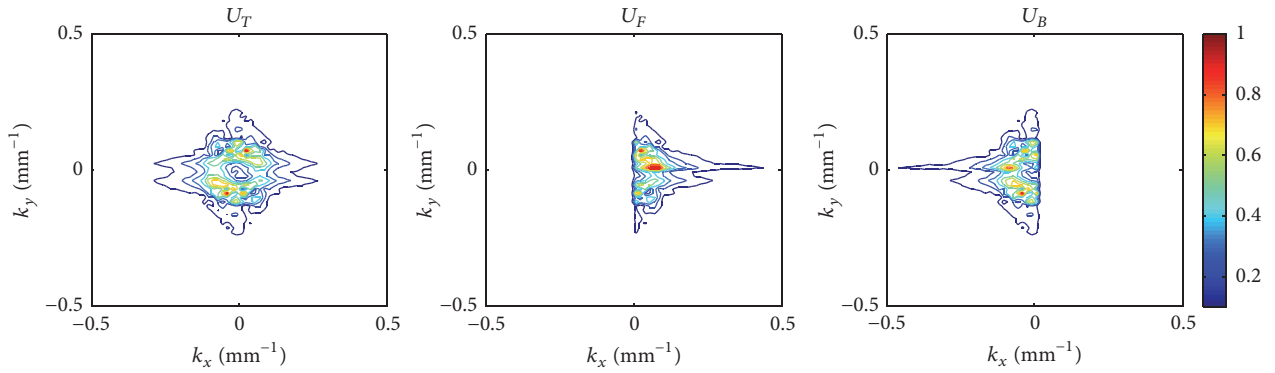


FIGURE 6: Wavenumber plots of  $U_T$ ,  $U_F$ , and  $U_B$ .

propagate from left- to right-hand side in the inspection area of interest as observed in Figure 5.

In order to more precisely investigate the wave decomposition process, the decomposed  $U_F$  and  $U_B$  in the  $f$ - $k$  domain are transformed into  $W_F$  and  $W_B$  in the  $t$ - $s$  domain, respectively, using the following inverse 3D Fourier transform:

$$W_{F(B)}(x, y, t) = \frac{1}{2\pi} \cdot \iiint_{-\infty}^{\infty} U_{F(B)}(k_x, k_y, \omega) e^{i(k_x x + k_y y + \omega t)} dk_x dk_y d\omega. \quad (7)$$

In (7),  $W_F$  and  $W_B$  contain only forward and backward propagating waves. The computed  $W_F$  and  $W_B$  images at 26.60  $\mu\text{s}$ , 34.80  $\mu\text{s}$ , and 43.01  $\mu\text{s}$  are shown in Figures 7(a) and 7(b), respectively. Incident waves transmitted through the delamination are clearly observed in Figure 7(a) while only reflected waves from the delamination boundary are shown in Figure 7(b). The decomposed wavefields of Figure 7 reveal that the proposed wave decomposition process works well for  $W_T$ .

Based on the validation results, the ZLCC values are subsequently computed using (6). Then, the denoising process described in Section 3 is applied to all ZLCC values. Here, TR is computed as 0.578. By assembling all ZLCC values exceeding TR at all spatial points of interest, the ZLCC image

is obtained as shown in Figure 8(a). The dotted circle with around 10 mm diameter shows the actual delamination size estimated by the thermographic image shown in Figure 8(b). By comparing the same dotted circle in Figure 8(a) with 8(b), it is confirmed that the proposed ZLCC imaging technique has high accuracy for hidden delamination localization and size estimation. Again, the ZLCC image reveals that only delamination is identified, localized, and quantified without any comparison of baseline data previously obtained from the pristine condition of the composite plate, making it possible to minimize false alarms caused by operational and environmental variations by avoiding pattern comparisons with the ultrasonic wavefield images previously obtained from the pristine condition of a target structure [21].

## 6. Conclusion

This study proposes a complete noncontact laser ultrasonic scanned zero-lag cross-correlation (ZLCC) imaging technique for impact-induced delamination visualization. In particular, the wave interactions with invisible delamination are precisely analyzed by employing a finite element method, and the corresponding standing waves are visualized by ZLCC imaging. The experimental validation using a complete noncontact laser ultrasonic imaging system revealed that impact-induced delamination is successfully visualized

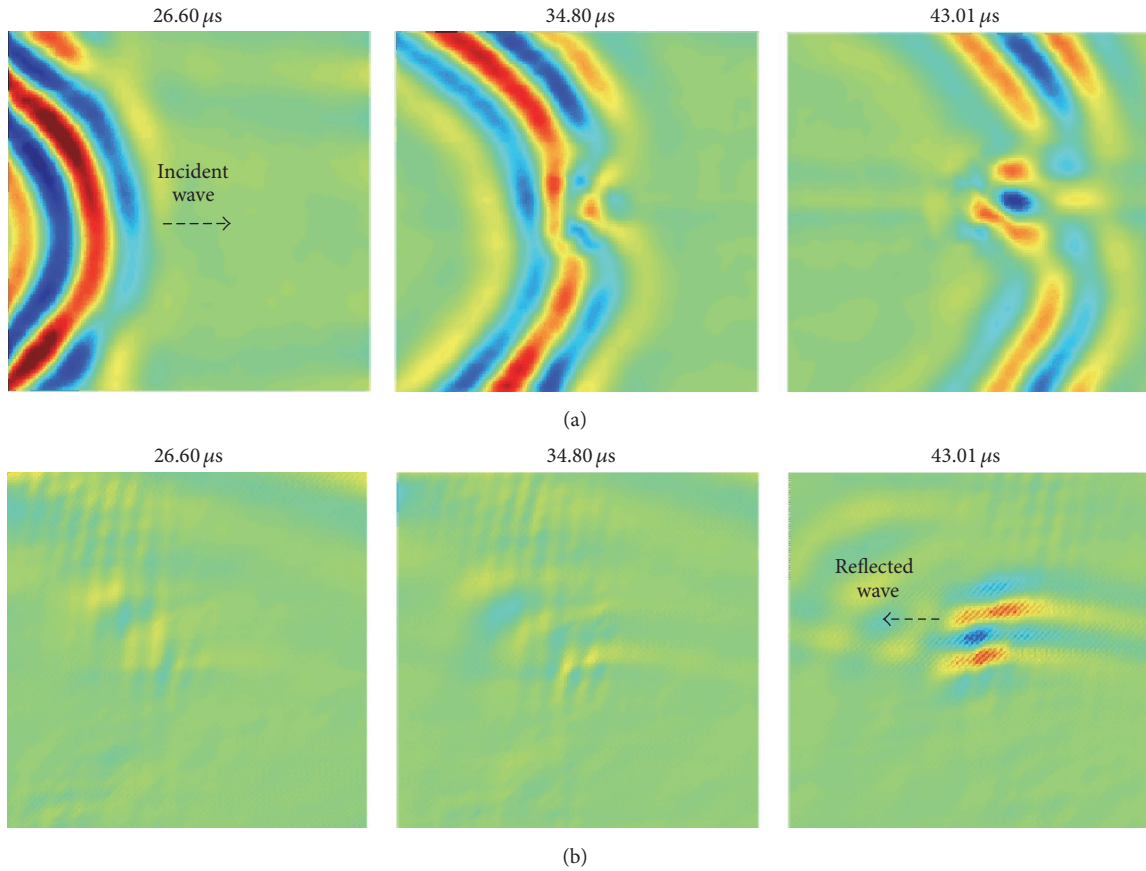


FIGURE 7: Decomposed wavefield images: (a)  $W_F$  and (b)  $W_B$  images.

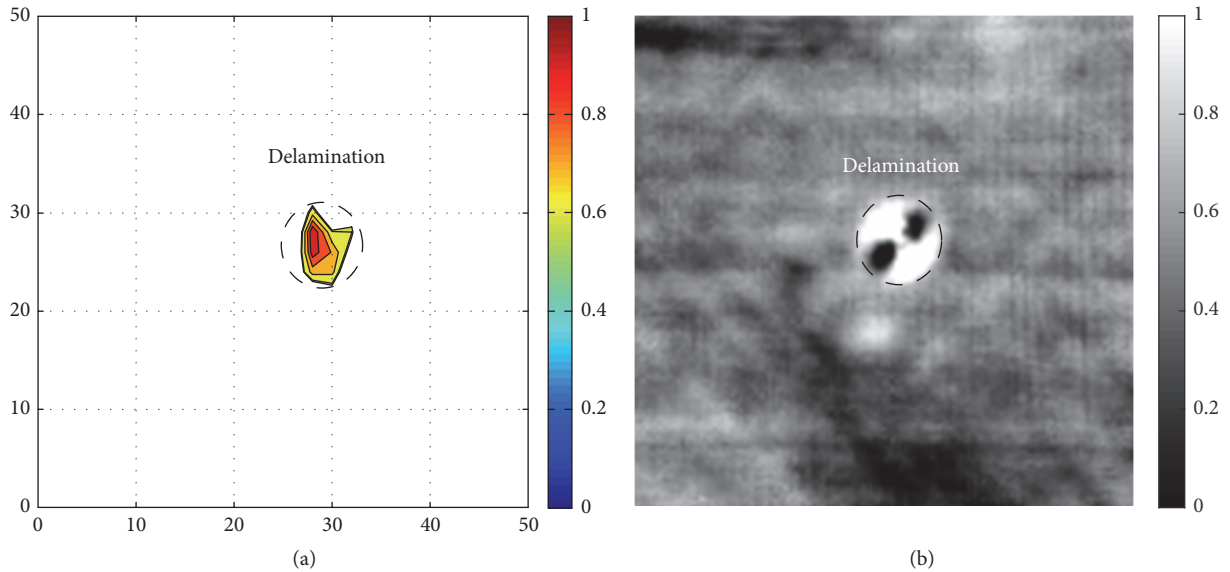


FIGURE 8: Automated delamination visualization results: (a) ZLCC image and (b) thermographic image.

without relying on baseline data, enabling minimization of false damage alarms due to changing operational and environmental conditions. Furthermore, fully automated damage diagnosis is accomplished without any users' intervention.

Although the ZLCC imaging technique is promising tool for hidden delamination identification, localization, and quantification, there are still some technical challenges associated with the sensing process for field applications: (1) because of

the required high spatial resolution, the data collection may take a relatively long time; (2) a special treatment of a target surface is often necessary to enhance the reflectivity of the sensing laser beam; and (3) there can be the eye safety issue associated with the class 4 excitation laser although the class 2 sensing laser is known to be safe. Indeed, these technical hurdles are critical issues to be resolved before the proposed technique is applied to various real structures. The equipment improvement such as high spatial resolution ultrasonic camera or high performance multipoint sensing laser interferometry might be promising solution for the prescribed limitations. Further studies are warranted to address these issues.

## Disclosure

Any opinion, finding, and conclusion or recommendation expressed in this material are those of the author and do not necessarily reflect the views of the funding agency.

## Competing Interests

The author declares no competing interests.

## Acknowledgments

This work is supported by Basic Science Research Program through the National Research Foundation of Korea (NRF) funded by the Ministry of Science, ICT and Future Planning (2015R1C1A1A01052625), and the experimental devices were supported by Professor Hoon Sohn at KAIST, Republic of Korea.

## References

- [1] X. Zhao, H. Gao, G. Zhang et al., "Active health monitoring of an aircraft wing with embedded piezoelectric sensor/actuator network: I. Defect detection, localization and growth monitoring," *Smart Materials and Structures*, vol. 16, no. 4, pp. 1208–1217, 2007.
- [2] F. L. Di Scalea, H. Matt, I. Bartoli, S. Coccia, G. Park, and C. Farrar, "Health monitoring of UAV wing skin-to-spar joints using guided waves and macro fiber composite transducers," *Journal of Intelligent Material Systems and Structures*, vol. 18, no. 4, pp. 373–388, 2007.
- [3] Y.-K. An, M. K. Kim, and H. Sohn, "Airplane hot spot monitoring using integrated impedance and guided wave measurements," *Structural Control and Health Monitoring*, vol. 19, no. 7, pp. 592–604, 2012.
- [4] D. Dhital and J. R. Lee, "A fully non-contact ultrasonic propagation imaging system for closed surface crack evaluation," *Experimental Mechanics*, vol. 52, no. 8, pp. 1111–1122, 2012.
- [5] Y.-K. An, B. Park, and H. Sohn, "Complete noncontact laser ultrasonic imaging for automated crack visualization in a plate," *Smart Materials and Structures*, vol. 22, no. 2, Article ID 025022, 2013.
- [6] C. C. Chia, J.-R. Lee, C.-Y. Park, and H.-M. Jeong, "Laser ultrasonic anomalous wave propagation imaging method with adjacent wave subtraction: application to actual damages in composite wing," *Optics & Laser Technology*, vol. 44, no. 2, pp. 428–440, 2012.
- [7] B. Park, Y.-K. An, and H. Sohn, "Visualization of hidden delamination and debonding in composites through noncontact laser ultrasonic scanning," *Composites Science and Technology*, vol. 100, pp. 10–18, 2014.
- [8] M. S. Harb and F. G. Yuan, "Non-contact ultrasonic technique for Lamb wave characterization in composite plates," *Ultrasonics*, vol. 64, pp. 162–169, 2016.
- [9] Y.-K. An, Y. Kwon, and H. Sohn, "Noncontact laser ultrasonic crack detection for plates with additional structural complexities," *Structural Health Monitoring*, vol. 12, no. 5-6, pp. 522–538, 2013.
- [10] *ABAQUS/Standard 6.11, User's Manual*, Dassault Systems, Vélizy-Villacoublay, France, 2011.
- [11] <http://www.americanpiezo.com/>.
- [12] O. Diligent, *Interaction between fundamental Lamb modes and defects in plates [Ph.D. thesis]*, Imperial College of Science, London, UK, 2003.
- [13] R. Zhu, G. L. Huang, and F. G. Yuan, "Fast damage imaging using the time-reversal technique in the frequency-wavenumber domain," *Smart Materials and Structures*, vol. 22, no. 7, Article ID 075028, 2013.
- [14] J. He and F.-G. Yuan, "Damage identification for composite structures using a cross-correlation reverse-time migration technique," *Structural Health Monitoring*, vol. 14, no. 6, pp. 558–570, 2015.
- [15] M. S. Harb and F. Yuan, "Damage imaging using non-contact air-coupled transducer/laser Doppler vibrometer system," *Structural Health Monitoring*, vol. 15, no. 2, pp. 193–203, 2016.
- [16] M. Ruzzene, "Frequency-wavenumber domain filtering for improved damage visualization," *Smart Materials and Structures*, vol. 16, no. 6, pp. 2116–2129, 2007.
- [17] T. E. Michaels, J. E. Michaels, and M. Ruzzene, "Frequency-wavenumber domain analysis of guided wavefields," *Ultrasonics*, vol. 51, no. 4, pp. 452–466, 2011.
- [18] H. W. Park and H. Sohn, "Parameter estimation of the generalized extreme value distribution for structural health monitoring," *Probabilistic Engineering Mechanics*, vol. 21, no. 4, pp. 366–376, 2006.
- [19] C. B. Scruby and L. E. Drain, *Laser Ultrasonics: Techniques and Applications*, Taylor & Francis, London, UK, 1990.
- [20] <http://www.polytec.com>.
- [21] Y.-K. An and H. Sohn, "Instantaneous crack detection under varying temperature and static loading conditions," *Structural Control & Health Monitoring*, vol. 17, no. 7, pp. 730–741, 2010.

## Research Article

# A Bridge Deflection Monitoring System Based on CCD

Baohua Shan,<sup>1,2</sup> Lei Wang,<sup>3</sup> Xiaoyang Huo,<sup>2</sup> Wenting Yuan,<sup>2</sup> and Zhilin Xue<sup>2</sup>

<sup>1</sup>Key Lab of Structures Dynamic Behavior and Control (Harbin Institute of Technology), Ministry of Education, Harbin 150090, China

<sup>2</sup>School of Civil Engineering, Harbin Institute of Technology, Harbin 150090, China

<sup>3</sup>School of Civil Engineering and Architecture, University of Jinan, Jinan 250022, China

Correspondence should be addressed to Baohua Shan; shanbaohua@hit.edu.cn

Received 9 June 2016; Revised 6 September 2016; Accepted 21 September 2016

Academic Editor: Ying Wang

Copyright © 2016 Baohua Shan et al. This is an open access article distributed under the Creative Commons Attribution License, which permits unrestricted use, distribution, and reproduction in any medium, provided the original work is properly cited.

For long-term monitoring of the midspan deflection of Songjiazhuang cloverleaf junction on 309 national roads in Zibo city, this paper proposes Zhang's calibration-based DIC deflection monitoring method. CCD cameras are used to track the change of targets' position, Zhang's calibration algorithm is introduced to acquire the intrinsic and extrinsic parameters of CCD cameras, and the DIC method is combined with Zhang's calibration algorithm to measure bridge deflection. The comparative test between Zhang's calibration and scale calibration is conducted in lab, and experimental results indicate that the proposed method has higher precision. According to the deflection monitoring scheme, the deflection monitoring software for Songjiazhuang cloverleaf junction is developed by MATLAB, and a 4-channel CCD deflection monitoring system for Songjiazhuang cloverleaf junction is integrated in this paper. This deflection monitoring system includes functions such as image preview, simultaneous collection, camera calibration, deflection display, and data storage. *In situ* deflection curves show a consistent trend; this suggests that the proposed method is reliable and is suitable for the long-term monitoring of bridge deflection.

## 1. Introduction

It is very significant that monitoring bridge deflection can evaluate the health status of bridge and can provide the important reference base for the structural performance and operational status of bridge. Currently, there are two kinds of deflection measurement methods which are the traditional measurement method and the automatic measurement method. The traditional measurement methods include dial indicator, level, and total station. The principle of dial indicator measuring bridge deflection is very simple [1]. However, due to the great height of bridge, it is very inconvenient to install the dial indicator on main girder of bridge. The level is usually used to measure bridge deflection along with a scale [2], and this increases the complexity of measurement work. Furthermore, the total station is easily influenced by temperature and humidity and is not suitable for long-term monitoring in the wild [3]. In a word, the traditional measurement methods are rarely used to execute

the long-term monitoring of bridge deflection, except for the temporary measurement.

The automatic measurement methods comprise accelerometer, microwave interferometer, GPS, connected pipe optoelectronic liquid level sensor, and so forth. The high-frequency component occupies a large proportion in the data collected by accelerometer, so the low-frequency component is drowned out when the displacement is obtained by computing the integral for acceleration data. However, the bridge deflection is exactly the low-frequency component. In the meantime, the double integral brings about errors. As a result, the accelerometer has lower precision [4]. The microwave interferometer can detect the bridge deflection according to the phase difference of reflected wave before and after deformation. Although the microwave interferometer has higher precision, this method is not suitable for the case that the transverse deformation and longitudinal deformation simultaneously occur on bridge [5]. GPS has very good practicability. Nevertheless, the cost of GPS is higher and the



$$\begin{aligned} X_d &= X_u + k_1 X_u r^2 + k_2 X_u r^4, \\ Y_d &= Y_u + k_1 Y_u r^2 + k_2 Y_u r^4, \end{aligned} \quad (2)$$

where  $r = \sqrt{X_u^2 + Y_u^2}$  and  $(X_d, Y_d)$  is the normalized coordinate of image point under distorted condition.  $(X_u, Y_u)$  is the normalized coordinate of image point under undistorted condition. Both  $k_1$  and  $k_2$  are the radial distortions coefficients. The matrix  $A$  in (1) and  $k_1, k_2$  are collectively called the intrinsic parameters of camera.

Zhang's calibration algorithm only requires the camera to observe a planar pattern shown at a few (at least two) different orientations. Either the camera or the planar pattern can be freely moved. The motion need not be known. The detailed calibration procedure of Zhang's algorithm is given as below.

*2.1. Solving the Intrinsic and Extrinsic Parameters of Camera.* As seen from (1), there exists the projective transformation relation between the world coordinate system and the image coordinate system. Suppose that the 2D planar pattern is selected as the model plane of the world coordinate system; namely,  $Z_w = 0$ . Let us denote the  $i$ th column of the rotation matrix  $R$  by  $r_i$ . From (1), we have

$$s \begin{bmatrix} u \\ v \\ 1 \end{bmatrix} = A [r_1 \ r_2 \ r_3 \ t] \begin{bmatrix} X_w \\ Y_w \\ 0 \\ 1 \end{bmatrix} \quad (3)$$

$$= A [r_1 \ r_2 \ t] \begin{bmatrix} X_w \\ Y_w \\ 1 \end{bmatrix}.$$

Let  $\bar{m} = [u \ v \ 1]^T$  and  $\bar{M} = [X_w \ Y_w \ 1]$ ; we have

$$s\bar{m} = H\bar{M}, \quad (4)$$

where  $H = \lambda A [r_1 \ r_2 \ t] = [h_1 \ h_2 \ h_3]$ , where  $\lambda$  is an arbitrary scalar.

Computing  $H$  is a process that solves the minimum residual error between the actual image coordinate  $m_i$  and the image coordinate  $\bar{m}_i$  which is calculated by (4); the objective function is  $\min \sum_i \|m_i - \bar{m}_i(H)\|^2$ .

After solving  $H$ , two basic constraints on the intrinsic parameters  $A$  are obtained according to the orthogonality and given as follows:

$$\begin{aligned} h_1^T A^{-T} A^{-1} h_2 &= 0, \\ h_1^T A^{-T} A^{-1} h_1 &= h_2^T A^{-T} A^{-1} h_2. \end{aligned} \quad (5)$$

Let

$$B = A^{-T} A^{-1} = \begin{bmatrix} B_{11} & B_{12} & B_{13} \\ B_{21} & B_{22} & B_{23} \\ B_{31} & B_{32} & B_{33} \end{bmatrix} = \begin{bmatrix} \frac{1}{f_x} & -\frac{r}{f_x^2 f_y} & \frac{v_0 \gamma - u_0 f_y}{f_x^2 f_y} \\ -\frac{r}{f_x^2 f_y} & \frac{\gamma^2}{f_x^2 f_y^2} + \frac{1}{f_y^2} & -\frac{\gamma(v_0 \gamma - u_0 f_y)}{f_x^2 f_y^2} - \frac{v_0}{f_y^2} \\ \frac{v_0 \gamma - u_0 f_y}{f_x^2 f_y} & -\frac{\gamma(v_0 \gamma - u_0 f_y)}{f_x^2 f_y^2} - \frac{v_0}{f_y^2} & \frac{(v_0 \gamma - u_0 f_y)^2}{f_x^2 f_y^2} + \frac{v_0^2}{f_y^2} + 1 \end{bmatrix}. \quad (6)$$

Note that  $B$  is symmetric, defined by a 6D vector  $b = [B_{11}, B_{12}, B_{22}, B_{13}, B_{23}, B_{33}]^T$ .

Let the  $i$ th column vector of  $H$  be  $h_i = [h_{i1}, h_{i2}, h_{i3}]^T$ ; then we have

$$h_i^T B h_j = v_{ij}^T b \quad (7)$$

with  $v_{ij} = [h_{i1} h_{j1}, h_{i2} h_{j1} + h_{i1} h_{j2}, h_{i2} h_{j2}, h_{i3} h_{j1} + h_{i1} h_{j3}, h_{i3} h_{j2} + h_{i2} h_{j3}, h_{i3} h_{j3}]^T$ .

Therefore, (5) can be expressed by the following equation:

$$\begin{bmatrix} v_{12}^T \\ v_{11} - v_{22} \end{bmatrix} b = 0. \quad (8)$$

If  $n$  images of the model plane are observed, by stacking  $n$  such equations as (8), we have

$$Vb = 0, \quad (9)$$

where  $V$  is a  $2n \times 6$  matrix. If  $n > 3$ , we will have in general a unique solution  $b$  defined up to a scale factor.

Once  $b$  is estimated, we can compute all camera intrinsic parameters. The matrix  $B$  is estimated up to a scale factor, that is,  $B = \lambda A^{-T} A^{-1}$ , with  $\lambda$  being an arbitrary scale. Without difficulty, we can uniquely extract the intrinsic parameters from matrix  $B$ . Once  $A$  is known, the extrinsic parameters for each image are readily computed. From (4), we have

$$r_1 = \lambda A^{-1} h_1,$$

$$r_2 = \lambda A^{-1} h_2,$$

$$\begin{aligned} r_3 &= r_1 \times r_2, \\ t &= \lambda A^{-1} h_3, \end{aligned} \quad (10)$$

where  $\lambda = 1/\|A^{-1}h_1\| = 1/\|A^{-1}h_2\|$ .

**2.2. Maximum-Likelihood Estimation.** In general case, the distortion of lens cannot be ignored. Therefore, in the second step, the intrinsic and extrinsic parameters derived in the first step are regarded as the initial values to execute optimization.

We are given  $n$  images of a 2D planar plane and there are  $m$  points on the planar plane. Assume that the image points are corrupted by independent and identically distributed noise. For different point on a planar plane, the initial values of distortion coefficients  $k_1, k_2$  can be solved from (2) by the least square method. The detailed process can refer to the technical report [16].

These initial values including the intrinsic and extrinsic parameters and the distortion coefficients are substituted into the objective function to optimize camera. The maximum-likelihood estimate can be obtained by minimizing the following function:

$$\sum_{i=1}^n \sum_{j=1}^m \left\| m_{ij} - \tilde{m}(A, k_1, k_2, R_i, T_i, M_j) \right\|^2, \quad (11)$$

where  $\tilde{m}(A, k_1, k_2, R_i, T_i, M_j)$  is the projection of point  $M_j$  in image  $i$  according to (4).

Minimizing (11) is a nonlinear minimization problem, which is solved with the Levenberg-Marquardt algorithm [17]. It requires an initial guess of  $A, [R_i, t_i]$  ( $i = 1, \dots, n$ ), which can be obtained using the technique described in the previous section.

Through the above two steps, the intrinsic and extrinsic parameters including nonlinear distortion coefficients of camera are all achieved.

### 3. Zhang's Calibration-Based DIC Deflection Monitoring Method

The DIC method is widely used to measure the surface displacement or strain according to the correlation of light intensity of speckles before and after deformation, which are distributed on specimen surface randomly [18]. When the DIC method is employed to detect deformation, a single CCD camera is usually required to be perpendicular to the measured surface and the angle between the optical axis of CCD camera and the vertical line of measured surface cannot be larger than  $5^\circ$  [18]. In engineering, the angle between the optical axis of CCD camera and the vertical line of measured surface is often larger than  $5^\circ$ . As a result, the DIC method cannot be directly used to measure deformation when the skew angle is larger than  $5^\circ$ . To deal with this problem, Zhang's calibration algorithm is introduced to figure out strict limit of the skew angle of CCD camera. Furthermore, Zhang's calibration algorithm can eliminate lens distortion and convert measurement unit.

**3.1. Principle of DIC.** The correlation criterion needs to be firstly confirmed when the DIC method is used to calculate deformation. The zero-mean normalized cross-correlation (ZNCC) criterion has the most robust noise-proof performance and is insensitive to the linear scale and offset in lighting on images. Considering the requirement of actual application, the ZNCC criterion is chosen to conduct area matching in this paper. The ZNCC criterion is given as follows [19]:

$$C_{\text{ZNCC}} = \frac{\sum_{x=-M}^M \sum_{y=-M}^M [f(x, y) - \bar{f}] \cdot [g(x^*, y^*) - \bar{g}]}{\sqrt{\sum_{x=-M}^M \sum_{y=-M}^M [f(x, y) - \bar{f}]^2} \cdot \sqrt{\sum_{x=-M}^M \sum_{y=-M}^M [g(x^*, y^*) - \bar{g}]^2}}, \quad (12)$$

where  $f(x, y)$  is the gray value of reference image subset,  $g(x^*, y^*)$  is the gray value of target image subset, and  $\bar{f}, \bar{g}$  are the mean gray of reference image subset and target image.

The conics fitting method is used to conduct subpixel search in this paper. Assume that the pixel position of a point whose absolute value is the largest in the matrix of correlation criterion  $C_{\text{ZNCC}}$  is  $Q(x_0, y_0)$ . Total nine points composed of point  $Q$  and its eight nearest-neighbor points can locally constitute the quadratic surface, and the surface equation is given as below:

$$\Phi(x, y) = ax^2 + by^2 + cxy + dx + ey + f. \quad (13)$$

Utilizing the pixel positions of nine points and the correlation coefficients of corresponding positions, the values of  $a \sim f$  in (13) can be solved, and the extreme point coordinates

of surface can be obtained, that is,  $((ce - 2bd)/(4ab - c^2), (cd - 2ae)/(4ab - c^2))$ . This extreme point is exactly the center of subset on the deformed image; the center coordinate's difference between the reference image and the deformed image is just the displacement of point  $Q$ , whose unit is pixel.

Before test, the traditional DIC method needs to paste the scale whose length is known on the measured surface for converting measurement unit from pixel into millimeter. In most cases, the scale may be the coordinate paper with a certain length or the geometry size of specimen. According to the ratio of the actual length of scale to the pixel length on image, the traditional DIC method can convert the measurement unit of displacement from pixel into millimeter.

**3.2. Displacement Calculation of Measured Point.** As shown in Figure 1, suppose that the coordinate of point  $P$  in the

world coordinate system  $O - X_w Y_w Z_w$  is  $(X_w, Y_w, Z_w)^T$ , and its coordinate in the camera system  $o - xyz$  is  $(x, y, z)^T$ . In the image coordinate system, the homogeneous image coordinate in millimeters is  $(X, Y, 1)^T$ , and the homogeneous image coordinate in pixels is  $(u, v, 1)^T$ . After subpixel search of DIC,  $(u, v, 1)^T$  has been given. As a result, the relation between  $(X, Y, 1)^T$  and  $(u, v, 1)^T$  can be described as follows [20]:

$$\begin{pmatrix} X \\ Y \\ 1 \end{pmatrix} = \begin{bmatrix} dX & 0 & -u_0 \times dX \\ 0 & dY & -v_0 \times dY \\ 0 & 0 & 1 \end{bmatrix} \begin{pmatrix} u \\ v \\ 1 \end{pmatrix}, \quad (14)$$

where  $dX$  and  $dY$  are the physical size of a pixel on  $x$ -axis and  $y$ -axis, respectively, in mm/pixel, and these two parameters are the intrinsic parameters.  $(u_0, v_0)^T$  is the coordinate of principal point, in pixels.

The relation between the coordinate  $(x, y, z)^T$  in the camera coordinate system and the homogeneous image coordinate in millimeters  $(X, Y, 1)^T$  is expressed as below:

$$\begin{pmatrix} x \\ y \\ z \end{pmatrix} = \begin{bmatrix} \frac{s}{f} & 0 & 0 \\ 0 & \frac{s}{f} & 0 \\ 0 & 0 & s \end{bmatrix} \begin{pmatrix} X \\ Y \\ 1 \end{pmatrix}, \quad (15)$$

where  $f$  is the focal length and  $s$  is the scale factor.

The coordinate  $(X_w, Y_w, Z_w)^T$  in the world coordinate system and the coordinate  $(x, y, z)^T$  in the camera system meet the following equation:

$$\begin{pmatrix} X_w \\ Y_w \\ Z_w \end{pmatrix} = R^{-1} \left( \begin{pmatrix} x \\ y \\ z \end{pmatrix} - T \right), \quad (16)$$

where  $R$  is the rotation matrix from the camera system into the world coordinate system and  $T$  is the translation matrix from the camera system into the world coordinate system.  $R$ ,  $T$  can be acquired by Zhang's calibration algorithm.

Equation (14) is substituted into (15), and (17) is given as below:

$$\begin{pmatrix} x \\ y \\ z \end{pmatrix} = \frac{s}{f} \begin{bmatrix} dX & 0 & -u_0 \times dX \\ 0 & dY & -v_0 \times dY \\ 0 & 0 & f \end{bmatrix} \begin{pmatrix} u \\ v \\ 1 \end{pmatrix}. \quad (17)$$

Combining (16) and (17), the coordinate  $(X_w, Y_w, Z_w)^T$  in the world coordinate can be solved from the homogeneous image coordinate in pixels  $(u, v, 1)^T$ .

In (17), the scale factor  $s$  must be obtained firstly. The value of  $s$  is related with the selection of world coordinate system. In this paper, the world coordinate system is established on the measured surface. The plane  $X_w Y_w$  of the world coordinate system coincides with the measured surface, and  $Z_w$  axis conforms to the right-handed coordinate system. Any three points in the world coordinate system are selected to

establish the plane equation, and the equation is described as follows:

$$Ax + By + Cz + D = 0, \quad (18)$$

where  $A$ ,  $B$ ,  $C$ ,  $D$  are the coefficients of plane equation.

Equation (17) can also be expressed by the equation set as follows:

$$\begin{aligned} x &= \frac{s(u - u_0)dX}{f}, \\ y &= \frac{s(v - v_0)dY}{f}, \\ z &= s. \end{aligned} \quad (19)$$

Equation (19) is substituted into (18);  $s$  can be given by the following equation:

$$s = \frac{-D}{A(u - u_0)(dX/f) + B(v - v_0)(dY/f) + C}. \quad (20)$$

Through the above calculation, the homogeneous image coordinate  $(u, v, 1)^T$  in pixels can be converted to the coordinate  $(X_w, Y_w, Z_w)^T$  in millimeters in the world coordinate system. Therefore, this paper implements the conversion of measurement unit from millimeters into pixels by Zhang's calibration algorithm.

The sketch map of target image acquired by each CCD camera is shown in Figure 2. The solid circle surrounded by a rectangle is exactly white spot in Figure 2, which is the target tracked by each CCD camera. The rectangle in Figure 2 is the matching subset extracted by DIC method, which is used for calculating deformation. Assume that the image coordinate of matching subset's center at  $t_0$  is  $(x_0, y_0)$ . Deformations are found on bridge under load, and the image coordinate of matching subset's center at  $t_i$  is  $(x_i, y_i)$ . Thereby, the displacement of measured point on bridge at  $t_i$  can be obtained by subtracting two coordinates, and the displacement equation is given by

$$\begin{aligned} \Delta x &= x_i - x_0, \\ \Delta y &= y_i - y_0, \end{aligned} \quad (21)$$

where  $\Delta x$  is the transverse displacement of measured point on bridge at  $t_i$  and  $\Delta y$  is the vertical displacement of measured point on bridge at  $t_i$ , which is exactly the bridge deflection in pixels.

Through the above conversion of measurement unit, the bridge deflection in millimeters can be acquired accordingly.

#### 4. Comparative Test of Calibration Algorithms

To testify effectiveness and feasibility of Zhang's calibration-based DIC deflection monitoring method proposed in this paper, the comparative test of two calibration methods is conducted in lab. One is Zhang's calibration algorithm and the other is the scale calibration adopted by traditional DIC method.

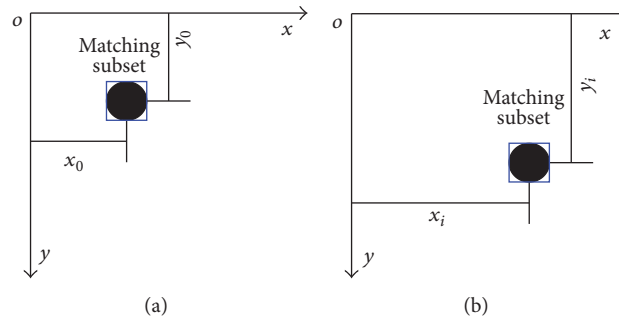


FIGURE 2: Schematic of change of target's position: (a) initial stage; (b) deformation stage.

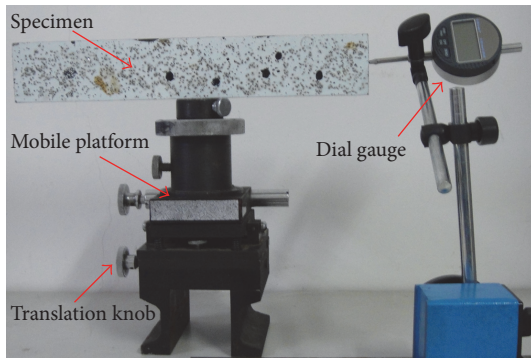


FIGURE 3: Experimental photo.

**4.1. Experimental Setup.** As illustrated in Figure 3, the specimen is 300 mm in length and 50 mm in width. The specimen surface is coated with white paint, and some silicon carbides sprayed randomly on white paint are regarded as speckles. The specimen is fixed on the mobile platform, the translation knob in Figure 3 can control the horizontal movement of specimen, and the moving range from left to right is 20 mm.

To compare with the detection results of the proposed method in this paper, the dial gauge is pressed against the measured specimen. The measurement range of dial gauge is 25 mm, and the precision is 0.001 mm. The measured specimen moved horizontally along with the mobile platform; each movement distance is about 1 mm. In test, the dial gauge read is recorded and the specimen image is simultaneously captured by CCD camera along with each rotation of translation knob. The CCD camera is placed 1 m away from the specimen. The cameras can record the high-definition images with a pixel resolution of  $1280 \times 960$  at 1 fps. The CCD camera is equipped with an optical zoom lens of F1.8–16 and focal length ranging between 12 and 36 mm.

During test, both Zhang's calibration algorithm and scale calibration are adopted to convert the measurement unit of horizontal displacement in this paper. The scale selected by the traditional DIC method is the actual length of specimen, which is 300 mm, and the corresponding length in image is 647.93 pixels. Therefore, the scale factor between actual size and pixel size is 0.4630 mm/pixel, and this value is exactly the conversion coefficient of measurement unit used by the traditional DIC method.

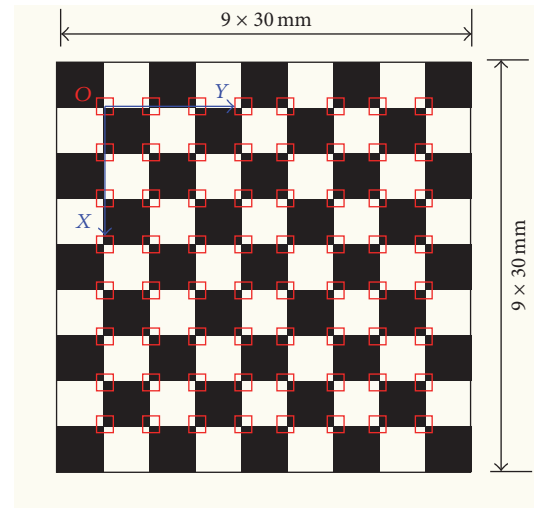


FIGURE 4: Planar pattern.

As shown in Figure 4, a planar pattern consisting of eighty-one  $30 \text{ mm} \times 30 \text{ mm}$  black and white squares is used to calibrate CCD camera. The open software "Camera Calibration Toolbox for MATLAB" [21], which is compiled according to Zhang's algorithm based on a planar pattern, is employed to execute the camera calibration in this paper. Before test, 9 images of the planar pattern in different postures are firstly captured by the CCD camera for camera calibration. Then,  $8 \times 8$  corner points on each image, which are expressed by the red rectangle in Figure 4, are selected to execute camera calibration by the calibration software. Finally, the intrinsic and extrinsic parameters including nonlinear distortion coefficients of CCD camera are all obtained by the calibration software.

**4.2. Experimental Result Analysis.** The displacement curves acquired by two different calibration algorithms are shown in Figure 5. It can be seen that two displacement curves have the same trend and agree very well. The displacement data obtained by dial gauge are regarded as the truth-value of displacement in this paper, and the displacement errors of the other two calibration algorithms are analyzed accordingly.

Figure 6 gives the absolute error and relative error curves of two calibration algorithms. As can be seen from Figure 6, the displacement precision of the proposed method is higher

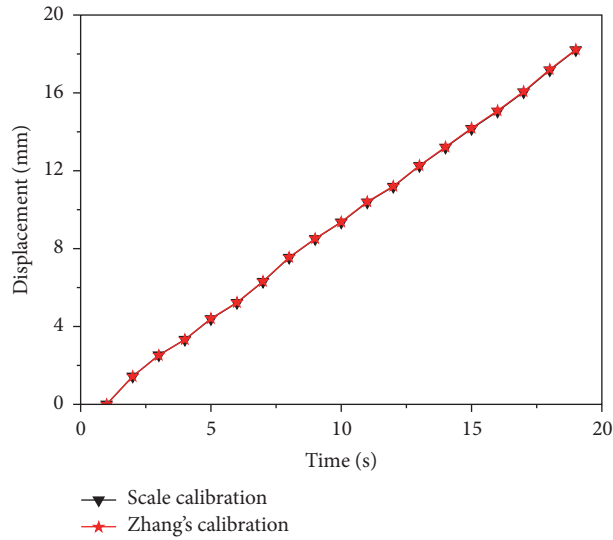


FIGURE 5: Displacement measurement results of two calibration methods.

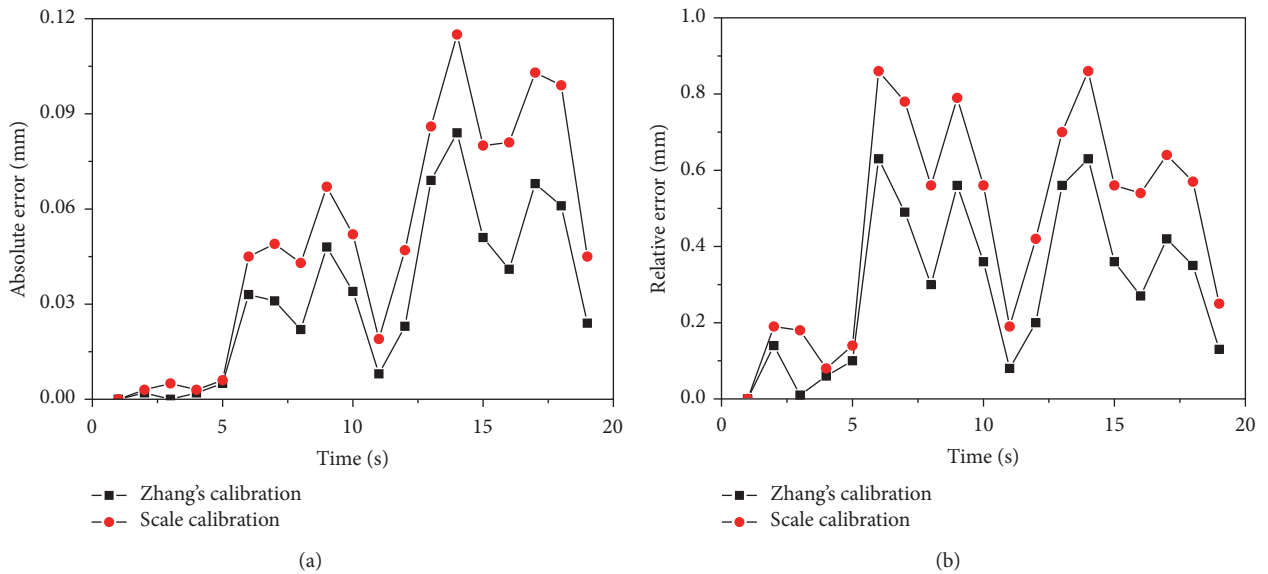


FIGURE 6: Error analysis of two calibration algorithms: (a) absolute error curve and (b) relative error curve.

that of traditional DIC method. The mean absolute error of displacement measured by the DIC method based on Zhang's calibration is 0.033 mm, and the relative error is floated at 0.5%. The mean absolute error of displacement detected by the DIC method based on scale calibration is 0.050 mm, and the relative error is larger than that of the former.

Results of comparative test of two calibration algorithms indicate that Zhang's calibration-based DIC deflection monitoring method has higher precision, and this testifies effectiveness and feasibility of the proposed method in this paper.

### 5. Deflection Monitoring for Songjiazhuang Cloverleaf Junction

Songjiazhuang cloverleaf junction is located on G309 National Highway, Zibo city, Shandong province. The total length of

bridge is 670.06 m. The superstructures of bridge are 22 m × 30 m prestressed concrete simply supported box beams and have 12 box girders in the transverse direction. The substructures of bridge are column piers and bored pile foundation. The deck width is 32 m, and the layout of deck is 0.5 m + 15 m + 1 m + 15 m + 0.5 m; it is a six-lane two-way bridge. The bridge was opened to traffic in 2005. The monitored bridge in this paper is crossing through Jiaozhou-Jinan railway, which is located under Songjiazhuang cloverleaf junction.

**5.1. Monitoring Scheme.** According to the deflection monitoring requirement of Songjiazhuang cloverleaf junction, the midspan deflections of the 3rd, 4th, 9th, and 10th box girders need to be detected (see Figure 7). Four targets are installed on the midspan position of the 3rd, 4th, 9th, and 10th box girders. As shown in Figure 7(b), every two CCD cameras are mounted on the middle pier of corresponding deck for

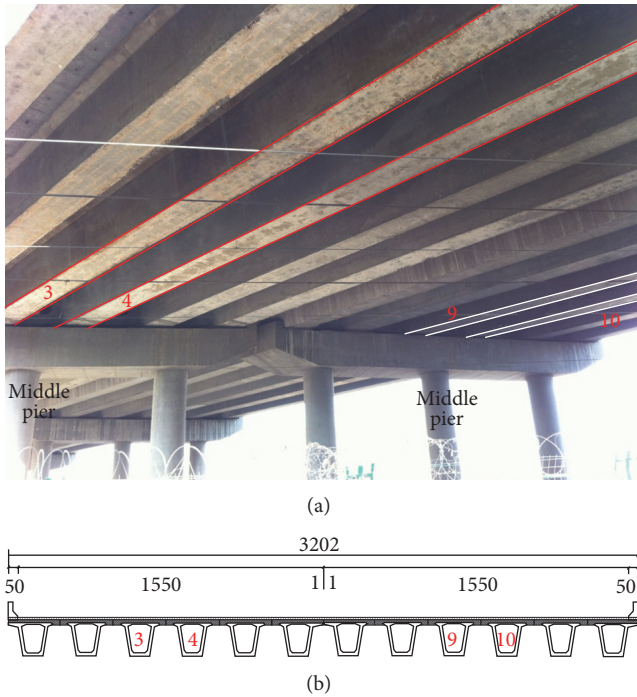


FIGURE 7: Box girder of Songjiazhuang cloverleaf junction. (a) Photo; (b) profile.

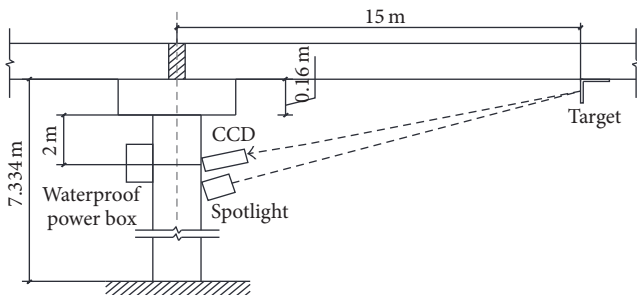


FIGURE 8: Installation location of CCD along longitudinal direction.

monitoring respective target and recording target image at each time.

As illustrated in Figure 8, a CCD camera is put 2 m away from the lower surface of the cap beam. The horizontal distance between each CCD camera and the corresponding target is about 15 m. In addition, the distance between the middle pier and the nearest box girder is 1.35 m under each deck. Thereby, the distance between each CCD camera and the corresponding target is about 15.19 m. For making CCD camera capture clear images, a spotlight is installed below each CCD camera and is used to provide illumination for the corresponding CCD camera at night.

Four targets are separately installed on the midspan position of 3rd, 4th, 9th, and 10th box girders, and the vertical surface of each target is perpendicular to the corresponding box girder (see Figure 8). Each target is made of stainless steel with 10 mm depth and is bent up to 90°. As shown in Figure 9, both the length and width of target's vertical surface

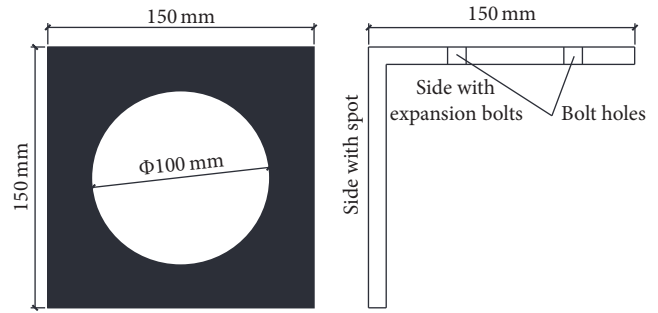


FIGURE 9: Schematic diagram of circular target.

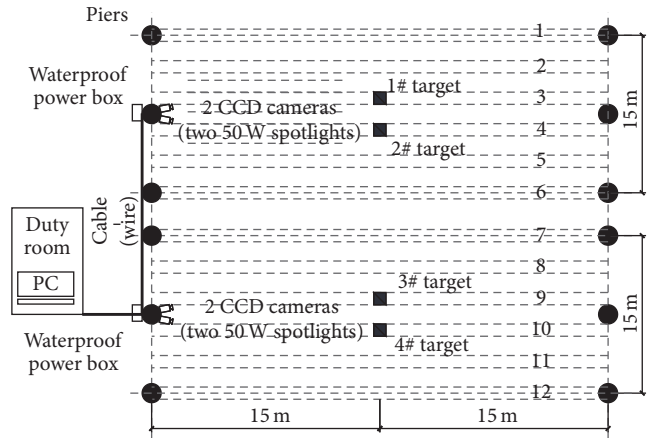


FIGURE 10: Schematic diagram of deflection monitoring system for Songjiazhuang cloverleaf junction.

are 150 mm, and the size of target's horizontal surface is same as that of vertical surface. The horizontal surface of target is fixed on the midspan position of corresponding box girder with expansion bolts. The background color of target is black, and there exists a white solid circle on the center of vertical surface, which is 100 mm in diameter. This white circle is exactly the target tracked by CCD camera at different time.

5.2. Deflection Monitoring System Based on CCD Cameras.

Based on the deflection monitoring scheme for Songjiazhuang cloverleaf junction, the corresponding deflection monitoring system for Songjiazhuang cloverleaf junction is integrated in this paper. As shown in Figure 10, the deflection monitoring system for Songjiazhuang cloverleaf junction includes a computer, CCD cameras, lenses, spotlights, and targets. The computer is the core of deflection monitoring system, which is placed in the duty room and controls the operation of deflection monitoring system. Considering the long-term requirement of deflection monitoring for Songjiazhuang cloverleaf junction, the computer chooses 8 GB memory, 1862 GB hard disk capacities. The computer's motherboard contains 5 cable interfaces, and four interfaces are connected to four CCD cameras through network cable.

The type of CCD camera used for monitoring deflection is AVT Company's GT1290, which utilizes network cable to transmit image. The CCD camera has the image resolution

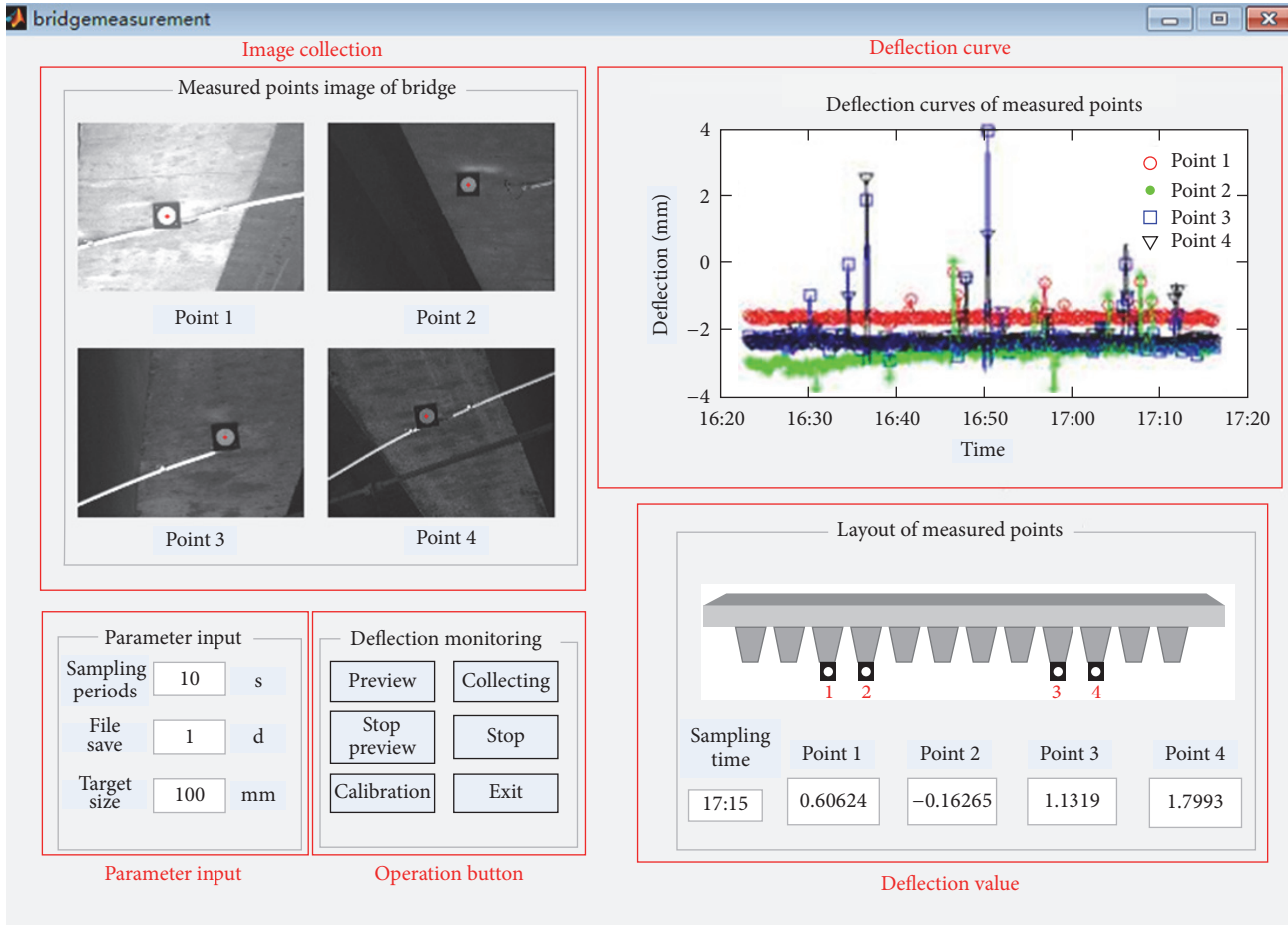


FIGURE 11: Deflection monitoring software interface for Songjiazhuang cloverleaf junction.

of 1280 × 960 and the sample frequency of 1 Hz. The CCD camera is set to shoot black and white images when monitoring deflection, and its range of operating temperature is -20°C–60°C. The lens with 50 mm focal length is employed to capture clear target images when the object distance is farther, which is made in Computar Company. Moreover, it is noted that the white circle on target should always appear in the field of view (FOV) of camera within the allowable range of bridge deflection.

Based on the deflection monitoring scheme for Songjiazhuang cloverleaf junction, the deflection monitoring software for Songjiazhuang cloverleaf junction is compiled by MATLAB. This deflection monitoring software is a stand-alone executable program. Running the deflection monitoring software for Songjiazhuang cloverleaf junction only needs installing MCRInstaller, which is the dynamic linking library (DLL) of MATLAB; no MATLAB compiler needs to be installed. The deflection monitoring software for Songjiazhuang cloverleaf junction has functions such as image preview, image collection, camera calibration, deflection display, and data storage.

As illustrated in Figure 11, the software interface includes five functional zones, namely, image collection, parameter input, operation button, deflection curve, and value display. For the convenience of adjusting the FOV size of CCD

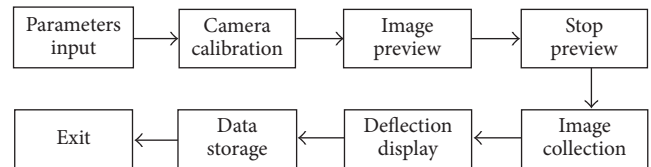


FIGURE 12: Operation flowchart of deflection monitoring software for Songjiazhuang cloverleaf junction.

cameras, the area of image collection in software interface can display the FOV of four CCD cameras in real time. The areas of parameter input and operation button are the core part of deflection monitoring software, which are used for controlling image acquisition and processing. The area of deflection curve and value display can show deflection curves and calculate deflection values in real time. The operation flowchart of deflection monitoring software for Songjiazhuang cloverleaf junction is given in Figure 12.

**5.3. In Situ Deflection Monitoring Results.** The *in situ* deflection data of Songjiazhuang cloverleaf junction are shown in Figure 13. Three deflection curves measured on Sep. 10–17, 2014; Oct. 9–17, 2014; and Oct. 20–28, 2014, are given in this paper, and the time period of each curve is one week.

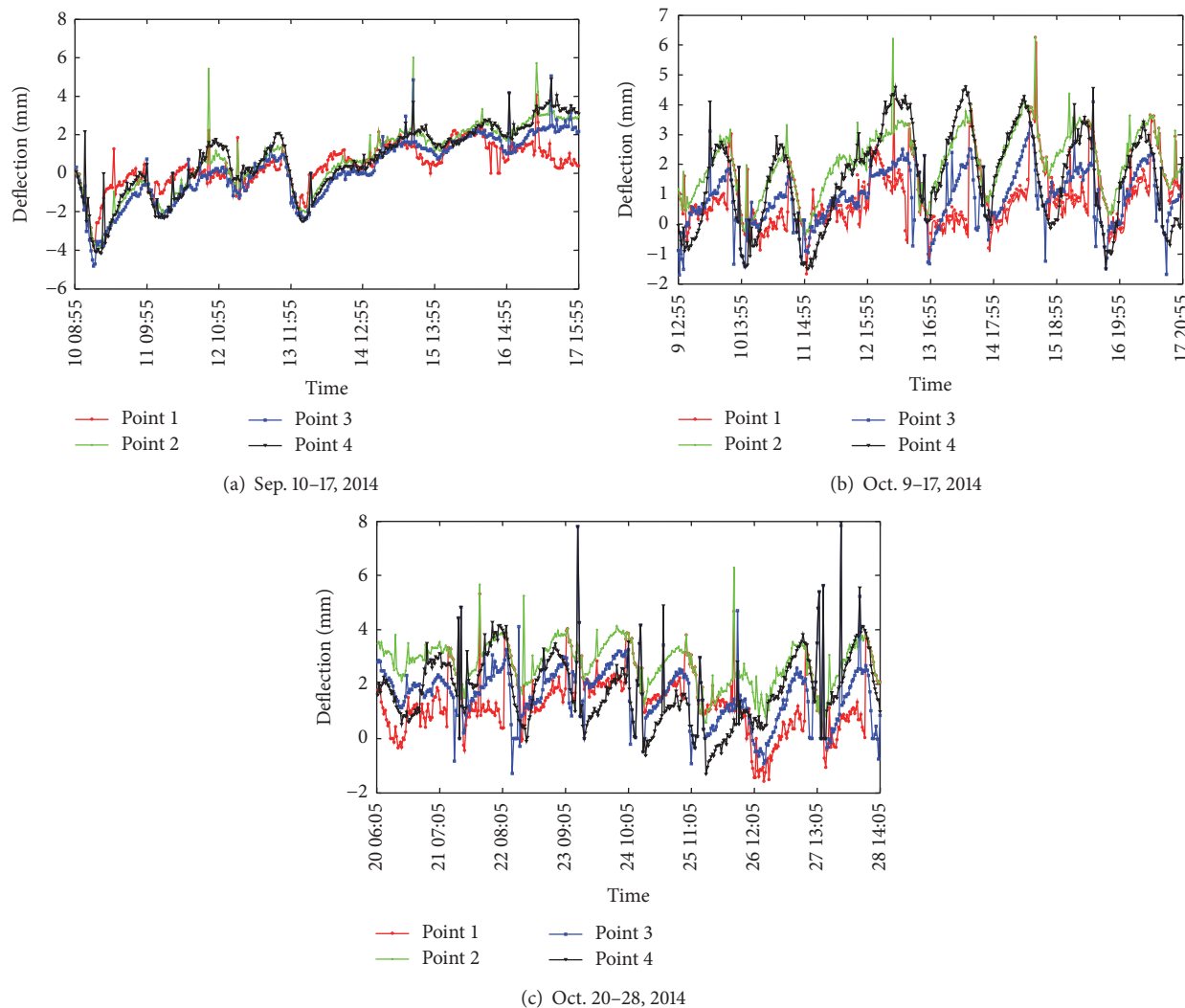


FIGURE 13: *In situ* deflection curves of Songjiazhuang cloverleaf junction.

As can be seen from Figure 13, the deflection curves of 4 measured points in each subgraph have jitters. The reason of jitters is vehicles passing across the bridge deck. However, the deflection curves' trends of four measured points are basically consistent. The trend consistency of four deflection curves indicates that four CCD cameras can work stably on site and the proposed method can accurately measure the deflection deformations of bridge, and the bridge works in the good condition. Experimental results verify the reliability of the proposed method, indicating that the proposed deflection monitoring method in this paper can meet the long-term requirements of bridge deflection.

## 6. Conclusions

Aiming at meeting the requirement of deflection monitoring for Songjiazhuang cloverleaf junction, Zhang's calibration-based DIC deflection monitoring method is proposed in this paper. According to the proposed method, the deflection monitoring software is developed by MATLAB, and

4-channel CCD deflection monitoring system for Songjiazhuang cloverleaf junction is integrated accordingly. The *in situ* deflection data show that deflection curves of four measured points have the consistent trends, and this suggests that Songjiazhuang cloverleaf junction works in good condition, and the proposed deflection monitoring method in this paper is reliable and accurate. Compared with other deflection measurement methods, the proposed method is simple to operate and costs less and is convenient to conduct automatic measurement and long-term monitoring. This proves that this method will have the broad application foreground in engineering.

## Competing Interests

The authors declare that they have no competing interests.

## Acknowledgments

This study is supported by the National Natural Science Foundation of China under Grants nos. 51478148 and 51408261, the

Natural Science Foundation of Heilongjiang under Grant no. E201434, and the foundation of Harbin City under Grant no. 2015RAQXJ028.

## References

- [1] S. Sumitro, Y. Matsui, M. Kono, T. Okamoto, and K. Fujii, "Long span bridge health monitoring system in Japan," in *Health Monitoring and Management of Civil Infrastructure Systems*, vol. 4337 of *Proceedings of SPIE*, pp. 517–524, Newport Beach, Calif, USA, March 2001.
- [2] C. M. Tse and H. Baki Iz, "Deflection of the vertical components from GPS and precise leveling measurements in Hong Kong," *Journal of Surveying Engineering*, vol. 132, no. 3, pp. 97–100, 2006.
- [3] M. Scherer and J. L. Lerma, "From the conventional total station to the prospective image assisted photogrammetric scanning total station: Comprehensive review," *Journal of Surveying Engineering*, vol. 135, no. 4, pp. 173–178, 2009.
- [4] M. Arraigada, M. N. Partl, S. M. Angelone, and F. Martinez, "Evaluation of accelerometers to determine pavement deflections under traffic loads," *Materials and Structures*, vol. 42, no. 6, pp. 779–790, 2009.
- [5] C. R. Farrar, T. W. Darling, A. Migliori, and W. E. Baker, "Microwave interferometers for non-contact vibration measurements on large structures," *Mechanical Systems and Signal Processing*, vol. 13, no. 2, pp. 241–253, 1999.
- [6] G. W. Roberts, C. Emily, X. Meng, and A. Dodson, "High frequency deflection monitoring of bridges by GPS," *Journal of Global Positioning Systems*, vol. 3, no. 1-2, pp. 226–231, 2004.
- [7] Y. Liu, Y. Deng, and C. S. Cai, "Deflection monitoring and assessment for a suspension bridge using a connected pipe system: a case study in China," *Structural Control and Health Monitoring*, vol. 22, no. 12, pp. 1408–1425, 2015.
- [8] P. Olaszek, "Investigation of the dynamic characteristic of bridge structures using a computer vision method," *Measurement*, vol. 25, no. 3, pp. 227–236, 1999.
- [9] Q. Yu, X. Ding, Z. Lei, and P. Huang, "Optical measurement system for bridge displacement and vibration," in *Third International Conference on Experimental Mechanics*, vol. 4537 of *Proceedings of SPIE*, pp. 174–177, Beijing, China, 2002.
- [10] S. Yoneyama, A. Kitagawa, S. Iwata, K. Tani, and H. Kikuta, "Bridge deflection measurement using digital image correlation," *Experimental Techniques*, vol. 31, no. 1, pp. 34–40, 2007.
- [11] J. Chen, G. Jin, and L. Meng, "Applications of digital correlation method to structure inspection," *Tsinghua Science and Technology*, vol. 12, no. 3, pp. 237–243, 2007.
- [12] B. Shan, S. Zheng, and J. Ou, "Free vibration monitoring experiment of a stayed-cable model based on stereovision," *Measurement*, vol. 76, no. 12, pp. 228–239, 2015.
- [13] R. Hartley and A. Zisserman, *Multiple View Geometry in Computer Vision*, Cambridge University Press, Cambridge, UK, 2nd edition, 2003.
- [14] Z. Y. Zhang, "A flexible new technique for camera calibration," *IEEE Transactions on Pattern Analysis and Machine Intelligence*, vol. 22, no. 11, pp. 1330–1334, 2000.
- [15] J. Weng, P. Cohen, and M. Herniou, "Camera calibration with distortion models and accuracy evaluation," *IEEE Transactions on Pattern Analysis and Machine Intelligence*, vol. 14, no. 10, pp. 965–980, 1992.
- [16] Z. Y. Zhang, "A flexible new technique for camera calibration," Tech. Rep. MSR-TR-98-71, Microsoft Research, 1999, <http://research.microsoft.com/en-us/um/people/zhang/Calib/>.
- [17] J. More, *The Levenberg-Marquardt Algorithm, Implementation and Theory, Numerical Analysis*, Springer, Berlin, Germany, 1977.
- [18] A. S. Michael, R. M. Stephen, D. H. Jeffrey, and Y. J. Chao, "Advances in two-dimensional and three-dimensional computer vision," *Topics in Applied Physics*, vol. 77, no. 1, pp. 323–372, 2000.
- [19] H. A. Bruck, S. R. McNeill, M. A. Sutton, and W. H. Peters III, "Digital image correlation using Newton-Raphson method of partial differential correction," *Experimental Mechanics*, vol. 29, no. 3, pp. 261–267, 1989.
- [20] G. Fu and A. G. Moosa, "An optical approach to structural displacement measurement and its application," *Journal of Engineering Mechanics*, vol. 128, no. 5, pp. 511–520, 2002.
- [21] J. Y. Bouguet, Camera calibration toolbox for Matlab, <http://www.vision.caltech.edu/bouguetj/index.html>.

## Research Article

# Experimental Research on Quick Structural Health Monitoring Technique for Bridges Using Smartphone

Xuefeng Zhao,<sup>1,2,3</sup> Kwang Ri,<sup>1,2,3,4</sup> Ruicong Han,<sup>1,2,3</sup> Yan Yu,<sup>5</sup>  
Mingchu Li,<sup>6</sup> and Jinping Ou<sup>1,2,3,7</sup>

<sup>1</sup>School of Civil Engineering, Dalian University of Technology, Dalian 116024, China

<sup>2</sup>State Key Laboratory of Coastal and Offshore Engineering, Dalian University of Technology, Dalian 116024, China

<sup>3</sup>Research Center of Structural Smartphone Cloud Monitoring, Dalian University of Technology, Dalian 116024, China

<sup>4</sup>School of Civil Engineering, Pyongyang University of Architecture, Pyongyang 1001, Democratic People's Republic of Korea

<sup>5</sup>School of Electronic Science and Technique, Dalian University of Technology, Dalian 116000, China

<sup>6</sup>School of Software Technology, Dalian University of Technology, Dalian 116000, China

<sup>7</sup>School of Civil Engineering, Harbin Institute of Technology, Harbin 150000, China

Correspondence should be addressed to Xuefeng Zhao; zhaoxf@dlut.edu.cn

Received 19 May 2016; Accepted 25 September 2016

Academic Editor: Chunhui Yang

Copyright © 2016 Xuefeng Zhao et al. This is an open access article distributed under the Creative Commons Attribution License, which permits unrestricted use, distribution, and reproduction in any medium, provided the original work is properly cited.

In the recent years, with the development and popularization of smartphone, the utilization of smartphone in the Structural Health Monitoring (SHM) has attracted increasing attention owing to its unique feature. Since bridges are of great importance to society and economy, bridge health monitoring has very practical significance during its service life. Furthermore, rapid damage assessment of bridge after an extreme event such as earthquake is very important in the recovery work. Smartphone-based bridge health monitoring and postevent damage evaluation have advantages over the conventional monitoring techniques, such as low cost, ease of installation, and convenience. Therefore, this study investigates the implementation feasibility of the quick bridge health monitoring technique using smartphone. A novel vision-based cable force measurement method using smartphone camera is proposed, and, then, its feasibility and practicality is initially validated through cable model test. An experiment regarding multiple parameters monitoring of one bridge scale model is carried out. Parameters, such as acceleration, displacement, and angle, are monitored using smartphone. The experiment results show that there is a good agreement between the reference sensor and smartphone measurements in both time and frequency domains.

## 1. Introduction

With the advances in sensor and computer technologies in the recent years, Structural Health Monitoring (SHM) has developed rapidly and has become a major research field in civil engineering, which provides a useful diagnostic tool for ensuring integrity and safety, detecting damage, and evaluating performance deterioration of civil infrastructures [1–3]. SHM systems have undergone significant development and been widely utilized on infrastructures, especially bridge structures [4, 5]. Present SHM systems have been mainly installed on some of large-scale structures or major construction projects with great significance [6], such as long-span bridges, due to the financial problems and

practical difficulties associated with instrumentation and monitoring.

Generally, there is possibility for the civil structures to be subjected to severe loadings during their service life owing to extreme disaster such as earthquake and typhoon, which causes serious damage to the integrity of the structures. When an extreme disaster occurs, the rapid damage detection of bridges will be helpful for the quick evaluation of transportation networks for the emergency response [7]. Although the SHM system installed on bridge provides real-time information for damage assessment after a disaster, not all bridges have been installed with the SHM system. Furthermore, the installed SHM systems can be easily destroyed in the disaster. Therefore, it is necessary to develop quick

SHM technique for rapid structure response monitoring and safety assessment, which will provide preliminary damage evaluation result before time-consuming common inspection can be conducted. The rapid SHM technique based on ubiquitous smartphone with built-in sensors would make it possible for personnel to evaluate initial damage and safety status quickly, because of its features such as low cost, ease of installation, and convenience.

Several researchers studied the monitoring ability of smartphones through laboratory and field tests and confirmed the potential usage of smartphones in the health monitoring of civil infrastructures. Yu et al. [8] proposed a new idea for mobile SHM using smartphone built-in sensors or external sensors board for the first time, carried out preliminary test to validate its feasibility and implementation, and then mentioned that mobile SHM system based on public participant under emergency condition is possible because of its features such as low cost and popularization. Morgenthal and Höpfner [9] investigated the effect of sampling rate on acceleration measurement. Android device (version 2.3) recorded acceleration data of shaking table with a sampling rate of 27 Hz under excitations of different frequencies. It was found that the vibration responses could not be accurately obtained for measuring vibration above Nyquist frequency of smartphone built-in accelerometer. Reilly et al. [10] developed a mobile application iShake using smartphones as seismologic sensors, which is possible for smartphones to measure and transmit ground motion data to a central server, and validated the accuracy of smartphone built-in sensors for seismic sensing application through shaking table tests. Sharma and Gupta [11] studied the use of smartphone in civil engineering and measured various field parameters including absolute location, distance, area, and perimeter using smartphone GPS receiver and also evaluated noise pollution using microphone of smartphone. Cimellaro et al. [12] developed multiple platforms including smartphones and Internet for rapid building damage assessment after a seismic event, which collected photos of damaged houses taken by residents or volunteers in damaged area as the first emergency response information. Han et al. [13] measured cable force of cable-stayed bridge with accelerometer embedded in smartphone, which showed that it is appropriate to estimate the cable force from smartphone inner sensors limited in precision of measurement because cable is relatively distinct in vibration rather than the other structural elements. Yu et al. [14] proposed a combination method of external sensor board and smartphone by a serial port or Wi-Fi interface to improve measurement accuracy, integrated high-precision micro electromechanical system (MEMS) sensors, and then validated its accuracy through vibration test on a three-layer steel frame model. Feng et al. [15] and Ozer et al. [16] studied the utilization of accelerometers embedded in smartphone for measuring different types of vibration and validated its capability for SHM through vibration response test on a reinforced concrete pedestrian bridge. Tan and Chen [17] verified the sensitivity and accuracy of smartphone inner sensors for measuring different vibration patterns such as sinusoidal waves of various frequencies, sinusoidal sweep, and earthquake waves through shaking table tests.

Tests results demonstrated that the measurement accuracy of smartphones mainly depends on the type of vibration, the vibration directions, and the installation manner. Zhao et al. [18–20] performed the hoisting monitoring for structural members of bridge based on real-time monitoring information feedback between one controller smartphone and several collector smartphones and also developed displacement monitoring software D-Viewer, which enable monitoring of structural dynamic displacements by recognizing a laser spot centroid or predefined circle target via smartphone camera. Meanwhile, an international data sharing platform for cloud-SHM based on smartphone has been established, which is possible to upload the SHM data information collected by smartphone application Orion-CC and share with the public. Peng et al. [21] developed smartphone software E-Explorer using mobile Bluetooth communication technology to realize information delivery without any external network in the emergency events such as earthquake. As can be seen from the above studies, the research of SHM based on smartphone has developed rapidly and received considerable attention from numerous countries. Furthermore, it progresses from the previous single smartphone monitoring to multismartphones monitoring and from local monitoring to global data sharing, and the parameter has also expanded from acceleration as traditional measuring parameter to multiparameters such as displacement and angle.

This paper carries out a comprehensive experimental study on the major structural members of cable-stayed bridge including deck and cable to verify the feasibility of the utilization of smartphone in the quick bridge health monitoring. First, one novel cable force measurement method is proposed, which enables the estimation of cable force based on the recognition for cable vibration using smartphone camera. And then comprehensive monitoring test regarding multiple structural parameters such as accelerometer, displacement, and angle is conducted on the bridge deck. The test results demonstrate the feasibility, accuracy, and reliability of bridge health monitoring method using smartphones.

## 2. D-Viewer and Orion-CC

Smartphone application provides users with a tool for extracting structural performance parameters by various integrated sensors, processing data automatically, and transmitting data wirelessly to a central server. D-Viewer and Orion-CC (Orion-Cloud Cell) are typical iOS (iPhone Operating System) smartphone applications developed by our research group for Structural Health Monitoring using smartphone, which are currently available for free at the iTunes Store [22, 23].

*2.1. D-Viewer.* In SHM practice, the displacement monitoring of bridges has an important effect on the evaluation of the structural safety and the damage detection. Recently, the laser projection-sensing technology has attracted growing interest for monitoring displacement in the field of bridge health monitoring owing to its low cost and ease of operation over traditional measuring methods [24].

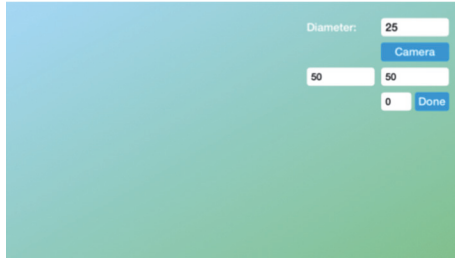


FIGURE 1: Initial setup interface.

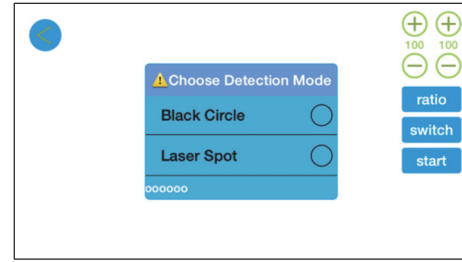


FIGURE 3: Interface of selecting a monitoring method.

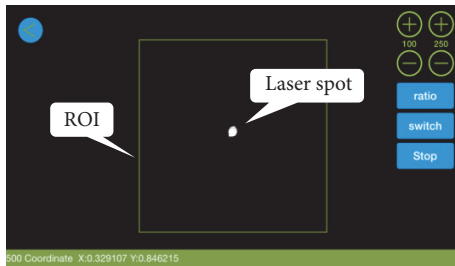


FIGURE 2: Monitoring interface.

D-Viewer is a smartphone application for monitoring structural dynamic displacement with the aid of laser device and projection plate. A laser device is installed on the monitored object, the movement of the laser spot shot on the projection plate is recognized by the camera of smartphone, and then the real-time structural displacement is obtained by means of image processing method. Figure 1 shows the initial setup interface. In this interface, the region of interest (ROI) and the function of front or rear camera can be selected for recognizing the movement of the laser spot; the diameter of a black circle as the calibration reference can be set to determine the ratio between the actual size and the pixel size of the black circle in advance. The interface of displacement monitoring is shown in Figure 2. Further details regarding operation guide and image processing method can be found in [18].

D-Viewer was designed to identify a black circle as well as the laser spot shot on the projection as shown in Figure 3; therefore, the structural static and dynamic displacements can be obtained easily by recognizing the movement of the preprinted black circle target attached on the structure using smartphone camera without laser device and projection plate, moreover, without professional expensive displacement sensors.

**2.2. Orion-CC.** Orion-CC was built for iOS 7.0 or higher platform, which can obtain not only acceleration and angle but also cable force by measuring structural vibration with the smartphone-embedded accelerometer and gyroscope. Figure 4 shows three screenshots of the iOS (iPhone Operating System) application interface, which enables users to interact with the smartphone sensors.

Orion-CC utilizes vibration method based on the iPhone built-in accelerometer to measure the cable force. In engineering application, the vibration method by which cable forces are estimated from measured frequency difference is often used for the measurement of cable forces due to its simplicity and speediness. In general, the frequency difference and the force calculation precision are influenced by mass, length, stiffness, and sag of the cable. Orion-CC uses the relationship between the frequency difference and cable force shown in (1), in which the effects of sag and stiffness are ignored to measure cable forces rapidly and conveniently using smartphone [25].

$$T = 4ml^2 (\Delta f)^2, \quad (1)$$

where  $m$  is the linear mass density,  $l$  is the cable length, and  $\Delta f$  is the frequency difference. The main function interface of cable force calculation is shown in Figure 5.

According to the cable vibrations, the power spectral density can be obtained from the acceleration time-history using FFT. And then the peak picking method is applied to extract the frequency difference from the power spectral density of the response acceleration. Finally, the cable force is estimated according to the cable length, cable linear density, and frequency difference. The interactive interface of Orion-CC reduces the need for professional training, as shown in Figures 4 and 5. Therefore, the cable force can be extracted directly and rapidly by the application Orion-CC without any professional inspection device and training. Orion-CC is a valuable tool for an actual application of Structural Health Monitoring (SHM) because the cable force measuring method by Orion-CC has many advantages over other measuring methods, such as economy, convenience, and ease of operation.

### 3. Vision-Based Cable Force Measuring Test

**3.1. Overview of Experiment.** As mentioned before, the structural static and dynamic displacements can be obtained easily by recognizing the movement of not only a laser spot but also a black circle target, by means of smartphone camera. Based on this fact, the cable force test on the model cable is conducted in order to investigate the feasibility of a novel vision-based cable force measuring method using smartphone.

The cable model is installed in the Bridge Lab of Dalian University of Technology. The model is a 15.53 m single

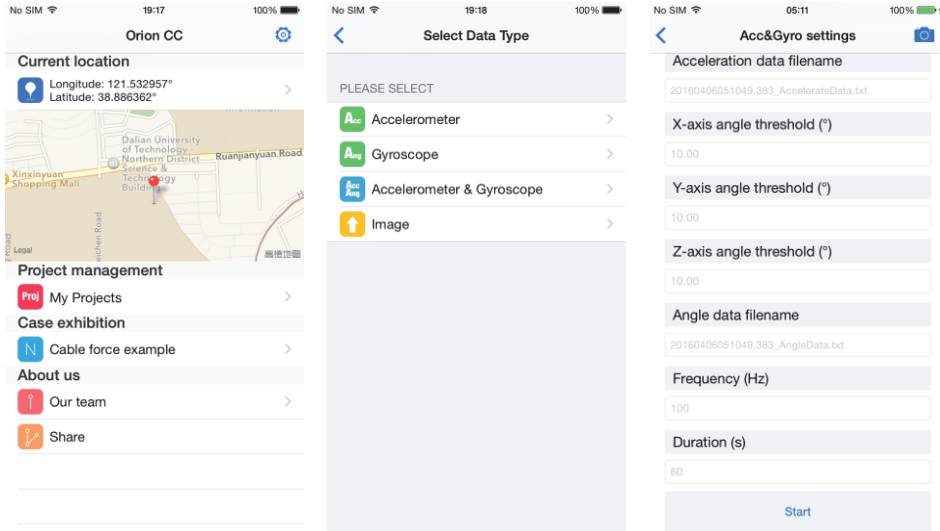


FIGURE 4: Main interface of Orion-CC.

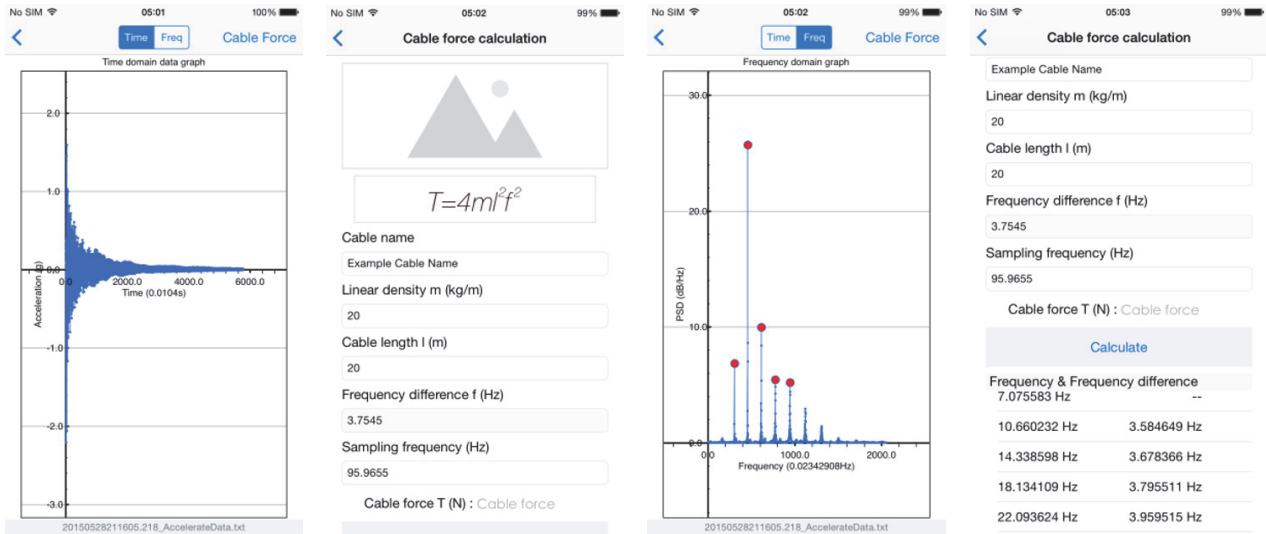


FIGURE 5: Main function interface of cable force calculation.

cable, and its linear mass density is 3.95 kg/m. As the smartphone for experiment, two smartphones, iPhone 6, are used; the one installed with APP D-Viewer is mounted on a tripod via double-sided adhesive tape in order to extract vibration characteristics of cable for determining cable force using smartphone camera, while the other installed with APP Orion-CC is fixed on the cable model via mobile phone jacket to obtain cable force using smartphone built-in accelerometer. An organic glass panel, on which there is a preprinted black circle, is attached to the model cable using superglue. The distance between smartphone and cable model is adjusted using the tripod according to the size of panel in order to ensure a whole white background. Figure 6 shows the installation of smartphones, and Table 1 shows the relevant parameters of iPhone 6 used in test [26].

Orion-CC is designed to collect data with a sampling rate of 100 Hz, and the sampling rate of D-Viewer is 30 Hz; namely,

it is the same as the frames per second (fps) of smartphone camera. Both of smartphones collect the vibration data of the cable simultaneously under the artificial excitation for one minute.

**3.2. Test Results.** Since the focus of this test is on the verification of feasibility of cable force measurement method using smartphone camera, the vibration data of the model cable acquired by Orion-CC and D-Viewer is analyzed using MATLAB. Figures 7 and 8 plot the acceleration and displacement time histories obtained, respectively, from D-Viewer and Orion-CC, together with corresponding PSD results.

As shown in figures, although the vibration amplitudes and PSD peak values are different due to the differences of sampling rate, measuring position, and measuring item, it is observed that the same frequency components can be accurately obtained by the different methods from both of

TABLE 1: Relevant parameters of iPhone 6.

Operating system	Display	Chips	Video recording	Sensors
IOS 9	Retina HD display 4.7-inch (diagonal) 1334-by-750-pixel resolution at 326 ppi 1400 : 1 contrast ratio (typical)	A8 chip with 64-bit architecture M8 motion coprocessor	1080 p HD video recording (30 fps or 60 fps)	Barometer Three-axis gyro Accelerometer Proximity sensor Ambient light sensor



FIGURE 6: The installation of smartphones.

smartphone applications. Moreover, it is noteworthy that the natural frequency of the first vibration mode for estimating cable force can be accurately obtained by the displacement response measurement of the cable using the application D-Viewer. In general, as the position at which smartphone is mounted is relatively low compared with the length of cable, the first peak in the corresponding PSD obtained by the vibration measurement of cable is not very clear, and thus it is usually difficult to identify the natural frequency of the first vibration mode for estimating cable force by the application Orion-CC using smartphone built-in accelerometer. As can be seen from Figure 8(b), it is impossible to extract the natural frequencies at the higher mode (above 15 Hz) by the application D-Viewer because of its low sampling rate. However, the result shows that the frequency components can be accurately obtained in the lower frequency domain, and it is clear that the fps of smartphone camera will be increased along with the improvement of smartphone performance in the future.

The frequency difference is obtained by means of peak picking method from PSD, and the cable force is determined from (1). Table 2 summarizes the frequency difference and cable force identified by two methods. As can be seen from Table 2, the cable forces obtained by D-Viewer and Orion-CC are highly comparable, with significantly small error of less than 1.1%. Therefore, it is concluded that vision-based cable

TABLE 2: Comparison of the results from Orion-CC and D-Viewer.

Item	Frequency difference (Hz)	Cable force (KN)
Orion-CC	3.72	52.466
D-Viewer	3.70	51.904
Error (%)	0.54	1.07

force measurement using smartphone camera is feasible in the sampling rate of 30 fps.

#### 4. Smartphone-Based Structural Health Monitoring Testing

*4.1. Overview of Experiment.* In order to investigate the implementation feasibility of the quick bridge health monitoring technique using smartphone, a comprehensive experiment is conducted for a laboratory-scale suspension bridge. The test focuses on the identification of natural frequency through the extraction of vibration response of different physical indices such as acceleration, displacement, and angle in different locations using smartphone application.

As the experiment object, a concrete self-anchored suspension bridge model, which is designed and constructed with 1/28 scale of Zhuanghe Construction Bridge located in Zhuanghe city of China shown in Figure 9, is selected in the Bridge Lab of Dalian University of Technology. This scale bridge model consists of a main span of 7.14 m, a box girder of reinforced concrete, main cables and hangers of twisted wire rope, and two towers.

To measure the dynamic characteristics of the bridge model, three smartphones and acceleration sensors are installed at mid span and one-quarter spans of the model via double-sided adhesive tape, respectively. The reference coordinate of smartphone for measuring vibration responses is shown in Figure 10.

Also the displacement monitoring system using smartphone, including a laser transmitter and a projection plate, is mounted on the bridge model to measure the displacement response of mid span. A sheet of A4 white paper, on which a black circle of 25 mm in diameter is preprinted, is attached to projection plate, and then the calibration is conducted in the initial setup interface for measuring. The laser transmitter is fixed at one end of the bridge model to remain stationary during experiment. To verify the accuracy of the displacement monitoring method based on the smartphone, a laser displacement sensor is fixed by means of steel frame at the

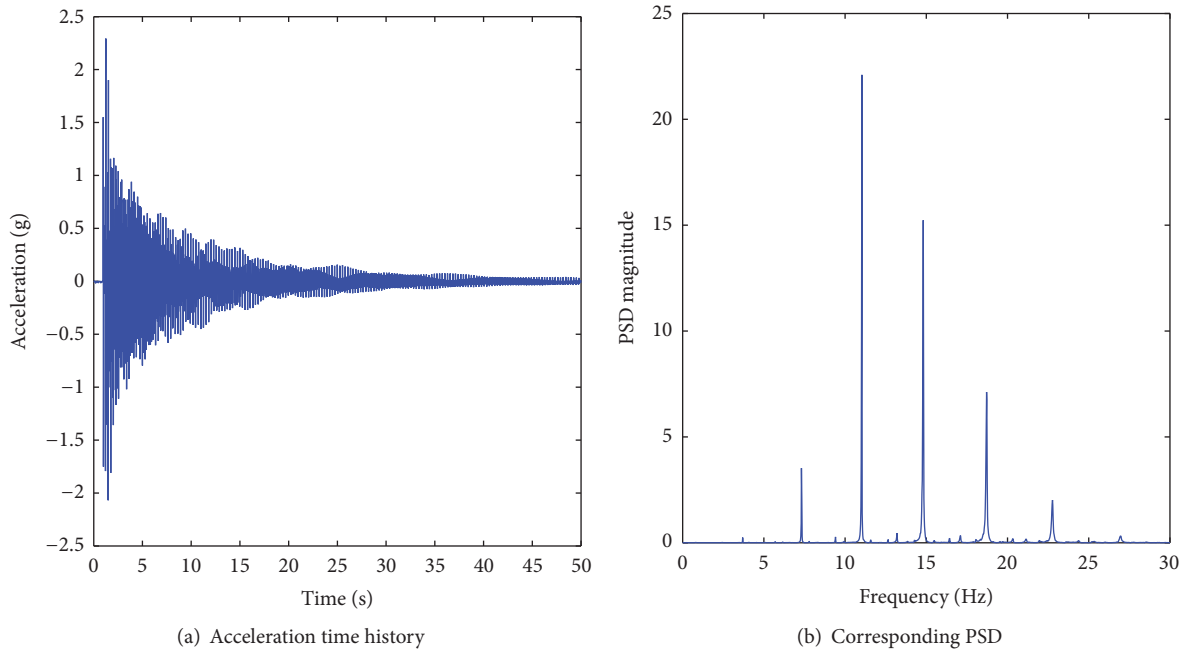


FIGURE 7: Results of Orion-CC.

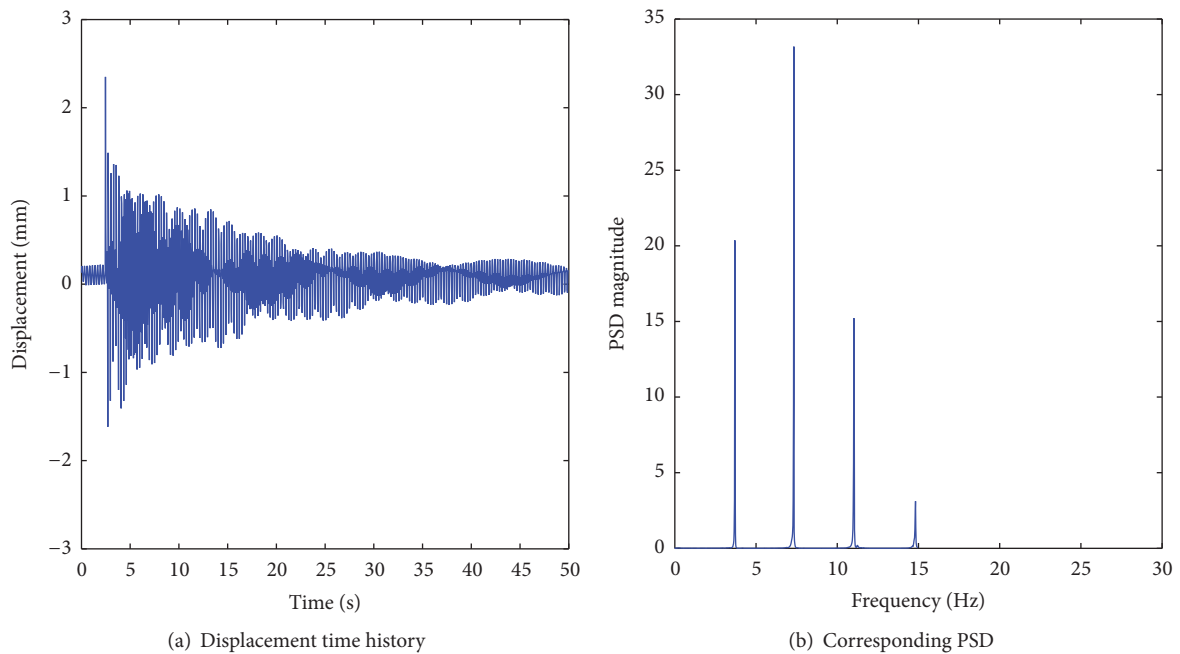


FIGURE 8: Results of D-Viewer.

mid span of the model. The main instrument parameters are indicated in Table 3.

All of the four smartphones used in experiment are iPhone 6 with a three-axis Bosch BMA280 accelerometer [27], a three-axis InvenSense MPU-6500 accelerometer, and a three-axis InvenSense MPU-6500 gyroscope [28]. The properties of two accelerometers and gyroscope are listed in Tables 4 and 5.

As mentioned before, the dynamic responses of acceleration and angle in the vibration of structure can be obtained by the application Orion-CC using the smartphone-embedded accelerometer and gyroscope, and also the dynamic displacement response of the structure can be extracted by recognizing the movement of the laser spot shot on the projection plate by means of the application D-Viewer using smartphone camera.

TABLE 3: Main instruments parameters.

Instrument	Brand	Model	Parameter
Piezoelectric accelerometer	SINOCERA	CA-YD-188	Sensitivity: 500 mV/g ± 5% Measurement range: 10 g Frequency range: 0.3–2500 Hz
Laser displacement sensor	MICR-EPSILON	ILD 11300	Measuring range: 50 mm to 150 mm Resolution (dynamic): 100 microns
Laser transmitter	Ruic	Red-light semiconductor laser	Output wavelength: 650 nm Overall dimensions: Φ 20 mm × 90 mm Light spot diameter is 3 mm at a 20 m distance



FIGURE 9: Zhuanghe Construction Bridge.

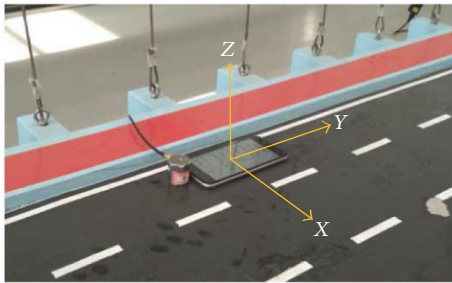


FIGURE 10: The reference coordinate system of smartphone.

In this experiment, three smartphones (1 (left), 2 (mid), and 3 (right)) installed with Orion-CC are used to measure both acceleration and angle responses of the model with a sampling rate of 100 Hz, and the other smartphone (4 (mid)) installed with D-Viewer monitors the dynamic displacement of the mid span of the model with a sampling rate of 30 Hz. All of reference sensors are connected to a sensor node through cable, respectively, and the vibration responses are recorded in computer during measurement. The scale bridge model and the layout of the smartphone and sensors are shown in Figure 11. The test is carried out simultaneously under the artificial impact excited on the mid span.

**4.2. Test Results.** The vibration responses obtained from smartphones and sensors are compared in both time and frequency domains. The natural frequency of the bridge model is identified by the peak picking method from the power spectral densities of different vibration responses. For brevity, the z-axis (direction of gravity) acceleration responses and the rotation angle responses around x-axis

TABLE 4: Bosch BMA280 and InvenSense MPU-6500 accelerometer properties.

Parameter	Bosch BMA280	InvenSense MPU-6500	Units
Digital resolution	14	16	Bits
Full-scale range	±2	±2	g
	±4	±4	g
	±8	±8	g
	±16	±16	g
Sensitivity scale	4096	16384	LSB/g
	2048	8192	LSB/g
	1024	4096	LSB/g
	512	2048	LSB/g
Cross-axis sensitivity	1	2	%
Nonlinearity	0.5	0.5	%
Zero-g offset	±50	±60	mg
Noise density	120	300	μg/√Hz

TABLE 5: InvenSense MPU-6500 gyroscope properties.

Parameter	Technical data	Units
Digital resolution	16	Bits
Full-scale range	±250	°/s
	±500	°/s
	±1000	°/s
	±2000	°/s
Sensitivity scale	131	LSB/(°/s)
	65.5	LSB/(°/s)
	32.8	LSB/(°/s)
	16.4	LSB/(°/s)
Nonlinearity	±0.1	%
Cross-axis sensitivity	±2	%
Noise density	0.01	°/s/√Hz
Initial zero-rate output	±5	°/s
Mechanical frequency	27	KHz

(vertical to span direction) are used to identify the natural frequency of the bridge model.

**4.2.1. Acceleration Response Results.** Figures 12–14 show the acceleration time history responses, comparisons in time

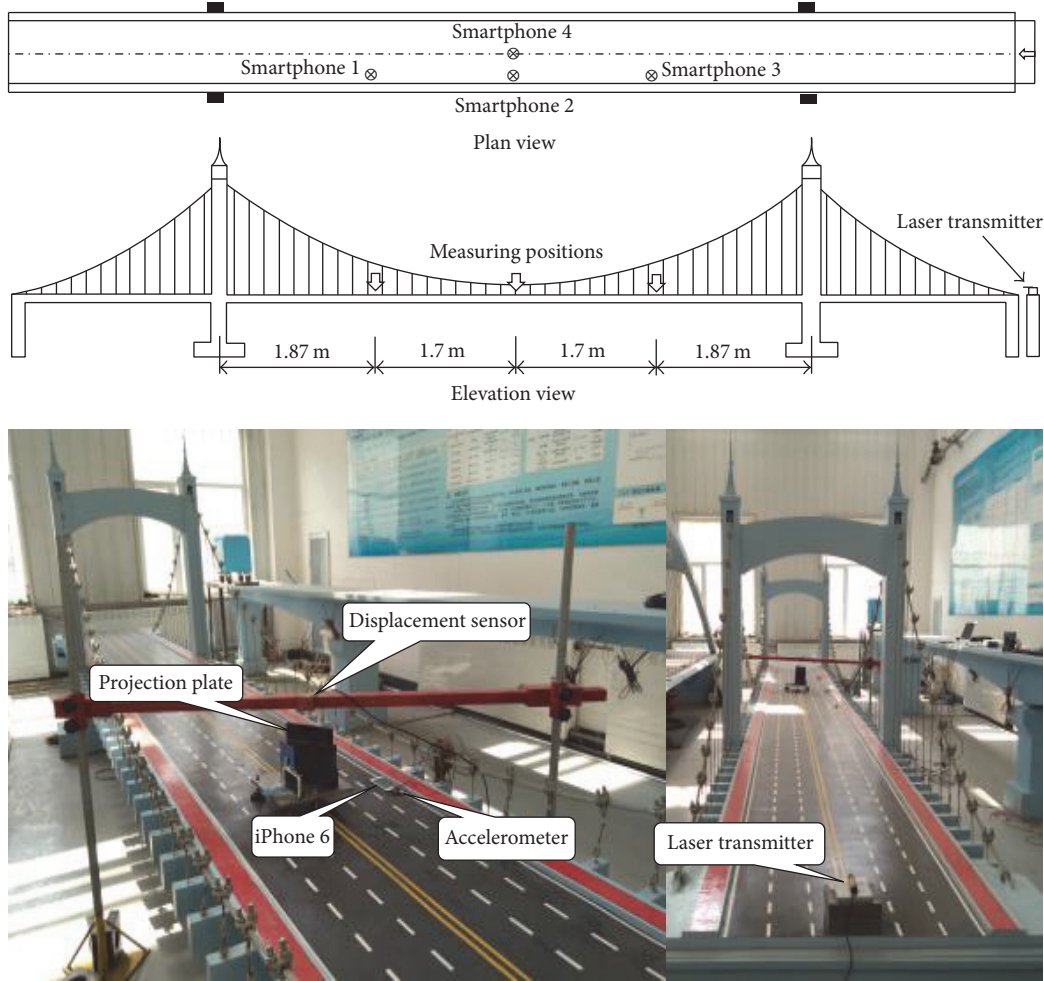


FIGURE 11: Setup of experiment.

domain, and the corresponding PSD measured by the smartphones and the reference accelerometers at three different points of the bridge model, respectively. Since the duration of vibration response on the artificial impact is less than 10 s, the plots of comparisons in time domain are enlarged (between 4 s and 5 s) to show more details. The peak responses are obtained as 0.38 g (left), 0.64 g (mid), and 0.29 g (right) by smartphones, respectively. A noticeable difference exists between the mid span and quarter span in terms of amplitude.

As can be seen from comparison figures, the measurements of smartphone agree well with the measurements of reference accelerometers in terms of amplitude characteristics. The identified natural frequencies of bridge model are summarized in Table 6. The natural frequency is identified as 4.58, 4.56, and 4.57 Hz, respectively, at three different measuring points by three reference accelerometers. Their counterparts measured by three smartphones are 4.56, 4.57, and 4.58 Hz. The excellent agreement is observed between the frequency values obtained by the reference accelerometers and smartphones at different measuring points, with a maximum error of 0.44%.

TABLE 6: Comparison of natural frequency identified from acceleration measurements.

Location	1 (left)	2 (mid)	3 (right)
Natural frequency (Hz)			
Accelerometer	4.56	4.57	4.58
Smartphone (Orion-CC)	4.58	4.56	4.57
Error (%)	0.44	0.22	0.22

**4.2.2. Angle Response Results.** The angle time history responses and corresponding PSD measured by three smartphones at different measuring points are shown in Figures 15–18, respectively. As can be seen from Figures 16 and 18, the angle vibration responses of the mid span obtained from smartphone 2 are not very clear in both time and frequency domains compared to the other ones because theoretically there is no change in the slope of the mid span according to the vibration in this test case. The natural frequencies extracted from PSD of angle measurements are compared with the previous ones measured by the reference accelerometers. Table 7 lists the identified natural frequency values. The natural frequency is not accurately extracted

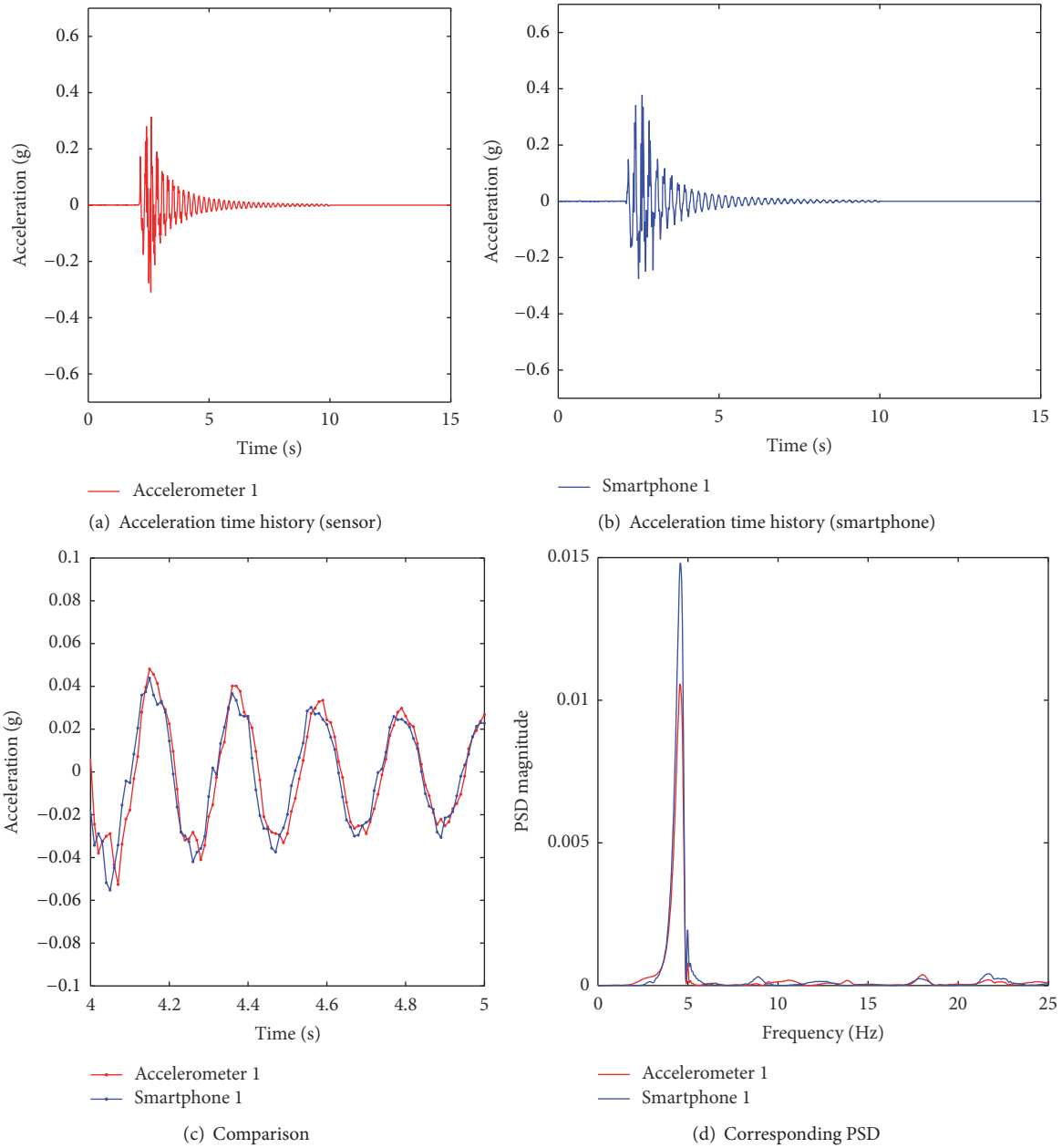


FIGURE 12: Acceleration measurements (left quarter span).

from the angle measurement of the mid span as shown in Table 7. The other ones are 4.68 and 4.59 Hz, while their counterparts measured by the reference accelerometers are 4.56 and 4.58 Hz. The errors in the natural frequency values at each measuring point are within 2.63%. It is observed that the bridge health monitoring based on the angle measurements using smartphones is feasible and reliable.

4.2.3. *Displacement Response Results.* Figure 19 plots the displacement time history responses, comparisons in time domain, and the corresponding PSD obtained from smartphone 4 and the laser displacement sensor at mid span of the bridge model. The identified natural frequencies of

TABLE 7: Comparison of natural frequency identified from angle measurements.

Location	1 (left)	2 (mid)	3 (right)
Natural frequency (Hz)			
Accelerometer	4.56	4.57	4.58
Smartphone (Orion-CC)	4.68	—	4.59
Error (%)	2.63	—	0.22

bridge model are summarized in Table 8. Since the sampling rate of the smartphone for displacement monitoring (30 Hz) is different with the reference one (100 Hz), the plots of

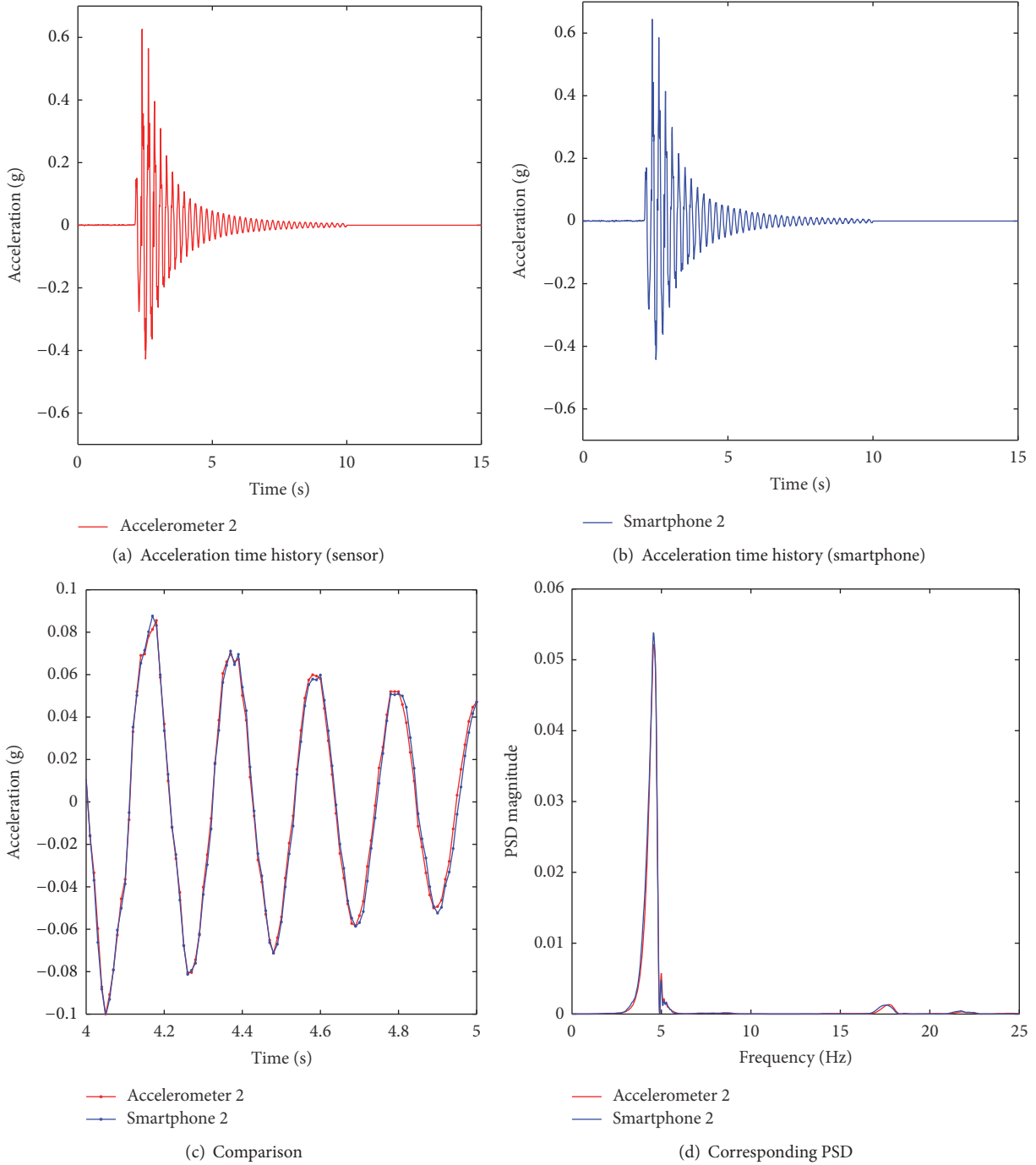


FIGURE 13: Acceleration measurements (mid span).

TABLE 8: Comparison of natural frequency identified from displacement measurements.

Location	4 (mid)
Natural frequency (Hz)	
Displacement sensor	4.56
Smartphone (D-Viewer)	4.68
Error (%)	2.63

comparisons in time domain are enlarged (between 4 s and 5 s) to show more details.

As can be seen in Figure 19(c), although the sampling rates are different, the displacement response time histories agree well with one another. The natural frequency of the bridge model measured by the laser displacement sensor is 4.56 Hz, while the one measured by smartphone 4 is 4.68 Hz. Again, the satisfactory agreement is observed between the

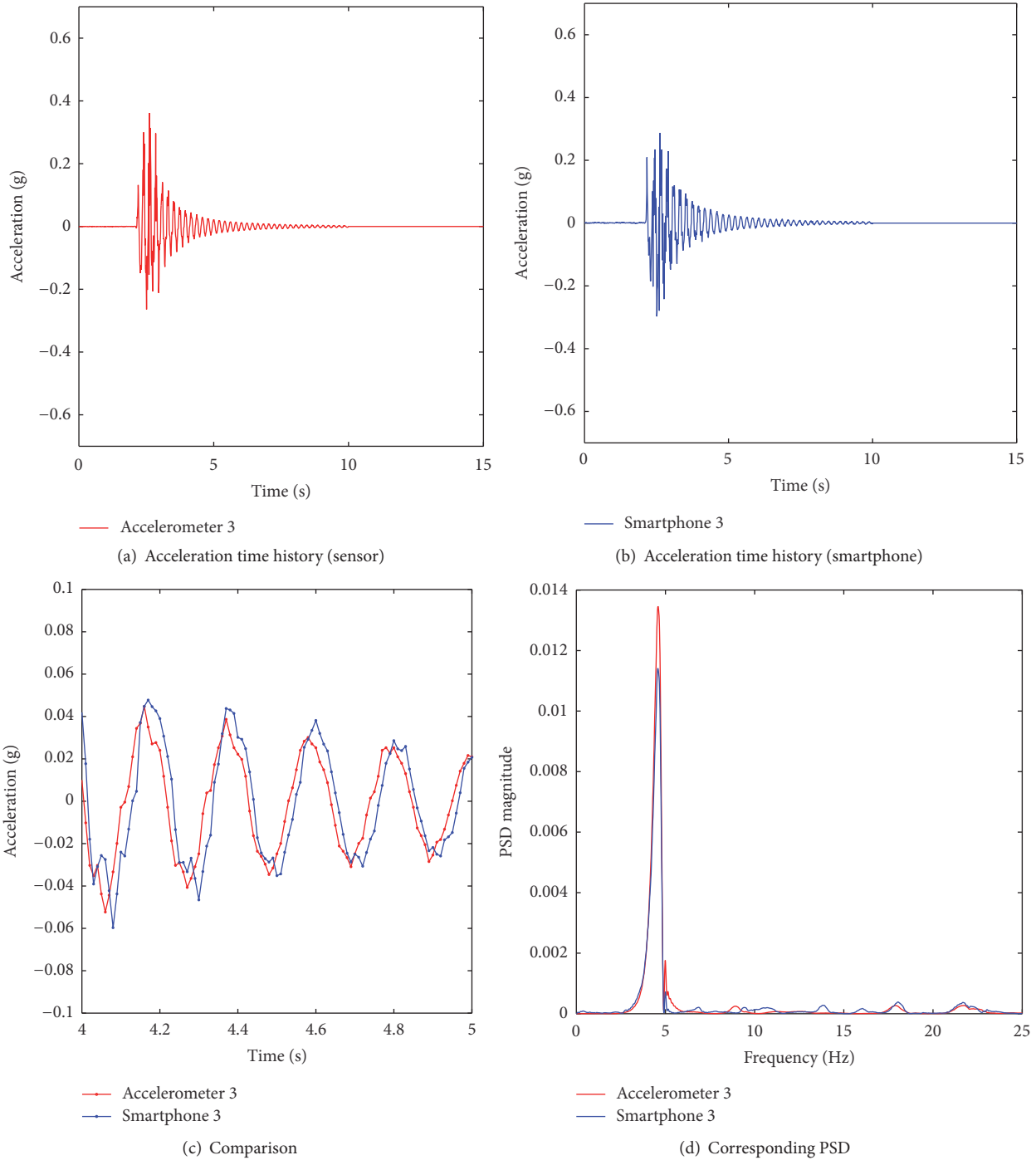


FIGURE 14: Acceleration measurements (right quarter span).

frequency values obtained by the reference sensor and smartphone.

### 5. Conclusion

In this study, a comprehensive experiment research, including cable force test and bridge model test, was carried out to verify the feasibility of the quick bridge health monitoring

technique using smartphone. First, the vision-based cable force measurement method was proposed in this paper, and then the comparison test was conducted on the cable model to verify the feasibility of proposed method. The natural frequency components and cable forces measured by the application D-Viewer were compared with the results measured by the application Orion-CC. While it is difficult to obtain the natural frequencies at the higher mode due

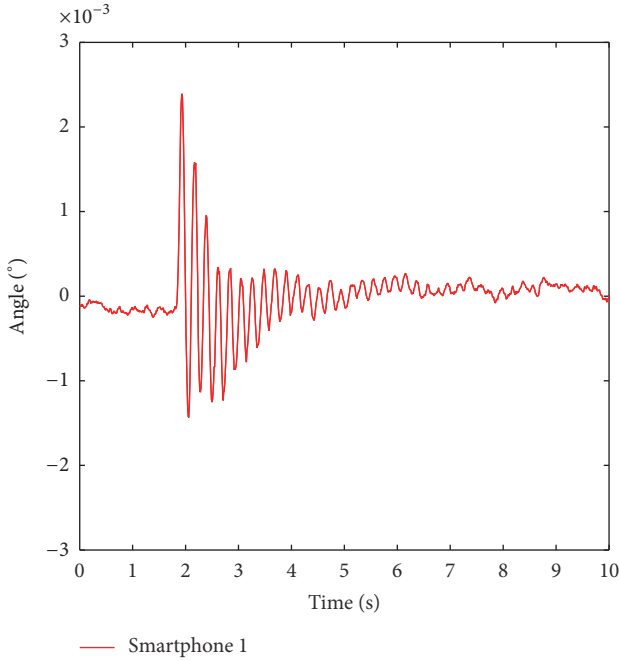


FIGURE 15: Angle measurement (left quarter span).

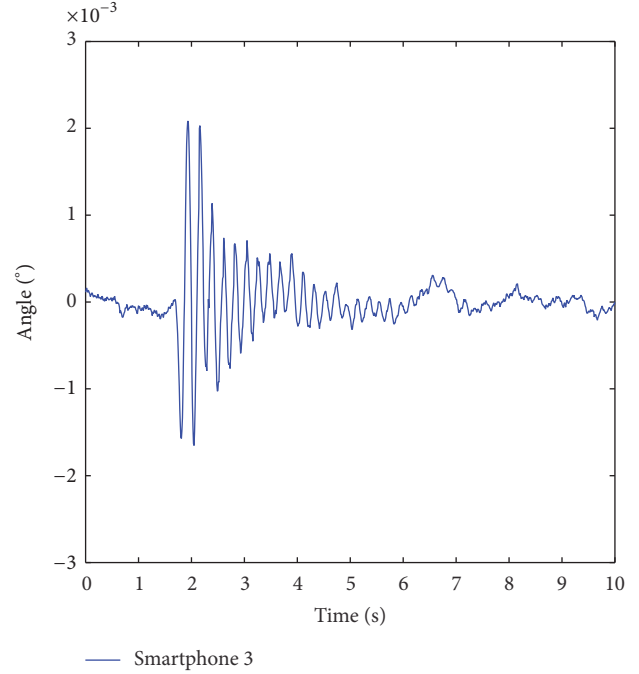


FIGURE 17: Angle measurement (right quarter span).

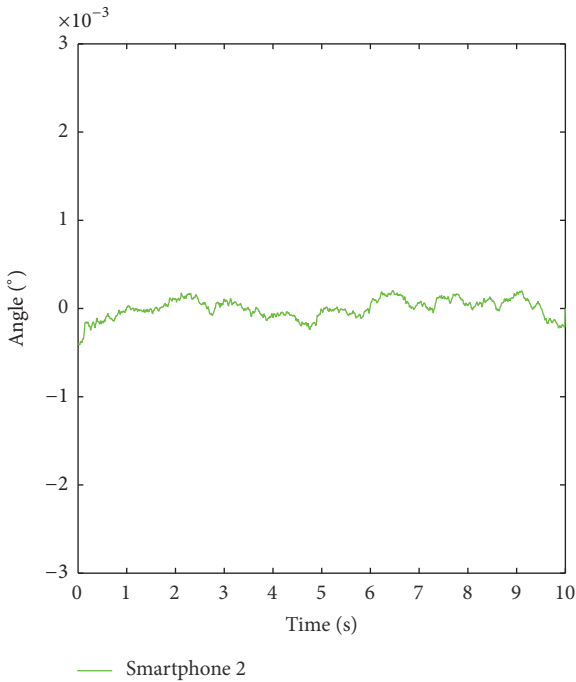


FIGURE 16: Angle measurement (mid span).

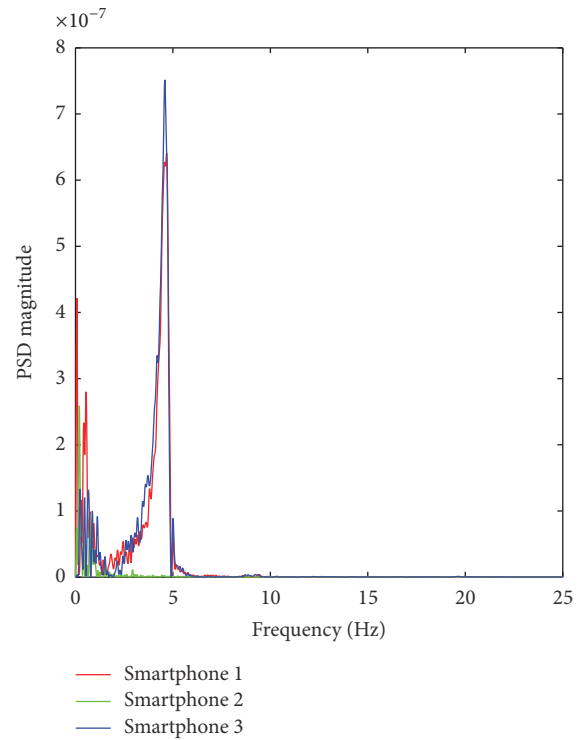


FIGURE 18: PSD of angle responses.

to the sampling rate of smartphone camera, the frequency components including the natural frequency of the first mode were estimated accurately at the lower vibration mode. The test result demonstrated the feasibility and accuracy of vision-based cable force measurement using smartphone, with significantly small error of less than 1.1%. Finally, the comprehensive monitoring test regarding multiple structural

parameters was conducted on the scale bridge model. The vibration responses obtained from smartphones and sensors were compared in both time and frequency domains. The natural frequency of the bridge model was estimated accurately from the vibration responses of multiple structural parameters such as acceleration, angle, and displacement,

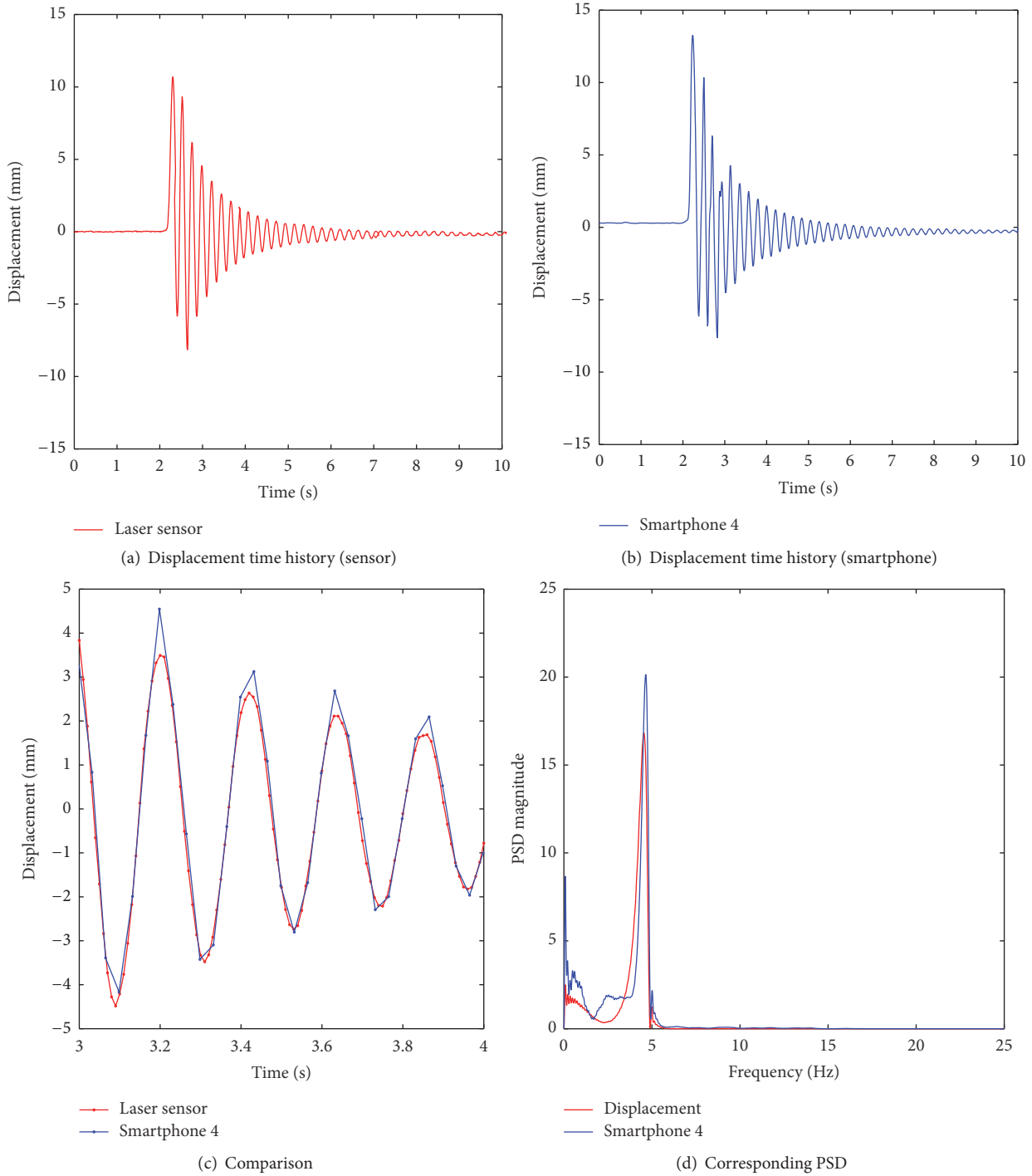


FIGURE 19: Displacement measurement.

with a maximum error of 2.63%. The tests demonstrated that it is possible to extract the dynamic characteristics of the bridge from the various kinds of vibration responses using smartphone and verified the feasibility, accuracy, and reliability of bridge health monitoring method using smartphones.

Based on these preliminary efforts, we are exploring the comprehensive and rapid postevent damage assessment application for bridges using smartphones.

**Competing Interests**

The authors declare that there is no conflict of interests regarding the publication of this paper.

**Acknowledgments**

Thanks are given to the financial support of the National Natural Science Foundation of China (51278085, 51221961).

## References

- [1] J. Ou and H. Li, "Structural health monitoring in mainland China: review and future trends," *Structural Health Monitoring*, vol. 9, no. 3, pp. 219–231, 2010.
- [2] C. R. Farrar and K. Worden, "An introduction to structural health monitoring," *Philosophical Transactions of the Royal Society A: Mathematical, Physical and Engineering Sciences*, vol. 365, no. 1851, pp. 303–315, 2007.
- [3] H. Sohn, C. R. Farrar, F. M. Hemez et al., "A review of structural health monitoring literature: 1996–2001," Los Alamos National Laboratory Report LA-13976-MS, 2004.
- [4] H. Wenzel, *Health Monitoring of Bridges*, John Wiley & Sons, New York, NY, USA, 2009.
- [5] J. M. Ko and Y. Q. Ni, "Technology developments in structural health monitoring of large-scale bridges," *Engineering Structures*, vol. 27, no. 12, pp. 1715–1725, 2005.
- [6] J. M. W. Brownjohn, "Structural health monitoring of civil infrastructure," *Philosophical Transactions of the Royal Society A: Mathematical, Physical and Engineering Sciences*, vol. 365, no. 1851, pp. 589–622, 2007.
- [7] H. Kobayashi, S. Unjoh, and T. Kanou, "Development of an earthquake damage evaluation method for bridge structures using acceleration sensors," *Structural Engineering/Earthquake Engineering*, vol. 25, no. 1, pp. 25s–32s, 2008.
- [8] Y. Yu, X. Zhao, and J. Ou, "A new idea: mobile structural health monitoring using smart phones," in *Proceedings of the 3rd International Conference on Intelligent Control and Information Processing (ICICIP '12)*, pp. 714–716, IEEE, Dalian, China, July 2012.
- [9] G. Morgenthal and H. Höpfner, "The application of smartphones to measuring transient structural displacements," *Journal of Civil Structural Health Monitoring*, vol. 2, no. 3–4, pp. 149–161, 2012.
- [10] J. Reilly, S. Dashti, M. Ervasti, J. D. Bray, S. D. Glaser, and A. M. Bayen, "Mobile phones as seismologic sensors: automating data extraction for the shake system," *IEEE Transactions on Automation Science and Engineering*, vol. 10, no. 2, pp. 242–251, 2013.
- [11] A. Sharma and D. Gupta, "Smartphone as a real-time and participatory data collection tool for civil engineers," *International Journal of Modern Computer Science (IJMCS)*, vol. 2, no. 5, pp. 22–27, 2014.
- [12] G. P. Cimellaro, G. Scura, C. S. Renschler, A. M. Reinhorn, and H. U. Kim, "Rapid building damage assessment system using mobile phone technology," *Earthquake Engineering and Engineering Vibration*, vol. 13, no. 3, pp. 519–533, 2014.
- [13] R. Han, X. Zhao, Y. Yu, and J. Ou, "Design and initial validation of mobile-structural health monitoring system based on smart phone," in *Proceedings of the 5th Asia-Pacific Workshop on Structural Health Monitoring Conference (AWPSHM '14)*, Shenzhen, China, 2014.
- [14] Y. Yu, X. Zhao, R. Han, and J. Ou, "Design and initial validation of external sensors board of smart phones for mobile structural health monitoring system," in *Proceedings of the 7th International Conference on Structural Health Monitoring of Intelligent Infrastructure (SHMII '15)*, Torino, Italy, 2015.
- [15] M. Feng, Y. Fukuda, M. Mizuta, and E. Ozer, "Citizen sensors for SHM: use of accelerometer data from smartphones," *Sensors*, vol. 15, no. 2, pp. 2980–2998, 2015.
- [16] E. Ozer, M. Q. Feng, and D. Feng, "Citizen sensors for SHM: towards a crowdsourcing platform," *Sensors*, vol. 15, no. 6, pp. 14591–14614, 2015.
- [17] H. Tan and J. Chen, "Experiment verification of mobile phones for vibration measurement," in *Proceedings of the 7th International Conference on Structural Health Monitoring of Intelligent Infrastructure*, Torino, Italy, 2015.
- [18] X. Zhao, H. Liu, Y. Yu et al., "Convenient displacement monitoring technique using smartphone," *Vibroengineering Procedia*, vol. 5, pp. 579–584, 2015.
- [19] R. Han, X. Zhao, and Y. Yu, "Convenient posture monitoring on girder hoisting of Dalian Xinghaiwan cross-sea bridge based on smart phone," in *Proceedings of the 7th International Conference on Structural Health Monitoring of Intelligent Infrastructure*, Torino, Italy, 2015.
- [20] X. Zhao, Y. Yu, and M. Li, "Research on Cloud-SHM and its applications," in *Proceedings of the 7th International Conference on Structural Health Monitoring of Intelligent Infrastructure*, Torino, Italy, 2015.
- [21] D. Peng, X. Zhao, Q. Zhao, and Y. Yu, "Smartphone based public participant emergency rescue information platform for earthquake zone—'E-Explorer,'" *Vibroengineering Procedia*, vol. 5, pp. 436–439, 2015.
- [22] X. Zhao, "Orion-CC," <https://itunes.apple.com/cn/app/orion-cc/id951253417?mt=8>.
- [23] X. Zhao, "D-Viewer," <https://itunes.apple.com/cn/app/d-viewer/id1006583231?mt=8>.
- [24] B. Zhang, H. Wan, and C. Mao, "Study on displacement sensor based on difference operation spot center location algorithm," *Chinese Journal of Sensors and Actuators*, vol. 24, no. 2, pp. 215–219, 2011.
- [25] Z. Fang and J.-Q. Wang, "Practical formula for cable tension estimation by vibration method," *Journal of Bridge Engineering*, vol. 17, no. 1, pp. 161–164, 2012.
- [26] "iPhone6," <http://www.apple.com/iphone-6/specs/>.
- [27] "BOSCH BMA280," [https://www.bosch-sensortec.com/bst/products/all\\_products/bma280/](https://www.bosch-sensortec.com/bst/products/all_products/bma280/).
- [28] "InvenSenseMPU-6500," <http://www.invensense.com/products/motion-tracking/6-axis/mpu-6500/>.

## Research Article

# Effect of Nanosilica on the Fresh Properties of Cement-Based Grouting Material in the Portland-Sulphoaluminate Composite System

Shengli Li and Tingting Xu

School of Civil Engineering, Zhengzhou University, Zhengzhou 450001, China

Correspondence should be addressed to Shengli Li; [lsl2009@126.com](mailto:lsl2009@126.com)

Received 24 April 2016; Revised 11 August 2016; Accepted 30 August 2016

Academic Editor: Chunhui Yang

Copyright © 2016 S. Li and T. Xu. This is an open access article distributed under the Creative Commons Attribution License, which permits unrestricted use, distribution, and reproduction in any medium, provided the original work is properly cited.

The effect of NS particle size and content on the fresh properties of the grouting material based on the portland-sulphoaluminate composite system was analyzed. The experimental results indicated that air content increased and apparent density decreased, with increased NS content, but the NS particle sizes have minimal effect on the air content and apparent density. The setting time of mortar was significantly shortened, with increased NS content; however, NS particle sizes had little influence on the setting time. The effect of fluidity on the mortars adding NS with particle size of 30 nm is larger than NS with particle sizes of 15 and 50 nm and the fluidity decreased with increased NS content, but the fluidity of mortars with the particle sizes of 15 and 50 nm is almost not affected by the NS content. XRD analysis shows that the formation of ettringite was promoted and the process of hydration reaction of cement was accelerated with the addition of NS. At the microscopic level, the interfacial transition zone (ITZ) of the grouting material became denser and the formation of C-S-H gel was promoted after adding NS.

## 1. Introduction

Nanomaterials are attracting increased attention in many fields [1]. When ultrafine particles are mixed into cement paste, mortar or materials with different characteristics from conventional materials were obtained [2–4]. The properties of cement-based grouting materials heavily rely on the properties of nanoscale solid particles, for example, particles of calcium-silicate-hydrates (C-S-H), or nanosized holes at the interfacial transition zone between cementitious material and aggregate particles [5]. The typical characteristics brought about by nanoscale particles or voids are strength, durability, and volume stability [6]. Nanoparticles of silica ( $\text{SiO}_2$ ) or nanosilica (NS) can fill the voids between particles of C-S-H gel, demonstrating interstitial filling. Furthermore, as the pozzolanic reaction with  $\text{Ca}(\text{OH})_2$ , the amount of C-S-H gel increases and leads to increased compacting formation [1].

Previous research has indicated that nanoparticles can improve fresh and hardened state properties [3, 7–12]. Amorphous silica can significantly affects  $\text{C}_3\text{S}$  hydration [7]. NS shortened the setting time of mortar when compared with

silica fume (SF) and reduced bleeding water and segregation; moreover, it also can improve the cohesiveness force of the cement-based grouting materials [8, 9]. When mixed with superfine fly ash, properties of the cement-based grouting materials better than those gained by the use of silica fume alone are guaranteed [3]. Moreover, the compressive strength of mortar with SF is enhanced compared with formulations without other additions [10–12]. The smaller size of NS particles permits them to function as filler by occupying spaces in the cement composites, thereby reducing porosity and reinforcing mechanical performance. Some researchers suggested that the optimal dosage of NS has to be small (1 wt%–5 wt%) because of the agglomeration caused by difficulties in the dispersal of particles during stirring. On the contrary, others declared that the improvement of the performance can also be obtained with higher dosages of approximately 10 wt%; if appropriate adjustments are made to the formulation to avoid excessive self-constriction and microcracking, which could prevent the strength from growth [8, 10–13].

The sizes and properties of NS, which are similar to SF, have been studied as a potential mineral admixture for

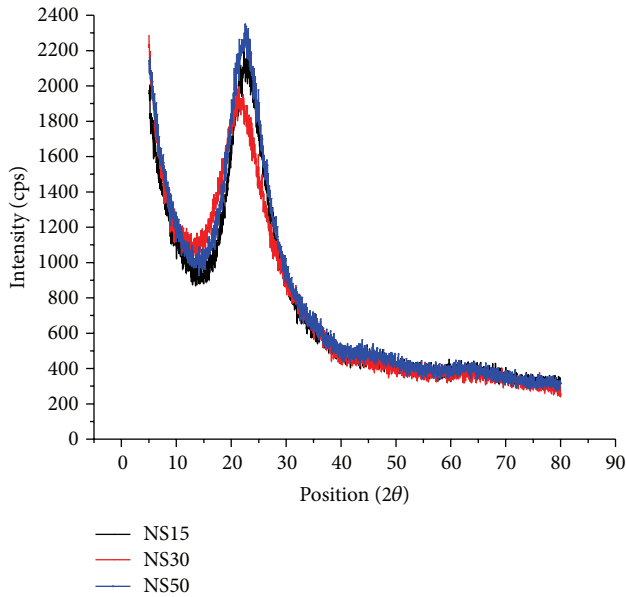


FIGURE 1: XRD analysis of NS materials.

cement pastes [2, 11–14]. Nevertheless, NS can also reveal additional features, such as reducing the setting time, changing the rheological property, and changing physical performance of portland cement pastes [8, 15–21]. The addition of nanoscale silica into the cement-based grouting materials is confirmed to be beneficial to civil engineering [22]. The use of NS has been studied in various fields with several types of materials [23–28].

Previous studies only include the cement grouting materials with the ordinary portland cement and only one size of NS. In this paper, three types of particle sizes of NS mixed with the cement-based grouting materials of portland-sulphoaluminate composite system were analyzed. This paper reports the effects of nanosilica on rheological properties, setting time, air content, and apparent density of cement-based grouting material in the portland-sulphoaluminate composite system. The phase determination (XRD and SEM) of cement pastes was also investigated.

## 2. Experimental Programs

**2.1. Materials.** The chemical composition of the materials in this work was investigated by X-ray fluorescence (XRF), X-ray diffraction (XRD), and transmission electron microscope (TEM). The chemical composition of the portland cement and sulphoaluminate cement is shown in Table 1. The NS material used in this work was provided by Hangzhou Wanjing New Material Co., Ltd. Three types of NS, namely, NS15, NS30, and NS50, were employed. The chemical composition of NS is shown in Table 2. The XRD of the NS materials was performed in a PANalytical X'Pert PRO MPD with a  $2\theta$  range of  $4.983^\circ$ – $79.983^\circ$  and a step of  $0.033^\circ$ . The XRD patterns of NS are shown in Figure 1. The intensity peaks were associated to  $2\theta$  angles of  $22^\circ$ ,  $21^\circ$ , and  $23^\circ$  for NS15, NS30, and NS50, respectively. Figure 2 shows a TEM image of NS,

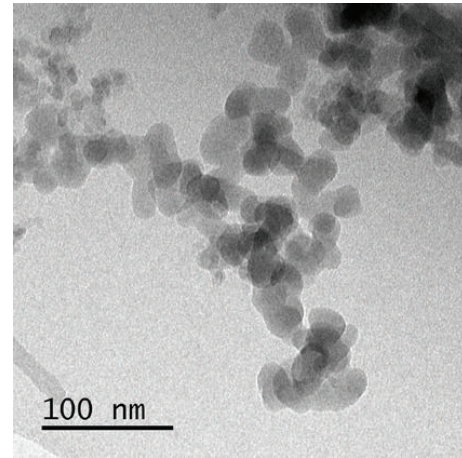


FIGURE 2: TEM image of NS30.

TABLE 1: Chemical composition of ordinary portland cement and sulphoaluminate cement.

Item	Chemical composition (%)	
	P-O42.5	R-SAC42.5
SiO <sub>2</sub>	15.80	4.23
Al <sub>2</sub> O <sub>3</sub>	5.47	11.60
Fe <sub>2</sub> O <sub>3</sub>	2.72	0.97
CaO	48.00	42.96
MgO	2.13	2.34
SO <sub>3</sub>	1.59	13.58

P-O42.5: ordinary portland cement 42.5.

R-SAC42.5: sulphoaluminate cement 42.5.

TABLE 2: Chemical composition of NS.

Item	Chemical composition (%)		
	NS15	NS30	NS50
SiO <sub>2</sub>	66.79	79.10	68.26

NS\*\*: NS particle size of \*\* nm.

thereby confirming that the silica was a nanomaterial. China ISO standard sand was used in this test and the parameter of ISO standard sand was shown in Table 3. The superplasticizer (SP) is a polycarboxylate high-range, water-reducing agent with pH = 6–8 and 40% solid content in powder form. In addition, the SP used in the experiments was produced by Ji'nan Sunny Chemical Science and Technology Co., Ltd. The chloride ion content was less than 0.03%. Tap water from the laboratory was used in the work.

**2.2. Paste and Mortar Mixing Process.** Fresh mortars were prepared with binder/aggregate weight ratio (B/A) of 1: 2 and water/binder (W/B) ratio of 0.35. Mortars were produced with 0%–5% NS in weight, replacing cement. The mixing compositions of mortars are listed in Table 4. The effects of different particle size of NS on the grouting materials also were studied with NS content 1.5 wt% in Table 4. The preparation of mortars involved (a) weighing the components, (b)

TABLE 3: Particle size distributions of ISO standard sand.

Side length of the square hole (mm)	Sieve residue (%)
2.0	0
1.6	7 ± 5
1.0	33 ± 5
0.5	67 ± 5
0.16	87 ± 5
0.08	99 ± 5

adding NS and SP into water with a glass, mixing them at high speed to form an aqueous suspension, and (c) pouring the solid components into water and mechanical mixing. During the mixing process, the stirring blade of the mortar mixer was rotation and revolution, and the mortar mixer blended mixture at a constant low speed (at the rotation speed of 140 r/min and at the revolution speed of 62 r/min) for 30 s. Next, the mortar mixer blended mixture at the same low speed for another 30 s and the sand was added into the mixing pot at the same time. Then, the mortar mixer blended mixture at a constant high speed (at the rotation speed of 285 r/min and at the revolution speed of 125 r/min) for 30 s and the mortar mixer stopped stirring for 90 s subsequently. Finally, the mortar mixer blended mixture at a constant high speed (at the rotation speed of 285 r/min and at the revolution speed of 125 r/min) for another 60 s. And then the mortar was completed.

To further study the effects of NS on the hydration of cement, paste was used in this work. Paste was prepared with a W/B ratio of 0.35, such that 0% and 4% NS30 by weight replaced cement. The mix composition of paste is given in Table 5. The preparation of paste involved (a) weighing the components, (b) adding NS30 and SP into water, mixing them at high speed to form an aqueous suspension, and (c) pouring the solid components into water and mechanical mixing. During the mixing, the stirring blade of the paste mixer was rotation and revolution, and the paste mixer blended mixture at a constant low speed (at the rotation speed of 140 r/min and at the revolution speed of 62 r/min) for 120 s. Then, the paste mixer stopped stirring for 15 s. Finally, the paste mixer blended mixture at a constant high speed (at the rotation speed of 285 r/min and at the revolution speed of 125 r/min) for another 120 s. And then the paste was completed.

**2.3. Experimental Parameter and Methods.** Apparent density was measured, according to the Standard Test Method for the performance of building mortar (JGJ/T 70-2009). Mortars were mixed by a planet-type cement sand mixing machine. Fresh mortar filled the capacity cylinder, which had a 108 mm inner diameter and a 109 mm net height. The thickness of the cylinder was 2 mm and its volume was 1L. First, the cylinder was cleaned with a damp cloth and weighed to measure the mass of the cylinder ( $m_1$ ). After artificial vibrating compaction, surplus mortars were stripped away. Finally, the weighed mass of the cylinder was  $m_2$  and the



FIGURE 3: Mortar air content-measuring instrument.

first apparent density value was calculated through (1). The apparent density of the mortar is calculated as

$$\rho = \left[ \frac{(m_2 - m_1)}{V} \right] \times 1000, \quad (1)$$

where  $\rho$  ( $\text{kg}/\text{m}^3$ ) is the apparent density of the mortar,  $m_1$  (kg) is the mass of the capacity cylinder,  $m_2$  (kg) is the combined mass of the capacity cylinder and mortar, and  $V$  (L) is the volume of the capacity cylinder. We repeated the prior steps to test and calculate the second apparent density through formula (1). Finally, we took the average of two values as our apparent density value, accurate to  $10 \text{ kg}/\text{m}^3$ .

The air content was measured by the mortar air content-measuring instrument in Figure 3, according to the Standard Test Method for the performance of building mortar (JGJ/T 70-2009). Fresh mortar was divided into three uniform amounts that were loaded into the amount of the bowl. After artificial vibrating compaction, surplus mortars were stripped away. The mortar surface should be smooth and without bubbles. The lid was attached and then clamped to the block buttons and carried air content of the mortar. We pressed the button and read the dial when the dial was stable. We repeated the prior steps to measure the other value and we took the average of two values as the end result. If the relative error of two test values was less than 0.2%, the average of two values was the final result. The test was invalid.

The setting time was measured by the concrete penetration resistance tester in Figure 4, according to the Test code for hydraulic concrete (SL 352-2006). Each setting time was tested by three samples. The test of setting time was started after mixing with water. Firstly, the mortar sample tube is placed on the penetration resistance tester. Secondly, the terminal of the pin was placed in contact with the mortar surface and the pin was vertically pressed into the mortar to a depth of 25 mm, slowly and uniformly. The penetration resistance values and time were recorded, at 30 min intervals. The times of the experiment should be six at least.

TABLE 4: Mix proportion of different cement mortars with different NS particle size.

NS (wt%)	W/B	Mixture components					
		Water (mL)	P·O42.5 (g)	R·SAC42.5 (g)	Sand (g)	NS (g)	SP (g)
0	0.35	87.5	160	90	500	—	5
0.5	0.35	87.5	158.75	90	500	1.25	5
1.0	0.35	87.5	157.5	90	500	2.5	5
1.5	0.35	87.5	156.25	90	500	3.75	5
2.0	0.35	87.5	155	90	500	5	5
2.5	0.35	87.5	153.75	90	500	6.25	5
3.0	0.35	87.5	152.5	90	500	7.5	5
3.5	0.35	87.5	151.25	90	500	8.75	5
4.0	0.35	87.5	150	90	500	10	5
4.5	0.35	87.5	148.75	90	500	11.25	5
5.0	0.35	87.5	147.5	90	500	12.5	5



FIGURE 4: Concrete penetration resistance tester.



FIGURE 5: Apparatus to measure the fluidity of cement mortar.

Approaching the initial and final time, we could increase the times of the experiment. Through the experiments, we got a series of data. Taking the test time as the abscissa axis and penetration resistance values as the ordinate axis, the curves were fitted. Then, we found the initial and final time. We repeated the prior steps in every sample (3 samples per group) and calculated the average of the 3 values as our setting time. However, the maximum value of 3 values was above 1.1 times the average or the minimum value of 3 values was below 0.9 times the average and we would take the average as our final result. Otherwise, the test was invalid.

The fluidity of the mortar was tested by the apparatus of fluidity of cement mortar in Figure 5, according to the Test Method for fluidity of cement mortar (GB/T 2419-2005). Fresh mortar was divided into two uniforms, which were loaded into the testing model. After artificial vibrating compaction, the conical die would be vertically and slightly lifted while the instrument was operated to jump. When the instrument completed the test, we should use a steel rule to

measure the two diameters, which are vertical to each other, and to calculate the average. The average should be rounding and then the integer value was the fluidity of the mortar.

### 3. Results and Discussion

**3.1. Apparent Density and Air Content.** The influence of NS30 content on air content and apparent density on the mortar is shown in Figure 6. The mix composition in this condition is shown in Table 4. Air content increased when the NS30 content was in the range of 0.0–2.5 wt%. When the NS30 content was 1.0 wt%, 1.5 wt%, 2.0 wt%, and 2.5 wt%, the air content of mortar increased by 2.1%, 1.9%, 2.2%, and 6.0%, respectively, compared with the mortars without NS30. By sequentially increasing the NS30 content (0 wt%, 1.0 wt%, 1.5 wt%, 2.0 wt%, and 2.5 wt%) the progression of apparent density was  $-10.0\%$ ,  $-7.8\%$ ,  $-12.8\%$ , and  $-14.2\%$  compared with mortars without NS30. This reduction can be attributed to the combined effect of air-entraining and the replacement

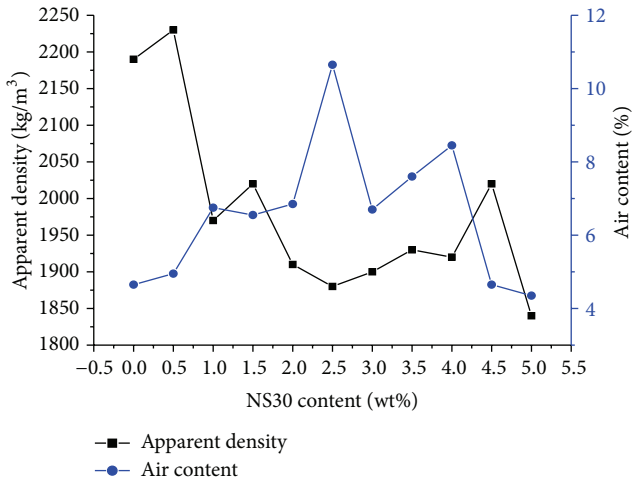


FIGURE 6: Influence of NS30 content on air content and apparent density of the mortar.

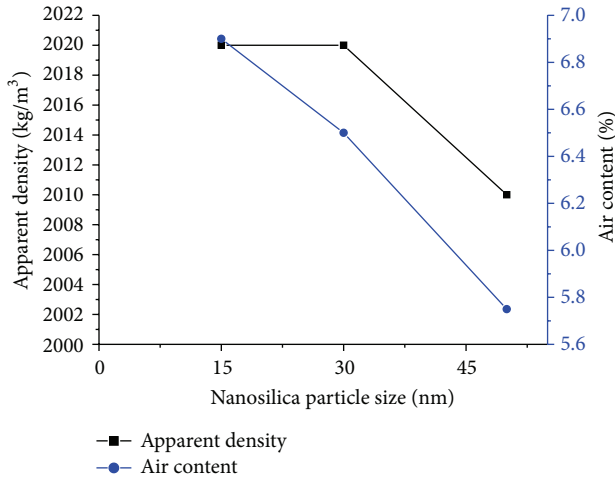


FIGURE 7: Influence of NS particle size on air content and apparent density of the mortar.

of denser cement particles by lighter NS particles. However, a less obvious regularity was observed when NS30 was incorporated into the mixture at 3.0 wt%–5.0 wt%.

To investigate the influence of NS particle size on air content and apparent density of the mortar, three particle sizes of 15, 30, and 50 nm were selected. In this case, the mix composition of the mortar is shown in Table 4 with the NS content determined at 1.5 wt%. Figure 7 presents the influence of NS particle size on air content and apparent density of the mortar. Air content of cement mortars with NS particle sizes of 30 and 50 nm declined by 0.4% and 1.15%, respectively, compared with the mortar with NS15. However, the apparent density of the mortar decreased to 10 kg/m<sup>3</sup> when the NS particle size was 50 nm. This trend was basically attributed to the specific surface area of the NS particle, which decreased with increased NS particle size. The effect of air-entraining also declined. Given the replacement of denser

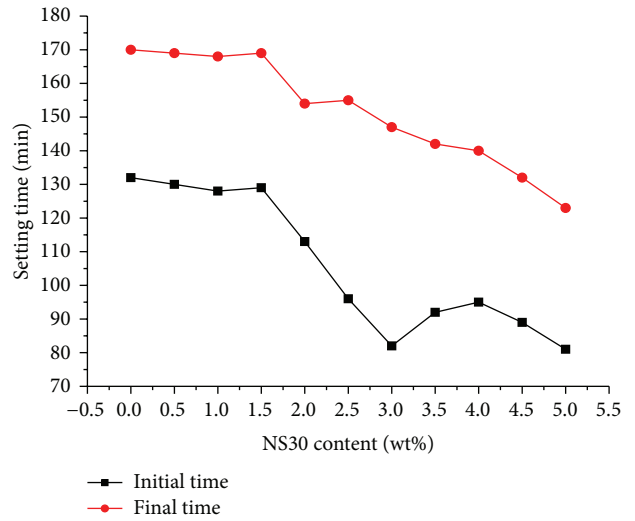


FIGURE 8: Variation in setting time (initial and final) on the mortar with the NS30 content.

cement particles by lighter NS particles, the apparent density of the mortar slightly decreased.

**3.2. Setting Time.** The variation in setting time of the mortar with the NS30 content is presented in Figure 8. The mix composition of the mortar is shown in Table 4. Results in Figure 8 indicated that the setting time of the mortar was slightly shortened with the NS30 content varying from 0.0 wt% to 1.5 wt%, by step increments of 0.5 wt%. With increased NS30 content from 2.0 wt% to 3.0 wt%, setting time sharply decreased. With increased NS30 content from 3.5 wt% to 5.0 wt%, the setting time of the mortar was slightly prolonged. With 2.0 wt% NS30, the initial and final setting were shortened by 19 and 16 min compared with samples without NS. With 5.0 wt% NS30, the initial and final setting time were reduced by 51 and 47 min, respectively, compared with the control samples (the content of NS30 is 0.0 wt%). This trend was mainly related to the pozzolanic activity of NS in the continuous hydration process of cement. NS reacts with the continuous hydration of cement clinker such as C<sub>3</sub>S and β-C<sub>2</sub>S, thereby producing C-S-H and CH [29, 30]. The decrease in free portlandite contents promoted further hydration of the clinker; thus, the acceleration of cement hydration shortened the curing time. The increased content of C<sub>4</sub>A<sub>3</sub> $\bar{S}$  was attributed to the portland cement mixed with the sulphoaluminate cement. The formation of ettringite and alumina gel became faster. Since the reaction of CH with C<sub>4</sub>A<sub>3</sub> $\bar{S}$  could produce ettringite, the content of CH and the alkalinity of the mortar decreased. Therefore, the hydration of C<sub>2</sub>S, C<sub>3</sub>S was accelerated, which shortened the setting time. NS had a large specific surface area with a nucleating effect for hydration; it accelerated the secondary hydration reaction to increase the hydration velocity of C<sub>4</sub>A<sub>3</sub> $\bar{S}$ . However, much ettringite and alumina gel may be attached onto the surface of the cement particles to prevent their further hydration. Consequently, when the NS30 content increased from 3.0 wt% to 5.0 wt%, the setting time was slightly prolonged.

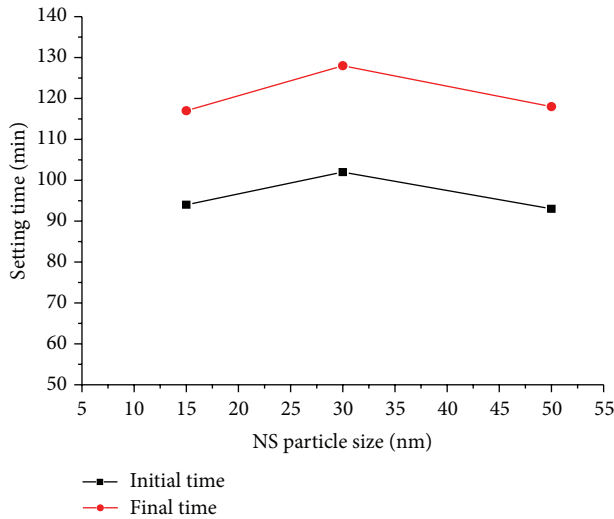


FIGURE 9: Variation in setting time (initial and final) on the mortar with the NS particle size.

The variation in setting time on the mortar with the NS particle size is shown in Figure 9. In this case, the mix composition of the mortar is shown in Table 4 with NS content 1.5 wt%. Cement mortar with NS particle sizes of 15 and 50 nm had a relatively shorter setting time than the mortar with NS particle size of 30 nm. These results showed that initial setting time was shortened by 7.8% and 8.9%, whereas the final setting time was shortened by 8.6 and 8.5%. As seen from Figures 8 and 9, the effect of NS content on the setting time of the cement mortar was more obvious than the effect of NS particle size on cement mortar. This trend was mainly related to weak dispersion of NS during the blending process. Thus, in the case of a high dosage NS, silica particles did not disperse well in cement matrix; this phenomenon has been studied by Khaloo et al. [31]. And due to the agglomeration of NS particles, the pozzolanic activity of NS particle was not performed very well during the hydration reaction. So the agglomeration of NS particles was found to be the main reason of the trend shown in Figure 9.

**3.3. Fluidity.** The influence of NS on the fluidity of the cement mortar is shown in Figure 10. Table 4 shows the mix composition of cement mortar under this condition. With 5.0 wt% NS30, the fluidity of the cement mortar was 225 mm, which did not meet the requirements of the code for the application of cementitious grout. However, cement mortar with NS particle sizes of 15 and 50 nm could meet the requirements of this code. Figure 10 presents the fluidity of cement mortar, which fluctuates between 275 and 303 mm after mixing NS15 and NS50. By contrast, the fluidity of the mortar decreased with increased NS30 content. While NS30 content was 5.0 wt%, the fluidity of the mortar sharply decreased. For instance, with 4.0 wt% NS15, the fluidity was reduced by 8.0%, whereas by increasing the NS50 content to 1.0 wt%, the fluidity decreased by 8.8% and the fluidity dropped by 25.4% with NS30 dosage at values of 5.0 wt%. Contrasting NS30 with NS15 and NS50, the maximum value and the minimum

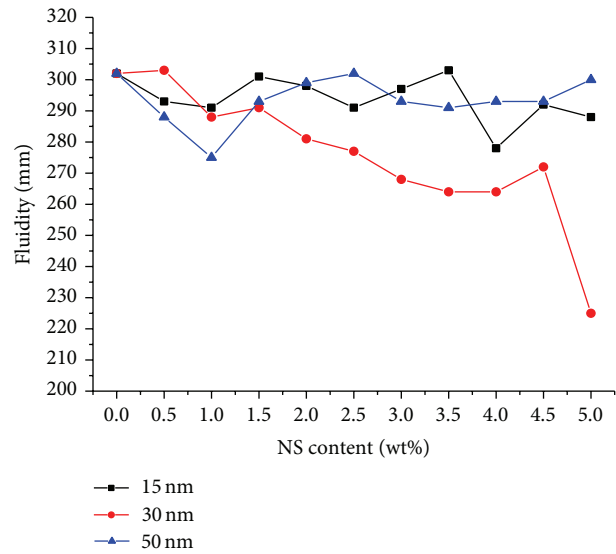


FIGURE 10: Variation in fluidity on the mortar with the NS content and NS particle size.

value of the fluidity were 225 and 303 mm with 0.5 wt% NS30 content and 5.0 wt% NS30 content, respectively. With the addition of NS15, the maximum value and the minimum value of the fluidity were 278 and 303 mm with 4.0 wt% NS30 content and 3.5 wt% NS15 content, respectively. With the increase of NS50, the maximum value and the minimum value of the fluidity were 275 and 302 mm with 1.0 wt% NS50 content and 2.5 wt% NS15 content, respectively. With the increased content of NS, the fluidity of mortars with NS15 and NS50 was fluctuated. However, the fluidity of mortars with NS30 declined. When the content of NS30 was added up to 5.0 wt%, the fluidity of mortars with NS30 had a sharp decrease. This trend was mainly related to the higher NS dosage and the agglomeration of NS particles.

In the mixing procedure, the NS and SP were stirred with water by the experimenter in the beaker. Therefore, this trend was mainly related to the hard to disperse NS particle during the stirring process, because the smaller the NS particle size is, the higher the surface area is; the cement was harder to mix with NS uniformly. Thus, in the case of the smaller and higher dosage NS, silica particles did not disperse well in cement matrix. The pozzolanic activity of NS particle was not performed very well during the hydration as a result of the agglomeration of NS particles. In this work, we also adopted the portland-sulphoaluminate composite system and the polycarboxylate SP. The hydrated products of calcium sulphoaluminate,  $C_4A_3\bar{S}$ , were mainly ettringite (Aft), alumina gel, calcium aluminate hydrates (AFm), and a small amount of a gelatinous substance.

However, NS particles were very small and extremely difficult to evenly disperse. Therefore, these particles often existed in the form of agglomerates in cement mortar. Furthermore, NS exhibited an extremely large specific surface area and high porosity. Hence, agglomerates can absorb a large amount of water. The effect of the mixing techniques on the properties of the mortar should be investigated. NS

TABLE 5: Mix proportion of different pastes.

NS30 (wt%)	W/B	Mixture components				
		Water (mL)	P-O42.5 (g)	R-SAC42.5 (g)	NS30 (g)	SP (g)
0	0.35	87.5	160	90	—	5
4.0	0.35	87.5	150	90	10	5

was difficult to disperse, and large agglomerates cannot fill the cement particles. Less free water was replaced, and the agglomerates significantly absorbed more water. For instance, fluidity slightly decreased at a low NS30 dosage ( $\leq 1.5\%$ ). Nanosilica could disperse into small agglomerates and filled the space between cement particles as filler. Consequently, more free water was replaced, and the fluidity was slowly reduced. With increased NS30 content from 2.0 wt% to 5.0 wt% accompanied by more rapid hydration, more C-S-H gel and  $\text{Ca}(\text{OH})_2$  crystals were produced. Consequently, more ettringite was obtained. Some ettringite was gained at the latter stage which filled the cement particles as fillers, but more of the ettringite covered the cement, thereby significantly increasing the absorbed water of the hydration reaction. The free water content of the slurry decreased and became insufficient to resist the flocculation of cement particles. Therefore, fluidity significantly declined.

**3.4. XRD and SEM Analyses.** The influence of NS on the hydration reactions and microcosmic interfaces on the mortar was studied. However, the particle size of sand was larger, thereby affecting the XRD and SEM analyses. Thus, the cement paste with NS was investigated in this work, and the mix composition of the paste is shown in Table 5. The rate of the hydration reactions of the cement became faster with the addition of NS. This finding was mainly ascribed to the chemical reactivity upon dissolution (pozzolanic activity) or to the high surface activity of NS particles, which caused the mortar to set and harden faster. The XRD analysis of hydration products of cement paste without NS and with NS30/4.0 hydrated at 1 day is illustrated in Figure 11. Moreover, the XRD curves of hydration products of cement paste without NS and NS30/4.0 hydrated at 3 days are exhibited in Figure 12. A comparison of these figures shows that the presence of AFm in the samples with NS addition could be observed after 1 day by XRD as shown in Figure 11(b). The rapid aggregation of AFm is mainly attributed to the sulphoaluminate cement. Therefore, the incorporation of NS can accelerate the hydration of sulphoaluminate cement. Note that NS\*\*/## = the content of \*\* nm NS is ## in the cement-based grouting material.

To study the characteristics of the surface microstructure on the interfacial transition zone (ITZ), SEM analysis was performed in this work. The broken specimens were analyzed by SEM to study the hydration products. Figures 13 and 14 present the surface microstructure of the ITZ. The SEM analysis of cement paste without NS is shown in Figure 13(a). The ITZ of cement paste without NS has massive crystals of AFt and  $\text{Ca}(\text{OH})_2$ . These effects can be explained by internal bleeding caused by the high local W/B ratio at the ITZ,

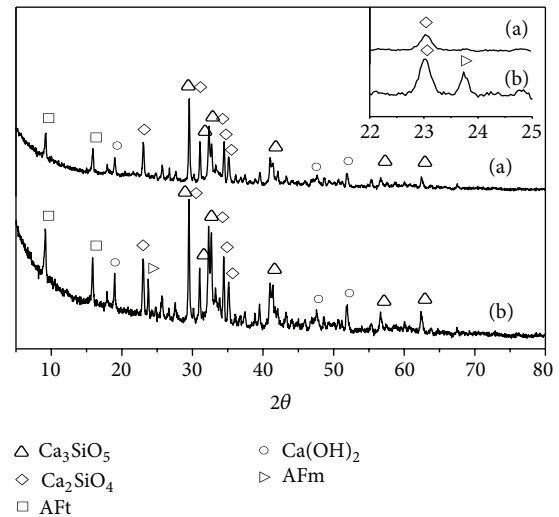


FIGURE 11: XRD of cement paste (a) without NS and (b) with NS30/4.0 at 1 day.

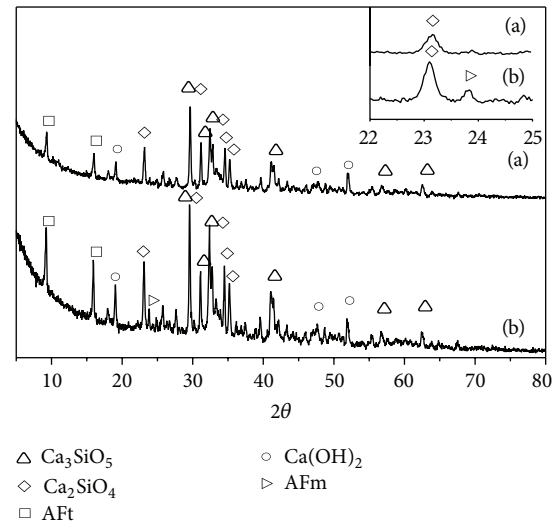


FIGURE 12: XRD of cement paste (a) without NS and (b) with NS30/4.0 at 3 days.

which produces large crystals and porous structures in plain samples.

Figure 13(b) shows the image of cement paste with NS30/4.0 at 1 day. Compared with Figures 13(a) and 13(b), the sample with NS30/4.0 had denser ITZ than the control sample. The ITZ with NS30/4.0 was denser because NS particles can fill the space between cement grains, a phenomenon called the packing effect of NS. Massive  $\text{Ca}(\text{OH})_2$  crystals

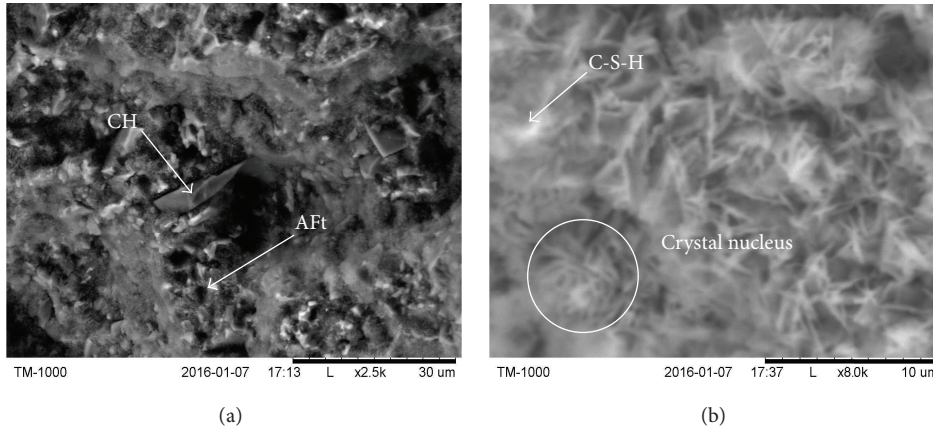


FIGURE 13: SEM of cement paste (a) without NS and (b) with NS30/4.0 at 1 day.

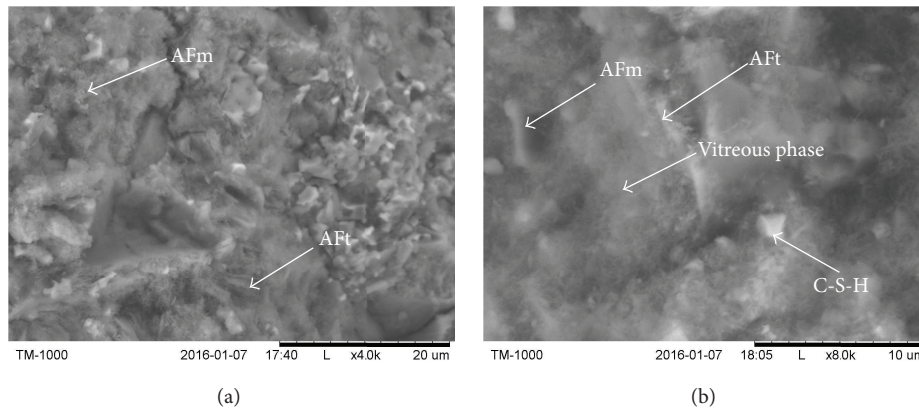


FIGURE 14: SEM of cement paste (a) without NS and (b) with NS30/4.0 at 3 days.

can react with NS to form the denser C-S-H gel. Nanosilica particles filled the gap between the cement particles as the packing effects of NS, making the particle size distribution of the cementitious material reach the state of dense packing. In addition, NSs could fill in the pores of the grouting material and provided the attachment point of the nucleus for hydrated products of C-S-H because of the small particle size, large specific surface area, and high surface activity. The network of C-S-H was continuously generated and developed outward until the surfaces of different crystal nuclei are close to one another. The C-S-H gel on the surface intertwined and formed a stable network skeleton. As the reaction continued, cement particles were surrounded by the accumulating hydration products, namely, AFt, AFm, and the C-S-H gel. This behavior could contribute to the microscopic and submicroscopic structure of the grouting material.

The differences in the surface microstructure of cement paste without NS and with NS30/4.0 at 3 days are shown in Figures 14(a) and 14(b). AFt and AFm crystals were observed in Figure 14(a). This behavior was related to the poor dispersion of the cement grains near the ITZ. With the addition of NS, the packing effects of NS can not only fill the capillary pores effectively but also reduce the gap at the joint of the aggregate interface, making the ITZ not

obvious. This case tended to accumulate water and other ionic species in the ITZ, thereby promoting the stability of these crystalline chemical structures. Cement paste with NS30/4.0 showed the aggregation of AFm and AFt, as well as the appearance of a vitreous phase. The latter was attributed to the pozzolanic reaction, which made the ITZ denser. Notably, the improvements can be related to other aspects, such as durability or even tensile strength [1, 31].

#### 4. Conclusions

The abovementioned findings led to the following conclusions:

- (1) With increased NS content, air content increased and apparent density decreased, but the NS particle sizes had minimal effect on the air content and apparent density.
- (2) With increased NS content, the setting time of mortar was significantly shortened; however, NS particle sizes had little influence on the setting time.
- (3) The effect of fluidity on the mortars adding NS with particle size of 30 nm was larger than NS with particle

sizes of 15 and 50 nm and the fluidity decreased with increased NS content, but the fluidity of mortars with the particle sizes of 15 and 50 nm was almost not affected by the NS content.

- (4) The formation of ettringite was promoted and the process of hydration reaction of cement was accelerated with the addition of NS.
- (5) With the addition of NS, the formation of C-S-H gel was promoted and the surface morphology of mortar was improved, making the interfacial transition zone denser.

## Competing Interests

The authors declare that they have no competing interests.

## Acknowledgments

The authors are grateful for the financial support from the National Natural Science Foundation of China (51208471), Outstanding Young Talent Research Fund of Zhengzhou University (1421322059), Science and Technology Planning project of Transportation in Henan Province (2016Y2-2), and the Specialized Research Foundation for the Doctoral Program of Higher Education (20114101120008).

## References

- [1] L. Senff, J. A. Labrincha, V. M. Ferreira, D. Hotza, and W. L. Repette, "Effect of nano-silica on rheology and fresh properties of cement pastes and mortars," *Construction and Building Materials*, vol. 23, no. 7, pp. 2487–2491, 2009.
- [2] H. Li, H.-G. Xiao, J. Yuan, and J. Ou, "Microstructure of cement mortar with nano-particles," *Composites Part B: Engineering*, vol. 35, no. 2, pp. 185–189, 2004.
- [3] I. Older, *Lea's Chemistry of Cement and Concrete*, Arnold, London, UK, 4th edition, 1998.
- [4] A. M. Neville, *Properties of Concrete*, ELBS with Addison Wesley Longman, Essex, UK, 4th edition, 1996.
- [5] M. Sonebi, E. García-Taengua, K. M. A. Hossain, J. Khatib, and M. Lachemi, "Effect of nanosilica addition on the fresh properties and shrinkage of mortars with fly ash and superplasticizer," *Construction and Building Materials*, vol. 84, article no. 6400, pp. 269–276, 2015.
- [6] S. Collepardi, A. Borsoi, J. J. Ogoumah Olagot et al., "Influence of nano-sized mineral additions on performance of SCC," in *Proceedings of the 6th International Congress, Global Construction, Ultimate Concrete Opportunities*, Dundee, UK, July 2005.
- [7] J. Björnström, A. Martinelli, A. Matic, L. Börjesson, and I. Panas, "Accelerating effects of colloidal nano-silica for beneficial calcium-silicate-hydrate formation in cement," *Chemical Physics Letters*, vol. 392, no. 1–3, pp. 242–248, 2004.
- [8] Y. Qing, Z. Zenan, K. Deyu, and C. Rongshen, "Influence of nano-SiO<sub>2</sub> addition on properties of hardened cement paste as compared with silica fume," *Construction and Building Materials*, vol. 21, no. 3, pp. 539–545, 2007.
- [9] M. Collepardi, J. J. Ogoumah Olagot, U. Skarp et al., "Influence of amorphous colloidal silica on the properties of self-compacting concretes," in *Proceedings of the International Conference in Concrete Constructions—Innovations and Developments in Concrete Materials and Constructions*, pp. 473–483, Dundee, Scotland, September 2002.
- [10] H. Li, M.-H. Zhang, and J.-P. Ou, "Abrasion resistance of concrete containing nano-particles for pavement," *Wear*, vol. 260, no. 11–12, pp. 1262–1266, 2006.
- [11] B.-W. Jo, C.-H. Kim, G.-H. Tae, and J.-B. Park, "Characteristics of cement mortar with nano-SiO<sub>2</sub> particles," *Construction and Building Materials*, vol. 21, no. 6, pp. 1351–1355, 2007.
- [12] G. Li, "Properties of high-volume fly ash concrete incorporating nano-SiO<sub>2</sub>," *Cement & Concrete Research*, vol. 34, no. 6, pp. 1043–1049, 2004.
- [13] J.-Y. Shih, T.-P. Chang, and T.-C. Hsiao, "Effect of nanosilica on characterization of Portland cement composite," *Materials Science and Engineering: A*, vol. 424, no. 1–2, pp. 266–274, 2006.
- [14] A. Nazari and S. Riahi, "The role of SiO<sub>2</sub> nanoparticles and ground granulated blast furnace slag admixtures on physical, thermal and mechanical properties of self compacting concrete," *Materials Science and Engineering A*, vol. 528, no. 4–5, pp. 2149–2157, 2011.
- [15] M.-H. Zhang and J. Islam, "Use of nano-silica to reduce setting time and increase early strength of concretes with high volumes of fly ash or slag," *Construction and Building Materials*, vol. 29, pp. 573–580, 2012.
- [16] R. M. Martins and A. J. F. Bombard, "Rheology of fresh cement paste with superplasticizer and nanosilica admixtures studied by response surface methodology," *Materials and Structures*, vol. 45, no. 6, pp. 905–921, 2012.
- [17] A. Nazari and S. Riahi, "Microstructural, thermal, physical and mechanical behavior of the self compacting concrete containing SiO<sub>2</sub> nanoparticles," *Materials Science and Engineering: A*, vol. 527, no. 29–30, pp. 7663–7672, 2010.
- [18] M. Stefanidou and I. Papayianni, "Influence of nano-SiO<sub>2</sub> on the Portland cement pastes," *Composites Part B: Engineering*, vol. 43, no. 6, pp. 2706–2710, 2012.
- [19] M. Choolaei, A. M. Rashidi, M. Ardjmand, A. Yadegari, and H. Soltanian, "The effect of nanosilica on the physical properties of oil well cement," *Materials Science and Engineering A*, vol. 538, pp. 288–294, 2012.
- [20] V. A. Doroganov, "Aspects of the modification of refractory concrete with nanosilica," *Refractories and Industrial Ceramics*, vol. 52, no. 6, pp. 409–413, 2012.
- [21] F. Sanchez and K. Sobolev, "Nanotechnology in concrete—a review," *Construction and Building Materials*, vol. 24, no. 11, pp. 2060–2071, 2010.
- [22] A. T. DiBenedetto, "Tailoring of interfaces in glass fiber reinforced polymer composites: a review," *Materials Science and Engineering: A*, vol. 302, no. 1, pp. 74–82, 2001.
- [23] J. M. Fraile, J. I. Garcia, J. A. Mayoral, and E. Vispe, "Comparison of hydrophilic and hydrophobic silicas as supports for titanium catalysts," *Applied Catalysis A: General*, vol. 276, no. 1–2, pp. 113–122, 2004.
- [24] F. Bauer, H.-J. Gläsel, E. Hartmann, H. Langguth, and R. Hinterwaldner, "Functionalized inorganic/organic nanocomposites as new basic raw materials for adhesives and sealants," *International Journal of Adhesion and Adhesives*, vol. 24, no. 6, pp. 519–522, 2004.

- [25] O. M. Al-Azzawi, C. M. Hofmann, G. A. Baker, and S. N. Baker, "Nanosilica-supported polyethoxyamines as low-cost, reversible carbon dioxide sorbents," *Journal of Colloid and Interface Science*, vol. 385, no. 1, pp. 154–159, 2012.
- [26] S. Rajendran, V. S. Bama, and M. R. Prabhu, "Effect of lithium salt concentration in PVAc/PMMA-based gel polymer electrolytes," *Ionics*, vol. 16, no. 1, pp. 27–32, 2010.
- [27] A. Dorigato, M. Sebastiani, A. Pegoretti, and L. Fambri, "Effect of silica nanoparticles on the mechanical performances of poly(lactic acid)," *Journal of Polymers and the Environment*, vol. 20, no. 3, pp. 713–725, 2012.
- [28] I. A. Rahman and V. Padavettan, "Synthesis of silica nanoparticles by sol-gel: size-dependent properties, surface modification, and applications in silica-polymer nanocomposites—a review," *Journal of Nanomaterials*, vol. 2012, Article ID 132424, 15 pages, 2012.
- [29] X. Xu and Z. Lu, "Effect of nano-silicon dioxide on hydration and hardening of portland cement," *Journal of the Chinese Ceramic Society*, vol. 35, no. 4, pp. 478–484, 2007.
- [30] Q. Lin, X. H. Lan, Y. B. Li et al., "Preparation and characterization of novel alkali-activated nano silica cements for biomedical application," *Journal of Biomedical Materials Research Part B: Applied Biomaterials*, vol. 95, no. 2, pp. 347–356, 2010.
- [31] A. R. Khaloo, A. G. Vayghan, and M. Bolhassani, "Mechanical and microstructural properties of cement paste incorporating nano silica particles with various specific surface areas," *Key Engineering Materials*, no. 478, pp. 19–24, 2011.

## Research Article

# Study on Acoustic Emission Characteristics of a Semirigid Base of Dense Skeleton Type during Complete Uniaxial Compression Tests

Shengli Li, Guangming Wu, and Hao Wu

School of Civil Engineering, Zhengzhou University, Zhengzhou 450001, China

Correspondence should be addressed to Shengli Li; [lsl2009@126.com](mailto:lsl2009@126.com)

Received 20 May 2016; Accepted 17 July 2016

Academic Editor: Ying Wang

Copyright © 2016 Shengli Li et al. This is an open access article distributed under the Creative Commons Attribution License, which permits unrestricted use, distribution, and reproduction in any medium, provided the original work is properly cited.

Acoustic emission testing of semirigid base specimens subjected to uniaxial compression was performed by a mechanical testing machine and AE system to find the AE criterion of the uniaxial compressive failure process of the semirigid base of dense skeleton types. AE counts, cumulative AE energy, and  $b$ -value were discussed. Results indicated that the AE parameters could reflect the failure process of semirigid bases of dense skeleton types. The failure process mainly underwent three stages that were divided based on AE parameters into initial stage of development, stable growth stage, and unstable stage. The knees of the AE parameter curve were at 25% and 85% of the ultimate load. The variation of the  $b$ -value could indicate the stress and be a precursor to the failure of the specimens. In general terms, a  $b$ -value greater than 3.5 indicates that specimens are at the initial stage of development. A  $b$ -value between 1 and 2 indicates that the specimens are at the stable growth stage. If the  $b$ -value seems to fluctuate and increase, the specimens are at the unstable stage. Moreover, the AE parameters indicated that attaching sensors to the waist of specimens was superior to that at other locations of a specimen.

## 1. Introduction

Semirigid bases possess many advantages such as high strength, good integrity, and low cost. Semirigid bases are used in the vast majority of high-grade asphalt pavements in China. Roads usually experience overload, and road damage that affects the normal operation of roads is a common occurrence. Applying nondestructive testing to road damage is essential in predicting the occurrence of road damage in advance, reducing the cost of road maintenance, and ensuring the normal operation of roads.

At present, ground penetrating radar (GPR) is the primary nondestructive detection method for road diseases. The GPR can easily detect a large size of disease [1, 2], for example, the void of road bases, but it has difficulty in detecting the crack of road bases that is a small size of disease. Acoustic emission (AE) is a propagation of elastic waves caused by the release of localized internal energy when a microfracture occurs in an elastic material [3]. An AE monitoring system can detect the development of damage

of a structure under load. We can identify changes and the condition of internal material by analyzing AE signals. Application of AE detection is very extensive; for example, AE has been used by scholars to study rocks under compression tests [4–7]. Research indicated that the AE counts of rocks increased with the increase of the load. Scholars also studied coal under compression tests with the AE system [8–10]. The relationship between AE parameters and the pressure of coal specimens was analyzed. The AE parameters could identify the damage characterization of coal specimens. In studying concrete under compression cracking, AE parameters could identify crack propagation in concrete specimens using the AE system [11–14]. Results provided guidance in evaluating the internal damage of concrete. The decrease of the  $b$ -value, which changed systematically with the different stages of the fracture process of rock [15–17] and concrete [18–20] under the load, indicated that the fracture process had moved from micro- to macrocracking as the material approached impending failure. However, the AE characteristics of semirigid bases of dense skeleton types have not yet been studied.

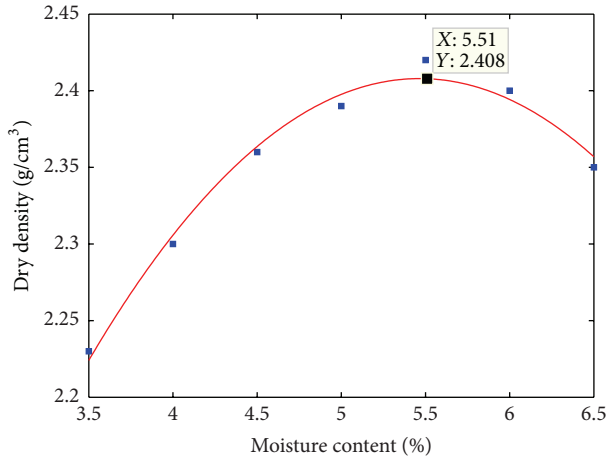


FIGURE 1: Relationship between moisture content and dry density.

Using AE requires damaging the structure under the load. The roads bear the load created by trucks; thus, we can acquire an AE signal when roads are being used. AE tests of semirigid base specimens subjected to uniaxial compression were conducted by using a TYE mechanical testing machine and an AE system to exploit the ability of AE to discover tiny cracks in the structure as well as to offset the shortage of GPR detected in the semirigid base asphalt pavement. AE counts, cumulative energy of AE signal waveform data, and  $b$ -value analysis of AE amplitude are discussed in detail. Support of AE detection of semirigid base of dense skeleton type was provided by the basic AE data which is discussed in this paper.

## 2. Material and Experimental Procedure

**2.1. Material and Specimen Preparation.** A compaction test was conducted in the laboratory to ensure optimum moisture content of semirigid mixtures. The relationship between moisture content and dry density is shown Figure 1, and optimum moisture content and maximal dry density were 5.51% and 2.41 g/cm<sup>3</sup>, respectively. The six specimens of the semirigid base of dense skeleton type were made at optimum moisture content by the molding of static pressure. The cylindrical specimens with a compaction degree of 98% had a diameter of 100 mm and a height of 100 mm, and the parallel of the end was under control at  $\pm 0.02$  mm for the nondestructive tests and compressive tests. The six specimens were cured for six days in a standard curing box where humidity was greater than 95% and temperature was at 20°C  $\pm$  2°C. Then, before the compressive tests, the six specimens were cured for one day in a curing tank filled with water. The semirigid mixture was composed of water, cement, and crushed stone, and the cement dosage was 4%. The design gradation of the semirigid base mixtures was determined as shown in Table 1.

**2.2. Test Setup and AE Instrumentation.** The compressive tests of the six specimens were performed by using the TYE mechanical testing machine with a maximum loading

TABLE 1: Design gradation of semi-rigid base mixtures.

Layer	Ratio (%) of crushed stone mass to crossed sieve (mm)							
	31.5	26.5	19	9.5	4.75	2.36	0.6	0.075
Base	100	100	77	48	27	22	11.5	1.5

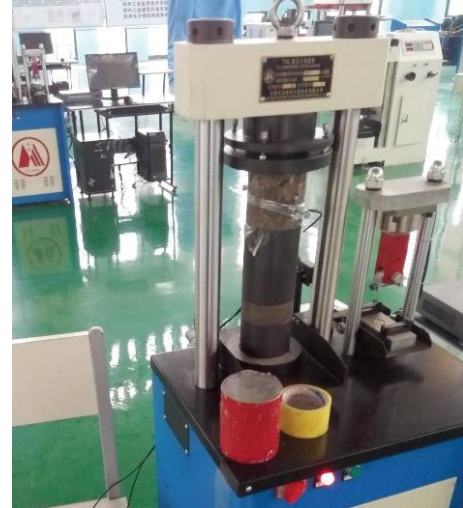


FIGURE 2: Mechanical testing machine.



FIGURE 3: AE data acquisition system.

capacity of 300 kN and variable loading input ranges. The AE signals were digitized by using an AE data acquisition system, which is a full-waveform data acquisition instrument. The amplitude distribution ranged from 0 to 100 dB (0 dB corresponds to 1  $\mu$ V at the sensor output). AE signals generated during the compression tests were recorded using a RS-2A piezoelectric AE sensor along with a 40 dB preamplifier. AE\_DS5 software was used to record and store AE waveform data with a low-pass filter ( $< 400$  kHz). In addition, the sampling rate was 2.5 MHz, and an AE trigger threshold of 35 dB was used in AE\_DS5 to remove the background noise. The TYE mechanical testing machine and AE data acquisition system are shown in Figures 2 and 3, respectively.

**2.3. Experimental Procedure.** Two schemes for sensor layout were used to comprehensively examine the AE characteristics of the semirigid base of dense skeleton type. The position

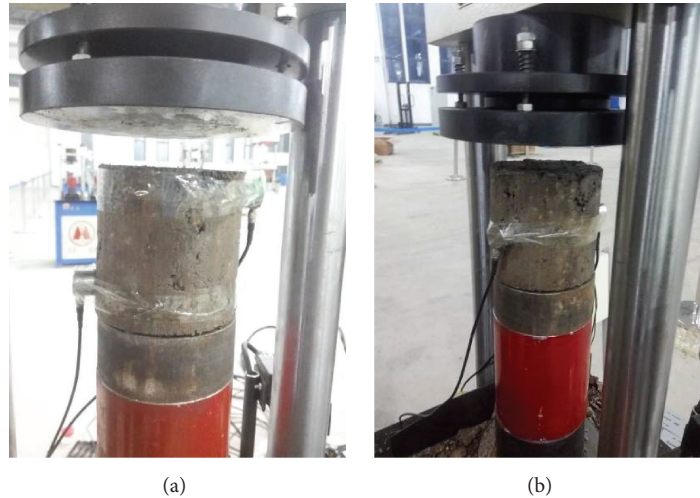


FIGURE 4: Schemes for sensor layouts: (a) sensors fixed in the middle of specimen and (b) sensors fixed on the end of specimen.

for laying sensors is shown in Figure 4. Vaseline was applied between the sensors and the specimen surface to improve AE coupling. The sensors were also secured by plastic tape to ensure that they would remain in place. The load was applied with a pressure rate of 0.39 kN/s to reduce the noise of the machine. The signal-to-noise ratio levels were improved by the instrument. The frequency of noise obtained from AE waveform by fast Fourier transform is lower than 4 kHz. The noise processing method is band-pass filtering, whose bandwidth is 5–400 kHz. The reasonable analysis parameter of AE\_DS5 was set to minimize the noise effect to obtain more accurate results. Through multiple comparisons of processing results, the fixed threshold was set at 40 dB. Peak definition time (PDT), hit definition time (HDT), and hit lockout time (HLT) were 150, 300, and 500  $\mu$ s, respectively. The experimental process is shown in Figure 5.

### 3. Results

The six specimens taken for the uniaxial compression test were divided into two groups corresponding to the two schemes for sensor layouts. Two channels were used to collect the AE signals generated as the specimens cracked. The result of each channel was similar in the same scheme. One channel of data in a group was analyzed in this paper. According to the AE parameter characteristic and the stress characteristic, the failure process of specimens mainly underwent three stages: an initial process of development (early period of loading), a stable growth stage (middle period of loading), and an unstable stage (end period of loading). The relations between AE hits and the stress level of the specimens under monotonic loading are indicated in Figures 6 and 7. The stress is normalized by peak stress to discuss the relations between stress level and AE parameters of specimens.

#### 3.1. AE Counts Analysis

**3.1.1. Sensor Fixed on End of Specimen.** As shown in Figure 6(a), AE counts rose quickly and continuously when

the stress of specimens was low. AE counts were relatively continuous and remained constant at a low level when the specimens were in the middle period of loading. Then, the AE counts increased rapidly at the final stress level. During the early period of loading, the AE counts escalated along with the increase of stress. At 7% of peak stress, the AE counts reached a short peak and then recovered calm. The AE generated was clearly active at low stress level of the specimen (relative stress less than 10%). The inside of specimens could not generate cracks because the stress was small. For the mixture of cement-stabilized macadam, original defects, for example, original microcracks, were generated unavoidably inside the specimens because of dry shrinkage, poor cementing materials, and so on. The original microcracks cracked because of stress concentration as the load on the specimens increased, and the AE events were generated by strain energy release. Therefore, during the early period of loading, the cracking of the original microcracks was the AE source. The specimens entered the middle period of loading as the stress increased. AE counts became few and relatively continuous, but the AE amplitude was larger than it was during the early period of loading, as shown in Figure 7(a). This figure indicates that the internal portion of specimens generated small microcracks as the stress increased; but the new microcracks were relatively stable and growth was slow at this stage. During the end period of loading, AE counts increased rapidly, and the specimens entered a critical state of ultimate bearing capacity. This result indicated the growth, propagation, and interconnection of new microcracks. Then, the interlocking effect of coarse aggregates disappeared, and the specimens were unstable and damaged.

**3.1.2. Sensor Fixed in the Middle of Specimen.** Figure 6(b) shows that the specimens generated few AE events at the initiation of compression. Then, AE counts increased quickly when the relative stress of specimens was between 15% and 25%. This observation implies that the original internal defects deteriorated as the relative stress was between 15%

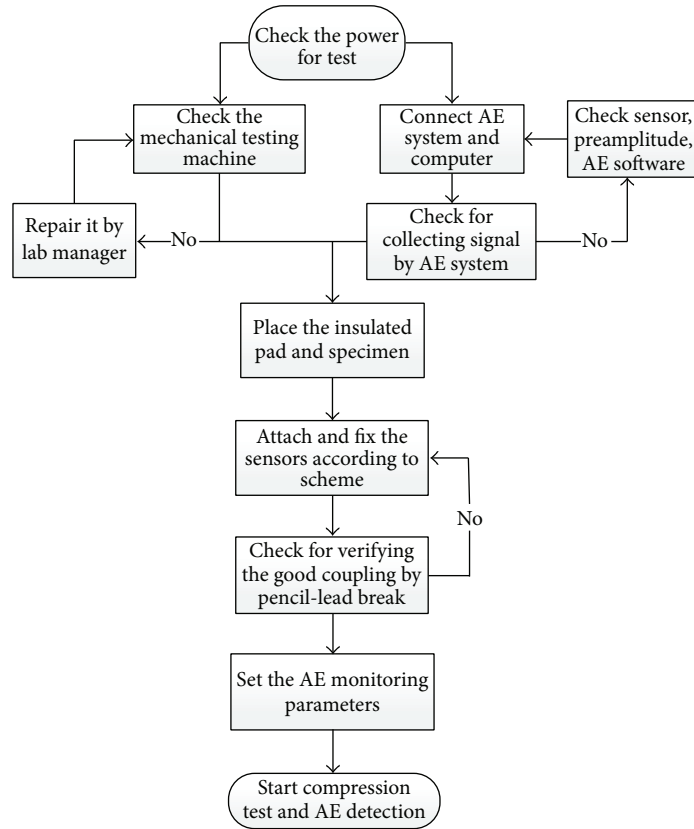


FIGURE 5: AE test process.

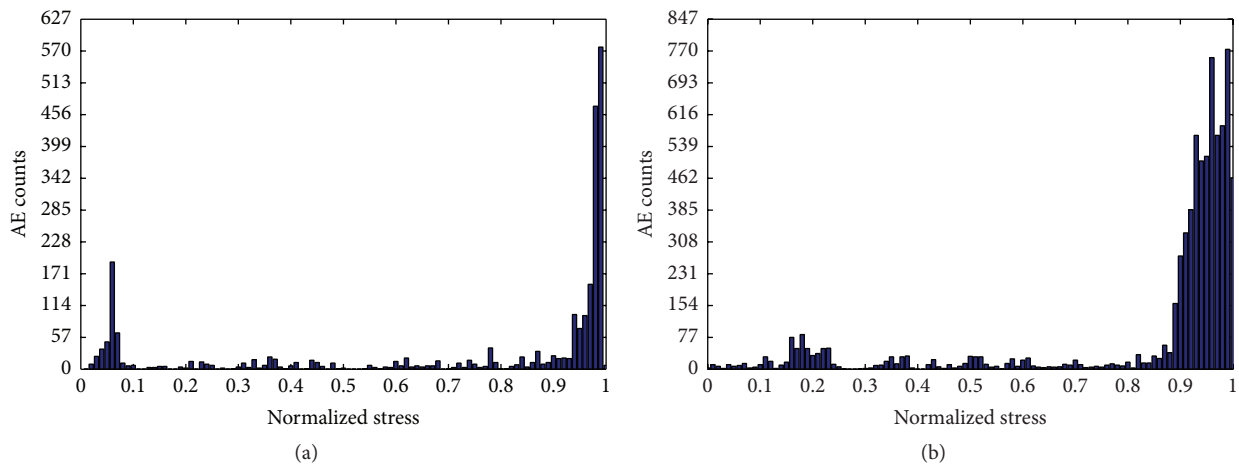


FIGURE 6: Variation of AE counts with relative stress: (a) sensor fixed on the end of specimen and (b) sensor fixed in the middle of specimen.

and 25%. During the middle period of loading, AE counts were continuous and remained low. Cumulative AE counts at this stage were equal to those in the early period of loading. This phenomenon can be explained that the degree of specimen damage during the middle period of loading is equal to the degree of specimen damage in the early period of loading. During the end period of loading, AE counts increased rapidly and lasted for a long time. This result indicates microcrack propagation and the generation

of numerous new microcracks that interconnected to become macrocracks. Then, the specimens lost carrying capacity.

*3.2. Cumulative AE Energy Analysis (AE Signal Strength Analysis).* AE energy is regarded as the area under the purified AE signal and over the duration of the AE waveform packet. It is generally referred to as relative energy, which relates to the amount of energy released by the material.

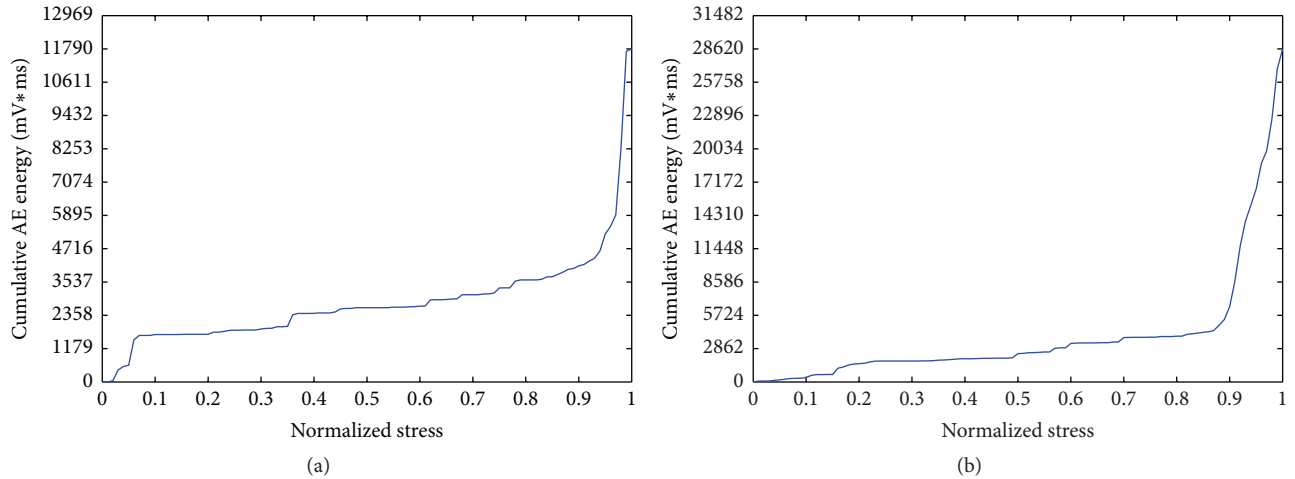


FIGURE 7: Variation of cumulative AE energy with relative stress: (a) sensor fixed on the end of specimen and (b) sensor fixed in the middle of specimen.

The cumulative AE energy data obtained from the specimens tested in this study are plotted in Figure 7.

**3.2.1. Sensor Fixed on the End of Specimen.** Figure 7(a) shows that, prior to the relative stress of 10%, cumulative AE energy obtained from the specimens increased quickly with the increase of stress, and it reached approximately 15% of the final value. The variation of the curve corresponded to the deterioration of the original defects. The slope of cumulative AE energy was flat, and the step phenomenon occasionally occurred during the middle period of loading. The increase of cumulative AE energy was estimated as equal to that in the previous stage. With the increase of load to the end period, the cumulative AE energy data curve ascended sharply and attained its maximum, indicating the failure of the specimen.

**3.2.2. Sensor Fixed in the Middle of Specimen.** Figure 7(b) shows that the cumulative AE energy increased gradually at the very beginning of the stress increase. The cumulative AE energy curve bent, and the slope of the curve was larger at the relative stress of 15%. The cumulative AE energy increased to 10% of total AE energy when the relative stress increased to 25%. The increment rate and increment of cumulative AE energy were inconspicuous during the middle period of loading, which indicates that few cracks were generated. At the relative stress of 85%, the curve abruptly steepened. This result indicates the propagation of microcracks and their interconnecting to form macrocracks. Then, the specimens lost carrying capacity.

**3.3.  $b$ -Value Analysis Based on AE Amplitude.** AE amplitude, expressed usually with unit of dB, is regarded as the peak value of the AE waveform packet. The parameter reflects the strength of an AE event. In this paper, AE amplitude characteristics are described by the  $b$ -value in the field of seismology. The  $b$ -value is a parameter defined originally by Gutenberg and Richter to estimate the likelihood of the

occurrence of earthquakes above a specified magnitude  $M$  [17]. The G-R equation is as follows:

$$\log_{10} N = a - bM, \quad (1)$$

where  $M$  is the Richter magnitude of earthquakes,  $N$  is the number of earthquakes with magnitude greater than  $M$ ,  $a$  is an empirical constant, and  $b$  is the slope, which is a linear relationship fitted between the magnitude of earthquakes and incremental frequency. However, the AE phenomenon is similar to an earthquake. Therefore, to apply the  $b$ -value to AE, the G-R formula is modified as follows:

$$\log_{10} N = a - b \left( \frac{A_{dB}}{20} \right), \quad (2)$$

where  $N$  is the incremental frequency (i.e., the number of AE hits with an amplitude greater than the threshold  $A_T$ ),  $a$  is an empirical constant, and  $b$  is the  $b$ -value that is defined as the log-linear slope of the cumulative amplitude distribution of AE [17, 21, 22].

**3.3.1. Sensor Fixed on the End of Specimen.** As shown in Figure 8(a), the  $b$ -value was a large number above 4 in the initial stages at which the relative stress ranged between 8% and 25%. With the increase in stress between 25% and 40%, the  $b$ -value decreased to less than 2. However, the  $b$ -value of AE hits commonly remained constant below 2 when the relative stress was larger than 40%. Finally, the relative stress rose to 85%, and the  $b$ -value began to fluctuate and enlarge.

**3.3.2. Sensor Fixed in the Middle of Specimen.** As shown in Figure 8(b), the shape of the curve is similar to that plotted in Figure 8(a). The  $b$ -value was a large number above 3.5 in the first instance where the relative stress was below 25%. However, it subsequently decreased and reached approximately 1.5 when the relative stress reached 60%. The  $b$ -value had almost no change until 90% of the relative stress. At the final stage, the  $b$ -value fluctuated and increased as expected.

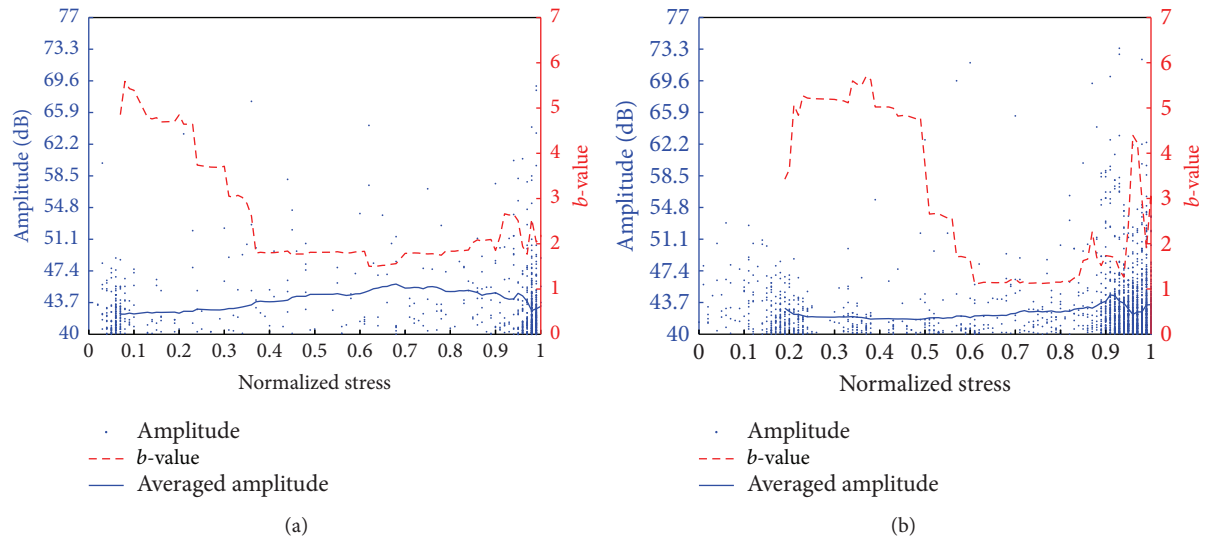


FIGURE 8: Variation of  $b$ -value: (a) sensor fixed on the end of specimen and (b) sensor fixed in the middle of specimen.

As Figure 8 shows, the  $b$ -value for estimating the semi-rigid base of dense skeleton type throughout the uniaxial compression tests changed schematically at different stages of fracture in specimens. The changes of  $b$ -value were concluded to four stages: early stage, where the  $b$ -value was large; middle stage, where the  $b$ -value gradually decreased; middle stage, where the  $b$ -value remained constant; and last stage, where the  $b$ -value increased again. For the mixture of cement-stabilized macadam, in the early stage, the energy of cracking of the original microcracks was small and the AE amplitude of weak elastic wave was less than 48 dB (the mean amplitude of 100 AE events was approximately 42.5 dB). Thus, the  $b$ -value based on the AE amplitude was large and generally larger than 3.5. In the middle stage of reducing value, the rate of AE hit was slow, and the AE data in the previous stage was used to calculate the  $b$ -value defined as the log-linear slope of the cumulative amplitude distribution of AE. However, the amplitude of AE generated by new internal cracks in the middle period of loading was larger; therefore, the  $b$ -value decreased with the increase in load, and this process was marked to the middle stage of reducing value. With the increase of stress, the accumulation of AE hits during the middle stage was enough to fit out the slope ( $b$ -value). Furthermore, the  $b$ -value was now stable without the effect of stress. In reality, all AE hits to fit out the  $b$ -value originated from the middle period of loading. Thus, the  $b$ -value in the middle stage of constant value was more prominent in the estimation for the condition of damage than in the middle stage of reducing value. In the middle period of loading, the original microcracks had cracked and the stress had been redistributed. With the increase in stress, the new crack generated AE hits whose amplitude was greater than 48 dB; thus, the  $b$ -value ranged between 1 and 2. In the end period of loading, numerous AE hits were recorded by sensors along with the occurrence of structural cracks of specimens. However, the ratio of low amplitude increased

because of weak cementation of material; thus, the  $b$ -value was fluctuant and increased with the increase in stress.

#### 4. Discussion

The AE characteristics of two different schemes for sensor layouts were qualitatively similar but still different to a certain extent. They are described as follows.

*Similarity.* According to the AE counts characteristic and cumulative AE energy characteristic versus stress, the failure process of specimens underwent three main stages: initial stage of development (early period of loading), stable growth stage (middle period of loading), and unstable stage (end period of loading). The initial stage of development lasted for a short period and the stable growth stage lasted for a long period, but the increments of AE counts in the two stages were almost equal, as well as the increments of cumulative AE energy. However, at the unstable stage, the AE counts and cumulative AE energy increased sharply. In addition, the  $b$ -value was categorized into four stages: the early stage with a large value, the middle stage with a reducing value, the middle stage with a constant value, and the last stage with an increasing value. The  $b$ -value was greater than 3.5 in the early stage. Then, the  $b$ -value was almost constant between 1 and 2 in the middle stage. Finally, the  $b$ -value fluctuated and increased but did not exceed 4 in the last stage of increasing value.

*Differences.* The AE counts and cumulative AE energy characteristics of sensors fixed on the end of specimens indicated that the end point of the initial stage of development was at 10% of peak stress, but the end point observed by the AE characteristics of sensors fixed in the middle of specimens was at 25% of peak stress. The stress cracking the original microcracks in the ends of the specimens was relatively lower

than the stress cracking the original microcracks in the waist of the specimens. This result occurred because the original defects at the specimen ends were weaker than that at the waist. The stable growth stage of specimens indicated that the stress was between 10% and 90% of ultimate stress by the AE parameter achieved from sensors fixed on the ends, and the percentages were between 25% and 85% according to the AE parameter achieved from sensors fixed at the waist. For the specimens of cement-stabilized macadam, the crack started from the middle of the specimens and propagated quickly to the ends. Furthermore, the end effect in the compression test also delayed the unstable cracking stress; thus, the stable growth stage was observed for a longer period by the AE parameter achieved from the sensor fixed on the ends. The unstable stage began from 90% of ultimate stress summarized by the AE parameter obtained from the sensor fixed on the ends and began from 85% of ultimate stress summarized by the AE parameter obtained from sensors fixed at the waist. In the unstable stage, the cumulative AE energy and AE counts recorded by the sensors fixed at the waist were larger than those recorded by sensors fixed on the end because numerous macrocracks had been generated on the waist of the specimens when the cracks propagated to the ends.

According to the above discussion and analysis, the failure process of a semirigid base of dense skeleton type was sensitively monitored by AE technology during the uniaxial compression tests, and the test method of sensors attached to the waist of the specimens was superior to that of the other sensors on reflecting the failure process. The crack state was detected by AE technology during the uniaxial compression tests in this paper, and the abrupt change of AE parameter and  $b$ -value indicated that the microcracks became the macrocracks in the specimens. The crack size was quite difficult to be quantified with AE analysis of the test. However, the AE detection combined with other detection technology was used to provide more credible information of the structural condition [23]. In future research, likewise, the research of AE detection combined with the GPR to detect and quantify the crack of semirigid base fast is carried out.

In addition, the variations of  $b$ -value of all specimens are similar in the same scheme for sensor layouts. Just a couple of  $b$ -values were analyzed because of limited space of the paper. The  $b$ -values regarding the crack developing stages are very much depending on the testing conditions. The effect of the testing conditions, for example, rate of loading, on the  $b$ -value is also a significant research.

## 5. Conclusions

The following conclusions are drawn:

- (1) AE parameters can reflect the failure process of a semirigid base of dense skeleton type. The failure process mainly underwent three stages that were divided by AE parameters into the initial stage of development (early period of loading), stable growth stage (middle period of loading), and unstable stage (end period of loading). The knees of the AE parameter curve occurred at 25% and 85% of ultimate load.

- (2) The variation of the  $b$ -value, which changed systematically with the different stages of the failure process, indicates the stress and is a precursor to specimen failure. In general terms, a  $b$ -value greater than 3.5 indicates that the specimens are at the initial stage of development. A  $b$ -value that remains stable between 1 and 2 indicates that the specimens are at the stable growth stage. Finally, a fluctuating and increasing  $b$ -value indicates that the specimens are at the unstable stage.
- (3) According to a comparison of the schemes of sensor layouts, the AE parameters saved by different test methods of position for attaching sensors indicated that the test method of sensors attached to the waist of the specimens reflected the failure process more effectively than that of the other sensors.

## Competing Interests

The authors declare that they have no competing interests.

## Acknowledgments

The authors are grateful for the financial support from the National Natural Science Foundation of China (51208471), Outstanding Young Talent Research Fund of Zhengzhou University (1421322059), Science and Technology Planning Project of Transportation in Henan Province (2016Y2-2), and the Specialized Research Foundation for the Doctoral Program of Higher Education (20114101120008).

## References

- [1] D. H. Chen, C. Tang, H.-B. Xiao, and P. Ying, "Utilizing electromagnetic spectrum for subsurface void detection—case studies," *Arabian Journal of Geosciences*, vol. 8, no. 9, pp. 7705–7717, 2014.
- [2] M. Li, R. Vilbig, R. Birken, D. Busuico, N. X. Sun, and M. Wang, "Novel miniaturized antenna designs for in-traffic air-coupled ground penetrating radar systems," *Journal of Environmental and Engineering Geophysics*, vol. 20, no. 1, pp. 71–79, 2015.
- [3] M. Shigeishi and M. Ohtsu, "Acoustic emission moment tensor analysis: development for crack identification in concrete materials," *Construction and Building Materials*, vol. 15, no. 5–6, pp. 311–319, 2001.
- [4] X.-J. Tang, J. Xu, and T. Deng, "Research on the rock acoustic emission rules under different experimental conditions," *Applied Mechanics and Materials*, vol. 170–173, pp. 237–241, 2012.
- [5] J.-S. Kim, K.-S. Lee, W.-J. Cho, H.-J. Choi, and G.-C. Cho, "A comparative evaluation of stress-strain and acoustic emission methods for quantitative damage assessments of brittle rock," *Rock Mechanics and Rock Engineering*, vol. 48, no. 2, pp. 495–508, 2014.
- [6] M. Rao, D. Murthy, G. Nagaraja Rao, S. K. Mohanty, and S. Udayakumar, "Stress-induced micro-cracking and brittle failure of Godhra granite, Gujarat: a laboratory investigation using acoustic emission," *Journal of the Geological Society of India*, vol. 64, no. 6, pp. 775–783, 2004.

- [7] Z.-Z. Zhang, F. Gao, and X.-J. Shang, "Rock burst proneness prediction by acoustic emission test during rock deformation," *Journal of Central South University*, vol. 21, no. 1, pp. 373–380, 2014.
- [8] M. S. A. Perera, P. G. Ranjith, and M. Peter, "Effects of saturation medium and pressure on strength parameters of Latrobe Valley brown coal: carbon dioxide, water and nitrogen saturations," *Energy*, vol. 36, no. 12, pp. 6941–6947, 2011.
- [9] P. G. Ranjith, D. Jasinge, S. K. Choi, M. Mehic, and B. Shannon, "The effect of CO<sub>2</sub> saturation on mechanical properties of Australian black coal using acoustic emission," *Fuel*, vol. 89, no. 8, pp. 2110–2117, 2010.
- [10] V. Vishal, P. G. Ranjith, and T. N. Singh, "An experimental investigation on behaviour of coal under fluid saturation, using acoustic emission," *Journal of Natural Gas Science and Engineering*, vol. 22, pp. 428–436, 2015.
- [11] Y. Yang, L. Zhang, J. Lv, and C. Wang, "Experimental study on fracture process of concrete by acoustic emission technology," *Przełąd Elektrotechniczny*, vol. 88, no. 9, pp. 55–58, 2012.
- [12] T. K. Haneef, K. Kumari, C. K. Mukhopadhyay, Venkatachalapathy, B. P. Rao, and T. Jayakumar, "Influence of fly ash and curing on cracking behavior of concrete by acoustic emission technique," *Construction and Building Materials*, vol. 44, pp. 342–350, 2013.
- [13] P. G. Ranjith, D. Jasinge, J. Y. Song, and S. K. Choi, "A study of the effect of displacement rate and moisture content on the mechanical properties of concrete: use of acoustic emission," *Mechanics of Materials*, vol. 40, no. 6, pp. 453–469, 2008.
- [14] T. Watanabe, S. Nishibata, C. Hashimoto, and M. Ohtsu, "Compressive failure in concrete of recycled aggregate by acoustic emission," *Construction and Building Materials*, vol. 21, no. 3, pp. 470–476, 2007.
- [15] X. Lei, K. Masuda, O. Nishizawa et al., "Detailed analysis of acoustic emission activity during catastrophic fracture of faults in rock," *Journal of Structural Geology*, vol. 26, no. 2, pp. 247–258, 2004.
- [16] X. Lei and T. Satoh, "Indicators of critical point behavior prior to rock failure inferred from pre-failure damage," *Tectonophysics*, vol. 431, no. 1–4, pp. 97–111, 2007.
- [17] M. Rao and K. Lakshmi, "Analysis of b-value and improved b-value of acoustic emissions accompanying rock fracture," *Current Science*, vol. 89, no. 9, pp. 1577–1582, 2005.
- [18] A. Carpinteri, G. Lacidogna, and S. Puzzi, "From criticality to final collapse: evolution of the 'b-value' from 1.5 to 1.0," *Chaos, Solitons & Fractals*, vol. 41, no. 2, pp. 843–853, 2009.
- [19] A. Carpinteri, G. Lacidogna, and G. Niccolini, "Fractal analysis of damage detected in concrete structural elements under loading," *Chaos, Solitons and Fractals*, vol. 42, no. 4, pp. 2047–2056, 2009.
- [20] R. V. Sagar and M. V. M. S. Rao, "An experimental study on loading rate effect on acoustic emission based b-values related to reinforced concrete fracture," *Construction and Building Materials*, vol. 70, pp. 460–472, 2014.
- [21] S. Colombo, I. G. Main, and M. C. Forde, "Assessing damage of reinforced concrete beam using 'b-value' analysis of acoustic emission signals," *Journal of Materials in Civil Engineering*, vol. 15, no. 3, pp. 280–286, 2003.
- [22] M. E. Zitto, R. Piotrkowski, A. Gallego, F. Sagasta, and A. Benavent-Climent, "Damage assessed by wavelet scale bands and b-value in dynamical tests of a reinforced concrete slab monitored with acoustic emission," *Mechanical Systems and Signal Processing*, vol. 60–61, pp. 75–89, 2015.
- [23] Y. Wang and H. Hao, "Integrated health monitoring for reinforced concrete beams: an experimental study," *Australian Journal of Mechanical Engineering*, vol. 8, no. 2, pp. 207–218, 2011.

## Research Article

# Emergency Communication and Quick Seismic Damage Investigation Based on Smartphone

Ruicong Han,<sup>1,2</sup> Xuefeng Zhao,<sup>1,2</sup> Yan Yu,<sup>3</sup> Quanhua Guan,<sup>4</sup> Deli Peng,<sup>1,2</sup>  
Mingchu Li,<sup>4</sup> and Jinping Ou<sup>1,2,5</sup>

<sup>1</sup>School of Civil Engineering, Dalian University of Technology, Dalian 116024, China

<sup>2</sup>State Key Laboratory of Coastal and Offshore Engineering, Dalian University of Technology, Dalian 116024, China

<sup>3</sup>School of Electronic Science and Technique, Dalian University of Technology, Dalian 116000, China

<sup>4</sup>School of Software Technology, Dalian University of Technology, Dalian 116000, China

<sup>5</sup>School of Civil Engineering, Harbin Institute of Technology, Harbin 150000, China

Correspondence should be addressed to Xuefeng Zhao; zhaoxf@dlut.edu.cn

Received 8 April 2016; Revised 31 May 2016; Accepted 20 June 2016

Academic Editor: Francesco dell'Isola

Copyright © 2016 Ruicong Han et al. This is an open access article distributed under the Creative Commons Attribution License, which permits unrestricted use, distribution, and reproduction in any medium, provided the original work is properly cited.

The communications in the quake-hit area are always cut off from the outside after the earthquake, and the traditional seismic field investigation method calls for immense time to accomplish house-to-house investigation, which goes against timeliness of the emergency rescue. In this paper, an emergency communication and quick seismic damage investigation method based on smartphone is proposed. Towards this, an application, E-Explorer, on iOS platform is initially developed. First, in the emergency communication module, the communication is available by using the Multipeer Connectivity Framework technology even without external network. A series of validation experiments are simulated without external network, and the results prove convincing. This module enhances the possibility of communication and increases the chances for rescue. Second, in the damage investigation module, E-Explorer integrates the functions of questionnaire and picture collection for damage phenomenon recording and image acquisition, following an intensity evaluation method according to seismic index. Last, a website, which provides guidance for rescue workers and collects damage information for quick intensity evaluation, is being built.

## 1. Introduction

The immediate resilience after the earthquake is becoming an important aspect worth being investigated [1, 2]. Emergency relief is the top priority. According to the Japan Kobe earthquake statistics, after the earthquake, 60% of buried people died shortly, while 40% of buried people are still alive and waiting for rescue [3]. A critical component of any successful rescue operation is time. However, the whole disaster areas are always cut off from the outside due to traffic congestion and communication interruption; the disaster rescue team cannot rush to the disaster area in a short time. So the direct involvement of residents is extremely important during the emergency, because it can improve the response and rescue process [4–9]. Thus, after the earthquake, residents in disaster areas actively and efficiently involved in mutual aid in

the earthquake zone are the most effective means to reduce casualties [10]. Our method can realize communication even without an external network, which will help officers get in touch with the trapped human which will be significant for saving lives.

The rapid assessment of losses at the first time after an earthquake can help officers determine the disaster affected areas and then provide scientific guidance for emergency response and rescue, which is significant to reduce casualties. However, the traditional damage investigation method after the earthquake needs multiple field investigation; the first-hand seismic disaster information cannot be mastered by the government. Moreover, the intensity values obtained by different investigators in one survey point may be different, which leads to great uncertainty in damage assessment. In fact, residents may help to identify an emergency and they can

play a significant role in the damage investigation progress. A higher number of residents will allow experts to better allocate government resources where they are needed and supplement the limited resources, helping them to go further [11]. So, a quick damage investigation method which can motivate residents is necessary.

Implementation of new information technologies in emergency response can potentially improve communication and coordination [12, 13]. Smartphones as a mobile-based information technology can be a solution to benefit quick seismic damage investigation and emergency communication in postdisaster relief experience. With an operating system, communication system, and built-in sensors, they have already been used in many fields other than the communication field, including human health monitoring [14], vehicle accident detection [15], motivation recognition [16], seismic sensing [17], and structural health monitoring [18–25]. What is more, smartphones and the Internet provide a means to use after an earthquake when a response is needed, especially since individuals are becoming very comfortable with the use of smartphones. Smartphones facilitate response in large-scale emergencies by enabling individuals to report information. Few examples of these applications are given by researchers [26–28], who developed a system for building damage assessment. However, their proposed application is only available in the Android operating system, which is a drastic limitation for the residents. Cimellaro et al. [29] developed an application, EDAM, on iOS and Android operating systems to survey the building earthquake damage, which is a perfect investigation system. But the emergency communication without external network is not considered, which is significant for saving lives. Fortunately, with the assistance of Wi-Fi hotspot and Bluetooth of various operating systems, smartphones can realize communication even without external networks.

In this paper, a new emergency response system based on smartphones is proposed. Towards this, the software E-Explorer which initially focused on the iOS operating system was developed with two main modules. First, the emergency communication is proposed by using Multipeer Connectivity Framework technology even without any external network. A series of experiments including connection experiment, connection distance experiment, and information transmission experiment were conducted to validate the feasibility of emergency communication under real conditions. Second, the quick seismic damage investigation is proposed to obtain first damage information right after the earthquake rapidly and efficiently by using smartphones which assist both specialists and residents to collect information about the disaster, following an intensity evaluation method based on seismic damage index according to Chinese Seismic Intensity Scale (2008). Last, a website (<http://www.e-explorer.cn/>) is built to gather disaster big data. On the one hand, trapped people's security status and positions are presented on the website to provide guidance for life relief, and, on the other hand, the damage pictures and questionnaire are integrated for intensity evaluation.



FIGURE 1: Main interface of E-Explorer.



FIGURE 2: Self-rescue knowledge after earthquake.

## 2. E-Explorer Overview

E-Explorer has been uploaded to Apple App Store for free download. And the Android version is being developed. The main interface is shown in Figure 1; two main modules, emergency communication and intensity evaluation, are developed. Emergency communication makes the information transmission possible even without an external network. Intensity evaluation is used to collect damage information by using questionnaire and pictures.

Emergency communication and intensity evaluation will be introduced in detail in the following parts. Except for these two modules, self-rescue is also developed in E-Explorer, which is shown in Figure 2. In this module, some general

TABLE 1: Wi-Fi standard and Bluetooth of each type.

iPhone type	Wi-Fi standard	Bluetooth
iPhone 4s	IEEE 802.11 b/g/n	Bluetooth 4.0
iPhone 5	IEEE 802.11 a/b/g/n	Bluetooth 4.0
iPhone 5c	IEEE 802.11 a/b/g/n	Bluetooth 4.0
iPhone 5s	IEEE 802.11 a/b/g/n	Bluetooth 4.0
iPhone 6	IEEE 802.11a/b/g/n/ac	Bluetooth 4.2
iPhone 6 Plus	IEEE 802.11a/b/g/n/ac	Bluetooth 4.2
iPhone 6s	IEEE 802.11a/b/g/n/ac, MIMO	Bluetooth 4.2
iPhone 6s Plus	IEEE 802.11a/b/g/n/ac, MIMO	Bluetooth 4.2
iPhone SE	IEEE 802.11a/b/g/n/ac, MIMO	Bluetooth 4.2

knowledge during or after earthquake is provided to save self-lives; also, some rescue examples are provided to increase the confidence of being rescued.

### 3. Emergency Communication without External Network

*3.1. Communication Principle.* The communication is based on Multipoint Connectivity, which is a framework that enables nearby devices to communicate over infrastructure Wi-Fi networks, peer-to-peer Wi-Fi, and Bluetooth personal area networks [30].

When the external network is available, E-Explorer can, as a general application, communicate with other devices freely. Otherwise, Wi-Fi hotspot or Bluetooth is selected to communicate with nearby devices according to the actual situation. The coverage radius of the Bluetooth is within 15 m, which is not enough for communication. However, once the WLAN is open even without Wi-Fi connection, the smartphone can serve as a Wi-Fi wireless hotspot to connect with the nearby devices according to the Wi-Fi standard, which will promote the communication range greatly. The connectivity properties of different devices are different because of the configuration. Table 1 shows the Bluetooth type and the Wi-Fi standard of iPhone [31].

IEEE 802.11 is the standard of the wireless local network. The characteristics such as bandwidth, transmission rate, and coverage radius of the protocol in iPhone are shown in Table 2 [32]. The physical tests about transmission distance in real conditions are conducted as Section 3.3.2 shows.

*3.2. Emergency Communication after Earthquake.* As Section 3.1 introduced, E-Explorer allows two mobile devices to exchange text and other formal information at a distance without external network connection. It may be an effective tool for emergency communication in the quake-hit area.

Figure 3 shows the realization flow chart of emergency communication. In E-Explorer, a database is built to store the important information for users under the special disaster background, including name, personal ID, position, whether they are trapped, injury status, and also the information notes of nearby people who call for help. The information needs to be filled and confirmed and then saved to the database. E-Explorer allows two nearby smartphones to share respective

information in the database automatically. Then, the important help information can be shared among the affected residents in this way theoretically. With more broad information sharing, more and more residents will get the information of trapped survivors. The information can be uploaded to the website as well, so that the relief rescue work can be implemented more efficiently with specific goals.

#### 3.3. Validation Experiments on Emergency Communication

*3.3.1. Connection Experiment.* Firstly, we conducted a connection test to check the communication without external network. Six residents, A, B, C, D, E, and F, were equipped with smartphones without any external network. Their positions and iPhone version are shown in Figure 4; the maximum distance between two residents is 20 m. Their personal information inputting interfaces are shown in Figure 5. It can be seen that the six smartphones' networks are not available. No SIM card is inserted; Bluetooth is available and WLAN is open without Wi-Fi connection.

After personal information submission, the six people are connected successfully and their information is shared. Taking C's screenshot as an example, Figure 6(a) shows the nearby people, and Figures 6(b) and 6(c) show the database. The communication among A, B, C, D, E, and F can be built, and everyone's messages can be received. The group chat is shown in Figure 6(d). A conversation between two people can be built by selecting one person in the database as in Figure 6(a). If E is chosen, C and E can communicate with each other freely. The conversation screenshot between them is shown in Figure 6(e).

From this experiment, it can be concluded that the communication can be built even if the external network is not available, and the information database can be uploaded to the website. Above all, after a major disaster, emergency communication through E-Explorer is very important for increasing residents' confidence of the emergency information and in promoting rescue efficiency.

*3.3.2. Connection Distance Experiment.* As experiment 1 validated, the communication can be built even without external network. The theoretical connection distance is given in Tables 1 and 2. The actual connection distance was tested by two iPhone 4s devices and two iPhone 6 devices.

In this experiment, iPhone 6 and iPhone 4s were tested indoors and outdoors, respectively. One person equipped with one smartphone stands close to the wall, while another person equipped with a smartphone moves away from the first person to connect the smartphone. The diagram is shown in Figure 7. Six groups of experiments are conducted; the solid line represents the notion that the smartphone can receive another smartphone's message, while the dotted line represents the notion that the smartphone cannot receive another smartphone's message.

Beyond the threshold value, which is defined as the maximum connection distance, a mobile phone cannot receive information from another one. The maximum connection distance and the penetrating walls capability tested are shown in Table 3.

TABLE 2: Characteristics of the communication protocol used in iPhone.

Protocol	Bandwidth (GHz)	Standard transmission rate (Mbit/s)	Max. transmission rate (Mbit/s)	Coverage radius (indoor)	Coverage radius (outdoor)
802.11a	5.15–5.35/5.47–5.725/5.725–5.875	25	54	30 m	45 m
802.11b	2.4–2.5	6.5	11	30 m	100 m
802.11g	2.4–2.5	25	54	30 m	100 m
802.11n	2.4 GHz or 5 GHz	300 (20 MHz * 4 MIMO)	600 (40 MHz * 4 MIMO)	70 m	250 m
802.11ac	5 GHz	433, 867 (80 MHz, 160 MHz)	867, 1730, 3470, 6930 (8 MIMO, 160 MHz)	35 m	

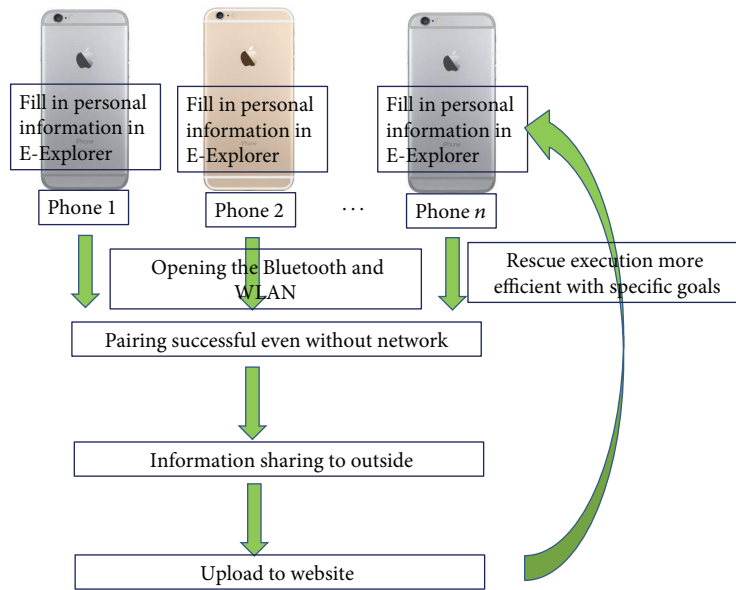


FIGURE 3: Emergency communication realization flow chart.

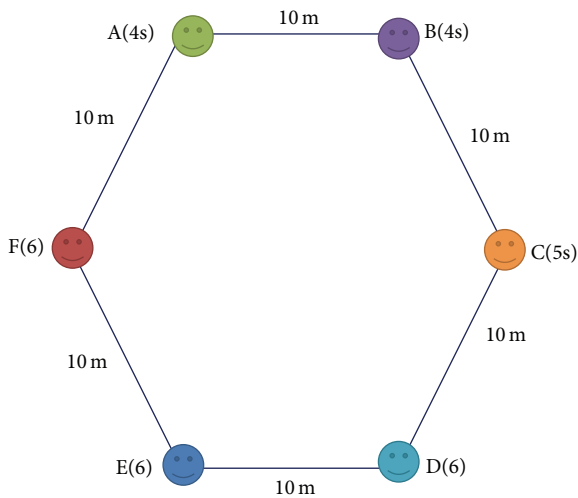


FIGURE 4: Positions and iPhone version of six residents.

TABLE 3: The tested maximum connection distance and through-walls ability.

Devices	Indoor maximum distance	Outdoor maximum distance	Through walls (load bearing wall)
4s & 4s	45 m	45 m	1
6 & 6	70 m	55 m	1
4s & 6	55 m	50 m	1

From Table 3, it can be seen that the maximum distance outdoors is less than that indoors, which does not coincide with the theoretical transmission. This may be due to

the more serious signal disturbance outdoors compared with that indoors. The communication distance of a higher version smartphone is better than that of a lower version smartphone. In the practical tests, the connection rate of iPhone 6 is better than that of iPhone 4s because of the bandwidth and transmission rate difference shown in Table 2. The capability of penetrating walls is not so perfect. This may be a limit for trapped people, whose condition is very complex. In general, it is difficult to determine the actual communication range, and connection failure is most likely to occur in the hit-quit



FIGURE 5: Inputting interfaces and networks.

area. But trapped people can call for help to nearby people who can communicate with the outside, and then the information can be delivered to the outside as a note on the nearby people's smartphones. This app offers more chances for disaster rescue and also provides the possibility of communicating with trapped people even when the external network is cut off.

3.3.3. *Information Transmission Experiment.* The experiments in Section 3.3.2 indicate that the connection distance is restricted; the connection of two smartphones may fail because of the large distance. So, information transmission is an issue to be considered. As Section 3.2 demonstrated, the connection node will contribute to information transmission. Two tests on different transmission patterns of smartphone node are given below.

(A) *Moving Node Pattern.* Figure 8 shows the experiment diagram. A, B, D, E, and F all opened up E-Explorer, and the distance between every two people is 80 m. The external networks of tested smartphones are not available. They cannot connect to each other because of the large distance. C is a moving person with E-Explorer opened and walks from A to F.

Figure 9 shows the test results of moving node experiment, Figures 9(a) and 9(c) show the information database on E and F, and Figures 9(b) and 9(d) show the nearby people of E and F. It can be seen that only two people can be connected; once C connected to one person, the information on C's smartphone can be shared. Consequently, the information of A-E can be transmitted to F.

From this experiment, it can be concluded that even if the connection is not available because of the long distance, once



FIGURE 6: Information on C's smartphone.

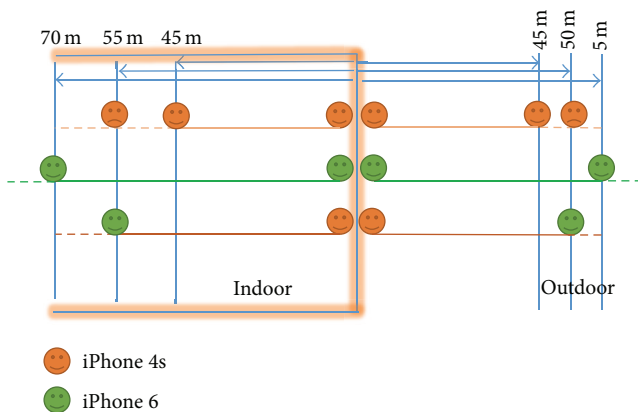


FIGURE 7: Connection distance experiment diagram.

a moving node exists, a temporary connection can be built and the information will be shared. This contributes to the earthquake relief work; a person who is not trapped can be a node to transmit information to the outside.

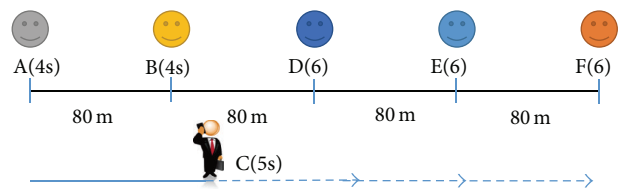


FIGURE 8: Moving node pattern experiment diagram.

(B) *Dense Node Pattern.* In order to build a distributed sensor network, a dense node experiment was conducted. The experiment diagram is shown in Figure 10. In the first step, A and F stand within a distance of 200 m. In the second step, B and C are added between A and F. Last, D and E are added between C and F. Their positions are shown in Figure 10.

For the first step, A and F cannot be connected because of the large distance.

For the second step, the information on C is shown in Figure 11(a); it can be seen that the information of A and B can be shared to C.



FIGURE 9: Results of moving node experiment.

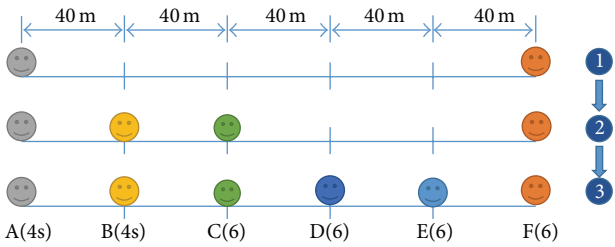


FIGURE 10: Dense node experiment diagram.

For the third step, D and E are added between C and F; the information on F's smartphone is shown in Figure 11(b); it can be seen that although only E is near to F, all their information can be shared.

From this experiment, it can be concluded that, with the quality of E-Explorer increasing, the information can be transmitted more widely. So, a smartphone equipped with E-Explorer can be used as a node in the information transmission network. The communication diagram is shown in Figure 12; each point is a node with E-Explorer, and a communication line can be built between them if the distance between two nodes is within the maximum communication distance; consequently, these two nodes can be connected successfully. As long as a sufficient number of nodes exist in the disaster zone, the communication between every two nodes can be built, and the help information can be shared. E-Explorer can build a temporary communication network system in the earthquake region, to overcome the communication difficulty under no external network connections. As Figure 12 shows, the help information of the trapped survivor A can be passed to relief worker B through several nodes; of course, the presented transmission line between A and B is not the only one.

From the validation experiments, it can be concluded that E-Explorer is an information storage and delivery platform. During the rescue, the rescued persons can transfer a large amount of help information of the survivors to the outside, which is helpful to take rescue measures quickly with the assistance of the obtained information about trapped condition and location.

#### 4. Quick Seismic Damage Investigation Based on E-Explorer

**4.1. Traditional Seismic Damage Investigation Method.** Disaster information acquired in a short time after an earthquake is the key to ensure the timeliness and accuracy of the intensity map and provide scientific guidance for rescue. Field investigation is the most common traditional method. As Figure 13 shows, experts need to gain a mount of seismic damage data in survey points and then go back to headquarters every day to summarize and analyze the damage information. The assessment of intensity relies on expert experience. The investigated building type, the damage level choice, and the difference between country and city—all these factors may lead to a different result.

Under this working pattern, the output of seismic intensity map needs much more time, especially in a serious earthquake. For example, after the earthquake in Wenchuan in 2008 occurred, experts were mobilized by China Earthquake Administration to investigate in many provinces. The final 8.0 seismic intensity map was obtained based on more than 50 square kilometers and more than 4150 survey points. It took more than 20 days to complete the intensity map of Wenchuan earthquake. The investigation speed was relatively low.

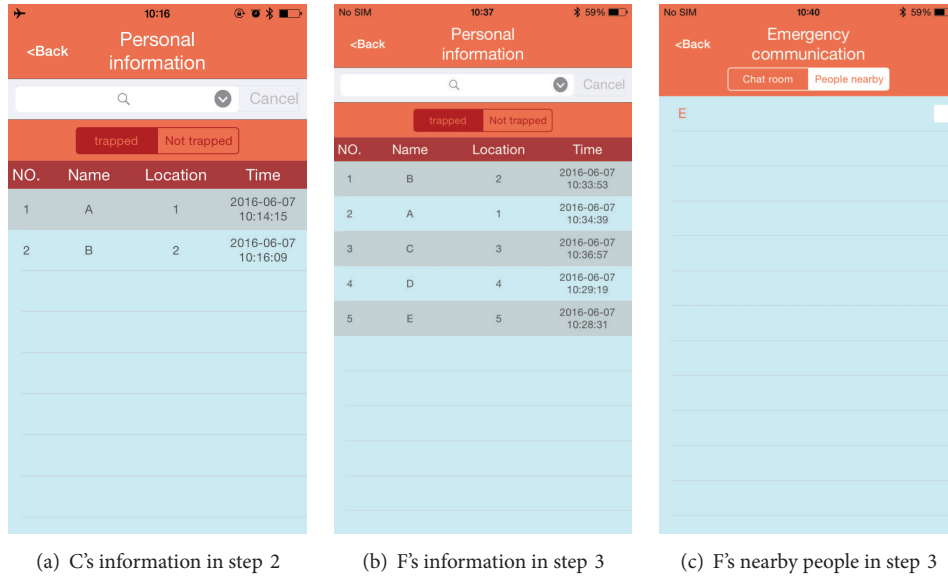


FIGURE 11: Results of dense node experiment.



FIGURE 12: Information transmission line schematic.

#### 4.2. Quick Seismic Damage Investigation Method Using E-Explorer

**4.2.1. Principle of the Method.** Immediate knowledge of the precise location and degree of damage saves time and saves lives. Such information is critical to disaster relief teams and public safety personnel to protect lives and reduce property loss. Previous traditional methods are ineffective and time-wasting. Therefore, a quick seismic investigation method using E-Explorer is proposed. The screenshot of seismic survey point with two purposes on E-Explorer is shown in Figure 14. The principle of this smartphone-based method is shown in Figure 15.

As Figure 15 shows, the smartphone-based investigation method employs E-Explorer to take damage photos, fill in

questionnaire, and collect position information and then upload the information to the data sharing website, and the information uploaded will be presented on the map. Last, the information is analyzed and summarized online to realize quick seismic damage assessment. Both professional staff and residents could collect information via smartphones; residents could report and receive information via the website to care about the situation of their own position, and communities could share information simultaneously to respond to a crisis of any damage magnitude.

**4.2.2. Questionnaire Investigation.** Seismic intensity indicates the seismic damage level and is evaluated by the consequences after the earthquake based on intensity scale. Intensity map expresses the damage level and disaster distribution intuitively, which is a basis for emergency relief works, such as the rapid deployment of rescue workers and materials. So, it is important to obtain the intensity map as soon as possible.

After the earthquake occurred, every person including seismic workers, volunteers, and residents can use E-Explorer to fill in the questionnaire according to the macroscopic phenomenon, which just takes a few minutes. Then, the result of the questionnaire with the location can be uploaded to the website. If there is no network in the investigation spot, the collected data can be stored and shared by using the emergency communication. Once one person's network is available, all information can be uploaded to the website. With this questionnaire, every smartphone with E-Explorer can help experts to accomplish intensity evaluation more efficiently.

The questionnaire is mainly based on the Chinese Seismic Intensity Scale (2008) [33] and takes macroscopic signs of seismic intensity as survey unit: feelings of people, reactions of objects, and conditions of building damage and earth's surface. The long-term practice shows that these macroscopic

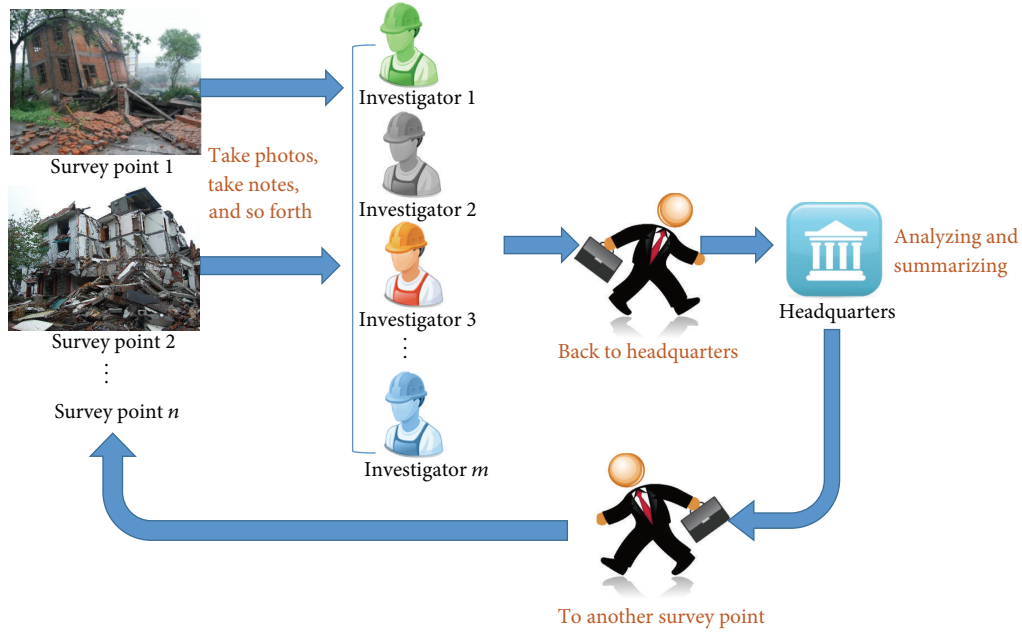


FIGURE 13: Traditional seismic damage investigation method.

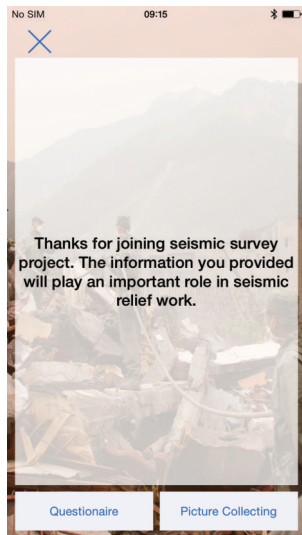


FIGURE 14: Screenshot of seismic survey.

signs are an effective criterion for seismic intensity evaluation, especially in China which has sparseness in seismic observation stations.

The questionnaire has seven questions which can be easily done by nonexperts (e.g., residents) who have not received professional training. Only with the strength of the masses at the real earthquake site can we get as much valuable and effective information as possible to carry out earthquake relief work in time. Figure 16 shows two questions of the questionnaire. Residents can choose the corresponding answer according to the actual situation. Then, the answers will be saved and uploaded to the website. The intensity value cannot be obtained directly according to the questionnaire on

E-Explorer, but the basic macrophenomenon information will be a reference for the damage assessment.

All questions and options are given in Table 4.

4.2.3. *Pictures Collection.* The answers may be different between nonexperts and experts, which may falsify the damage evaluation dramatically. Therefore, it was decided to focus on smartphones' cameras and consider the questionnaire as a supplement of the pictures. Residents can serve as “moving sensors” that can collect data information following the directions given by E-Explorer without any evaluation [27]. Pictures are the most important proof to assess the damage level. The screenshot of the pictures collection is shown in Figure 17.

### 4.3. Intensity Evaluation

4.3.1. *Houses Type.* The damage levels of different house types are obviously different, so house type is an important parameter for intensity evaluation. House type is classified into three categories according to the Chinese Seismic Intensity Scale (2008) [33].

*Type A.* This type is timber frame and antique house constructed by soil, stone, and brick.

*Type B.* This type is monolayer or multilayer brick masonry buildings without seismic fortification.

*Type C.* This type is monolayer or multilayer brick masonry buildings designed according to the 7-degree seismic fortification.

4.3.2. *Definition of Quantifier.* The descriptions for seismic influence and damage phenomena are macroscopic in

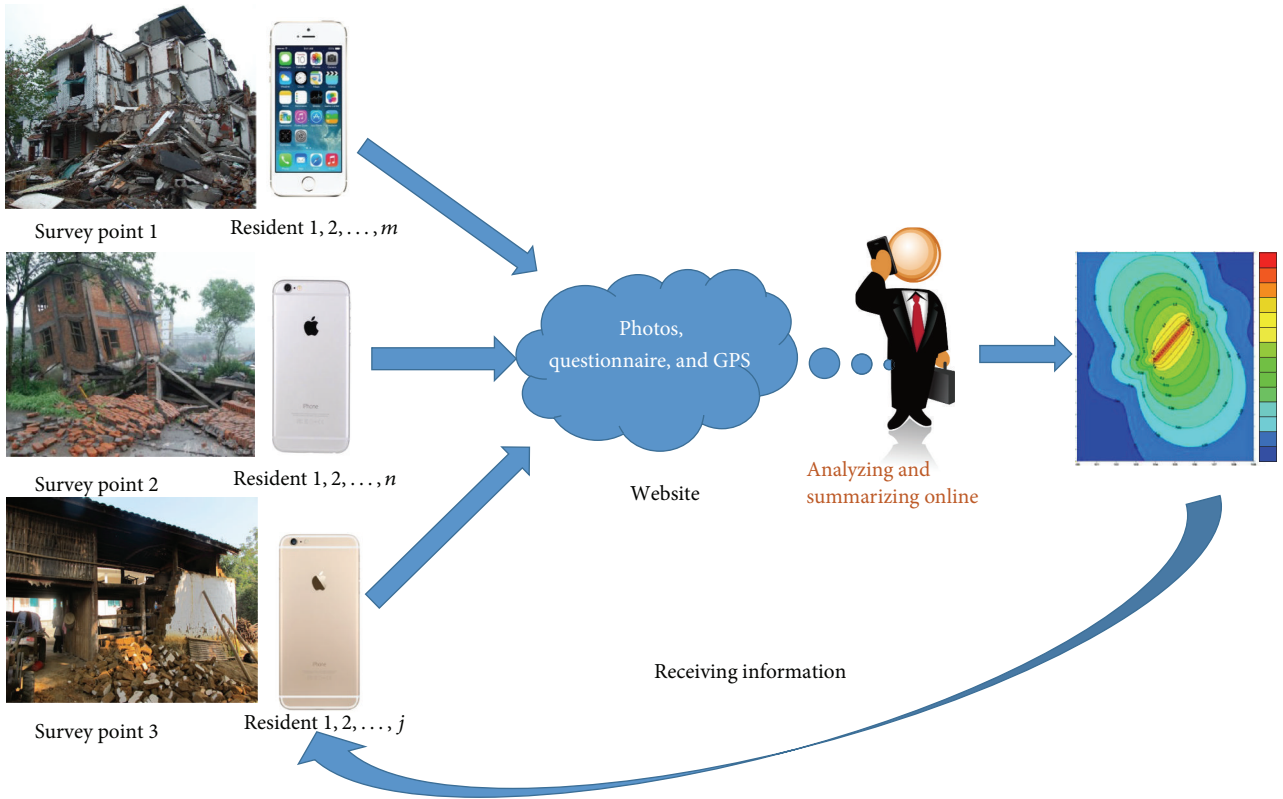
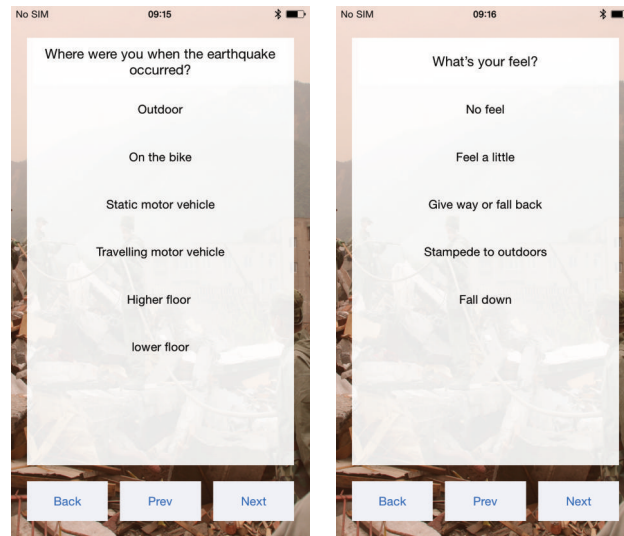


FIGURE 15: Flow chart of seismic damage investigation using smartphone.



(a) Question 1

(b) Question 2

FIGURE 16: Screenshots of the questionnaire.

the intensity scale and are expressed by fuzzy words. Their range is specified as follows:

- (a) Several: 0–10%.
- (b) Minority: 10–45%.
- (c) Majority: 40–70%.

(d) Great majority: 60–90%.

(e) Vast majority: 80–100%.

**4.3.3. Earthquake Damage Index.** Earthquake damage index grades the damage levels of houses. The damage index not only can evaluate the damage of a single house conveniently,

TABLE 4: All questions and options on questionnaire.

Question	Options
Where were you when the earthquake occurred?	(a) Outdoor
	(b) On the bike
	(d) Static motor vehicle
	(e) Travelling motor vehicle
	(c) Higher floor
What's your feel?	(d) lower floor
	(a) No feel
	(b) Feel a little
	(c) Give way or fall back
What's the reaction of hanging objects?	(d) Stampede to outdoors
	(e) Fall down
	(a) Slight shaking
	(b) Obvious shaking
	(c) Substantially shaking
What's the reaction of the implements?	(d) Objects dropped
	(a) Slight shaking
	(b) Obvious shaking
	(c) Implements in higher place overturned
What's the condition of the surface of the earth?	(d) Unstable implements are overturned
	(a) Cracks appears on soft soil
	(b) Cracks appears on dry ground
	(c) Large surface fractures, landslide occurs
How about your house?	(d) Mountains fall and the earth splits
	(a) Largely intact
	(b) Slight damage (several obvious cracks)
	(c) Moderate damage (more obvious cracks)
	(d) serious damage (collapsed partially)
What's the type of your house?	(e) Destruction (collapsed totally)
	(a) Old houses built by wood, soil, stone and brick
	(b) Monolayer or multilayer brick masonry building without the seismic fortified
	(c) Monolayer or multilayer brick masonry building design according to 7 degree earthquake
	(d) Other

but also can evaluate the damage of one survey point (e.g., take a village as a unit) based on statistics. It is a refining and quantitative expression for damage level. Damage index ranges from 0.00 (no damage) to 1.00 (completely destroyed).

The gradation of damage is divided into five levels: largely intact level, minor damage level, moderate damage level,



FIGURE 17: Screenshot of picture collection.

serious damage level, and destruction level. Their descriptions and corresponding damage index are shown in Table 5.

The mean damage index of one house type in one survey point is calculated according to

$$D_j = \sum_{i=1}^5 d_{i,j} \lambda_{i,j}, \quad (1)$$

where  $D_j$  is the mean damage index of house type  $j$ ,  $d_{i,j}$  is the damage index of house type  $j$  in  $i$ th damage level, and  $\lambda_{i,j}$  is the ratio of the damage level  $i$  of type  $j$  and is expressed as

$$\lambda_{i,j} = \frac{S_{i,j}}{\sum_{i=1}^5 S_{i,j}}, \quad (2)$$

where  $S_{i,j}$  is the house area or quantity of type  $j$ , in  $i$ th damage level.

Mean damage index  $D$  in one survey point can be obtained by solving the weighted average of  $D_j$  according to the area of each house type. And it is calculated as

$$D = \sum_j D_j \lambda_j, \quad (3)$$

where  $\lambda_j$  is the ratio between house type  $j$  and total houses and is expressed as

$$\lambda_j = \frac{S_j}{S}, \quad (4)$$

where  $S_j$  is the house area or quantity of type  $j$  and  $S$  is the total house area or quantity in a survey point.

The intensity evaluation progress based on E-Explorer is shown in Figure 18.

As Figure 18 shows, in one survey point, the damage pictures and questionnaire can be uploaded to the website by residents; the professionals can evaluate the damage index based on the pictures and then obtain the mean damage index.

TABLE 5: Quantization table of earthquake damage level.

Earthquake damage level	Earthquake damage index
Level 1: largely intact; bearing and nonbearing component in good condition or several nonbearing components have minor damage and can continue to be used without repair.	0–0.1
Level 2: minor damage; several bearing components have visible cracks; nonbearing components have obvious cracks; several nonbearing components suffer severe damage and can continue to be used after general repair.	0.1–0.3
Level 3: moderate damage; majority of bearing components have invisible cracks; minority of bearing components have obvious cracks; several nonbearing components suffer severe damage and can continue to be used after general repair.	0.3–0.55
Level 4: serious damage; majority of bearing components suffer severe damage; nonbearing components exhibit local collapse; it is hard to repair the house.	0.55–0.85
Level 5: destruction; majority of bearing components suffer severe damage; it is impossible to repair the house.	0.85–1

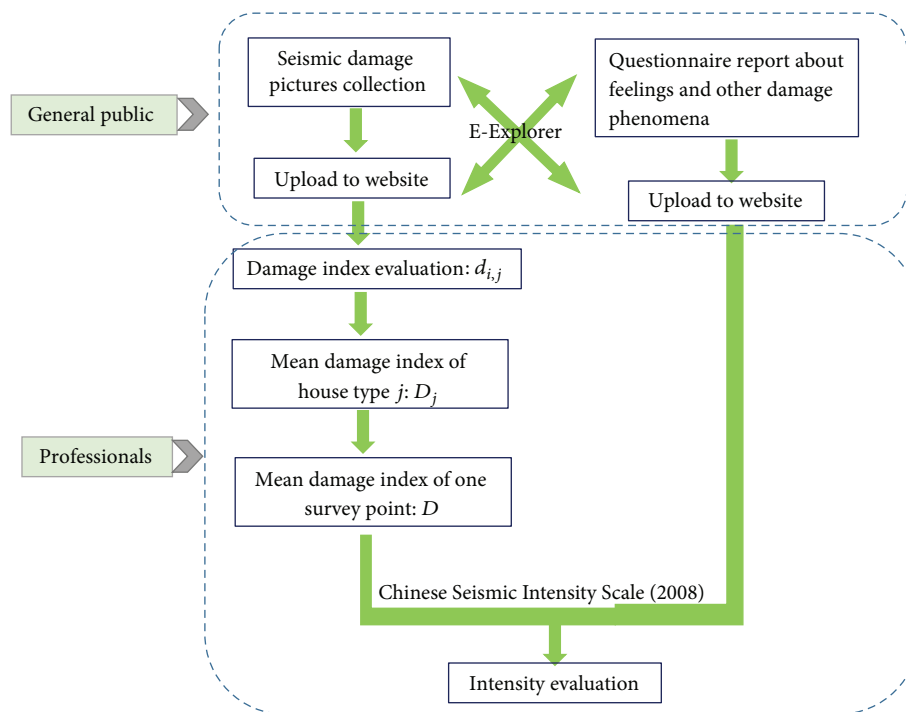


FIGURE 18: Intensity evaluation progress based on E-Explorer.

The intensity can be judged according to Table 6 by using the damage index and questionnaire answers. Intensity I to intensity V is judged mainly based on people's feelings and is omitted in the paper. Table 6 shows the intensity macroscopic description and corresponding damage index according to Chinese Seismic Intensity Scale (2008).

In conclusion, according to Chinese Seismic Intensity Scale (2008), the following steps are essential for quick intensity evaluation. First, motivate the residents to take photos and fill in the questionnaire on E-Explorer by using their smartphones and then upload the information to the website. Professionals check and assess the intensity from epicenter to outside according to the map on the website. Take natural village as an investigation element in the countryside, and take blocks as an investigation element in the city. Last, determine

the house type and mean damage index to assess intensity in seismic area. This method makes residents play a significant role in collaborating with experts to obtain damage information in a short time.

## 5. The Establishment of the Website

In order to build an emergency response system, a website is built to manage the big data uploaded from E-Explorer. The URL is <http://www.e-explorer.cn/>, which is shown in Figure 19.

There are two purposes of the website. The first is to release the name, location, and other information of the trapped people, which can be visually displayed on the map.

TABLE 6: Macroscopic description of intensity level and corresponding damage index.

Intensity	House type	Macroscopic description	Mean damage index
VI	A	Minority in moderate damage level, majority in minor damage level and/or largely intact level	0.00–0.11
	B	Several in moderate damage level, minority in minor damage level, majority in largely intact level	
	C	Several in minor damage level, majority in largely intact level	
VII	A	Minority in serious damage level and/or destruction level, majority in moderate damage level and/or minor damage level	0.09–0.31
	B	Minority in moderate damage level, majority in minor damage level and/or largely intact level	
	C	Minority in moderate damage level and/or minor damage level, majority in largely intact level	
VIII	A	Minority in destruction level, majority in serious damage level and/or moderate damage level	0.29–0.51
	B	Several in destruction level, minority in serious damage level, majority in moderate damage level and/or minor damage level	
	C	Minority in serious damage level and/or moderate damage level, majority in minor damage level	
IX	A	Majority in serious damage level and/or destruction level	0.49–0.71
	B	Minority in destruction level, majority in serious damage level and/or moderate damage level	
	C	Minority in destruction level and/or serious damage level, majority in moderate damage level and/or minor damage level	
X	A	Vast majority in destruction level	0.69–0.91
	B	Great majority in destruction level	
	C	Majority in destruction level and/or serious damage level	
XI	A	Vast majority in destruction level	0.89–1.00
	B		0.78–1.00
	C		
XII	A	Almost all in complete destruction level	1.00
	B		
	C		



(a) Main page on the website



(b) People on the map

FIGURE 19: The website.

Figure 19(a) shows the main map of the website, and Figure 19(b) shows the local information with marks, which are the submitted information by users. The blue mark refers to people not trapped, and the red mark stands for people trapped. The detailed information can be shown by clicking the mark. According to the data on the website, officers can obtain casualties statistics quickly, and the information on the website can also provide scientific guidance for rescue.

The second purpose is to collect the damage information from smartphones, reduce the field investigation time, and realize the quick seismic damage evaluation by checking the information on the website.

## 6. Conclusions

In this paper, an application, E-Explorer, and a website are developed on iOS operating system to realize emergency communication and quick seismic damage investigation. E-Explorer is made up of two basic modules. The emergency communication module makes the information transmission possible without external network connections, which can provide important information to others for personal survival, enhance the possibility of communication, and increase the chances for rescue. Three experiments validated the connection, connection distance, and information transmission of emergency communication. The damage investigation module provides a quick investigation method for seismic damage with the assistance of picture collection, questionnaire, and data uploading. Last, a website, <http://www.e-explorer.cn/>, is built to gather big data of the personal information and damage information, and then more scientific responses can be carried out after analyzing the uploaded information. So, this technique promises to be an efficient tool for postdisaster relief. A resident with a smartphone is a potential rescuer to help trapped people, a potential investigator of emergency information, a potential reporter to transmit information, and a potential recipient of information that might prove lifesaving. The application will be developed and discussed on other operating systems in our future work, and the adaptability of the seismic intensity assessment in other regions will be involved in the next stage.

## Competing Interests

The authors declare that there are no competing interests regarding the publication of this paper.

## Acknowledgments

This research was financially supported by the National Natural Science Foundation of China (51278085, 51479031, and 51161120359), the National Basic Research Program of China (2011CB013705), Program for Liaoning Excellent Talents in University (LJQ2015028), and the Fundamental Research Funds for the Central Universities (DUT15ZD117).

## References

- [1] M. Domaneschi and L. Martinelli, "Earthquake-resilience-based control solutions for the extended benchmark cable-stayed bridge," *Journal of Structural Engineering*, Article ID C4015009, 2015.
- [2] C. W. Zobel and L. Khansa, "Characterizing multi-event disaster resilience," *Computers and Operations Research*, vol. 42, pp. 83–94, 2014.
- [3] Y. Kuwata and S. Takada, "Rescue ability for earthquake casualty during the 1995 Kobe Earthquake," *Departmental Bulletin Paper*, pp. 215–220, 2000.
- [4] G. P. Cimellaro, A. M. Reinhorn, and M. Bruneau, "Framework for analytical quantification of disaster resilience," *Engineering Structures*, vol. 32, no. 11, pp. 3639–3649, 2010.
- [5] G. P. Cimellaro, A. M. Reinhorn, and M. Bruneau, "Seismic resilience of a hospital system," *Structure and Infrastructure Engineering*, vol. 6, no. 1-2, pp. 127–144, 2010.
- [6] M. Pelling, *The Vulnerability of Cities: Natural Disasters and Social Resilience*, Earthscan, 2012.
- [7] S. L. Cutter, L. Barnes, M. Berry et al., "A place-based model for understanding community resilience to natural disasters," *Global Environmental Change*, vol. 18, no. 4, pp. 598–606, 2008.
- [8] B. Maguire and H. Patrick, "Disasters and communities: understanding social resilience," *Australian Journal of Emergency Management*, vol. 22, no. 2, pp. 16–20, 2004.
- [9] M. G. Kweit and R. W. Kweit, "Citizen participation and citizen evaluation in disaster recovery," *The American Review of Public Administration*, vol. 34, no. 4, pp. 354–373, 2004.
- [10] Y. Shu, M. Xu, and Y. Liu, "Self-help and mutual rescue—the relief work in serious earthquake," *Journal of Hebei Institute of Technology: Social Science Edition*, vol. 3, no. 3, pp. 33–35, 2003 (Chinese).
- [11] M. Schoch-Spana, C. Franco, J. B. Nuzzo, and C. Usenza, "Community engagement: leadership tool for catastrophic health events," *Biosecurity and Bioterrorism*, vol. 5, no. 1, pp. 8–25, 2007.
- [12] L. K. Comfort, *Shared Risk: Complex Systems in Seismic Response*, Emerald Group Publishing, Somerville, Mass, USA, 1999.
- [13] L. K. Comfort and N. Kapucu, "Inter-organizational coordination in extreme events: the world trade center attack," *Natural Hazards*, vol. 39, pp. 309–327, 2001.
- [14] S. L. Lau and K. David, "Movement recognition using the accelerometer in smartphones," in *Proceedings of the IEEE Future Network and Mobile Summit*, pp. 1–9, Florence, Italy, June 2010.
- [15] H. Ketabdar and T. Polzehl, "Fall and emergency detection with mobile phones," in *Proceedings of the 11th International ACM SIGACCESS Conference on Computers and Accessibility (ASSETS '09)*, pp. 241–242, Pittsburgh, Pa, USA, October 2009.
- [16] M. Mladenov and M. Mock, "A step counter service for Java-enabled devices using a built-in accelerometer," in *Proceedings of the ACM 1st International Workshop on Context-Aware Middleware and Services: Affiliated with the 4th International Conference on Communication System Software and Middleware (COMSWARE '09)*, pp. 1–5, Dublin, Ireland, June 2009.
- [17] J. Reilly, S. Dashti, M. Ervasti, J. D. Bray, S. D. Glaser, and A. M. Bayen, "Mobile phones as seismologic sensors: automating data extraction for the shake system," *IEEE Transactions on Automation Science and Engineering*, vol. 10, no. 2, pp. 242–251, 2013.

- [18] Y. Yu, X. Zhao, and J. Ou, "A new idea: mobile structural health monitoring using Smart phones," in *Proceedings of the 3rd International Conference on Intelligent Control and Information Processing (ICICIP '12)*, pp. 714–716, Dalian, China, July 2012.
- [19] X. Zhao, R. Han, Y. Ding et al., "Portable and convenient cable force measurement using smartphone," *Journal of Civil Structural Health Monitoring*, vol. 5, no. 4, pp. 481–491, 2015.
- [20] Y. Yu, R. Han, X. Zhao et al., "Initial validation of mobile-structural health monitoring method using smartphones," *International Journal of Distributed Sensor Networks*, vol. 2015, Article ID 274391, 14 pages, 2015.
- [21] X. Zhao, D. Peng, W. Hu et al., "Quick seismic intensity map investigation and evaluation based on cloud monitoring method using smart mobile phone," in *Proceedings of the in SPIE Smart Structures and Materials+ Nondestructive Evaluation and Health Monitoring*, vol. 9437 of *Proceedings of SPIE*, p. 94372, The International Society for Optics and Photonics, San Diego, Calif, USA, March 2015.
- [22] G. Morgenthal and H. Höpfner, "The application of smartphones to measuring transient structural displacements," *Journal of Civil Structural Health Monitoring*, vol. 2, no. 3-4, pp. 149–161, 2012.
- [23] H. Höpfner, G. Morgenthal, M. Schirmer, M. Naujoks, and C. Halang, "On measuring mechanical oscillations using smartphone sensors: possibilities and limitation," *ACM SIGMOBILE Mobile Computing and Communications Review*, vol. 17, no. 4, pp. 29–41, 2013.
- [24] M. Feng, Y. Fukuda, M. Mizuta, and E. Ozer, "Citizen sensors for SHM: use of accelerometer data from smartphones," *Sensors*, vol. 15, no. 2, pp. 2980–2998, 2015.
- [25] E. Ozer, M. Q. Feng, and D. Feng, "Citizen sensors for SHM: towards a crowdsourcing platform," *Sensors*, vol. 15, no. 6, pp. 14591–14614, 2015.
- [26] M. Fujii, M. Ohara, and K. Meguro, "Development of remote building damage assessment system during large-scale earthquake disaster," in *Proceedings of the 15th World Conference on Earthquake Engineering (WCEE '12)*, pp. 24–28, Lisbon, Portugal, September 2012.
- [27] V. Arcidiacono and G. P. Cimellaro, "Damage report with smartphones during Emilia earthquake, 2012," in *Proceedings of the 4th International Conference on Computational Methods in Structural Dynamics and Earthquake Engineering (COMPdyn '13)*, pp. 517–526, Kos Island, Greece, June 2013.
- [28] G. Scura, V. Arcidiacono, G. P. Cimellaro, C. Renschler, and A. M. Reinhorn, "Integrated damage assessment communication system using smartphone network during 2012 Emilia earthquake," in *Proceedings of the Vienna Congress on Recent Advances in Earthquake Engineering and Structural Dynamics & 13. D-A-CH Tagung (VEESD '13)*, Vienna, Austria, August 2013.
- [29] G. P. Cimellaro, G. Scura, C. S. Renschler, A. M. Reinhorn, and H. U. Kim, "Rapid building damage assessment system using mobile phone technology," *Earthquake Engineering and Engineering Vibration*, vol. 13, no. 3, pp. 519–533, 2014.
- [30] <http://nshipster.com/multipeer-connectivity/>.
- [31] <https://www.apple.com/cn/iphone-6s/specs/>.
- [32] [https://zh.wikipedia.org/wiki/IEEE\\_802.11](https://zh.wikipedia.org/wiki/IEEE_802.11).
- [33] GB/T, "Chinese seismic intensity scales," GB/T 17742-2008, 2008.

## Research Article

# Magnetodielectric and Metalomagnetic 1D Photonic Crystals Homogenization: $\epsilon$ - $\mu$ Local Behavior

**J. I. Rodríguez Mora,<sup>1,2</sup> J. Flores Méndez,<sup>1,2</sup> B. Zenteno Mateo,<sup>1</sup>  
F. Severiano Carrillo,<sup>1</sup> and R. C. Ambrosio Lázaro<sup>1</sup>**

<sup>1</sup>*Benemérita Universidad Autónoma de Puebla, Ciudad Universitaria, Boulevard Valsequillo Esquina, Avenida San Claudio s/n, Colonia San Manuel, Apartado Postal J-39, 72570 Puebla, PUE, Mexico*

<sup>2</sup>*División de Estudios de Posgrado e Investigación, Maestría en Ciencias en Ingeniería Mecánica, Instituto Tecnológico de Puebla, Avenida Tecnológico 420, Maravillas, 72220 Puebla, PUE, Mexico*

Correspondence should be addressed to J. Flores Méndez; [xavier\\_snk@hotmail.com](mailto:xavier_snk@hotmail.com)

Received 23 February 2016; Accepted 12 April 2016

Academic Editor: Francesco dell'Isola

Copyright © 2016 J. I. Rodríguez Mora et al. This is an open access article distributed under the Creative Commons Attribution License, which permits unrestricted use, distribution, and reproduction in any medium, provided the original work is properly cited.

A theory for calculating the effective optic response of photonic crystals with metallic and magnetic inclusions is reported, for the case when the wavelength of the electromagnetic fields is much larger than the lattice constant. The theory is valid for any type of Bravais lattice and arbitrary form of inclusions in the unitary cell. An equations system is obtained for macroscopic magnetic field and magnetic induction components expanding microscopic electromagnetic fields in Bloch waves. Permittivity and permeability effective tensors are obtained comparing the equations system with an anisotropic nonlocal homogenous medium. In comparison with other homogenization theories, this work uses only two tensors: nonlocal permeability and permittivity. The proposal showed here is based on the use of permeability equations, which are exact and very simple. We present the explicit form of these tensors in the case of binary 1D photonic crystals.

## 1. Introduction

The material properties and their potential applications research are very important in the industry and scientific areas. However, all these impacts could not be possible without the great advances developed in the last 100 years in materials science. Thanks to metallurgy, ceramics, and plastics advances, engineers have been able to modify a wide range of mechanical and electrical properties in materials. Semiconductor physics advances have allowed adjusting the conductive properties of certain materials, initiating the electronics revolution. Scientists have discovered high-temperature superconductors with new alloys and ceramics. It is impossible to cite all applications derived from materials science. In recent years, scientists have a new challenge, to study artificial materials and their optical properties. A similar challenge is to study the mechanical properties of artificial materials [1, 2]. A great advance in this area is known as nanophotonics,

which tries to solve the information transmission lossless problem through light. Continuous search for new technologies has brought surprising properties to a new materials class known as photonic crystals (PC) [3]. These artificial materials can serve as the new raw material for photonic circuits age. These applications include both submicron sized laser sources as conducting channels (optical waveguides) and logical components (amplifiers, transistors photonic, etc.). Essentially, a photonic crystal is a material with a periodic arrangement composed of multiple elements distributed which scatters light in a coherent and cooperative way. This produces, a similar mechanism that have the electrons in semiconductors, a forbidden energy range for photons propagation, in this case a photonic forbidden gap (gap), which allows control light propagation. By combination and structuration of these elements, photonic circuits can be designed similar to electronics with cables, switches, splitters, and so forth.

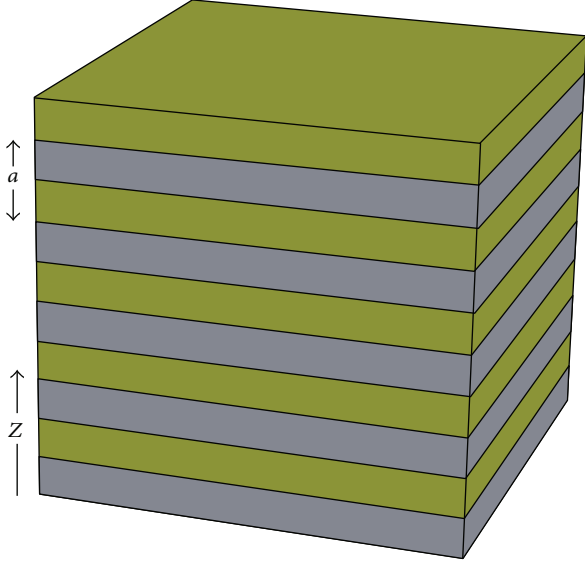


FIGURE 1: Superlattice or 1D binary photonic crystal. Periodicity in Z direction.

If the wavelength of the light is greater than the photonic crystal lattice constant, the properties can be described by means of homogeneous medium effective parameters. These parameters can explain the optical properties of photonic crystals in a simple and clear manner. The calculation of these parameters is one of the great interesting theoretical problems.

Homogenization theory of photonic crystals with metallic and magnetic inclusions is presented. Explicit formulas for permittivity and not local permeability tensors calculation are obtained and the application of these relations to calculate the effective parameters of a dielectric-magnetic 1D periodicity photonic crystal is illustrated. Finally, the theoretical results are compared with respect to theories based on bianisotropic response.

## 2. Material Characterization

*2.1. Lattice Homogenization with Metalomagnetic Inclusions.* Let us consider a 1D PC composed of metallic and magnetic inclusions. A 1D binary crystal (composed of two materials) representation is shown in Figure 1.

The metalomagnetic isotropic inclusions properties of the photonic crystal will be fully described by two material parameters: the permittivity and permeability, which are position functions; therefore,

$$\begin{aligned} \varepsilon(z) &= \varepsilon_0 + \frac{i}{\omega} \hat{\sigma}(z), \mu(z) \\ \hat{\sigma}(z) &= \sigma(z) - i\omega\varepsilon_0\chi(z), \end{aligned} \quad (1)$$

having the same periodicity as the 1D PC. Here,  $\sigma(z)$  and  $\chi(z)$  are the usual conductivity and electric susceptibility for isotropic materials in the unit cell. Note that, for metals,  $\hat{\sigma} = \sigma$ , for dielectrics,  $\hat{\sigma} = -i\omega\chi$ , and, for air,  $\hat{\sigma} = 0$  [4].

According to these assumptions, you can study electromagnetic fields behavior in PC at structural level using “microscopic” Maxwell’s equations:

$$\nabla \times \mathbf{h}(\mathbf{r}) = \mathbf{j}(\mathbf{r}) - i\omega\varepsilon_0\mathbf{e}(\mathbf{r}), \quad (2)$$

$$\nabla \cdot \mathbf{e}(\mathbf{r}) = -\frac{i}{\varepsilon_0\omega} \nabla \cdot \mathbf{j}(\mathbf{r}), \quad (3)$$

$$\nabla \times \mathbf{e}(\mathbf{r}) = i\omega\mathbf{b}(\mathbf{r}), \quad (4)$$

$$\nabla \cdot \mathbf{b}(\mathbf{r}) = 0. \quad (5)$$

Furthermore, current density  $\mathbf{j}$  and magnetic induction  $\mathbf{b}$  are related to magnetic field  $\mathbf{h}$  and electric field  $\mathbf{e}$  by materials equations:

$$\mathbf{j}(\mathbf{r}) = \hat{\sigma}(z)\mathbf{e}(\mathbf{r}), \quad (6)$$

$$\mathbf{b}(\mathbf{r}) = \mu(z)\mathbf{h}(\mathbf{r}).$$

Given the 1D PC periodicity, the generalized conductivity and magnetic permeability can be expanded in Fourier series:

$$\begin{aligned} \hat{\sigma}(z) &= \sum_{G_z} \hat{\sigma}(G_z) e^{iG_z z}, \\ \mu(z) &= \sum_{G_z} \mu(G_z) e^{iG_z z}, \end{aligned} \quad (7)$$

$G_z$  being the 1D lattice reciprocal vectors.

## 3. Average Fields

The  $\mathbf{e}(\mathbf{r})$  and  $\mathbf{b}(\mathbf{r})$  “microscopic” fields within the periodic structure obey the Bloch theorem. Therefore, fields are obtained in Bloch wave form:

$$\begin{aligned} \mathbf{e}(\mathbf{r}) &= e^{i\mathbf{k}\cdot\mathbf{r}} \sum_{G_z} \mathbf{e}(G_z) e^{iG_z z} \\ &= e^{i\mathbf{k}\cdot\mathbf{r}} \mathbf{e}(G_z = 0) + e^{i\mathbf{k}\cdot\mathbf{r}} \sum'_{G_z} \mathbf{e}(G_z) e^{iG_z z}, \\ \mathbf{b}(\mathbf{r}) &= e^{i\mathbf{k}\cdot\mathbf{r}} \sum_{G_z} \mathbf{b}(G_z) e^{iG_z z} \\ &= e^{i\mathbf{k}\cdot\mathbf{r}} \mathbf{b}(G_z = 0) + e^{i\mathbf{k}\cdot\mathbf{r}} \sum'_{G_z} \mathbf{b}(G_z) e^{iG_z z}, \end{aligned} \quad (8)$$

where  $\sum'$  indicates that  $G_z = 0$  term is excluded from the sum.

For macroscopic electromagnetic fields, the corresponding microscopic fields (8) are averaged over a length  $L$  much greater than the lattice constant  $a$  but much smaller than the wavelength  $2\pi/k$  ( $a \ll L \ll 2\pi/k$ ). This averaging procedure smooths the rapid oscillations of the microscopic fields within the interval of length  $L$ . Thus, in the case of wavelengths much larger than the lattice constant  $a$ ,

$$ka \ll 1, \quad (9)$$

and macroscopic fields are described as plane waves:

$$\begin{aligned}\mathbf{E}(\mathbf{r}) &\equiv \langle \mathbf{e}(\mathbf{r}) \rangle = \mathbf{e}(G_z = 0) e^{i\mathbf{k}\cdot\mathbf{r}} = \mathbf{E}_0 e^{i\mathbf{k}\cdot\mathbf{r}}, \\ \mathbf{B}(\mathbf{r}) &\equiv \langle \mathbf{b}(\mathbf{r}) \rangle = \mathbf{b}(G_z = 0) e^{i\mathbf{k}\cdot\mathbf{r}} = \mathbf{B}_0 e^{i\mathbf{k}\cdot\mathbf{r}}.\end{aligned}\quad (10)$$

Another equivalent way to define the macroscopic fields is to eliminate the  $G_z \neq 0$  terms in (8) expansions. This definition is correct when inequality (9) is accomplished and the  $G_z = 0$  component in such expansions proves to be a smooth function in variations over distances much larger than the lattice constant.

#### 4. Permittivity and Permeability Effective

In a homogeneous magnetic medium, the constitutive equations that describe the relationship of the displacement  $\mathbf{D}$  and the magnetic induction  $\mathbf{B}$  vectors to the electric field  $\mathbf{E}$  and magnetic field  $\mathbf{H}$  can be written as

$$\begin{aligned}\mathbf{D} &= \overleftrightarrow{\varepsilon} \cdot \mathbf{E}, \\ \mathbf{B} &= \overleftrightarrow{\mu} \cdot \mathbf{H},\end{aligned}\quad (11)$$

where  $\overleftrightarrow{\varepsilon}$  and  $\overleftrightarrow{\mu}$  are the permittivity and permeability tensors. Maxwell's equations in this case are written in the form

$$\nabla \times \mathbf{H} = -i\omega \overleftrightarrow{\varepsilon} \cdot \mathbf{E}, \quad (12)$$

$$\nabla \cdot \mathbf{D} = 0, \quad (13)$$

$$\nabla \times \mathbf{E} = i\omega \mathbf{B}, \quad (14)$$

$$\nabla \cdot \mathbf{B} = 0. \quad (15)$$

Removing the magnetic field  $\mathbf{H}$  in (12) and (14) and using (11), the wave equation is obtained in electric field  $\mathbf{E}$  terms:

$$\mathbf{k} \times \overleftrightarrow{\mu}^{-1} \cdot (\mathbf{k} \times \mathbf{E}_0) + \omega^2 \overleftrightarrow{\varepsilon} \cdot \mathbf{E}_0 = 0. \quad (16)$$

Equivalently, the electric field  $\mathbf{E}$  can be eliminated from (12) and (14), and write the wave equation for magnetic field  $\mathbf{H}$ :

$$\mathbf{k} \times \overleftrightarrow{\varepsilon}^{-1} \cdot (\mathbf{k} \times \mathbf{H}_0) + \omega^2 \overleftrightarrow{\mu} \cdot \mathbf{H}_0 = 0. \quad (17)$$

To obtain photonic crystal effective tensors, (16) and (17) must be compared with macroscopic fields exact equations that satisfy  $\mathbf{E}_0 = \mathbf{e}(0)$  and  $\mathbf{H}_0 = \mathbf{h}(0)$  amplitudes. Equations (6)–(8) are substituted in (2) and (4) and expansions are used:

$$\frac{1}{\varepsilon(z)} = \sum_{G_z} \eta(G_z) e^{-iG_z z}, \quad (18)$$

$$\frac{1}{\mu(z)} = \sum_{G_z} \xi(G_z) e^{-iG_z z}.$$

Removing the magnetic field components, an electric field components equations system is obtained:

$$\sum_{G'_z} \overleftrightarrow{\mathbf{D}}_{\mathbf{E}}(\mathbf{k}; G_z, G'_z) \cdot \mathbf{e}(G'_z) = 0, \quad (19)$$

where

$$\begin{aligned}\overleftrightarrow{\mathbf{D}}_{\mathbf{E}}(\mathbf{k}; G_z, G'_z) &= (\mathbf{k} + G_z \hat{z}) \\ &\times \xi(G_z - G'_z) (\mathbf{k} + G'_z \hat{z}) \times \overleftrightarrow{\mathbf{I}} \\ &+ (i\omega \hat{\sigma}(G_z - G'_z) + \varepsilon_0 \omega^2) \overleftrightarrow{\mathbf{I}}.\end{aligned}\quad (20)$$

Here  $\overleftrightarrow{\mathbf{I}}$  is the unitary dyadic. From equations with  $G_z \neq 0$  (19),  $\mathbf{e}(G_z)$  components can be expressed in  $\mathbf{e}(0)$  component terms. Substituting in the  $G_z = 0$  equation, equations system (19) takes the form

$$\left\{ \overleftrightarrow{\mathbf{D}}_{\mathbf{E}}^{-1}(\mathbf{k}; G_z = 0, G'_z = 0) \right\}^{-1} \cdot \mathbf{e}(G_z = 0) = 0. \quad (21)$$

Here,  $\overleftrightarrow{\mathbf{D}}_{\mathbf{E}}^{-1}(0, 0)$  is a  $3 \times 3$  block, obtained from the inverse of the matrix (20). Similarly, the magnetic field  $\mathbf{e}(G_z)$  components equations system is obtained:

$$\sum_{G'_z} \overleftrightarrow{\mathbf{D}}_{\mathbf{H}}(\mathbf{k}; G_z, G'_z) \cdot \mathbf{h}(G'_z) = 0, \quad (22)$$

where

$$\begin{aligned}\overleftrightarrow{\mathbf{D}}_{\mathbf{H}}(\mathbf{k}; G_z, G'_z) &= (\mathbf{k} + G_z \hat{z}) \\ &\times \eta(G_z - G'_z) (\mathbf{k} + G'_z \hat{z}) \times \overleftrightarrow{\mathbf{I}} \\ &+ \omega^2 \mu(G_z - G'_z) \overleftrightarrow{\mathbf{I}}.\end{aligned}\quad (23)$$

Eliminating  $G_z$  nonzero components in (22), an  $\mathbf{h}(0)$  homogeneous algebraic equation is obtained:

$$\left\{ \overleftrightarrow{\mathbf{D}}_{\mathbf{H}}^{-1}(\mathbf{k}; G_z = 0, G'_z = 0) \right\}^{-1} \cdot \mathbf{h}(G_z = 0) = 0, \quad (24)$$

where  $\overleftrightarrow{\mathbf{D}}_{\mathbf{H}}^{-1}(0, 0)$  is a  $3 \times 3$  block, from the inverse of the matrix (23).

#### 5. Effective Parameters

Equating (16) and (17) with (21) and (24), respectively, a system of two algebraic equations that define the effective tensors  $\overleftrightarrow{\varepsilon}$  and  $\overleftrightarrow{\mu}$  is obtained:

$$\begin{aligned}\overleftrightarrow{\varepsilon}_{\text{eff}}(\mathbf{k}) &= \frac{1}{\omega^2} \left\{ \left[ \overleftrightarrow{\mathbf{D}}_{\mathbf{E}}^{-1}(\mathbf{k}; 0, 0) \right]^{-1} - \mathbf{k} \times \overleftrightarrow{\mu}_{\text{eff}} \cdot \mathbf{k} \times \overleftrightarrow{\mathbf{I}} \right\}, \\ \overleftrightarrow{\mu}_{\text{eff}}(\mathbf{k}) &= \frac{1}{\omega^2} \left\{ \left[ \overleftrightarrow{\mathbf{D}}_{\mathbf{H}}^{-1}(\mathbf{k}; 0, 0) \right]^{-1} - \mathbf{k} \times \overleftrightarrow{\varepsilon}_{\text{eff}} \cdot \mathbf{k} \times \overleftrightarrow{\mathbf{I}} \right\}.\end{aligned}\quad (25)$$

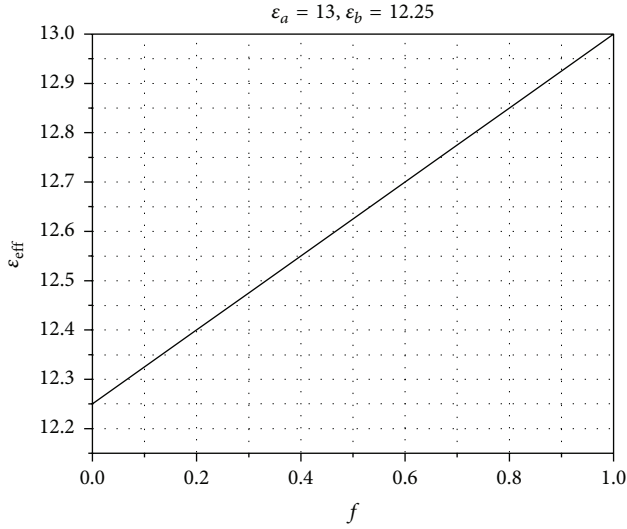


FIGURE 2: Effective permittivity versus filling fraction.

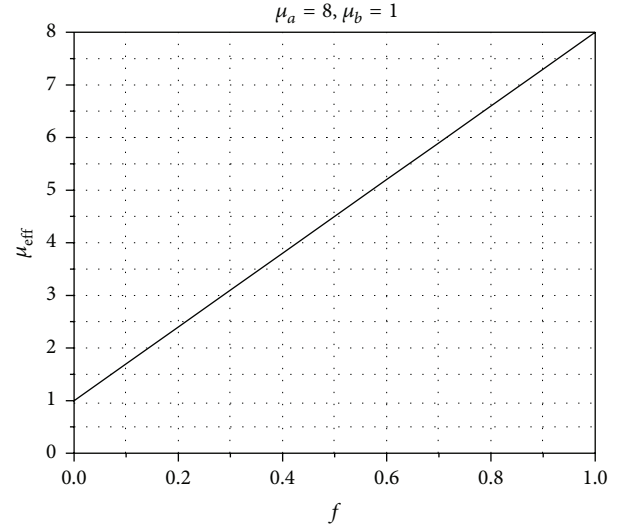


FIGURE 3: Effective permeability versus filling fraction graphic representation.

In the long wavelengths limit case ( $k = 0$ ), the effective tensors are given explicitly by

$$\begin{aligned} \overleftrightarrow{\epsilon}_{\text{eff}}(0) &= \frac{1}{\omega^2} \left[ \overleftrightarrow{\mathbf{D}}_{\mathbf{E}}^{-1}(0; 0, 0) \right]^{-1}, \\ \overleftrightarrow{\mu}_{\text{eff}}(0) &= \frac{1}{\omega^2} \left[ \overleftrightarrow{\mathbf{D}}_{\mathbf{H}}^{-1}(0; 0, 0) \right]^{-1}. \end{aligned} \quad (26)$$

## 6. Results

The results obtained with the theory developed in the previous section are described in this section. The effective permittivity and permeability for a 1D photonic crystal composed of alternating layers of dielectric and magnetic materials in the direction of  $z$  are calculated. The set of parameters for the calculation are:  $\epsilon_b = 12.25$  and  $\mu_b = 1$  for dielectric matrix (host) and  $\epsilon_a = 13$  and  $\mu_a = 8$  for isotropic ferrite layer (inclusion) [5].

In Figures 2 and 3, effective permeability and permittivity tensors perpendicular components  $\epsilon_{\text{eff}} = \epsilon_{xx} = \epsilon_{yy}$  and  $\mu_{\text{eff}} = \mu_{xx} = \mu_{yy}$  behavior is showed versus magnetic inclusion filling fraction ( $f = d_a/a$ , where  $d_a$  is the magnetic layer thickness).

Local approach was used in calculations; that is,  $\mathbf{k} = 0$  (see (26) formulas).  $\epsilon_{\text{eff}}$  permittivity and  $\mu_{\text{eff}}$  permeability calculated are filling fraction  $f$  functions and are in agreement with classical quasistatic results:  $\epsilon_{\text{eff}} = \epsilon_a f + \epsilon_b(1 - f)$ ,  $\mu_{\text{eff}} = \mu_a f + \mu_b(1 - f)$ .

The formulas obtained in the previous section are validated with these results and open the possibility for future studies of electromagnetic waves propagation in 1D PC non-local effects. In such case, it will be necessary to include in the formulas obtained in this work (25) the dispersion relation  $\mathbf{k}(\omega)$ . Considering the condition  $ka \ll 1$  (9) gives nonlocal effective permittivity and permeability corrections.

## 7. Conclusions

The analytical relationships for 1D periodical photonic crystal effective permittivity and permeability tensors with periodicity  $a$  were obtained. Demonstrating that effective  $\epsilon$ - $\mu$  material response of photonic crystal is not local (25), thus the photonic crystal homogenized effective parameters depend on wave vector. We point out that theoretical formalism developed in this work uses only two effective tensors: permittivity and permeability (25), unlike the bianisotropic response [4–7], which uses four effective tensors (permittivity, permeability, and two magnetoelectric tensors). Obviously, permittivity and permeability definitions used here and the bianisotropic approach [4–7] are different for finite wave vectors. However, in the local case ( $\mathbf{k} = 0$ ) the definitions are in agreement. Unlike the previous works [5–11], in this limit, our formulas provide the dependence of the effective parameters in photonic crystals upon the filling fraction of the inclusions.

## Competing Interests

The authors declare that they have no competing interests.

## Acknowledgments

This work was supported by Faculty of Electronic Science (FCE), BUAP, Mexico.

## References

- [1] G. De Felice and N. Rizzi, "Homogenization for materials with microstructure," *Pressure Vessels and Piping Division of the American Society of Mechanical Engineers*, vol. 369, pp. 33–38, 1997.
- [2] A. Cecchi and N. L. Rizzi, "Heterogeneous elastic solids: a mixed homogenization-rigidification technique," *International Journal of Solids and Structures*, vol. 38, no. 1, pp. 29–36, 2000.

- [3] J. D. Joannopoulos, S. G. Johnson, J. N. Winn, and R. D. Meade, *Photonic Crystals: Molding the Flow of Light*, Princeton University Press, Princeton, NJ, USA, 2008.
- [4] P. Halevi and F. Pérez-Rodríguez, "From photonic crystals (via homogenization) to metamaterials," in *Proceedings of the Complex Photonic Media*, vol. 6320 of *Proceedings of SPIE*, San Diego, Calif, USA, August 2006.
- [5] E. Reyes-Ayona and P. Halevi, "Mean field theory of metallo-dielectric photonic crystals with magnetic components: the long-wavelength limit," in *Photonic Metamaterials, 66380G*, vol. 6638 of *Proceedings of SPIE*, September 2007.
- [6] V. Cerdán-Ramírez, B. Zenteno-Mateo, M. P. Sampedro, M. A. Palomino-Ovando, B. Flores-Desirena, and F. Pérez-Rodríguez, "Anisotropy effects in homogenized magnetodielectric photonic crystals," *Journal of Applied Physics*, vol. 106, Article ID 103520, 2009.
- [7] J. A. Reyes-Avendaño, U. Algreto-Badillo, P. Halevi, and F. Pérez-Rodríguez, "From photonic crystals to metamaterials: the bianisotropic response," *New Journal of Physics*, vol. 13, Article ID 073041, 2011.
- [8] A. A. Krokhnin and E. Reyes, "Homogenization of magnetodielectric photonic crystals," *Physical Review Letters*, vol. 93, no. 2, Article ID 023904, 2004.
- [9] E. Reyes, A. A. Krokhnin, and J. Roberts, "Effective dielectric constants of photonic crystal of aligned anisotropic cylinders and the optical response of a periodic array of carbon nanotubes," *Physical Review B*, vol. 72, no. 15, Article ID 155118, 2005.
- [10] A. A. Krokhnin, E. Reyes, and L. Gumen, "Low-frequency index of refraction for a two-dimensional metallodielectric photonic crystal," *Physical Review B*, vol. 75, no. 4, Article ID 045131, 2007.
- [11] G. P. Ortiz, B. E. Martínez-Zérega, B. S. Mendoza, and W. L. Mochán, "Effective optical response of metamaterials," *Physical Review B*, vol. 79, no. 24, Article ID 245132, 9 pages, 2009.